UNIVERSITY OF OKLAHOMA

GRADUATE COLLEGE

MULTISCALE MODELING OF NANOPARTICLES TRANSPORT, AGGREGATION, AND IN SITU GELATION IN POROUS MEDIA

A DISSERTATION

SUBMITTED TO THE GRADUATE FACULTY

in partial fulfillment of the requirements for the

Degree of

DOCTOR OF PHILOSOPHY

By

ELSAYED ABDELFATAH
Norman, Oklahoma
2017

MULTISCALE MODELING OF NANOPARTICLES TRANSPORT, AGGREGATION, AND IN SITU GELATION IN POROUS MEDIA

A DISSERTATION APPROVED FOR THE
MEWBOURNE SCHOOL OF PETROLEUM AND GEOLOGICAL ENGINEERING

BY

_____
Dr. Maysam Pournik, Chair

_____
Dr. Jeffrey Harry Harwell

_____
Dr. Bor-Jier (Ben) Shiau

_____
Dr. Ahmad Jamili

_____
Dr. Ahmad Ghassemi

DEDICATION

This dissertation is dedicated to my wife Samar, my kids Hana and Adam, my parents Raafat and Umm Kulthum, and my sisters Fatima and Zeinab, my brothers Mohamed and Mahmoud, my parents-in-law Salah Eldin and Bahia, and my brothers-in-law Mahmoud and Abdelrahman.

Thank you for endless love, sacrifices and supports.

Acknowledgements

First and most importantly, I would like to express my deepest appreciation to my adviser, Dr. Maysam Pournik for all his invaluable guidance and constant support during my doctoral study at University of Oklahoma. His insightful knowledge and experience have been very influential in both my research and study. I have learned tremendously from working with him and I am truly grateful to be one of his students. His moral standards and sincerity will be always a role model for me.

I would like to thank Dr. Jeffrey Harwell and Dr. Bor Jier (Ben) Shiau, for their time and insightful discussion during my doctoral study. Our discussions and meeting have enriched my knowledge of colloids and surface science. I would like also to thank the members of committee, Dr. Ahmad Jamili, and Dr. Ahmad Ghassemi, for spending their precious time reading this dissertation and giving very valuable comments and suggestions.

I would like to extend my appreciation to all faculties, staff, and colleagues in the Mewbourne School of Petroleum and Geological Engineering for all their support and advice and for making my doctoral study so meaningful and inspiring. My very special thanks go to Sangho Bang and Kang Kang for always being my biggest supporter and to my officemates Amirhossein Kamali, Behzad Hemami, Laura Hernandez, Ruben Gonzalez, and Michael Janis for all the nice moments and discussions. I would also like to thank the undergraduate students who worked with me during my doctoral study: David Craig, Scott C. Zickefoose, Oleksandr B. Romanyuk, and Sergio Silva. Finally, I

would like to thank my friend Rida Elgaddafi and his wife Manal for all their support and nice moments we spent together.

I want to express my gratitude to Abu Dhabi National Oil Company (ADNOC) for the funding support of this dissertation.

I am indebted to my parents Raafat and Umm Kulthum, and my sisters Fatima and Zeinab, my brothers Mohamed and Mahmoud, my parents-in-law Salah Eldin and Bahia, and my brothers-in-law Mahmoud and Abdelrahman for their unconditional love and support. I have great thanks and gratitude to my lovely wife, Samar and my kids, Hana and Adam. I would not be the person I am today without them in my life and for that, I am truly deeply grateful.

Table of Contents

List of Tables

List of Figures

Abstract

Nanoparticle applications in the petroleum industry have grown recently especially in EOR and well stimulation. Transport of nanoparticles in porous media involves different interaction mechanisms either between nanoparticles and porous media (adsorption and release from pore surface, single-particle plugging, and multi-particles plugging) or inter-nanoparticle (aggregation and gelation). This dissertation aims to provide mathematical and numerical framework for multiscale modeling of nanoparticles transport in porous media including all these different interaction mechanisms for the first time.

First, mechanistic model based on Extended DLVO theory is developed to study the rate of deposition and release of nanoparticles in porous media at different temperature, ionic strength, and pH. Empirical equation has been derived to calculate zeta potential at different conditions. The effect of surface roughness has been included in the model using the effective height and density of the surface roughness distribution. Numerical model has been used to compare the theoretically calculated rates with several experimental data. The model shows good fitting with different experimental results.

Secondly, although the nanoparticles are small, they can be retained in the porous media by three different damage mechanisms i.e. surface deposition, mono-particle plugging, and multi-particles plugging. We have developed a mathematical model that captures these different damage mechanisms. The model is validated with experimental data to obtain the model parameters. Sensitivity analysis is presented using the proposed numerical model. The preliminary numerical results demonstrate that nanoparticle size,

concentration, injection rate and permeability are the dominant factors that control the degree of formation damage.

Thirdly, Population Balance Equation (PBE) is used to model the kinetics of aggregation and gelation of nanoparticles in batch. Quadrature Method of Moments (QMOM) is used to convert the PBE with continuous distribution of nanoparticle size into a set moment equations for efficient computation. The modeled developed in this study is used to compare between the kinetics of aggregation and gelation of fumed silica and colloidal silica nanoparticles at the same conditions. The case studies presented show a unique behavior of fumed silica over colloidal silica nanoparticles for forming a gel network at significantly low concentration.

Finally, QMOM-PBE is coupled with fluid flow model to predict the nanoparticles aggregation and interactions in porous media. Changes in nanoparticle size and shape due to inter–particle interactions (i.e. aggregation) may significantly affect particle mobility and retention in porous media. Model sensitivity analysis shows the influence of particle concentration and interstitial velocity gradient on inter–particle, and, consequently, particle–collector interactions. Also, filtration prevents the buildup of viscosity of the fluid in porous media compared to batch. However, in free media where filtration is negligible like fractures, viscous fluid or soft gel can be formed.

This dissertation attempts to answer the critical questions pertaining the coupling of aggregation and in situ gelation on the nanoparticles transport in porous media. The model can be further extended to simulate different nanoparticles-based applications in

oil and gas reservoirs such as acid diversion, water shutoff, conformance control, and hydraulic fracturing.

Chapter 1 Introduction

1.1.Background

Nanotechnology has gained a wide interest in the oil and gas industry during the past decade. Nanotechnology is the science and engineering of particles at the nanoscale (nanoparticles), which are about 1 to 100 nanometers in size. Nanoparticles have been applied in many aspects of the upstream petroleum industry such as enhanced oil recovery (Ogolo et al. 2012, Fletcher and Davis 2010), well stimulation (McElfresh et al. 2012a), drilling fluids (Mahmoud et al. 2016) , hydraulic fracturing fluids (Fakoya and Shah 2014, 2016), well cementing (Omosebi et al. 2017), formation softening in shale (Mehana et al. 2017), and fines fixation (Huang et al. 2008). Different types of nanoparticles has been used such as silica nanoparticles, alumina nanoparticles, and carbon nanotubes (Pham et al. 2016, Chen et al. 2016, Kadhum et al. 2015, Weston et al. 2014).

Transport of nanoparticles in porous media involves different interaction mechanisms either between nanoparticles and porous media or between inter-nanoparticles (Fig. 1-1). The interaction between nanoparticles and porous media involves three different mechanisms; adsorption and release from pore surface, single-particle plugging, and multi-particles plugging (Abdelfatah et al. 2017a, Abdelfatah et al. 2017b, Abdelfatah et al. 2017d, Abdelfatah et al. 2017c). The effect of these different mechanisms depends on nanoparticle size, concentration, injection rate, salinity, temperature, and permeability of the porous media as explained in chapter 2 and chapter 3.

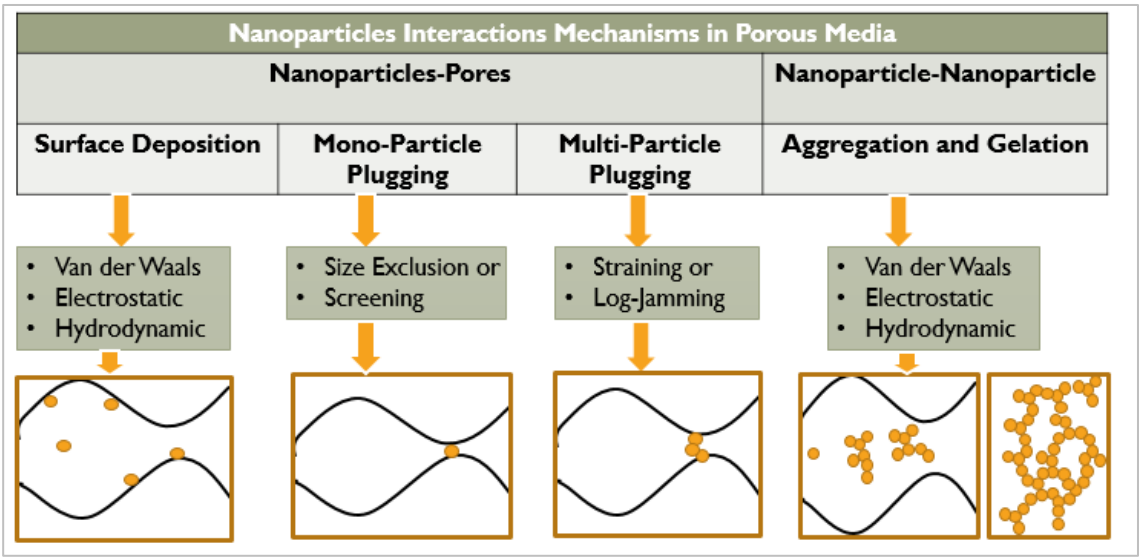

Figure 1-1—Schematic ilustration of nanoparticles interaction mechanisms in porous media.

Inter-nanoparticles interaction is significantly effective when the nanoparticles and salt concentrations are high enough to promote aggregations of nanoparticles (Chen et al. 2005). The aggregation of nanoparticles is due to particles brought close together via two main mechanisms; perikinetic (diffusion-induced) and orthokinetic (shear-induced). The sticking efficiency of nanoparticles depends on the energy barrier between the particles. The height of the energy barrier depends on the salt concentration, temperature, and pH of the solution. Aggregate size distribution evolves as aggregation continues, and once it spans the space, it forms a gel (Metin et al. 2014, Weston et al. 2014). Aggregation and gelation of nanoparticles have significant effect on the transport of nanoparticles in porous media. The kinetics of aggregation and gelation of nanoparticles and coupled transport and aggregation will be discussed further in details in chapter 4 and chapter 5.

1.2.Outlines of dissertation

The dissertation consists of a set of papers that has been published in, submitted to or prepared for submission to scholarly journals.

Chapter 2 is the paper titled *Mechanistic Study of Nanoparticles Deposition and Release in Porous Media*. This paper is submitted to Journal of Petroleum Science and Engineering.

Chapter 3 is the paper titled *Mathematical Modeling and Simulation of Nanoparticles Transport in Heterogeneous Porous Media*. This paper is published in Journal of Natural Gas Science and Engineering.

Chapter 4 is the paper titled *Modeling of Aggregation and Gelation of Nanoparticles Using Quadrature Method of Moments*. This paper will be submitted soon.

Chapter 5 is the paper titled *Modeling Coupled Transport, Aggregation and In Situ Gelation of Nanoparticles in Porous Media*. This paper will be submitted soon.

Chapter 6 summarizes the general conclusions from the current research study.

Chapter 2 Mechanistic Study of Nanoparticles Deposition and Release in Porous Media

Abstract

Physicochemical interaction between the nanoparticles and the pore walls can cause significant retention of nanoparticles in porous media. The objective here is to provide mechanistic model based on Extended DLVO theory to study the rate of deposition and release of nanoparticles in porous media at different temperature, ionic strength, and pH. Empirical equation has been derived to calculate zeta potential at different temperature, ionic strength, and pH. The interaction energy can be with/without energy barrier between the nanoparticles and the pore surface. The rate of deposition and release of nanoparticles in each case has been derived. Numerical model has been used to compare the theoretically calculated rates with several experimental data. Increasing the temperature decreases the energy barrier height and increases the rate of deposition. With increasing the ionic strength, the thickness of the electrostatic double layer decreases and hence the rate of deposition increases. The effect of pH on the rate of deposition depends on the location of environment pH with respect to the isoelectric point of the nanoparticles and rock. For the extreme values of pH, energy barrier exists and rate of deposition is low. However, when the pH of the solution is between the isoelectric points of the nanoparticles and rock, the energy barrier decreases and the rate of deposition increases. The rate of deposition is time dependent as it decreases with increasing the covered rock surface. The effect of surface roughness has been included in the model using the effective height and density of the surface roughness distribution. Finally, these theoretically calculated rate values are used in a numerical model of the advection-

dispersion equation with source/sink term. Several experimental results have been perfectly matched that validate the theoretical calculations of the rate of deposition. The new mechanistic model for nanoparticles can be used to determine the fate of nanoparticles in porous media under different conditions of temperature, ionic strength, concentration, and pH. This model can help to understand the nanoparticles transport in porous media and effectively design nanoparticles fluid for injection into oil and gas reservoirs.

Keywords:
Extended DLVO theory; Zeta Potential; Nanoparticles; Deposition; Release; Porous media

2.1. Introduction

In the past decade, the applications of nanotechnology in the oil and gas industry have attracted many researchers (Mahmoud et al. 2016, Esfandyari Bayat et al. 2015, Abdelfatah et al. 2014, Hendraningrat and Torsæter 2014, McElfresh et al. 2012a, Caldelas et al. 2011, Ju and Fan 2009, Binks et al. 2008, Huang et al. 2008). However, the injection of nanofluid into reservoir may cause formation damage by the retention of nanoparticles (NPs) in porous medium (Ju and Fan 2009). Both experimental and modeling investigations were carried out to study the transport and retention of nanoparticle in reservoir rocks (Rahman et al. 2014, Yu et al. 2012, Zhang 2012). The mechanism of nanoparticle retention at the pore scale is a complex phenomenon. McCarthy et al. (1989) introduced two main types of retention in saturated granular medium, deposition and straining. Deposition and release of nanoparticles to the rock pore surface is mainly due to the physicochemical interactions, while straining is the

mechanical entrapment of single or multiple nanoparticle plugging at pore throat which are too small to allow nanoparticles to pass. When the size of nanoparticle is several orders of magnitude smaller than the rock grains or the rock pore space, all retention of nanoparticles is contributed by deposition (Zhang 2012, Yao et al. 1971). Derjaguin-Landau-Verwey-Overbeek (DLVO) theory can be used to evaluate the physicochemical interactions between the nanoparticles and rock pore surface, where van der Waals attraction and electrical double layer interaction are the two major interactions (Derjaguin and Landau 1993, Verwey and Overbeek 1948). DLVO theory has been successfully employed to analyze colloid stability in aqueous suspensions assuming the total DLVO interaction energy is the sum of van der Waals energy and electrostatic double layer energy (Adamczyk and Weroński 1999). When the separation distance between two surfaces are less than a few nanometers, short-range repulsions such as Born repulsion and hydration repulsion present (Hoek and Agarwal 2006). Adding these repulsions, which are called non-DLVO forces, into the classical DLVO theory more accurate total DLVO interaction energy is obtained (Ghosh 2009). Particle size, separation distance, surface charge, ionic strength, pH, temperature, and surface roughness of the rock are the main factors that control the total DLVO interaction energy (Yu et al. 2012). Rate of deposition of different nanoparticles (NPs) through different reservoir rocks varies widely and was found to be strongly dependent on nanoparticle and rock grain surface charge. Many researches indicated the significant effect of ionic strength on deposition of nanoparticles, because the electrical double layer interaction is highly dependent on ionic strength. Rahman et al. (2014) showed that alumina nanoparticle deposition increased with increasing ionic strength. Caldelas (2010) found a noticeable increase of surface-

coated silica nanoparticles deposition on Boise sandstone at higher ionic strengths. Brant et al. (2005) indicated that zeta potential as a function of pH and ionic strength, affects the deposition rate. Reyes Bahena et al. (2002) showed zeta potential of alumina nanoparticle decreases as pH increases at constant ionic strength, and decreases as ionic strength increase at the same pH. Zeta potential of nanoparticles and rock grain surface charge control the double layer interaction which governs the total DLVO interaction. Caldelas et al. (2011) studied the effect of temperature on deposition of silica nanoparticle through sandpack with crushed Boise sandstone. They found a slight increase of deposition when the temperature was raised from 55^{o}C to 80^{o}C. Besides, several experimental investigations on colloids transport through porous media suggested that rate of deposition is affected by the surface roughness of porous media. It is observed consistently that higher rate of deposition occurs on rougher surfaces, where the roughness is generally recognized by average height and density of protrusions (Shellenberger and Logan 2002, Hoek et al. 2003).

The goal of this paper is to provide a mechanistic model for nanoparticle deposition in porous media. First, the modified equation for zeta potential is presented in section 2.2. This equation accounts for the effect of the environment variables i.e. pH, ionic strength, nanoparticle size, and temperature. In section 2.3, DLVO theory considering non-DLVO forces is used to analyze the interaction between nanoparticles and rock surface at different conditions. Equations for rate of deposition and release are presented based on the DLVO theory in section 2.4. Then, a numerical solution of the convection-diffusion equation with source/sink term accounting for nanoparticles retention in porous media is presented in section 2.5. This numerical model is used to validate the theoretical equations

for rate of deposition and release, by comparing the model results with the data in literature (section 2.6.1). The numerical model is also used for sensitivity analysis of the different environmental conditions on nanoparticles interaction in porous media (section 2.6.2). In section 2.7, the summary and conclusion are presented.

2.2. Zeta Potential

Zeta potential is the key parameter that controls the electrostatic interaction between dispersed nanoparticles and the rock surface. Zeta potential (ζ) cannot be measured directly but can be calculated from Henry's equation (Kim and Lawler 2005). However, as long as the absolute value of Zeta potential is less than $40\,mv$ in 1:1 electrolyte solution at room temperature, Henry's equation is the best approximation for zeta potential (Ohshima 1994). Henry's equation can be rearranged to calculate the zeta potential as the following,

$$\zeta = \frac{3U_E\mu}{2\epsilon f(\kappa a_p)} \tag{1}$$

U_E is electrophoretic mobility of a nanoparticle measured from electrokinetics experiment, ϵ is dielectric constant; μ is viscosity, kg.m^{-1}s^{-1}; κ is the inverse Debye length, m^{-1}; a_p is nanoparticle radius, m. $f(\kappa a_p)$ is the Henry's function. A simpler form of Henry's equation in which $f(\kappa a_p)$ = 1.5 is known as the Smoluchowski equation (Kaszuba et al. 2010), and applies for large particle ($\kappa a_p \sim 100$) in high ionic strength with thin double layer. However, for small particle in low ionic strength with thick double layer another simplification can be used that $f(\kappa a_p)$ = 1. (Eq. 2).

$$\kappa^{-1} = \sqrt{\frac{\epsilon k_B T}{2000 e^2 N_A I}} \tag{2}$$

$$I = \frac{1}{2}\sum_i z_i^2 M_i \tag{3}$$

where M_i is the molar concentration of the symmetric $(z{:}\,z)$ electrolyte of i[th] ion, in the unit of $\frac{mole}{dm^3}$; I is ionic strength, M; N_A is the Avogadro number; k_B is the Boltzmann constant; T is the temperature, K; e is the elementary charge, C.

To analyze DLVO interaction energy at various conditions, an empirical correlation is modified to estimate zeta potential of nanoparticle and rock grain at different pH, ionic strength and temperature based on experimental measurements reported in literatures. The effect of ionic strength is corrected by Henry's function through the Debye length. Ohshima (1994) presented a simple approximate expression for Henry's function which is applicable for any value of κa_p

$$f(\kappa a_p) = 1 + \frac{1}{2[1 + \frac{2.5}{\kappa a_p (1 + e^{-\kappa a_p})}]} \tag{4}$$

Based on the treatment of double layer at a solid particle/electrolyte solution interface by Gouy–Chapman–Stern model, the electrical potential measured at the shear plane can be referred to as the zeta potential (Oldham 2008). Fig. 2-1 shows potential (ψ_x) at a distance x from colloid surface decreases exponentially from surface potential. Ding et al. (2014) indicated that the shear plane is far away from the stern plane and very close to the Gouy plane, which locates at the characteristic thickness of electrical double layer ($x_s \approx \kappa^{-1}$). Accordingly, the following expression can be used to related zeta potential and the surface potential.

$$\zeta = \psi_s \exp(-\kappa x_s) = \psi_s \exp(-1) \quad (5)$$

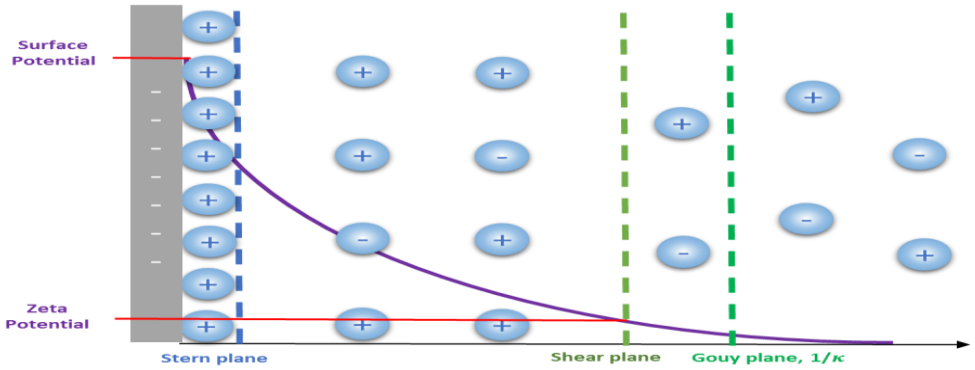

Figure 2-1—Position of shear plane and corresponding zeta potential in electrical double layer.

Counterions binding reactions can change the charge of the surface significantly. Hence, the pH of the solution has an important role on the interaction between nanoparticles and the rock surface (Bousse et al. 1983). According to Pfeiffer et al. (2014), the influence of pH of colloidal nanoparticles is affected by oxidation of surface atoms and a pH-dependent equilibrium between AO^-/AOH and AOH/AOH_2^+ species. van den Vlekkert et al. (1988) developed a theoretical model to determine the surface potential depending on pH of the environment:

$$2.303(pH_{IEP} - pH) = -\frac{e\psi_s}{k_B T} + sinh^{-1}(\frac{e\psi_s}{\beta k_B T}) \quad (6)$$

Where pH_{IEP} is the isoelectric point of the surface. ψ_s is the surface potential, mV. β is a parameter that characterize the sensitivity of the surface that is nearly equal 0.4 for SiO_2 and 4.8 for Al_2O_3 (Bousse and Meindl 1987, Bousse et al. 1983). The model can be linearly approximated around the isoelectric point (IEP).

$$\psi_s = \frac{\beta}{\beta+1}\frac{2.3k_BT}{e}(pH_{IEP} - pH) = m_1\frac{2.3k_BT}{e}(pH_{IEP} - pH) \quad (7)$$

Bousse and Meindl (1987) and Reyes Bahena et al. (2002) discussed the surface reactions of oxide particles in aqueous electrolyte. At low pH, the surface will be charged positively by the adsorption of AOH_2^+, while it will be negatively charged by AO^- at high pH. For the oxide, whose surface OH sites only undergo amphoteric acid /base reactions, the two-surface acidic and basic reaction for surface site AOH are:

$$\begin{aligned} &\text{Acidic reaction: } AOH + H^+ \rightleftharpoons AOH_2^+;\ K_{a1} = \frac{[AOH_2^+]}{[H^+][AOH]} \\ &\text{Basic reaction: } AOH + OH^- \rightleftharpoons AO^- + H_2O;\ K_{a2} = \frac{[H_2O][AO^-]}{[AOH][OH^-]} \end{aligned} \quad (8)$$

Where K_{a1} and K_{a2} are the equilibrium constant of acidic and basic reaction. Pfeiffer et al. (2014) discussed the buffer effect away from IEP which leads to zeta potential changing at a lower rate within a region determined by the surface dominated acidic/basic reaction. The dominated reaction prevents the gain of negative/positive charges at the surface. The zeta potential can then be interpreted by two linear lines with a greater slope m_1 inside the fast change region and a smaller slope m_2 inside the slow change region. These two regions are divided by a cut-off point fitted from experiment measurements (Fig. 2-2).

$$\zeta = \begin{cases} m_1\dfrac{0.85k_BT}{f(\kappa a_p)e}(pH_{IEP} - pH), & fast\ change\ region \\ \zeta_{cut-off} + \dfrac{m_2}{f(\kappa a_p)}\left(pH_{cut-off} - pH\right), & slow\ change\ region \end{cases} \quad (9)$$

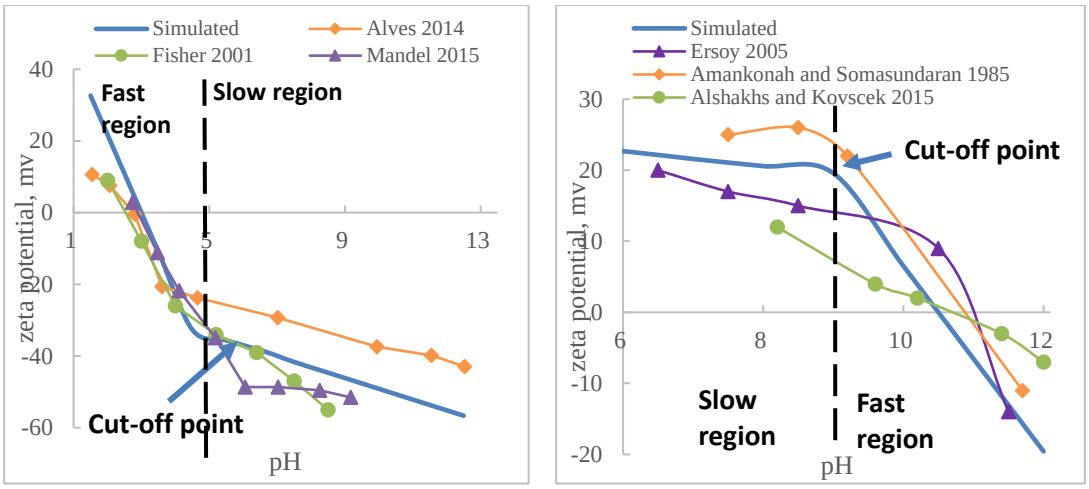

(a) (b)

Figure 2-2—Calculated zeta potential comparing with (a) zeta potential of silica nanoparticle(Antonio Alves Júnior and Baptista Baldo 2014, Fisher et al. 2001, Mandel et al. 2015) (b) Zeta potential of Calcite limestone grain or powder (Amankonah and Somasundaran 1985, Ersoy 2005, Alshakhs and Kovscek 2015)

Revil et al. (1999) proposed a linear relationship between zeta potential of silica nanoparticle and temperature at pH of 7:

$$\zeta(T) = \zeta(T_0) * \left[1 + v_\zeta (T - T_0)\right] \tag{10}$$

Where, v_ζ is temperature sensitivity coefficient and is fitted from experimental data for different particles; T_0 is reference temperature and always taken as 25ºC. The final equation of zeta potential can be expressed as Eq. 11 with empirical parameters shown in Table 2-1:

$$\zeta = \begin{cases} m_1 \dfrac{0.85 k_B T}{f(\kappa a_p) e} (pH_{IEP} - pH)\left[1 + v_\zeta (T - T_0)\right] \\ \zeta_{cut-off} + \dfrac{m_2}{f(\kappa a_p)} \left(pH_{cut-off} - pH\right)\left[1 + v_\zeta (T - T_0)\right] \end{cases} \tag{11}$$

Table 2-1—Empirical parameters for zeta potential calculation

	Limestone grain	Silica nanoparticle	Alumina nanoparticle
pH_{IEP}	10.5	3	9.5
Cut-off point	9	5	6
m_1	0.6	0.6	0.8
m_2 (V/pH)	0.001	0.003	0.002
v_ζ (1/°C)	0.02	0.008	0.01

2.3. DLVO theory

The effect of ionic strength, pH, and temperature on DLVO interaction can be introduced in terms of zeta potential of nanoparticles and rock as explained in section 2.2. The classical DLVO theory only includes Van der Waals and electrical double layer interaction. Extended DLVO theory also includes the short-range Born and hydration repulsions to obtain more accurate DLVO energy profile. Nevertheless, a quantitative model considering surface roughness of porous media is provided to yield a more realistic DLVO energy profile.

2.3.1. Extended DLVO theory

For the interaction energy between a sphere and a flat plate, Derjaguin's approximation is usually employed to derive linear equations when the separation distance between the two surfaces is less than 100 nanometers (Zhang 2012). The van der Waals interaction energy between a spherical particle and flat surface is (Gregory 1981):

$$\emptyset_{VDW} = -\frac{A_H * a_p}{6y(1+\frac{14y}{\lambda})} \tag{12}$$

Where A_H is Hamaker constant, J; y is separation distance, m; λ is characteristic London wavelength, has a value of 100 nm.

Verwey and Overbeek (1948) gave the expression of electrical double layer interaction energy between a spherical particle and flat surface through linear superposition approximation:

$$\emptyset_{EDL} = 64\pi\epsilon a_p * \left(\frac{k_B T}{Ze}\right)^2 * \tanh\left(\frac{Ze\psi_{s,1}}{4k_B T}\right) * \tanh\left(\frac{Ze\psi_{s,2}}{4k_B T}\right) * \exp(-\kappa y) \qquad (13)$$

Where, Z is of the valence of the electrolyte, $\psi_{s,1}$ and $\psi_{s,2}$ are the surface potential of nanoparticles and rock grain, respectively, V. Zeta potential ζ, can be used as approximation to the surface potential. This equation is valid when the zeta potential of both nanoparticle and the rock grain is less than 60 mV.

The short-range non-DLVO forces considered to be included in the model are Born repulsion and hydration repulsion. For colloidal particles in aqueous fluid, the Born repulsion originates due to the overlap of electron clouds (Adamczyk and Weroński 1999).Ruckenstein and Prieve (1976) first published a formula obtained in the same manner as Van der Waals attraction for the sphere-plate Born repulsion:

$$\emptyset_{BORN} = \frac{A_H * y_{BORN}}{7560} * \left[\frac{8a + y}{(2a + y)^7} + \frac{6a - y}{y^7}\right] \qquad (14)$$

Where y_{BORN} is the minimum separation distance caused by Born repulsion, which is typically taken to be the Lennard–Jones separation distance of 0.4 nm (Elimelech et al. 1995, Visser 1995). Hydration repulsion originates from the overlap of structured layer of water molecules at the surfaces of hydrophilic nanoparticles (Pashley and Israelachvili 1984). Eq. 15 has been successfully used to fit the experimental results of hydration force between hydrophilic surfaces because it decays exponentially over the separation distance

(Pashley 1982, Churaev and Derjaguin 1985). Eq. 16 is the expression of hydration interaction energy between a spherical particle and flat surface derived from Eq. 15:

$$F_{HYD} = a_p[C_1\, exp\left(-\frac{y}{\lambda_1}\right) + C_2\, exp\left(-\frac{y}{\lambda_2}\right)] \quad (15)$$

$$\emptyset_{HYD} = a_p[C_1\, \lambda_1 exp\left(-\frac{y}{\lambda_1}\right) + C_2\, \lambda_2 exp\left(-\frac{y}{\lambda_2}\right)] \quad (16)$$

Where C_1 and C_2 are hydration force constants, N/m. λ_1 and λ_2 are decay lengths, m. Eq. 15 is a fully empirical equation. For 1:1 electrolytes such as NaCl and KCl, Ghosh (2009) suggested the values of C_1 lie between 0.017 and 0.025 N/m, values of C_2 lie between 0.014 and 0.06 N/m, values of λ_1 lie between 0.17 and 0.3 nm and values of λ_2 lie between 0.6 and 1.1 nm.

The total DLVO interaction energy and the total DLVO force are:

$$\emptyset_{DLVO} = \emptyset_{VDW} + \emptyset_{EDL} + \emptyset_{BORN} + \emptyset_{HYD} \quad (17)$$

$$F_{DLVO} = \frac{d\emptyset_{DLVO}}{dy} \quad (18)$$

It is noticed that Born and hydration interaction energy only act within a few nanometers of separation distance. Over a wide range of separation distance, van der Waals and electrical double layer interactions are analyzed first and then short-range interaction energy is corrected by including Born and hydration repulsions. For a given nanoparticle/rock system in certain electrolyte solution, Eq. 12, 14 and 16 illustrates the dependence of van der Waals, Born, and hydration interaction on nanoparticle size and Eq. 13 illustrates the dependence of electrical double layer interaction on zeta potential. Trefalt et al. (2016) indicated that pH and ionic strength are the critical parameters affecting zeta potential. Therefore, pH and ionic strength are considered in analyzing DLVO energy profile. Fig. 2-3 shows an energy barrier presents when the silica

nanoparticle and sandstone rock grain are likely charged. Conversely, Fig. 2-4 shows that the energy barrier vanishes as the silica nanoparticle and limestone rock grain are oppositely charged. The effect of ionic strength and pH on surface charge, or zeta potential are then shown in Fig 2-5 and 2-6, respectively. Fig. 2-5 shows the high dependence of DLVO energy profile on ionic strength. At low ionic strength, an energy barrier presents due to strong electrical double layer repulsion. Increasing ionic strength weakens the double layer repulsion and lowers the height of energy barrier. At high ionic strength, the energy barrier vanishes because the electrical double layer repulsion is less than the van der Waals attraction. Fig. 2-6 shows the dependence of DLVO energy profile on pH at low ionic strength. The height of energy barrier increases as pH increases because the magnitude of zeta potential and electrical double layer repulsion increases. Moreover, pH does not affect DLVO energy profile very much at high ionic strength. The reason is electrical double layer interaction has little contribution to total DLVO interaction and thus van der Waals attraction dominants at high ionic strength (Zhang 2012). Fig. 2-7 and 2-8 show the comparison between the classical DLVO theory and the extended DLVO theory considering Born and hydration repulsion. Hydration repulsion has a slightly wider effective range (3 nm) than Born repulsion (0.4 nm). Compared to the classical DLVO energy, the short-range repulsions raise energy barrier and results in a shallower primary minimum.

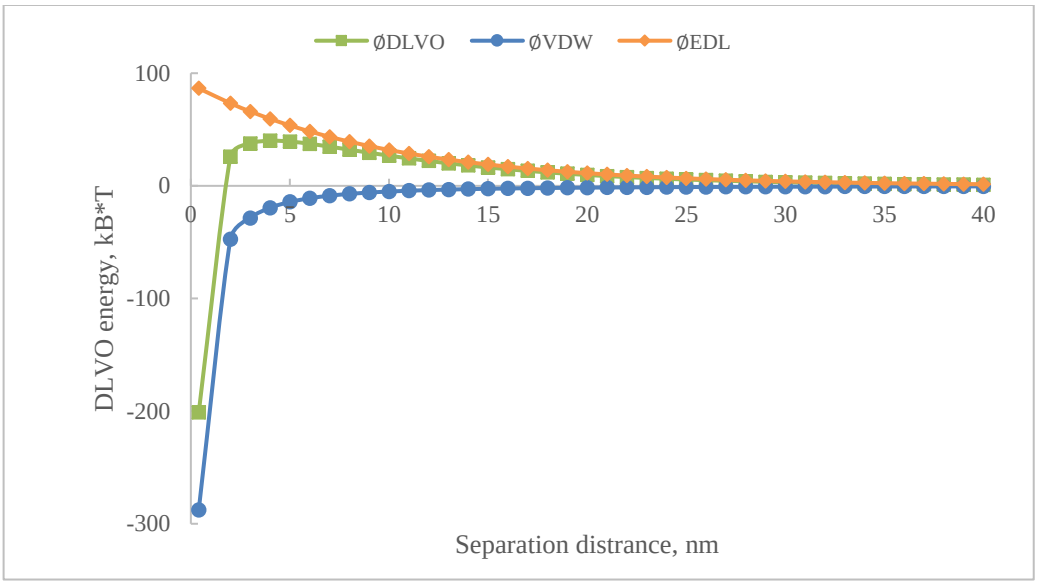

Figure 2-3—Classical DLVO interaction energy profile between a 100-nm silica nanoparticle (-30 mV) and sandstone grain (-30mV) in 0.001M NaCl at pH of 6 and 25ºC.

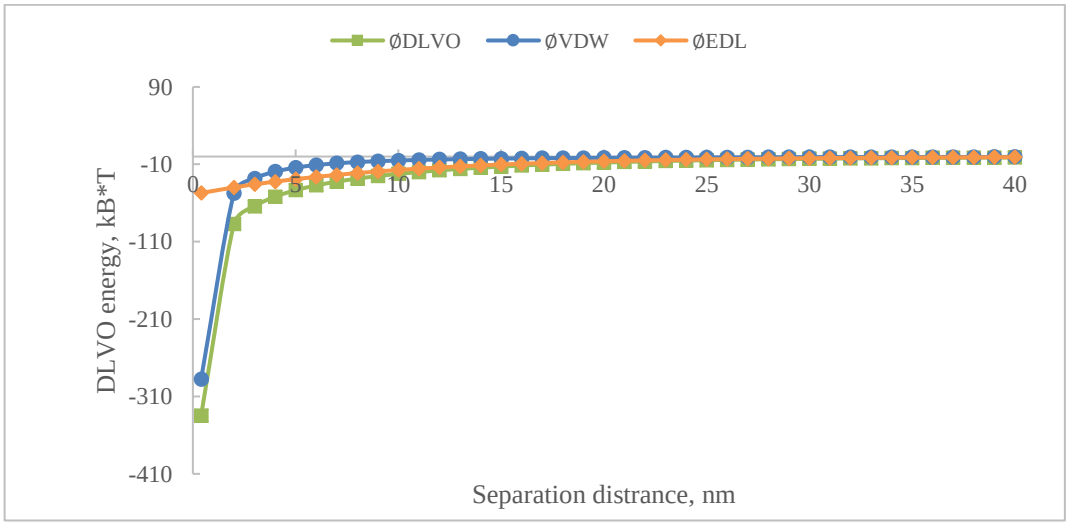

Figure 2-4— Classical DLVO interaction energy profile between a 100-nm silica nanoparticle (-30 mV) and limestone grain (16 mV) in 0.001M NaCl at pH of 6 and 25ºC

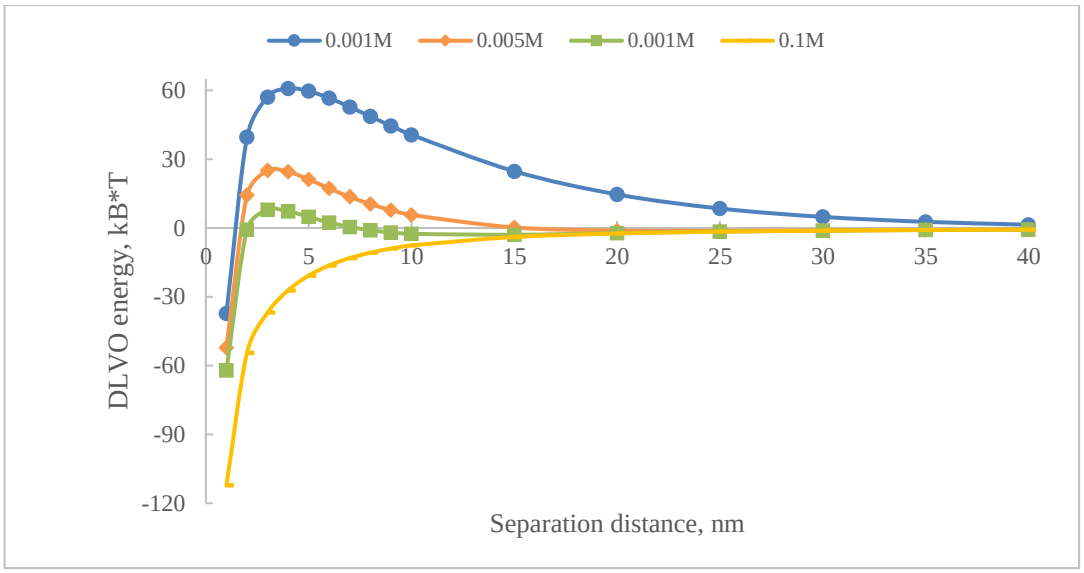

Figure 2-5— Classical DLVO interaction energy profile between a 100-nm silica nanoparticle (-30 mV) and sandstone grain (-30 mV) at 25ºC at different ionic strength.

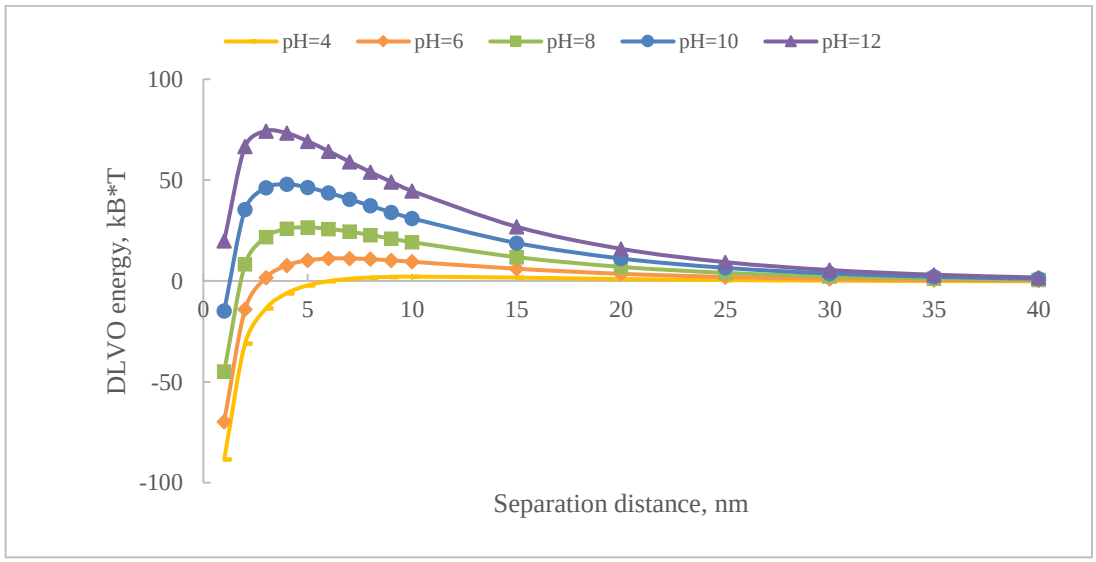

Figure 2-6— Classical DLVO interaction energy profile between a 100-nm silica nanoparticle and sandstone grain in 0.001M NaCl at 25ºC at different pH.

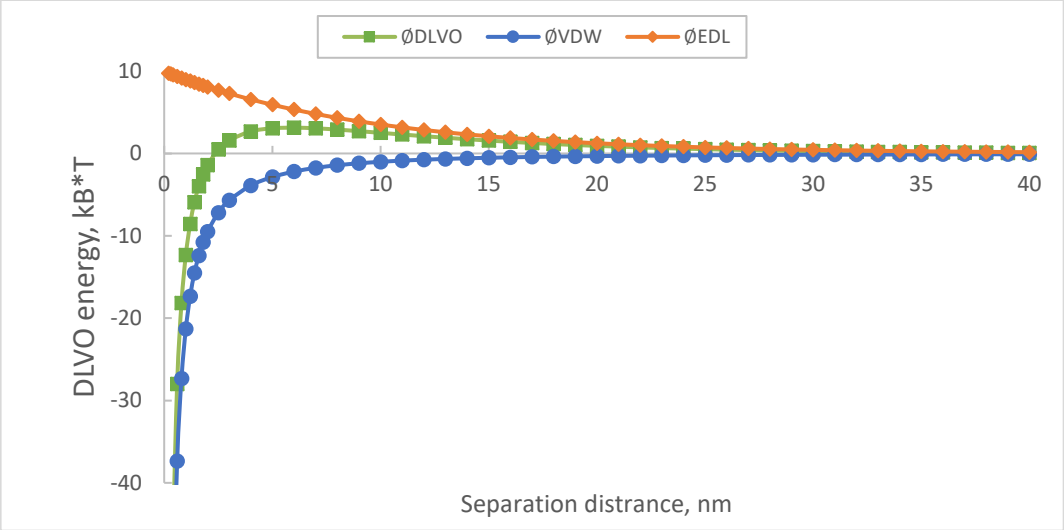

Figure 2-7— Classical DLVO interaction energy profile between a 10-nm silica nanoparticle (-30 mV) and sandstone grain (-30 mV) in 0.001M NaCl at 25°C.

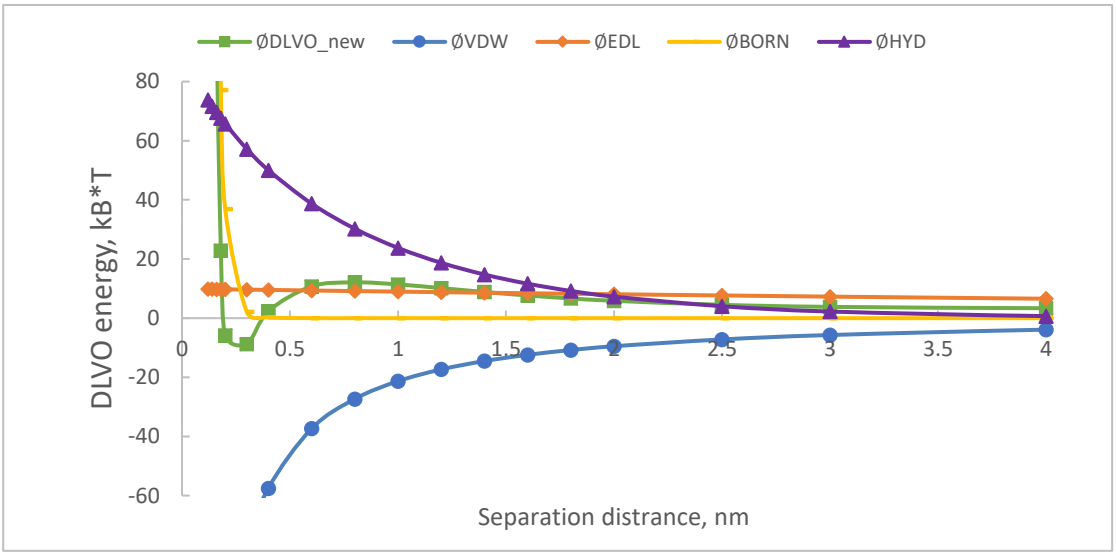

Figure 2-8— Extended DLVO interaction energy profile considering Born and hydration repulsion between a 10-nm silica nanoparticle and sandstone grain in 0.001M NaCl at 25°C.

2.3.2. Surface roughness

The DLVO theory assumes smooth surfaces, which leads to the discrepancies of interaction energy between experiment observations and theoretical predictions

(Bhattacharjee et al. 1998). Based on DLVO theory, varying surface roughness result in different DLVO energy profile, and therefore result in different rate of deposition and release. Surface roughness is included in the model using the height and the density of roughness (Hoek et al. 2003, Hoek and Agarwal 2006). In this study, a DLVO energy profile was generated by a representative height of surface roughness obtained from laboratory measurements with certain roughness density. The overall rate of deposition and release then will be calculated based on the DLVO energy profile considering surface roughness.

There are many parameters that could represent surface roughness on the surface of martial. The two popular statistical characterizations of the roughness height are: arithmetic average of the absolute height deviation (h_{abs}) and the root mean square average of height deviation (h_{rms}) measured from the mean plane. Root-mean-square roughness, h_{rms} effectively describes the standard deviation of an entire distribution of values for a large sample size and is more sensitive to topography changes of grain surface (Lieu 2014). Therefore, the root mean square average is always been used to express the surface roughness of glass beads, membranes, and rock grains. In this study, the representative surface roughness height of sandstone is assumed to be equal to the root mean square average of quartz obtained from Lieu's experiments.

$$h_{rms} = \sqrt{\frac{1}{N}\sum_{n=1}^{N} Z_n^2} \tag{19}$$

$$h_{abs} = \frac{1}{N}\sum_{n=1}^{N} Z_n \tag{20}$$

Where Z_n indicates the height of each roughness on the surface. N is the number of roughness. Lieu (2014) measured the surface roughness of Rotliegend sandstone samples taken from the Lower Saxony Basin in northern Germany with a digital Confocal Laser Scanning Microscope (CLSM). The root mean square of roughness height for quartz mineral is about 14 nm. As DLVO interaction energy varies between rough and smooth surface, the density of roughness determines the fraction of roughness on smooth surface. If surface roughness is approximated as hemispherical protrusions on smooth surface (Fig. 2-9), the relationship between rough and smooth surface area is:

$$S_{rough} = S_{smooth} + \rho_r * S_{smooth} * \pi h_{rms}^2 \quad (21)$$

Where S_{rough} is rough surface area, m^2. S_{smooth} is smooth surface area, m^2. ρ_r is density of roughness, which is number of roughness per unit smooth surface area, $1/m^2$. The fraction of roughness presenting on smooth surface (η_r) is:

$$\eta_r = \frac{\rho_r * S_{smooth} * 2\pi h_{rms}^2}{S_{rough}} = \frac{\rho_r * 2\pi h_{rms}^2}{1 + \rho_r * \pi h_{rms}^2} \quad (22)$$

Where the maximum density can be derived from $\eta_r \leq 1$:

$$\rho_{rmax} = \frac{1}{\pi h_{rms}^2} \quad (23)$$

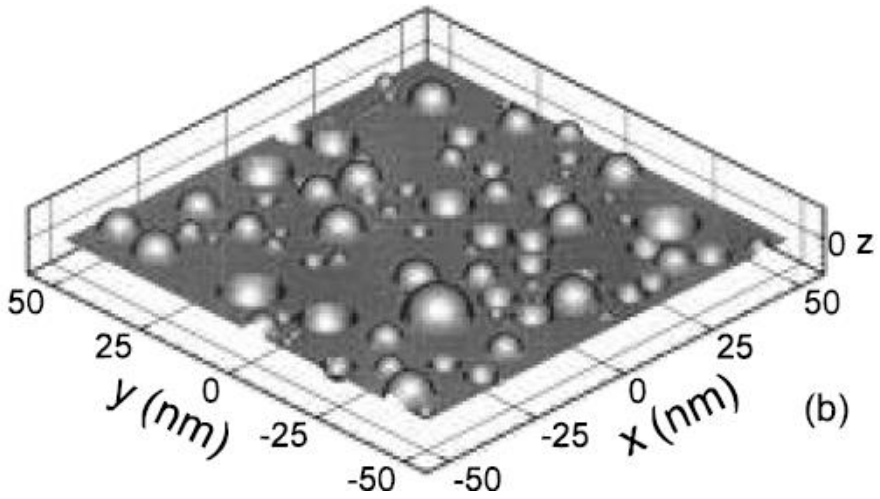

Figure 2-9— Hemispherical surface roughness on smooth surface (Bhattacharjee et al. 1998).

Bhattacharjee et al. (1998) indicated that the DLVO energy profile varies when considering the surfaces of particles and solids are rough instead of smooth. Elimelech and O'Melia (1990) approximated the surface roughness as hemispherical protrusions on the surface. Then the total DLVO interaction energy is calculated as a linear superposition of energy associated with hemispherical protrusion top and the underlying smooth surface. The calculation of nanoparticle-roughness energy uses equations of sphere-sphere DLVO energy, and calculation of nanoparticle-smooth surface energy uses equations of sphere-flat surface DLVO energy. The sphere-sphere energy is calculated by replacing a_p in sphere-flat surface equation (Eq. 12, 13 and 16) by $(\frac{a_p * h_{rms}}{a_p + h_{rms}})$, where h_{rms} is the representative height of roughness, or the representative radius of hemispherical protrusions.

$$\emptyset_{DLVO_{flat}} = \emptyset_{VDW} + \emptyset_{EDL} + \emptyset_{HYD} \quad (24)$$

$$\emptyset_{DLVO_{sphere}} = \emptyset_{DLVO_{flat}} * (\frac{h_{rms}}{a_p + h_{rms}}) \quad (25)$$

$$\emptyset_{DLVO_{rough}}(y) = \emptyset_{DLVO_{flat}}(y + h_{rms}) + \emptyset_{DLVO_{sphere}}(y) + \emptyset_{BORN}(y) \quad (26)$$

The representative DLVO energy by Extended DLVO theory can be calculated by introducing fraction of roughness on total surface area (Hoek and Agarwal 2006).

$$\emptyset_{DLVO} = \eta_r * \emptyset_{DLVO_{rough}}(y) + (1 - \eta_r) * \emptyset_{DLVO}(y) \quad (27)$$

2.4. Rate of deposition and rate of release

Spielman and Friedlander (1974) and Ruckenstein and Prieve (1976) divided nanoparticle deposition and release into two cases based on the DLVO-energy profile: case 1 with the presence of energy barrier and case 2 without energy barrier. The dominant mechanism of nanoparticle deposition and release of two cases varies due to the strong resistance on the nanoparticle deposition to and release from the surface brought by the energy barrier. Ryan and Elimelech (1996) described the colloid deposition and release as two-step processes: the colloid diffusion from bulk fluid to surface and deposition on surface, and colloid detachment from surface and diffusion back to the bulk fluid. For case 1, repulsive DLVO force are applied to nanoparticle as it approaches the pore surface, and nanoparticles must overcome the energy barrier to be adsorbed on the surface or to release from the surface. Therefore, the rate of deposition and release depend on the magnitude or height of energy barrier. However, for case 2 every nanoparticle approaching to the surface will be attracted due to the attractive DLVO force. The rate of deposition and release are then controlled by the diffusion process.

To model the transport of nanoparticle in pore space, the pore is conceptualized as a cylindrical flow channel. This cylinder can be divided into two main layers, a convection flow layer and a diffusion boundary layer (Fig. 2-10). Inside the diffusion boundary layer, the effect of convection is much smaller than diffusion and fluid convection is neglected. A DLVO layer is considered close to the surface, inside which the DLVO interactions become important. Ryan and Gschwend (1994) reported the thickness of diffusion boundary layer (δ_{Diff}) is between 11 to 28 microns for 250-micron quartz grains and the thickness of DLVO layer (δ_{DLVO}) is between 7 to 110 nm for 150-nm iron oxide nanoparticles.

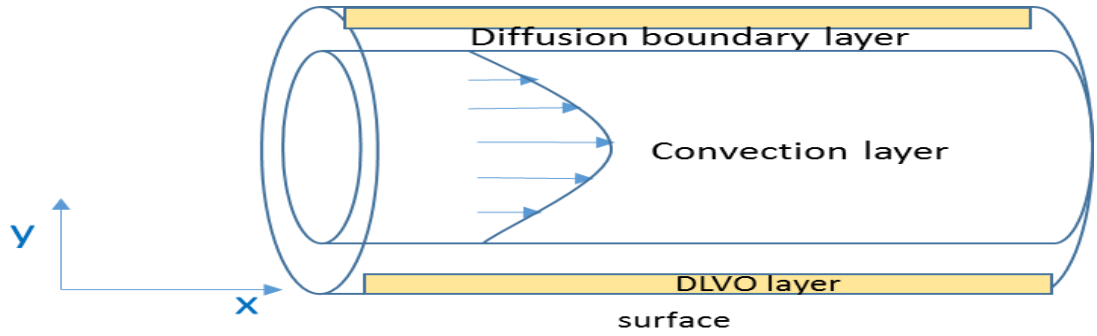

Figure 2-10— Schematic of cylindrical flow channel, which simulates a pore throat

2.4.1. Rate of deposition and release for case 1

Nanoparticles transport through the saturated porous medium is described by the convection-diffusion equation lumping with DLVO interaction assuming no source or sink Spielman and Friedlander (1974):

$$\frac{\partial C}{\partial t} + u \cdot \nabla C = \nabla \left[D \cdot \nabla C + \frac{DC}{k_B T} . \nabla \emptyset_{DLVO} \right] \quad (28)$$

Where C is nanoparticle concentration, $\frac{g}{m^3}$; D is diffusion coefficient of nanoparticle, $\frac{m^2}{s}$. Nanoparticle deposition occurs at the pore surface, which is inside the diffusion boundary layer where convection term is neglected. Assuming $\frac{\partial^2 C}{\partial x^2} \ll \frac{\partial^2 C}{\partial y^2}$, the nanoparticle deposition flux perpendicular to the rock surface (J_y) is controlled by diffusion and external DLVO interaction.

$$J_y = -D\left[\frac{\partial C}{\partial y} + \frac{C}{k_B T}.\frac{\partial \emptyset_{DLVO}}{\partial y}\right] \tag{29}$$

Spielman and Friedlander (1974) integrated Eq. 29 and reduced the problem of nanoparticle deposition with an energy barrier near the surface to the solution of the usual convection diffusion equation with a first-order surface reaction. The boundary condition becomes:

At y = 0: $$C = -\frac{J_0}{D(y)}\left[\int_0^\infty (e^{\frac{\emptyset_{DLVO}(y)}{k_B T}} - 1)dy\right] = -\frac{J_0}{K_{dep}} \tag{30}$$

Rearrange: $$K_{dep} = \frac{D(y)}{\int_0^\infty (e^{\frac{\emptyset_{DLVO}(y)}{k_B T}} - 1)dy} \tag{31}$$

Where J_0 is the nanoparticle deposition flux perpendicular to the rock surface $\left(J_y\right)$ at the surface and K_{dep} is the rate coefficient of deposition. The energy decays rapidly as $|y - y_{max}|$ increases. Expanding $\emptyset_{DLVO}(y)$ using Taylor series and truncating after second-order term gives:

$$\emptyset_{DLVO}(y) = \emptyset_{max} - 0.5\gamma_{max}(y - y_{max})^2 \tag{32}$$

Where y_{max} is the separation distance at primary maximum and $\gamma_{max} = -\frac{d^2 \emptyset_{DLVO}}{dy^2}|_{y=y_{max}}$. Substituting the Taylor expansion of DLVO energy into Eq. 31 the

rate coefficient of deposition of case 1 is exponentially related to the height of energy barrier $\emptyset_{max}$ by Ruckenstein and Prieve (1976).

$$K_{dep} = D(y_{max}) * (\frac{\gamma_{max}}{2\pi k_B T})^{\frac{1}{2}} * \exp(\frac{-|\emptyset_{max}|}{k_B T}) \quad (33)$$

$$D(y_{max}) = \frac{k_B T}{6\pi\mu a_p} * \frac{y_{max}}{a_p} \quad (34)$$

Following Ruckenstein and Prieve (1976), nanoparticles deposited in primary minimum must possess sufficient thermal energy to overcome the activation energy of $(\emptyset_{max} - \emptyset_{min})$ to release from primary minimum. The rate of release controlled by DLVO energy barrier was derived in the same way as Eq. 33 by Ruckenstein and Prieve (1976).

$$K_{rel,1} = D(y_{max}) * \frac{(\gamma_{max}\gamma_{min})^{\frac{1}{2}}}{2\pi k_B T} * \exp(\frac{-|\emptyset_{max} - \emptyset_{min}|}{k_B T}) \quad (35)$$

Where $\gamma_{min} = -\frac{d^2\emptyset_{DLVO}}{dy^2}|_{y=y_{min}}$.

2.4.2. Rate of deposition and release for case 2

Ryan and Elimelech (1996) and Ryan and Gschwend (1994) proposed models of colloid deposition and release when energy barrier vanishes. It is assumed for case 2 the deposition and release are fast and the diffusion of nanoparticle across the diffusion boundary layer to the bulk fluid is the limiting step. The nanoparticle flux from interface between convection layer and diffusion boundary layer to the proximity of the pore surface is explained as:

$$J_y = -D\frac{\partial C}{\partial y} = -K_{dep} * C_{bulk} \quad (36)$$

The perfect sink model assumes deposited nanoparticles are irreversibly consumed by a very fast immobilization reaction and disappear from the flowing system (Ryan and Elimelech 1996). With the boundary conditions of $C = 0\ at\ y = \delta_{DLVO}$ and $C = C_{bulk}\ at\ y = \delta_{Diff}$ the rate of deposition for case 2 is:

$$K_{dep,2} = \frac{D}{\delta_{Diff} - \delta_{DLVO}} \approx a_g^{-\frac{2}{3}} * D^{\frac{2}{3}} * u^{\frac{1}{3}} \tag{37}$$

Where δ_{Diff} and δ_{DLVO} are thickness of diffusion boundary layer and DLVO layer, respectively. $\delta_{Diff} = a_g(\frac{D}{u*a_g})^{\frac{1}{3}}$ given by Spielman and Friedlander (1974). The diffusion-controlled rate coefficient of release for case 2 given by Ryan and Gschwend (1994) is :

$$K_{rel,2} = a_g^{-\frac{4}{3}} * D^{\frac{1}{3}} * u^{\frac{2}{3}} \tag{38}$$

Where a_g is the radius of rock grain. It is worth mentioning that the height of surface roughness is much less than the thickness of diffusion boundary layer. Therefore, the rate of deposition is independent of surface roughness. Meanwhile, for case 2 the deposited nanoparticles to be released from surface is controlled in the first place by surface roughness (Ryan and Elimelech 1996). The kinetics of mobilization has been analyzed by balance of torques applied on a nanoparticle adhered to a flat surface in a moving fluid. Fig. 2-11 shows the resisting torque, T_{DLVO}, drag torque, T_{drag}, drag moment by surface stress, M_d on a nanoparticle adhered on surface resisted by a surface roughness of height, h. The drag force acting at the center of the nanoparticle is calculated from a modified Stokes law (O'Neill 1968) and the corresponded drag torque is the product of drag force and drag arm l_d:

$$F_d = 1.7 * 6\pi\mu a_p u_p \quad (39)$$

$$T_d = F_d l_d \quad (40)$$

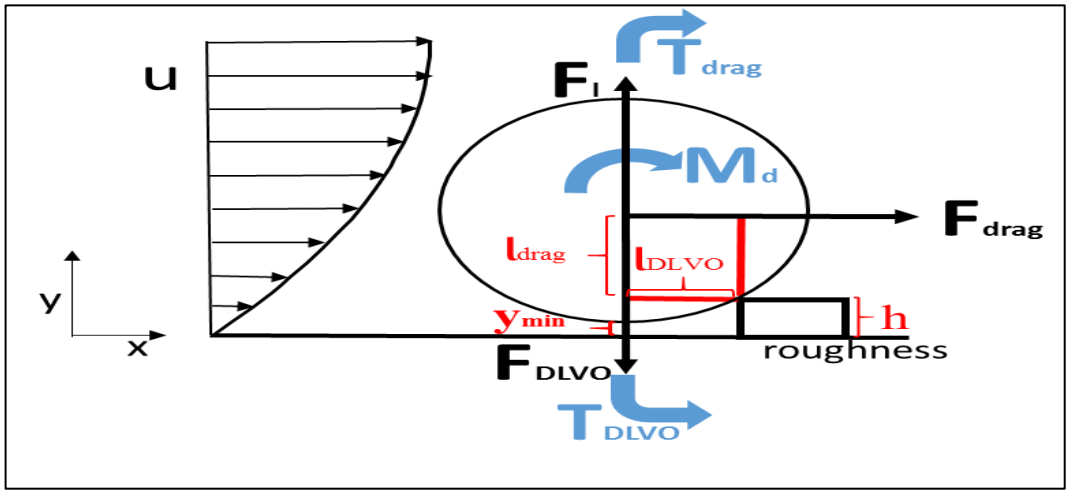

Figure 2-11— Schematic of torque balance on a nanoparticle deposited on flat pore surface resisted by a surface roughness with a parabolic velocity profile in the flow channel.

Assuming laminar flow in pore throat obeys the Poiseuille law and adopts a parabolic flow velocity profile, the flow velocity acting at the center of the nanoparticle (u_p) is (Bos et al. 1999):

$$u_p = 4 * u_{max} \frac{a_p}{d_{pore}} (1 - \frac{a_p}{d_{pore}}) \quad (41)$$

Where d_{pore} is the diameter of the cylindrical pore throat. u_{max} is the maximum flow velocity along the flow direction in the cylindrical pore throat. The lifting force acting at the center of the particle is (Ryan and Elimelech (1996):

$$F_l = \chi * a_p^2 \sqrt{\rho_{fluid} * \mu * u_p^3} \quad (42)$$

where the lifting force coefficient χ is 81.2. When the separation distance between the nanoparticle and pore surface is less than 1 nm, strong repulsive interactions become

significant to prevent surfaces of nanoparticles and pore wall from contacting each other. The existence of this short-range Born repulsion causes a minimum separation distance between deposited nanoparticle and pore surface , which is typically taken to be the Lennard–Jones separation distance of 0.4 nm (Elimelech et al. 1995, Visser 1995). Therefore, it determines the separation distance of the primary minimum, where the strongest DLVO attractive interaction presents. The net attractive DLVO force between the deposited nanoparticle and pore surface then is calculated at this separation distance:

$$F_{DLVO} = \frac{\partial \phi_{DLVO}}{\partial y}|_{y_{min}=0.4nm} \tag{43}$$

and the corresponded DLVO torque is the product of DLVO force and DLVO arm l_{DLVO}:

$$T_{DLVO} = F_{DLVO} l_{DLVO} \tag{44}$$

From Fig.8 the relationship between the arms and roughness height can be obtained as:

$$l_d = \sqrt{a_p^2 - l_{DLVO}^2} \tag{45}$$

$$h = 0.4 + a_p - l_d \tag{46}$$

The moment of surface stresses given by O'Neill (1968) is:

$$M_d = 0.944 * 8\pi\mu a_p^2 * u_p \tag{47}$$

Burdick (2001) discussed three mechanisms of particle release from surface hydrodynamically: lifting, sliding and rolling. Lifting occurs when lifting force is greater than adhesive DLVO force (Eq. 36) while sliding occurs when hydrodynamic drag force overcomes the static friction between the nanoparticle and surface (Eq. 37). Rolling occurs when the drag torque exceeds the adhesive torque acting on the nanoparticle (Eq. 38).

Lifting criteria: $$F_l > F_{DLVO} \tag{48}$$

Sliding criteria: $$F_d > \mu_f * |F_{DLVO} - F_l| \quad (49)$$

Rolling criteria: $$M_d + F_d l_d + F_l l_{DLVO} > F_{DLVO} l_{DLVO} \quad (50)$$

Where μ_f is the static friction coefficient and assumed to be unity (Burdick et al. 2001). The parameters (Table 2-2) are used for a sample calculation of force and torque balance (Table 2-3) using Eq. 39 through Eq. 43. It is found that in similar chemical environment, for nanoparticles with the size of 10 nm, the drag force is several orders of magnitude less than the DLVO attraction, and the lifting force is several orders of magnitude less than drag force (Table 2-3). Hence, the criteria of lifting and sliding are neglected and rolling becomes the dominant mechanism of hydrodynamic release. Substitute Eq. 39 through Eq. 47 into Eq. 50 with neglecting lifting torque, a critical velocity for release acting at the center of nanoparticle can be identified as:

$$u_{p,cr} = \frac{F_{DLVO} l_{DLVO}}{0.944 * 8\pi\mu a_p^2 + 1.7 * 6\pi\mu a_p * \sqrt{a_p^2 - l_{DLVO}^2}} \quad (51)$$

Surface roughness is an important parameter in initiating particle to release from rock surface by affecting the length of arms l_{DLVO} and l_d (Burdick et al. 2001). Hubbe (1984) proposed a relationship between the height of roughness, h, and l_{DLVO} considering the minimum separation distance y_{min}:

$$l_{DLVO} = a_p \sqrt{\frac{2(h - y_{min})}{a_p} - \frac{(h - y_{min})^2}{a_p^2}} \quad (52)$$

Through the SEM analysis, the surface of sandstone is smooth while the surface of limestone and sandstone is rough and full of dents and bumps (Esfandyari Bayat et al. 2015). For hard and relatively smooth surface Hubbe (1984) mentioned height of roughness is so small relative to radius of nanoparticle that the term $\frac{(h - y_{min})^2}{a_p^2}$ can be neglected. It is then assumed that $h = 0.5\, nm$ for small surface roughness that prevent

nanoparticles from sliding. The results of torque balance and rate of release are shown in Table 2-3.

Table 2-2— Variables and parameters used in sample torque calculation

Injection rate (ml/min)	1
Flow velocity (m/s)	4.24E-4
Flow velocity on center of nanoparticle (m/s)	8.06E-5
Height of small surface roughness (Ding et al.)	0.5
Minimum separation distance (Ding et al.)	0.4
Nanoparticle radius (Ding et al.)	5
Sandstone grain radius (Zhang (2012) (Ding et al.)	75000
Diffusion Coefficient (m^2/s)	4.37E-11
Fluid viscosity (cp)	1
Solution pH	6
Ionic strength (M)	0.0001
Temperature (K)	298
Zeta potential of nanoparticle (mV)	-20
Zeta potential of rock grain (mV)	-22
Hamaker constant (J)	6E-20
Boltzmann constant (J/K)	1.38E-23
Dielectric constant	6.94E-10
Elementary charge (C)	1.60E-19
Avogadro number	6.02E+23

Table 2-3— Results from sample torque calculation.

DLVO force (kg.m/s)	3.12E-10
Hydrodynamic drag force (kg·m/s)	1.35E-15
Lifting force (kg·m/s)	4.98E-23
Surface stress moment (kg·m^2/s)	5.10E-21
DLVO arm (Ding et al.)	0.99
Critical velocity on nanoparticle (m/s)	0.22
Rate coefficient of diffusion-controlled release if Critical injection rate is reached (1/s)	3.34E-3
Rate coefficient of energy-controlled release (1/s)	2.60E-14

According to results shown in Table 2-3, it is concluded that for case 1 with energy barrier, the energy-barrier-controlled rate of release is quite small, which is consistent with literatures which treat the deposition in this case as irreversible deposition (Ruckenstein and Prieve 1976, Ryan and Elimelech 1996). Moreover, for case 2 where energy barrier vanishes, the hydrodynamic drag force which is proportional to the flow velocity acting on the nanoparticle is much less than the attractive DLVO force. For small nanoparticle with radius of 5 nm, the injection flow velocity on nanoparticle of $2.61 * 10^{-6} \frac{m}{s}$ is too small to meet the critical value of $0.22 \frac{m}{s}$ to initiate the release hydrodynamically. The calculated critical velocity and the finding of no hydrodynamic release are consistent with Zhang (2012). Therefore, in the following simulations diffusion-controlled rate of release is neglected for case 2.

The mass balance of net nanoparticle deposition per unit time is expressed as the concentration of deposition minus the concentration of release from the nanoparticle already deposited. The rate of release for case 2 will be neglected if the injection velocity is less than the critical value.

Case 1: $$R = \frac{\partial C_{dep}}{\partial t} = (K_{dep,1} * S_{SA}) * C_{bulk} - K_{rel,1} * C_{dep}$$

Case 2: $$R = \frac{\partial C_{dep}}{\partial t} = (K_{dep,2} * S_{SA}) * C_{bulk} - K_{rel,2} * C_{dep} \quad (53)$$

Where R is the rate of changing in concentration of retained nanoparticle in the porous medium. The diffusion-controlled release is always neglected in following simulations because the critical injection rate is too high to reach. S_{SA} is the specific surface area of sandpack, $5.83 * 10^5 \frac{1}{m}$ for Boise sandstone and $2 * 10^6 \frac{1}{m}$ for Texas Cream limestone measured by Zhang (2012).

$$S_{SA} = \frac{total\ surface\ area}{total\ pore\ volume} \quad (54)$$

2.4.3. Long-time deposition

The rate of deposition calculated above assumed all the rock pore surface is available to interact with nanoparticle. However, with the nanoparticle deposited on the pore surface, the available surface for interaction with nanoparticles decreases. Nanoparticles deposited on the surface form monolayer or multilayer which cover the surface and change the surface properties. The covering layer prevents the nanoparticle in bulk fluid from interacting with the rock pore surface. Then the rate of deposition is determined by the particle-particle interactions (Ryan and Elimelech 1996). In this model, monolayer coverage is assumed because the particle-particle interaction is assumed to be repulsive and no aggregation occurs. The accumulation of nanoparticle on the pore surface will decrease the rate of deposition. Johnson and Elimelech (1995) proposed a linear relationship of the deposition rate correction $B(\theta)$ as a function of fractional surface coverage.

$$B(\theta) = 1 - \frac{\theta}{\theta_{max}} = 1 - \frac{C_{dep} * V_{pore} * A_p}{\eta_{packing} * S_{SA} * V_{pore}} = 1 - \frac{C_{dep} * A_p}{\eta_{packing} * S_{SA}} \quad (55)$$

Where, A_p is the projected cross-section area of a spherical nanoparticle; C_{dep} is net concentration of nanoparticle deposited on rock surface; V_{pore} is pore volume; $\eta_{packing}$ is the hexagonal packing efficiency, 90.69%. The time-dependent rate of deposition is:

$$K_{dep}(t) = K_{\mathrm{dep}}(\mathrm{t} = 0) * B(\theta) \quad (56)$$

2.5. Numerical Model:

To validate the theoretical calculations of rate of deposition and release of nanoparticles in porous media, numerical simulation has been conducted to compare the model results with the experimental data in the literature at the same conditions. One-dimensional advection-dispersion equation with a sink/source term is solved using explicit finite difference method (Thongmoon and McKibbin 2006). The model assumed a piston like displacement, that the velocity is constant as the injection velocity.

$$\frac{\partial(\phi C)}{\partial t} + u\frac{\partial C}{\partial x} = D\phi\frac{\partial^2 C}{\partial x^2} + R \quad (57)$$

Here, $C(x,t)$ is the concentration of nanoparticles at any point x $(0 < x < L)$and time t.u is the constant injection velocity in the x direction and D is the diffusion coefficient. ϕ is the porosity of the porous medium. R is the sink/source term that accounts for deposition and/or release of nanoparticles on/from the rock pore surface. The following boundary and initial conditions are used to close the system:

$$C(x,0) = 0,$$
$$C(0,t) = C_{inj}, \quad (58)$$

$$\frac{\partial C(L,t)}{\partial x} = 0$$

Forward time-centralspace (FTCS) method (Zhang 2012) is used to discretize the advection-dispersion equation. This method is a second order in space and first order in time. The equation is discretized on finite mesh points. The grid points are $0 = x_1 < x_i < x_N = L$. The approximate solution on these grid points is

$$\frac{C_i^{n+1} - C_i^n}{\Delta t} + \frac{u}{\phi}\frac{C_{i+1}^n - C_{i-1}^n}{\Delta x} = D\frac{C_{i+1}^n - 2C_i^n + C_{i-1}^n}{(\Delta x)^2} + R^n + o(\Delta t, (\Delta x)^2) \qquad (59)$$

for $i = 2, 3, \ldots, N-1$. While for $i = 1$, the boundary condition is applied. For $i = N$, one-sided finite difference scheme is used

$$\frac{C_i^{n+1} - C_i^n}{\Delta t} + \frac{u}{\phi}\frac{3C_N^n - 4C_{N-1}^n + C_{N-2}^n}{\Delta x} = D\frac{2C_N^n - 5C_{N-1}^n + 4C_{N-2}^n + C_{N-3}^n}{(\Delta x)^2} + R^n + o(\Delta t, (\Delta x)^2) \qquad (60)$$

2.6. Results and Discussion

2.6.1. Model validation

Several simulations were run to compare the model results with existing experimental data in literature for injection of different kinds of silica nanoparticles into Boise sandstone and Texas Cream limestone. The deposition of silica nanoparticles onto rock pore surface were divided into three different categories: high, moderate, and low rate of deposition based on DLVO energy profile. Each category has a characteristic DLVO energy profile. Table 2-4 shows the parameters used in the experiments and simulations, related to DLVO profile characteristic and rate of deposition. As discussed before, higher

energy barrier means stronger repulsion between the nanoparticle and pore surface, thus the lower rate of deposition.

Table 2-4— Input parameters for the three categories of DLVO energy profile

nanoparticle type	Nexsil 20K Silica	3M Fluorescent Silica	3M Silica with PEG coating
Nanoparticle radius (Ding et al.)	10	5	5
rock type	Boise Sandstone	Boise Sandstone	Boise Sandstone
Solution	D.I. water	D.I. water	0.5M NaCl and API brine
Zeta potential of rock grain (mV)	-22	- 22	-22
Zeta potential of nanoparticle (mV)	-50	-20	3
Reference	Caldelas (2010)	Zhang (2012)	Caldelas (2010)
DLVO profile character	high barrier, case 1	low barrier, case 1	no barrier, case 2
rate of deposition	low	moderate	high

2.6.1.1.Low rate of deposition by high energy barrier

Caldelas (2010) used Nexsil 20K silica nanoparticle without surface coating and Boise sandstone. Zeta potential of Nexsil 20K silica nanoparticle was measured as -50 mV. In low salinity environment (D.I.Water), electric double layer repulsion is strong because magnitude of zeta potential of Nexsil 20K silica nanoparticle is high. Fig. 2-12 shows the total DLVO energy profile with a high primary maximum, or energy barrier of 10 k_B*T and a low primary minimum over -30 k_B*T, resulting in low rate of deposition and release. Wang et al. (2012) indicated the secondary minimum does not present and the deposition in secondary minimum is neglected in this study.

Fig. 2-13a and b show good matches between simulation and experimental breakthrough curves, which plot the ratio of nanoparticle effluent concentration (C) to injection concentration (C_0) against pore volume injected (PVI). Calculated rate of deposition keeps the same because the chemical environment and physical properties of nanoparticles and grains do not change. With low rate of deposition the injection rate and concentration does not affect the breakthrough curves very much. The delay of breakthrough and long tail of breakthrough curve shown in Fig. 2-13c may be caused by highly viscous nanoparticle dispersion as a 40 wt%, or equivalently 15 vol% nanofluid is used. Caldelas (2010) indicated the post flush fingered through the more viscous nanofluid and the nanoparticle released from pore surface retained in the porous medium instead of flowing out of sandpack with post flush fluid. Therefore, many pore volumes of post flush are needed to sweep the retained nanoparticles.

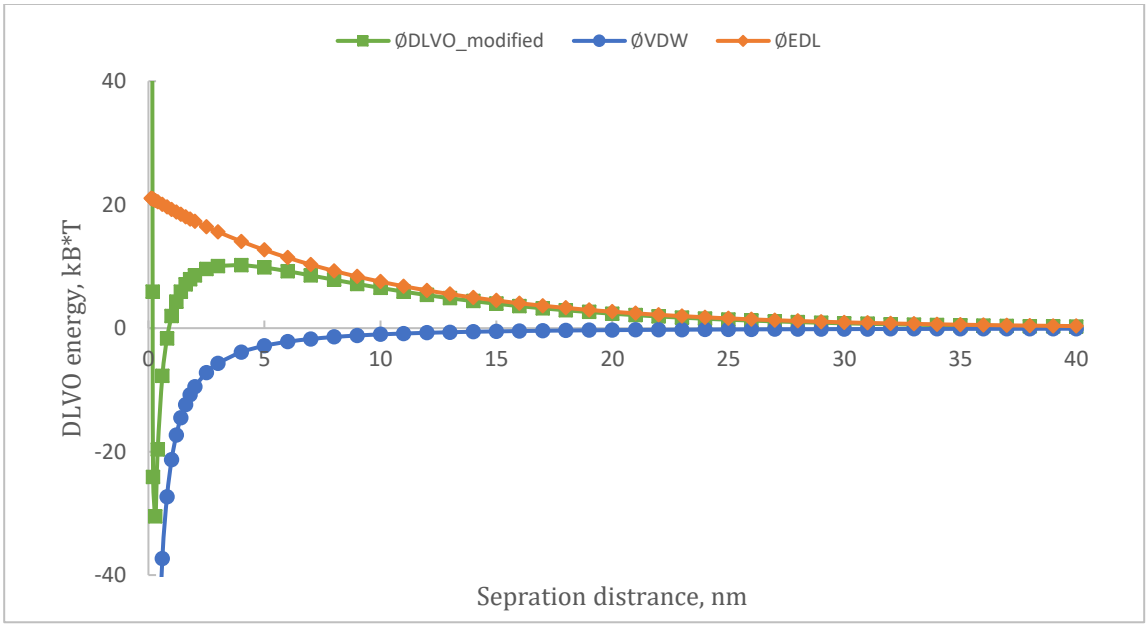

Figure 2-12— DLVO energy profile of Nexsil 20K silica nanoparticle (-50 mV) and Boise sandstone (-22 mV) with high energy barrier.

Table 2-5 — Calculated rate of deposition and release of the

Simulation #	Q_{inj} (ml/min)	C_{inj} (wt%)	C_{inj} (vol%)
1	1	5	2
2	3	5	2
3	1	40	15
Case 1 with energy barrier presents. Calculated rate of deposition $K_{dep,1}$ is $1.03 \cdot 10^{-7}$ $m \cdot s^{-1}$. Calculated rate of release $K_{rel,1}$ is $1.0 \cdot 10^{-20}$ s^{-1}. Experiment data of effluent concentration in simulation 1, 2 and 3 are from experiment 33, 35 and 26 by (Caldelas 2010), respectively.			

2.6.1.1.Moderate rate of deposition with low energy barrier

Fig. 2-14 shows the DLVO energy curves with the 3M fluorescent silica nanoparticles used by Zhang (2012) with Boise sandstone. The zeta potential of nanoparticle was measured as -20 mV. Compared to the previous case, a smaller electric double layer repulsion presents due to smaller zeta potential of nanoparticle. A small energy barrier of 3.5 k_B*T and primary minimum of -10 k_B*T leads to lower resistance to deposition and higher calculated rate coefficient of deposition (Table 2-6). With higher initial rate of deposition the injection rate and concentration significantly affect the breakthrough curves. High injection rate and concentration lead to fast coverage of rock surface and fast drop of rate of deposition. The faster drop of rate of deposition is reflected by steeper

slope of dimensionless concentration curve during the injection shown in Fig. 2-15a, b, c and d.

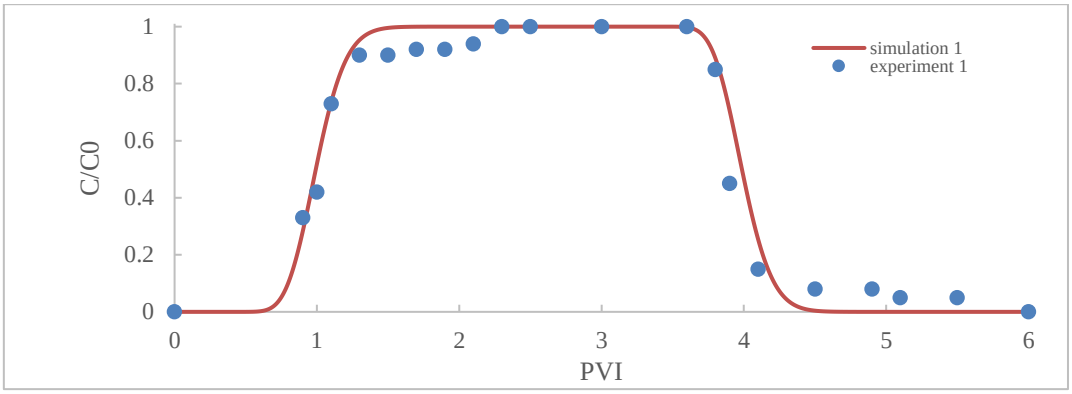

(a)

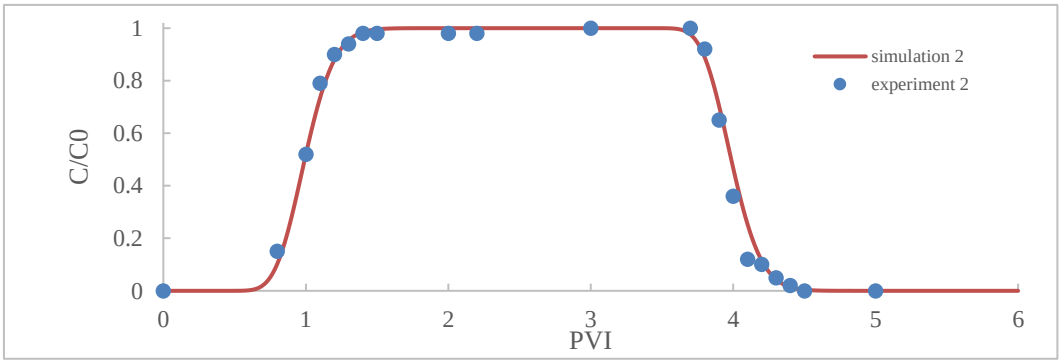

(b)

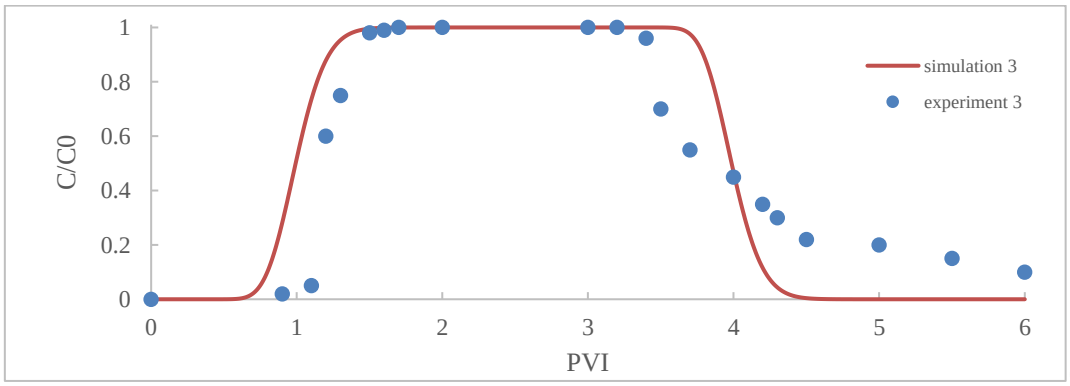

(c)

Figure 2-13— Experiment and simulated effluent concentration (breakthrough curves) of 3 pore volumes of Nexsil 30K silica nanoparticle injected into a 1-ft sandpack of Boise sandstone grains: (a) simulation 1; (b) simulation 2 and (c) simulation 3.

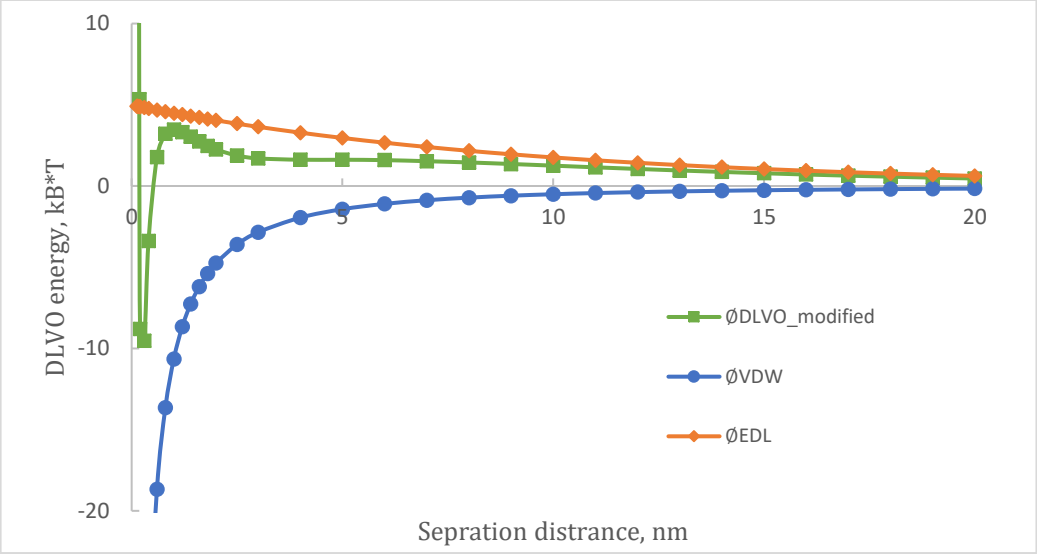

Figure 2-14— DLVO energy profile of silica nanoparticle (-20 mV) and Boise sandstone (-22 mV) with low energy barrier

Table 2-6— Calculated rate of deposition and release of the case by low energy barrier.

Simulation #	Q_{inj} (ml/min)	C_{inj} (wt%)	C_{inj} (vol%)
4	1	0.5	0.19
5	1	1	0.38
6	1	5	1.89
7	10	1	0.38

Case 1 with energy barrier presents.

Calculated rate of deposition $K_{dep,1}$ is $2.08 \cdot 10^{-6}$ $m \cdot s^{-1}$.

Calculated rate of release $K_{rel,1}$ is $1.7 \cdot 10^{-6}$ s^{-1}.

Experiment data of effluent concentration in simulation 4, 5, 6 and 7 are from experiment 104, 96, 102 and 107 by (Caldelas 2010), respectively.

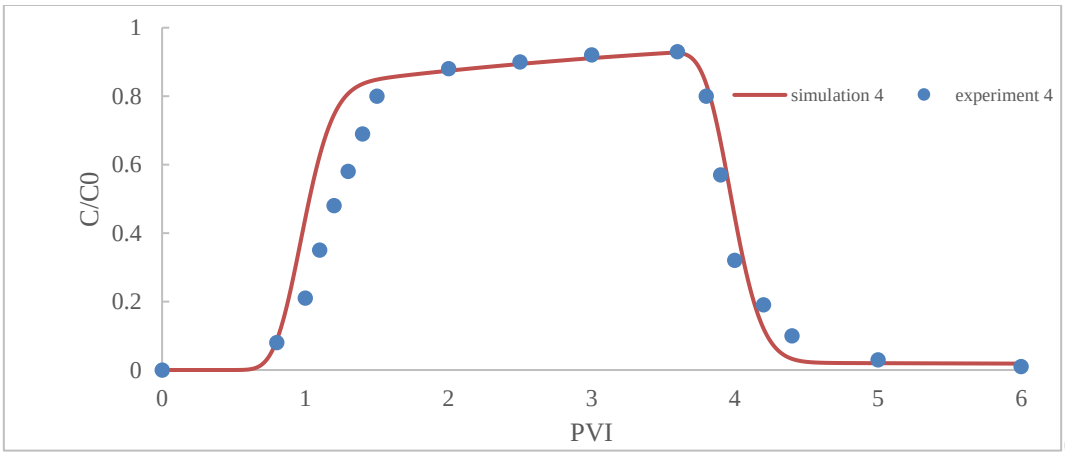
C/C0
PVI
simulation 4
experiment 4

(a)

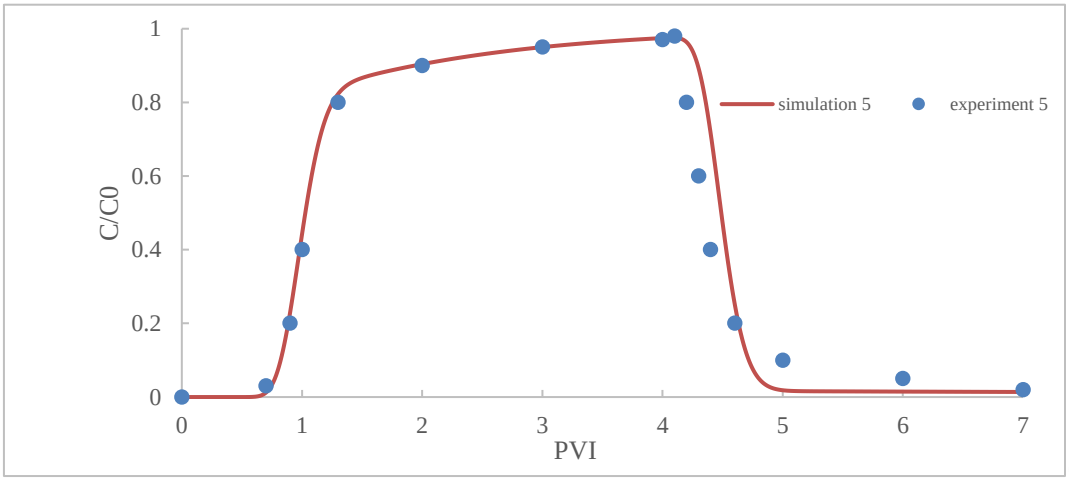
C/C0
PVI
simulation 5
experiment 5

(b)

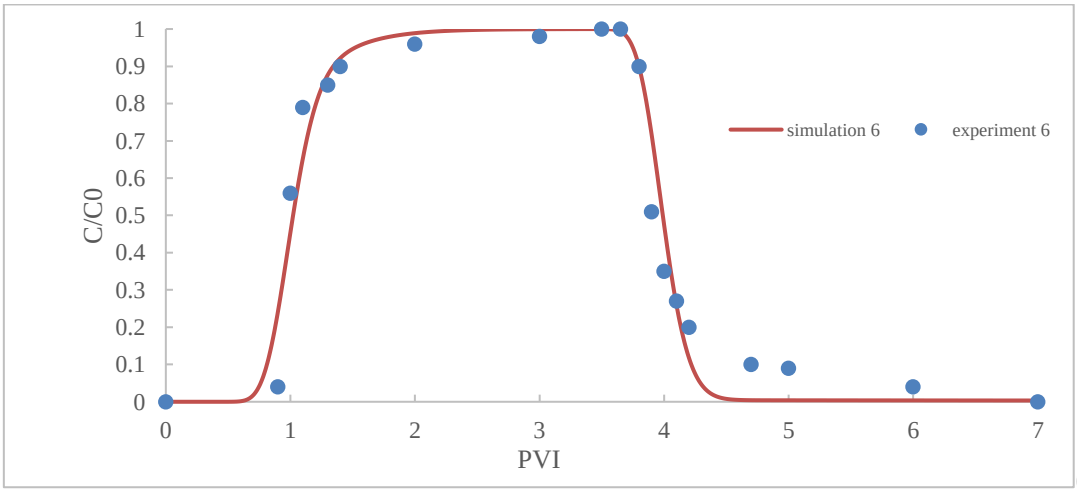
C/C0
PVI
simulation 6
experiment 6

(c)

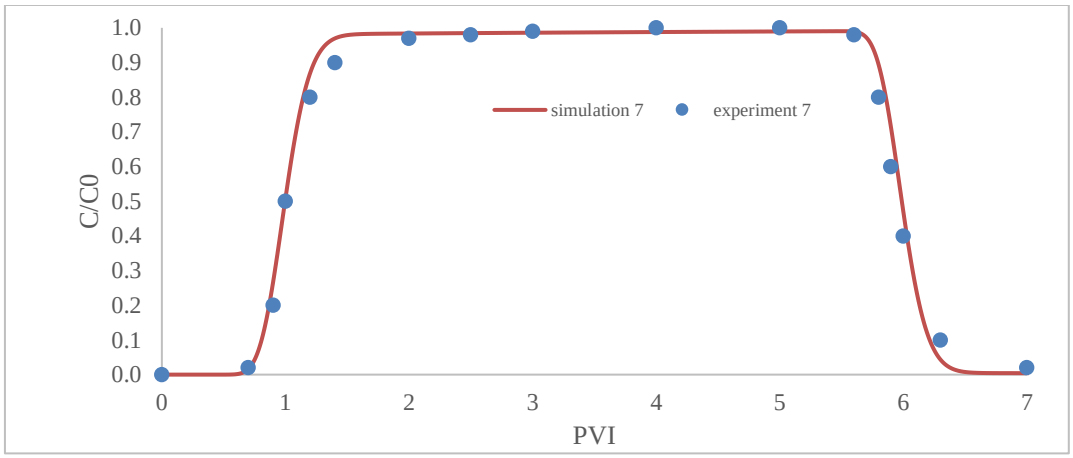

(d)

Figure 2-15— Experiment and simulated effluent concentration (breakthrough curves) of 3 pore volumes (simulation 4, 5, and 6) and 5 pore volumes (simulation 7) of 3M fluorescent silica nanoparticle injected into a 1-ft sandpack of Boise sandstone grains: (a) simulation.

2.6.1.2.High rate of deposition by no energy barrier

Fig. 2-16 shows the DLVO energy curves with the 3M silica nanoparticles with PEG coating and Boise sandstone system (Caldelas 2010). The zeta potential of nanoparticle was measured as about 3 mV±6 mV, which means the PEG coating effectively blocked the silica surface charge. Solution of high salinity (greater than 0.5 M) was used in the experiments. Under high ionic strength, the electrical double layer is highly compressed by high concentration of ions in electrolyte. Thus, the magnitude of electrical double layer interaction is much smaller than the van der Waals attraction at any separation distance. It is then concluded that the electrical double layer energy can be neglected and van der Waals energy dominates under high ionic strength condition. Therefore, the total DLVO energy is always attraction, resulting in very high rate of deposition when no energy barrier presents. Calculated rate coefficient of deposition increases as ionic strength increases (Table 2-7).

Fig. 2-17a and b show concentration ratio increases slower at higher ionic strength. Assuming a monolayer deposition at high ionic strength, the surface of pores will be covered by nanoparticle fast. However, high ionic strength may enhance coagulation of nanoparticles because attractive van der Waals force dominates the interaction energy between nanoparticles (Ryan and Elimelech 1996). Liu (1994) has reported the alumina nanoparticle takes more time to break through the quartz sand column at high ionic strength due to coagulation. As nanoparticles deposited on and covered the surface, the rate of deposition decreases due to the repulsive particle-particle interaction at low ionic strength. Whereas, as ionic strength increases, the particle-particle repulsion is weakened and coagulation of deposited nanoparticles may lead to multi-layer coverage close to the surface. Fig. 2-17c shows the best match to the experiment data with a triple-layer coverage.

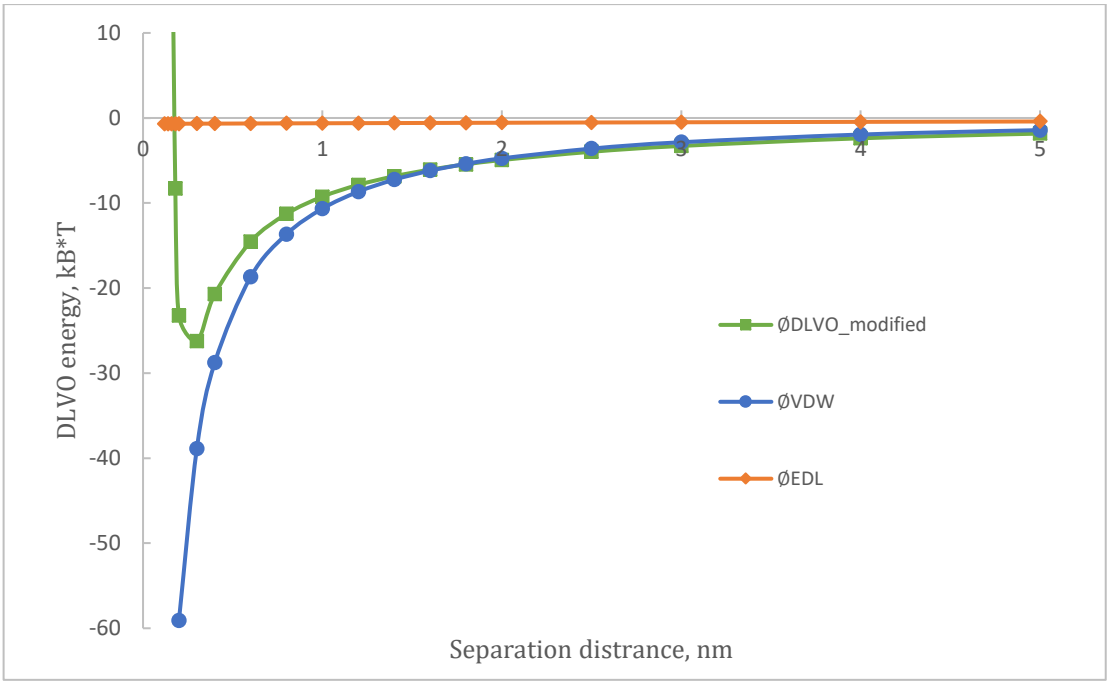

Figure 2-16— DLVO energy profile of silica nanoparticle with PEG coating (3 mV) and Boise sandstone (-22 mV) with no energy barrier, electric double layer energy is negligible and thus total DLVO energy equals to the van der Waals energy.

Table 2-7— Calculated rate of deposition and release of the case with no energy barrier

Simulation #	Q_{inj} (ml/min)	Ionic strength (M)
8	1	0.55
9	1	1.85
Case 2 without energy barrier. Calculated rate of deposition $K_{dep,2}$ is $5.27 \cdot 10^{-6}$ $m \cdot s^{-1}$. Calculated rate of release $K_{rel,2}$ is $2.74 \cdot 10^{-3}$ s^{-1} but is neglected because the critical velocity on nanoparticle of 0.23 $m \cdot s^{-1}$ is not reached. Experiment data of effluent concentration in simulation 8 and 9 are from experiment 25 and 45 by (Caldelas 2010), respectively.		

2.6.2. Sensitivity Analysis

The base case used in the sensitivity analysis is at temperature of 298 K, pH of 7 and silica nanoparticle radius of 5 nm. As mentioned in section 2.4, for 5-nm nanoparticles, release of both case 1 and case 2 are so small that are neglected. Only deposition is simulated in this analysis.

2.6.2.1. Effect of nanoparticle size

Table 2-8 shows large nanoparticles have less deposition than small nanoparticles, especially for case 1. Rate coefficient of SiO_2/Limestone system changes much slower than SiO_2/Sandstone system because DLVO energy profile of SiO_2/Limestone system is always case 2. It indicates that the deposition is more sensitive on nanoparticle size for case 1 rather than case 2. Fig. 2-18 and 2-19 show the effect of nanoparticle size on the

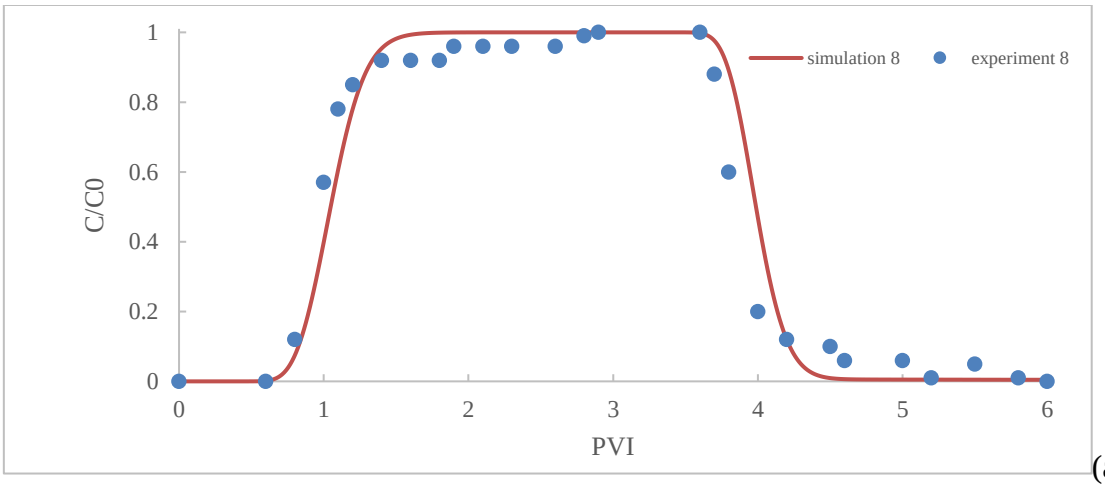

(a)

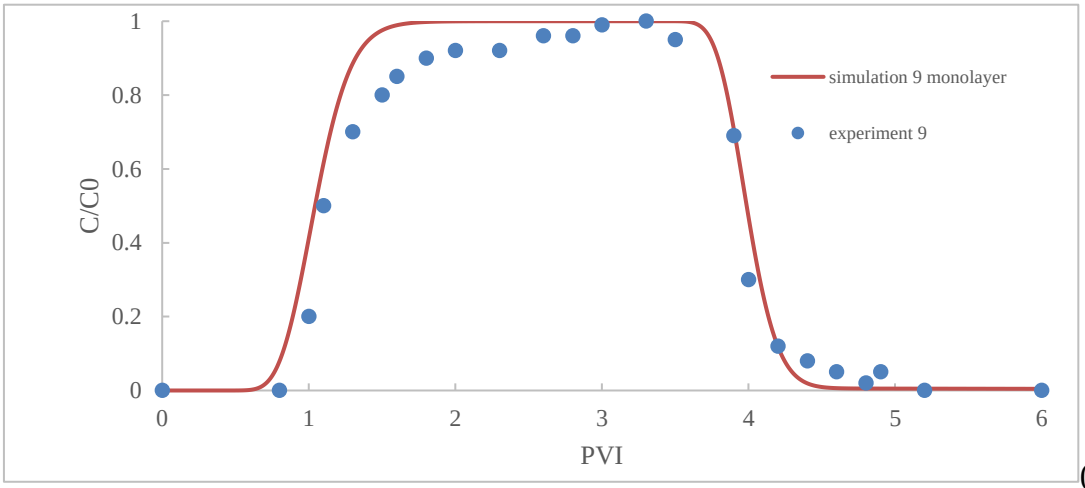

(b)

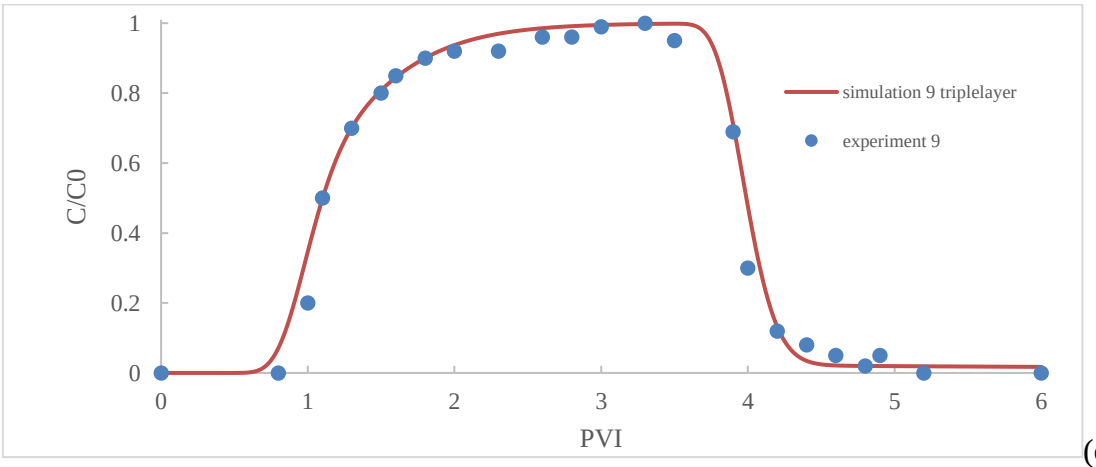

(c)

Figure 2-17— Experiment and simulated effluent concentration (breakthrough curves) of 3 pore volumes of 3M PEG coated silica nanoparticle injected into a 1-ft sandpack of Boise sandstone: (a) simulation 8; (b) simulation 9 assuming monolayer deposition and (c) simulation

simulated breakthrough curves and more deposition is observed for SiO_2/Limestone system, especially with small nanoparticles. This observation is consistent with the experiment results from Caldelas (2010).

Table 2-8— Calculated initial rate of deposition at high ionic strength of 0.001 M with different nanoparticle size.

a_p	Case 1, $K_{dep,1}$ ($m \cdot s^{-1}$)	Case 2, $K_{dep,2}$ ($m \cdot s^{-1}$)
5	2.55E-6	5.26E-6
10	2.12E-7	3.32E-6
50	3.62E-13	1.14E-6

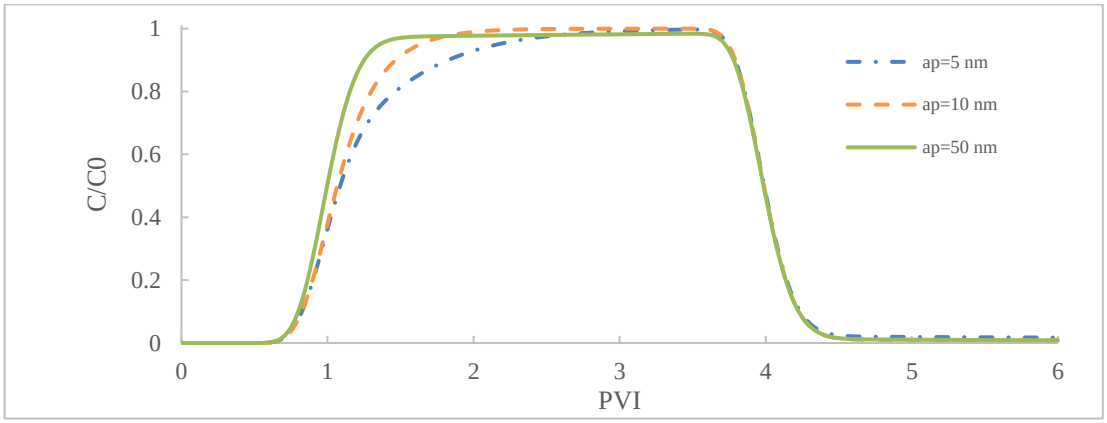

Figure 2-18— Simulated breakthrough curve of silica nanoparticle with different size on sandstone.

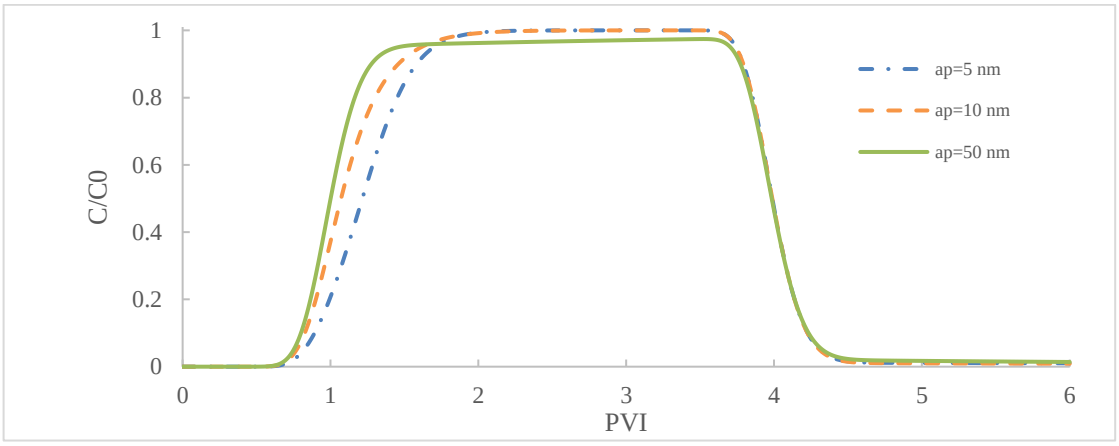

Figure 2-19— Simulated breakthrough curve of silica nanoparticle with different size on limestone.

2.6.2.2. Effect of pH and Temperature

Ryan and Gschwend (1994) indicates that solution chemistry is the critical to remove the energy barrier. Raising pH will lower and even remove the energy barrier. This treatment guarantees attractive DLVO interaction with no energy barrier (case 2) presents and high rate of deposition is always expected. When the solution salinity is low, the electrical double layer interaction plays an important role in determining the total DLVO interaction profile. Zeta potential is a function of pH and temperature significantly affects the magnitude of electrical double layer interaction, the behavior of deposition is studied at different pH and temperature. Table 2-9 shows the threshold of pH that switch the character of DLVO interaction profile from one case to another. At low pH, the nanoparticles and rock grain are oppositely charged with no energy barrier. Raising pH above 12 for SiO_2/Limestone system and 4 for SiO_2/Sandstone system switches DLVO energy profile from case 2 to case 1. Once the pH is adjusted above the threshold value, the nanoparticles and rock grain are similarly charged and thus energy barrier presents. The electrical double layer interaction and total DLVO interaction are then repulsive and results in low rate of deposition. For SiO_2/Sandstone system the silica nanoparticle and sandstone grain are always similarly charged and electrical double layer interaction is always repulsive. However, at low pH which is close to IEP of quartz the electrical double layer repulsion is less than the van der Waals attraction, resulting attractive total DLVO energy without energy barrier and high rate of deposition. As pH increases, zeta potential increases to produce stronger electrical double layer repulsion to turn the DLVO interaction profile to case 1. Higher energy barrier is then built up, resulting in lower rate of deposition.

Table 2-10 shows the rate of deposition of SiO_2/Limestone system is independent of temperature because its DLVO interaction profile is always case 2 at pH of 7. Whereas, the DLVO interaction profile SiO_2/Sandstone system is always case 1. Raising temperature increases the magnitude of zeta potential, and therefore enhances the repulsive DLVO interaction and lowers the rate of deposition. Fig. 2-20 and 2-21 show the simulated breakthrough curves of SiO_2/Sandstone system with less deposition at higher pH or temperature. Rate of deposition does not change much for SiO_2/Limestone system so the breakthrough curves are not plotted.

Table 2-9— Calculated initial rate of deposition at ionic strength of 0.0001 M and 25°C at different pH.

SiO_2/Limestone		SiO_2/Sandstone	
pH	Case 2, $K_{dep,2}$ ($m \cdot s^{-1}$)	pH	Case 2, $K_{dep,2}$ ($m \cdot s^{-1}$)
3	5.27E-6	3	3.32E-06
5	5.27E-6		Case 1, $K_{dep,1}$ ($m \cdot s^{-1}$)
7	5.27E-6	5	2.61E-06
9	5.27E-6	7	1.21E-07
11	5.27E-6	9	3.05E-09
	Case 1, $K_{dep,1}$ ($m \cdot s^{-1}$)	11	6.08E-11
13	4.20E-09	13	8.73E-13

Table 2-10— Calculated initial rate of deposition at ionic strength of 0.0001 M and pH of 7 at different temperature.

SiO_2/Limestone		SiO_2/Sandstone	
Temperature (Pfeiffer et al.)	Case 2, $K_{dep,2}$ ($m \cdot s^{-1}$)	Temperature (Pfeiffer et al.)	Case 1, $K_{dep,1}$ ($m \cdot s^{-1}$)
25	5.27E-6	25	1.21E-07
50	5.27E-6	50	6.71E-08
75	5.27E-6	75	1.58E-09
100	5.27E-6	100	1.50E-11

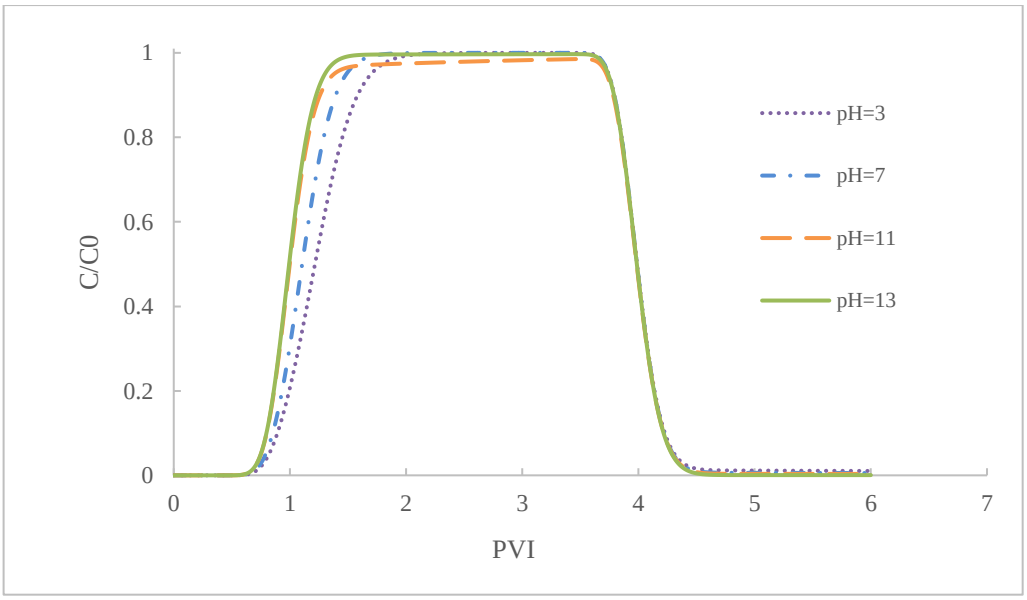

Figure 2-20— Simulated breakthrough curve of silica nanoparticle on sandstone at different pH.

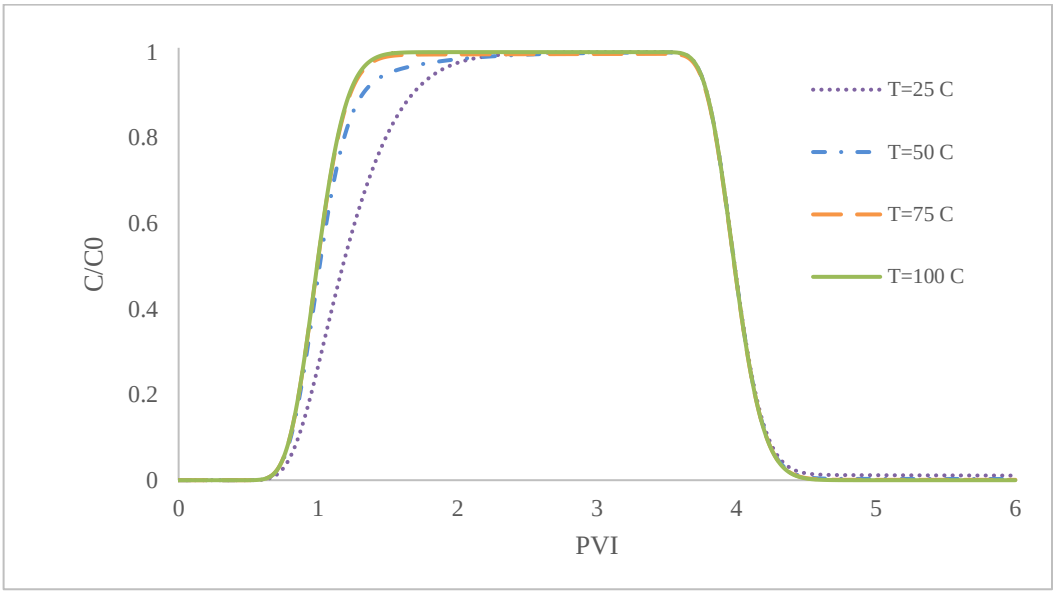

Figure 2-21— Simulated breakthrough curve of silica nanoparticle on sandstone at different temperature.

2.6.2.3. Effect of ionic strength

Raising ionic strength will lower and even remove the energy barrier. Once the ionic strength is greater than 0.01M, the electrical double layer interaction, no matter attraction or repulsion, becomes smaller than the van der Waals attraction (Zhang 2012). Per Eq. 12 and 13, van der Waals interaction is independent of ionic strength and electrical double layer interaction is weakened as ionic strength is increased. Table 2-11 shows the rate of deposition of SiO_2/Limestone system is independent of ionic strength because its DLVO interaction profile is always case 2 at pH of 7. However, raising ionic strength can turn the DLVO interaction profile from case 1 to case 2 for SiO_2/Sandstone system. The electrical double repulsion creates an energy barrier at low ionic strength, resulting in low rate of deposition. As ionic strength increases, this repulsion is weakened until it cannot balance the van der Waals attraction any more. From this simulation, the energy barrier

is removed when the ionic strength is above 0.005M, which is close to the value of 0.01M reported by Zhang (2012) for the same system. It is then inferred that for similarly-charged particle-rock system, ionic strength is a key factor on deposition behavior.

Table 2-11— Calculated initial rate of deposition at pH of 7 and 25oC at different ionic strength.

SiO_2/Limestone			SiO_2/Sandstone		
I (M)	I (wt%)	Case 2, $K_{dep,2}$ ($m \cdot s^{-1}$)	I (M)	I (wt%)	Case 1, $K_{dep,1}$ ($m \cdot s^{-1}$)
0.0001	0.001%	5.27E-6	0.0001	0.001%	1.21E-07
0.001	0.005%	5.27E-6	0.001	0.003%	9.03E-07
0.01	0.054%	5.27E-6			Case 2, $K_{dep,2}$, $m \cdot s^{-1}$
0.1	0.541%	5.27E-6	0.005	0.015%	3.32E-06
			0.01	0.054%	3.32E-06
Energy barrier vanishes for SiO_2/Sandstone system when the ionic strength is above 0.001M.					

2.6.2.4. Effect of surface roughness

In this model, surface roughness affects the DLVO energy-controlled deposition and release of case 1 but not the diffusion-controlled deposition and rate of release of case 2. The two main parameters considering are roughness height-nanoparticle radius ratio (h_{rms}/a_p) and roughness density (ρ_r), or roughness fraction (η_r) equivalently. As

h_{rms}/a_p or η_r increases, the height of energy barrier decreases, resulting in higher rate of deposition and release. It is consistent of experiment observations that more deposition will occur on rougher surface or using smaller nanoparticle on the same surface (Shellenberger and Logan 2002, Hoek et al. 2003). Table 2-12 and 2-13 show the increase of rate of deposition and release with higher roughness density, and more deposition with smaller nanoparticles. Table 2-14 show fast decrease of deposition as the size of nanoparticle is larger than the height of surface roughness.

Table 2-12— Calculated initial rate of deposition of SiO2/Sandstone system with different surface roughness density, assuming $h_{rms} = 14\ nm, a_p = 5\ nm$.

ρ_r (1/m^2)	η_r	$\emptyset_{max}$ (k_B*T)	$K_{dep,1}$ (m·s^{-1})	$K_{rel,1}$ (m·s^{-1})
1.62E+15	1.00	10.5	5.60E-07	3.20E-05
5.14E+14	0.50	10.9	3.47E-07	7.06E-06
1.80E+14	0.20	11.2	2.62E-07	2.79E-06
6.01E+13	0.07	11.4	1.51E-07	1.58E-06

Table 2-13— Calculated initial rate of deposition of SiO2/Sandstone system with different surface roughness density, assuming $h_{rms} = 14\ nm, a_p = 10\ nm$.

ρ_r (1/m^2)	η_r	$\emptyset_{max}$ (k_B*T)	$K_{dep,1}$ (m·s^{-1})	$K_{rel,1}$ (m·s^{-1})
1.62E+15	1.00	17.4	1.90E-10	4.24E-07
5.14E+14	0.50	20.1	1.28E-11	3.56E-09
1.80E+14	0.20	21.7	2.58E-12	2.08E-10
6.01E+13	0.07	22.7	9.48E-13	3.68E-11

Table 2-14— Calculated initial rate of deposition of SiO2/Sandstone system with different roughness height-nanoparticle radius ratio, assuming $\eta_r = 1$

$\frac{h_{rms}}{a_p}$	$\emptyset_{max}$ (k_B*T)	$K_{dep,1}$ ($m \cdot s^{-1}$)	$K_{rel,1}$ ($m \cdot s^{-1}$)
3	10.2	6.10E-07	2.80E-05
2	13.5	2.63E-08	5.67E-06
1	21.7	1.56E-12	5.75E-08
0.5	32.7	9.18E-18	4.57E-09

2.7. Summary and Conclusion

Rate of deposition of silica nanoparticles onto limestone/sandstone surface widely varies as physical properties of material and chemical environment change. Our mechanistic model well quantifies the rate of deposition and release under various physical and chemical conditions. The simulation results demonstrate the dependence of nanoparticle deposition on several physical and chemical parameters based on DLVO theory:

- Small nanoparticles tend to have higher rate of deposition.
- For silica/Sandstone system, rate of deposition decreases as pH and temperature increases.
- Rate of deposition of silica/Limestone system is almost independent of pH, temperature and ionic strength because its DLVO interaction profile is always case 2.
- Rate of deposition of silica/Sandstone system is highly dependent of pH, temperature and ionic strength because its DLVO interaction profile is case 1 in many conditions. Therefore, rate of deposition is expected to be higher for silica/Limestone system than silica/Sandstone system.

- Adjusting pH and ionic strength can turn the DLVO interaction profile from one case to another, resulting a huge change on rate of deposition. For silica/Sandstone system, rising pH above 5 turns case 2 to case 1 and raising ionic strength above 0.005 M turns case 1 to case 2. Moreover, high ionic strength may lead to more accumulative deposition due to multi-layer coverage on rock pore surface.
- Rough surface of rock grain promotes the nanoparticle deposition and release.

Acknowledgement

This work is supported by the Abu Dhabi National Oil Company (ADNOC) [grant number 880005].

Nomenclature

a_g	Radius of rock grain
a_p	Radius of nanoparticle
A_H	Hamaker constant
A_p	Projected cross-section area of a spherical nanoparticle
$B(\theta)$	Deposition rate correction
C	Nanoparticle concentration
C_{bulk}	Nanoparticle concentration in bulk fluid
C_{dep}	Concentration of deposited nanoparticle on pore surface
C_{inj}	Nanoparticle injection concentration
C_0	Nanoparticle injection concentration
d_{pore}	Diameter of the cylindrical pore throat.
D	Diffusion coefficient of nanoparticles in aqueous suspension
e	Elementary charge
F_d	Hydrodynamic drag force
F_{DLVO}	Net DLVO force
F_{HYD}	Hydration force
F_l	Lifting force
h	Critical height of surface roughness for nanoparticle release
h_{rms}	Root mean square of surface roughness height
h_{abs}	Absolute mean of surface roughness height
I	Ionic strength
J	Nanoparticle deposition flux
J_0	Nanoparticle deposition flux at surface
K_{a1}	Equilibrium constant of surface acidic reaction

K_{a2}	Equilibrium constant of surface basic reaction
K_B	Boltzmann constant
K_{dep}	Rate coefficient of deposition
K_{rel}	Rate coefficient of release
$K_{dep,1}$	Rate coefficient of deposition for case 1
$K_{dep,2}$	Rate coefficient of deposition for case 2
$K_{rel,1}$	Rate coefficient of release for case 1
$K_{rel,2}$	Rate coefficient of release for case 2
l_d	Arm of hydrodynamic drag torque
l_{DLVO}	Arm of DLVO torque
m_1	Slope of fast region of zeta potential calculation
m_2	Slope of slow region of zeta potential calculation
M_d	Moment of surface stresses
M_i	Molar concentration of ith ion
N_A	Avogadro number
$pH_{cut-off}$	Fitted cut-off point
pH_{IEP}	Isoelectric point of the surface
PVI	Pore volume injected
Q_{inj}	Injection rate
R	Nanoparticle retention
S_{rough}	Rough surface area
S_{smooth}	Smooth surface area
S_{SA}	Specific surface area of rock
T	Temperature
T_d	Drag torque
T_o	Reference temperature at 25^{o}C
T_{DLVO}	DLVO torque
u	Superfacial velocity
u_{max}	Maximum flow velocity
u_p	Flow velocity acting at the center of the nanoparticle
$u_{p,cr}$	Critical flow velocity acting on center of nanoparticle for release
U_E	Electrophoretic mobility
V_{pore}	Pore volume
x_s	Distance from surface to shear plane
y_{max}	Separation distance at primary maximum
y_{min}	Separation distance at primary minimum
y	Separation distance between nanoparticle and pore surface
Z	Valence of the electrolyte
β	Sensitivity parameter of surface for zeta potential
δ_{DLVO}	Thickness of DLVO layer
δ_{Diff}	Thickness of diffusion boundary layer
ζ	Zeta potential
$\eta_{packing}$	Hexagonal packing efficiency
η_r	Fraction of rough surface area over total surface area

θ	Pore surface coverage area
κ	Inverse Debye length
λ	Characteristic London wavelength
μ	Viscosity of the fluid
μ_f	Static friction coefficient
ϵ	Dielectric constant;
ρ_{fluid}	Fluid density
ρ_r	Roughness density
ρ_{rmax}	Maximum roughness density
ψ_s	Surface potential
v_ζ	Temperature sensitivity coefficient
ϕ	Porosity
$\emptyset_{BORN}$	Born interaction energy
$\emptyset_{DLVO}$	DLVO interaction energy
$\emptyset_{DLVO_{flat}}$	DLVO interaction energy between sphere and flat surface
$\emptyset_{DLVO_{sphere}}$	DLVO interaction energy between sphere and sphere
$\emptyset_{DLVO_{rough}}$	DLVO interaction energy between sphere and rough surface
$\emptyset_{EDL}$	Electrical double layer interaction energy
$\emptyset_{HYD}$	Hydration interaction energy
$\emptyset_{max}$	DLVO interaction energy at primary maximum
$\emptyset_{min}$	DLVO interaction energy at primary minimum
$\emptyset_{VDW}$	Van der Waals interaction energy
χ	Lifting force coefficient
ψ_s	Surface potential

Chapter 3 Mathematical Modeling and Simulation of Nanoparticles Transport in Heterogeneous Porous Media

Abstract

Nanoparticle applications in the petroleum industry have grown recently especially in EOR and waterflooding. Although the nanoparticles are small, they can be retained in the porous media by three different damage mechanisms i.e. surface deposition, mono-particle plugging, and multi-particles plugging. This could severely decrease the porosity and permeability of the porous medium. Consequently, a numerical model that accurately describes these damage mechanisms is essential for forecasting and optimization of nanoparticles transport in porous media. In this paper, we have developed a mathematical model that combines Darcy and convection-diffusion equation to describe fluid flow, nanoparticles transport, and interaction in porous media. Pore throat size distribution is used to characterize the heterogeneity. Permeability field is generated as a function of the pore throat size distribution. Pore throat size and permeability distributions are dynamic functions of the nanoparticles deposition and plugging. The mathematical model is solved on a two-dimensional domain using alternating direction implicit scheme. The model is validated with experimental data to obtain the model parameters. Sensitivity analysis is presented using the proposed numerical model. The model shows that each of the three damage mechanisms could be dominant at specific conditions. Dimensional analysis is then used to derive a correlation that relates the degree of damage to main dimensionless numbers that control the efficiency of nanoparticle transport. The preliminary numerical results demonstrate that nanoparticle size, concentration, injection rate and permeability are the dominant factors that control the degree of formation damage.

Keywords:
Nanoparticles; Porous Media; Mathematical Modeling; Numerical Simulation; Formation Damage

3.1. Introduction

Nanotechnology has gained a wide interest in the oil and gas industry during the past decade. Nanotechnology is the science and engineering of particles at the nanoscale (nanoparticles), which are about 1 to 100 nanometers in size. The applications of Nanotechnology in petroleum reservoirs can be categorized into Nanofluid, Nanoemulsion, and Nanocatalyst (Abdelfatah et al. 2014). Nanofluid is the dispersion of nanoparticle in a solvent fluid (mostly dispersed in a liquid water). Nanofluids have been applied in many aspects of the upstream petroleum industry such as enhanced oil recovery (Ogolo et al. 2012, Fletcher and Davis 2010), well stimulation (McElfresh et al. 2012a), drilling fluids (Mahmoud et al. 2016) , hydraulic fracturing fluids (Fakoya and Shah 2014, 2016), and fines fixation (Huang et al. 2008). Nanoemulsion is a new version of the Pickering emulsions that is stabilized by nanoparticles instead of surfactants. Nanoemulsions can maintain stability despite harsh reservoirs conditions due to the irreversible adsorption of the nanoparticles on their droplet surface (Zhang et al. 2010). Nanoemulsions with a small droplet size (50–500 nm) are small enough to pass through rock pores without much retention (Mandal et al. 2012). Nanoemulsions have several potential applications in oil and gas upstream industry such as enhanced oil recovery and mobility control (Mandal et al. 2012). Nanotechnology has also the potential to improve the efficiency of steam injection and heavy oil recovery by working as a Nanocatalyst (Shokrlu and Babadagli 2010, Greff and Babadagli 2011). Steam injection does not only reduce the viscosity of heavy oil by heat transfer to oil but also, there are chemical

reactions that occur between oil and steam, called aquathermolysis reactions (Hyne 1986). Aquathermolysis reactions in situ upgrade the heavy oil by breaking down the carbon-sulfur bond in asphaltene, increasing the saturates and aromatic content and Hydrogen-carbon ratio. Nanoparticles of transition metals such as VO^{2+}, Mo^{3+}, Ni^{2+} and Fe^{3+} (that are referred as Nanocatalyst) can catalyze these aquathermosis reactions that can further upgrade the heavy oil (Greff and Babadagli 2011). Nanoparticles of transition metal can easily transport through the reservoir rock. Nanocatalyst such as Nickel nanoparticles can improve the recovery of the steam stimulation process by 10% (Shokrlu and Babadagli 2011).

The stability of the nanoparticles dispersion is a key factor that affects nanoparticles transport in porous media. Nanoparticles can easily aggregate since they have a large specific surface area to volume ratio (Hendraningrat and Torsæter 2014). The primary size of the nanoparticle can be a few nanometers. However, Esfandyari Bayat et al. (2015) found that nanoparticles aggregates in D.I.W and that the aggregate size is an order of magnitude greater than the original nanoparticle size. Nanoparticles have a surface charge such as a negative charge for Silica and positive charge for Alumina. Therefore, the nanoparticles can be adversely affected by oppositely charged ions either in the solution or on the rock surface. These ions limit the ability of nanoparticles to repel each other and shrink the hydrodynamic radius (McElfresh et al. 2012b). The stability of nanofluid can be achieved by manipulating the surface charge on the nanoparticles. The common techniques to improve nanofluid stability are particle surface modification by coating or controlling the ionic strength of the dispersant fluid via stabilizers (Ghadimi et al. 2011).

Yet, for nanofluid to be applied in the oil and gas field scale, nanoparticles should have the ability to be transported long distance in the reservoir rock. Transport of nanoparticles in porous media has been studied by many researchers to explore how nanoparticles interact inside the porous media and what factors affect this process (Abdelfatah et al. 2014, Ju and Fan 2009). The nanoparticle concentration, injection rate, salinity, and temperature are among several factors that affect nanofluid stability and also the efficiency of nanoparticles transport in porous media. There are three mechanisms of interaction between particles and porous media that affect the efficiency of nanoparticle transport i.e. surface deposition, mono-particle pore throat plugging (screening) and multi-particles pore throat plugging (log-jamming) (Herzig et al. 1970, Gruesbeck and Collins 1982, Civan 2007, Ju and Fan 2009). Surface deposition is an electrokinetic interaction between nanoparticles and the rock surface that can be either attractive or repulsive (Alaskar et al. 2012). The salinity of the environment has a major effect on the electrokinetic interaction by changing the thickness of the electrostatic double layer. Conversely, pore throat plugging is a mechanical process that includes the formation of momo-particle or multi-particles plug across the pore throat entry. For mono-particle pore throat plugging, nanoparticles' aggregates larger than the pore throat size are excluded at the entry of the pore throat (Hendraningrat and Torsæter 2014, Hendraningrat et al. 2012). Mono-particles plugging depends on the nanoparticle size and the stability of the nanofluids that controls the aggregate size. Yet, multi-particles plugging (Log-Jamming) occurs when several small nanoparticles come together at the pore throat entry to form a plug (Skauge et al. 2010). Injection rate, nanoparticles size, and concentration are the

critical factors that control the multi-particles plugging. The higher the injection rate and the nanoparticle concentration, the more severe is the multi-particle plugging effect.

Finite difference method is widely used for solving petroleum reservoir problems (Aziz and Settari 1979). Other methods such as Green function, finite volume, and orthogonal collocation are used also for solving reservoir fluid flow problems (Vaferi and Eslamloueyan 2015, Khadivi and Soltanieh 2014, Vaferi et al. 2012, Ghanaei and Rahimpour 2010, Gringarten and Ramey 1973). Herein, finite difference method is used to simulate nanoparticles transport in heterogeneous carbonate rock. To account for the heterogeneous nature of the carbonate rock, pore size distribution measured from mercury injection is included in the model to study the effect of the heterogeneity on the nanoparticle transport efficiency. A random permeability distribution is assigned to each gridblock.

The objective of this paper is to introduce a mathematical model that effectively describes the formation damage mechanisms associated with nanoparticles transport in porous media. Also, we present the numerical solution of the model on a two-dimensional domain. The paper is organized as the following. The mathematical model is introduced in section 3.2. The geological model constructed to represent the porous medium section is in section 3.3. The numerical solution algorithm is presented in section 3.4. Finally, the numerical model is validated using experimental data in section 3.5.1. The sensitivity analysis of nanoparticle size, concentration, injection rate and permeability is presented in section 3.5.2. Dimensional analysis is presented in section 3.5.3. Conclusions from this work are presented in section 3.6.

3.2. Mathematical Model

3.2.1. Transport of the fluid in porous media

Nanoparticles dispersion in water can be modeled as single phase-two component system (water and nanoparticles). Transport of the bulk fluid can be represented by Darcy's law and the continuity equation (Aziz and Settari 1979). The continuity equation represents the mass conservation and accounts for the porosity (ϕ) change by nanoparticles entrapment in the porous media.

$$\frac{\partial(\phi)}{\partial t} + \nabla.\ (u) = 0 \tag{1}$$

where ϕ is the porosity of the porous media, and u is the superfacial velocity, m/s. Then Darcy's law can be used to compute the volumetric flux (u).

$$u = -\frac{K}{\mu}\ \nabla p \tag{2}$$

where K is the permeability of the porous media, m^2, μ is the viscosity of the Nanofluid, Pa.s and ∇p is the pressure drop across the porous media, Pa. The boundary conditions applied to the continuity equation are constant injection rate at the inlet, constant effluent pressure at the outlet and no-flow boundary at the peripheral.

3.2.2. Transport of nanoparticles in porous media

Convection-diffusion equation with source term representing the nanoparticles retention inside the porous media is used to model the transport of nanoparticles in porous media (Chang and Civan 1991). However, due to retention of nanoparticles, the structure properties of the rock changes and a portion of the pore system can no longer contribute to flow due to plugging. The mass balance of the nanoparticles has been derived using

the fraction of the domain that's accessible to nanoparticles (flowing fraction *f*). The adjusted Convection-diffusion equation can be written as the following:

$$\frac{\partial(\phi C)}{\partial t} + \nabla(fuC) - \nabla(D\phi f.\nabla C) + R = 0 \quad (3)$$

where, C is the volume fraction of the nanoparticles inside the core, *R* is the net rate of nanoparticles entrapment per unit bulk volume of the porous media, and *D* is the diffusion coefficient, m^2/s. Nanoparticles are submicron in size, so the Brownian motion is much more effective. The diffusion coefficient is inversely proportional to the nanoparticle diameter and can be calculated using the Stokes-Einstein equation (Bird et al. 2007).

$$D = \frac{K_B T}{3\pi\mu D_{p.avg}}, \quad (4)$$

where K_B is the Boltzmann constant, T is the absolute temperature of the environment, K, $D_{p.avg}$ is the average nanoparticle diameter, m, and μ is the fluid viscosity, Pa.s. The initial and boundary applied to the Convection-diffusion equation should be defined on the computational domain to close the mathematical model. The initial conditions are defined as, C = 0 and, R = 0 at t = 0. The boundary conditions at the inlet are constant injection rate and constant injected concentration of nanoparticles equals the injected concentration, $C=C_{inj}$. Herein, C_{inj} is the injected concentration. At the outlet, there is no diffusion that means $\frac{\partial C}{\partial x} = 0$. At the peripheral, no flow boundary conditions are used. The source term represents the net rate of nanoparticles entrapment (*R*) that is the amount of nanoparticle deposited on the pore surface and that plugged the pore throats per unit bulk volume of the porous media (Gruesbeck and Collins 1982).

$$R = \frac{\partial \varepsilon_d}{\partial t} + \frac{\partial \varepsilon_{pt}}{\partial t}, \quad (5)$$

ε_d is the volume fraction of nanoparticles deposited on the pore surface and ε_{pt} is the volume fraction of nanoparticles that plugged the pore throat. The rate of nanoparticle deposition ($\frac{\partial \varepsilon_d}{\partial t}$) and the rate of pore throat plugging ($\frac{\partial \varepsilon_{pt}}{\partial t}$) can be computed using Gruesbeck and Collins (1982) model.

$$\frac{\partial \varepsilon_d}{\partial t} = \begin{cases} k_d u\, C & ;u \le u_c \\ k_d u\, C - k_e \varepsilon_d\, (u - u_c) & ;u > u_c \end{cases} \quad \text{and,} \tag{6}$$

$$\frac{\partial \varepsilon_{pt}}{\partial t} = k_{pt} u\, C$$

where k_d, k_e and k_{pt} are the rate coefficient for deposition, entrainment and pore throat plugging, respectively. u_c is the critical velocity to release the deposited particles from the surface into the bulk fluid. These equations can be solved with the initial conditions, $\varepsilon_d = 0$ and $\varepsilon_{pt} = 0$ at $t = 0$. Then the total volume fraction of the nanoparticles entrapped in the porous media (ε) can be computed as the summation of those deposited at the pore surface (ε_d)and those plugged the pore throat (ε_{pt}).

$$\varepsilon = \varepsilon_d + \varepsilon_{pt}, \tag{7}$$

3.2.3. Pore size distribution

The interaction between nanoparticles and the porous medium depends on the interplay between the nanoparticle size and pore throat size distribution. The bimodal distribution function is used to fit the measured pore throat size distribution from mercury injection (Popplewell et al. 1989, Chang and Civan 1991).

$$F(D_{pt}) = wF_1(D_{pt}) + (1 - w)F_2(D_{pt}), \tag{8}$$

where $F_1(D_{pt})$ is the distribution function for the fine fraction of the pore throats smaller than 1 micron, $F_2(D_{pt})$ is the distribution function for the coarse fraction of the pore

throats larger than 1 micron, and *w* is the weight of the fine fraction of the pore throats. $F_1(D_{pt})$ and $F_2(D_{pt})$ can be written as the following (Popplewell et al. 1989).

$$F_1(D_{pt}) = \frac{(D_{pt} - D_{pt,min})^{a_1 m_1}(D_{pt,max} - D_{pt})^{m_1}}{\int_{D_{pt,min}}^{D_{pt,max}}(D_{pt} - D_{pt,min})^{a_1 m_1}(D_{pt,max} - D_{pt})^{m_1} dD_{pt}} \quad (9)$$

$$F_2(D_{pt}) = \frac{(D_{pt} - D_{pt,min})^{a_2 m_2}(D_{pt,max} - D_{pt})^{m_2}}{\int_{D_{pt,min}}^{D_{pt,max}}(D_{pt} - D_{pt,min})^{a_2 m_2}(D_{pt,max} - D_{pt})^{m_2} dD_{pt}} \quad (10)$$

where $D_{pt,min}$ and $D_{pt,max}$ are the minimum and maximum pore throat diameters, and $a_1, m_1, a_2 \; and \; m_2$ are empirical parameters that can be matched with the experimental data from mercury injection. Unlike pore throat size distribution, nanoparticles distribution has a narrow spectrum (Evonik 2016). Based on this, the average nanoparticles size is used as an approximation, which simplifies the calculations without causing significant error. In this model, the average nanoparticle size for the experimental data used in section 5.1 is around 150 nm for hard aggregates.

3.2.4. Flowing fraction (f):

Flowing fraction is a fraction of the pores that contributes nanoparticles transport (Chang and Civan 1991). The flowing fraction is a dynamic function of the nanoparticles entrapment in the porous media. If we only consider mono-particle plugging, the flowing fraction can be calculated as the following,

$$f = 1 - \int_{D_{pt,min}}^{D_{p,ave}} F(D_{pt}) dD_{pt} \quad (11)$$

On the other hand, if both mono-particle and multi-particle plugging are considered, the flowing fraction can be calculated as the following (Chang and Civan 1991).

$$f = 1 - \int_{D_{pt,min}}^{D_{pt,cr}} F(D_{pt}) dD_{pt} \tag{12}$$

For calculating the critical diameter for pore throat plugging, Civan (2007) suggested the following equation that is a function of the particle Reynolds number:

$$D_{pt,cr} = D_{p.avg} \,.\, (A(Re_p)^{B} + G) \tag{13}$$

where A, B, and *G* are empirical parameters. The particle Reynolds number (Re_p) can be calculated as follows (Civan 2007).

$$Re_p = \frac{\rho_p \, C \, D_{p.avg} \, u \, \tau}{\mu \phi} \tag{14}$$

where ρ_p is the density of the nanoparticle, Kg/m^3 and τ is the tortuosity of the porous media. Herein, it's considered that, $D_{pt,min}$ and $D_{pt,max}$ are dynamic functions of pore surface deposition and pore throat plugging. Assuming that the change in the pore throat size is linear function of the net rate of deposition, the mean pore throat diameter ($D_{pt,m}$) can be computed using the following equation (Ohen 1989) if deposition is the only considered damage mechanism:

$$-\frac{\partial D_{pt,m}}{\partial t} = \beta(\dot{\varepsilon_d} - \dot{\varepsilon_e}) \tag{15}$$

where β is an empirical parameter and $(\dot{\varepsilon_d} - \dot{\varepsilon_e})$ is the net rate of nanoparticle deposition on the pore surface. To close the problem, the following integrals can be solved simultaneously to calculate $D_{pt,min}$ and $D_{pt,max}$. Total probability of the statistical sample,

$$\int_{D_{pt,min}}^{D_{pt,max}} F(D_{pt}) dD_{pt} = 1 \tag{16}$$

The mean pore throat diameter ($D_{pt,m}$) can be calculated as follows (Civan 2007).

$$\int_{D_{pt,min}}^{D_{pt,max}} D_{pt}.F(D_{pt})dD_{pt} = D_{pt,m} \quad (17)$$

3.2.5. Instantaneous porosity and permeability

To compute the instantaneous porosity, the volume fraction of the nanoparticles entrapped per unit bulk volume of the porous media is subtracted from the original porosity to get the new porosity.

$$\phi = \phi_o - \varepsilon \quad (18)$$

For instantaneous permeability, Chang and Civan (1991) suggested a power relationship between the permeability reduction and the pore throat plugging. Herein, an exponential relationship has been modified from Civan and Nguyen (2005) as the following,

$$\frac{K}{K_o} = exp(-\alpha(1-f)^{n1}) * (\frac{\phi}{\phi_o})^{n2} \quad (19)$$

where α, n_1 and n_2 are imperical constants.

3.3. Geological Model

Geological model is constructed to represent the heterogeneity of carbonates. The geological model involves two scales of heterogeneity i.e. pore scale represented by pore size distribution and macroscopic scale represented by permeability distribution. First, for the pore scale, mercury injection of Indiana limestone cores used in section 3.5 was conducted. Popplewell et al. (1989) and Chang and Civan (1991) used the bimodal distribution functions to model the pore throat size distribution of porous media. The pore size distribution data from mercury injection (Fig. 3-1a) is fitted with bimodal distribution function to determine the empirical parameters of the distribution function (Eqs. 8, 9, and10). These parameters determine the shape of the pore throat size distribution curve.

Levenberg-Marquardt algorithm (Moré 1978) is used to fit the mercury injection data for pore throat size distribution to find the parameters ($a_1, m_1, a_2\ and\ m_2$). Fig. 3-1b presents the probability distribution function that fitted the mercury injection data. Meanwhile, the minimum and maximum pore sizes are dynamic functions of deposition and plugging. Hence, the initial minimum and maximum pore size distribution are assigned to the computational domain. The whole domain is divided into gridblocks and it is assumed that each gridblock has a pore throat size distribution with a specific minimum and maximum value. The distribution of the maximum pore throat size is assumed to follow a right-skewed distribution while the distribution of the minimum pore throat size is assumed to be left-skewed. In this way, the minimum and maximum pore throat sizes in each gridblock are determined and restricted within a proper range. This could effectively represent Indiana limestone core used in this paper in which the dominant porosity is interparticle and well connected (Ziauddin and Bize 2007). The continuous probability densities of minimum and maximum pore throat size are generated following type I Pearson distribution (Pearson 1895). The parameters used for generating Pearson system random numbers are listed in Table 1 with the generated range of minimum and maximum size for all gridblocks. According to the pore throat size data of Indiana limestone cores from mercury injection experiments, the pore throat size of the whole domain is observed to follow a bimodal distribution that skews to the right. It is assumed that the pore throat size in each gridblock follows the same distribution of the whole domain. For each gridblock, with the randomly assigned minimum and maximum pore throat size the bimodal function can be generated using Eqs. 8, 9, and 10. Figs. 3-2,

3-3, and 3-4 show the distribution of the minimum, maximum and average pore throat size for the whole domain, respectively.

Table 3-1—Parameters for generating Pearson distribution

Parameter	Minimum pore throat size, micron	Maximum pore throat size, micron
Mean	0.15	22
Standard deviation	0.03	4
Skewness	-1	1
Kurtosis	4	4
Distribution range	[0.05,0.2]	[15,40]

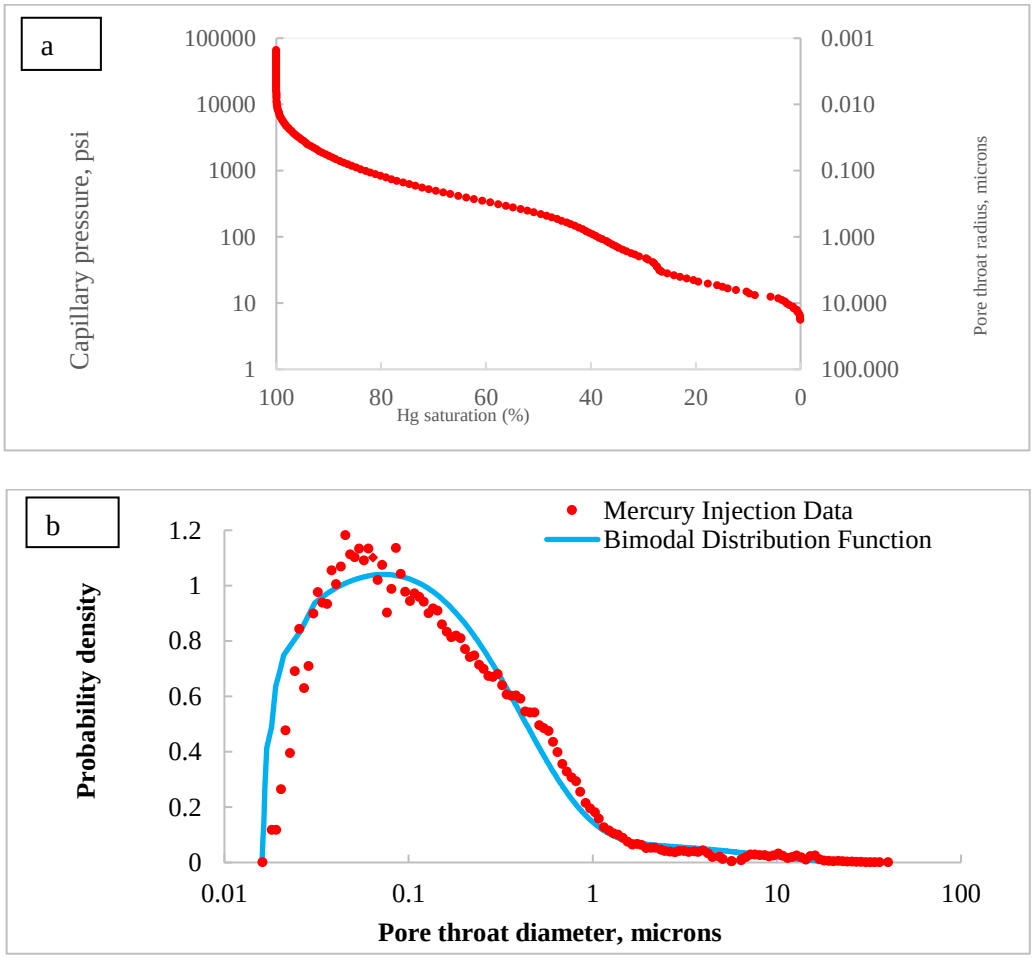

Figure 3-1—(a) high-pressure mercury injection, (b) pore throat size distribution measured by mercury injection fitted with a bimodal distribution function.

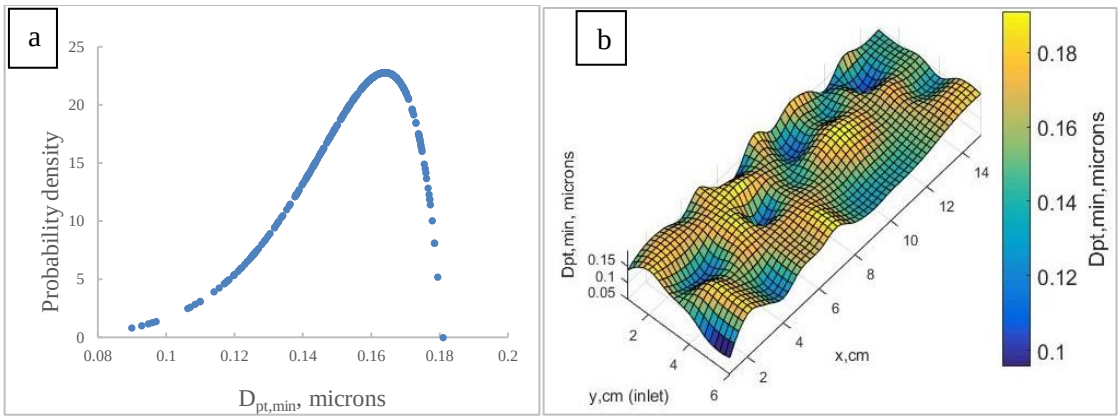

Figure 3-2—Minimum pore throat diameter ($D_{pt,min}$) distribution (a) Probability distribution function. (b) Three-dimensional map of minimum pore throat size in each gridblock.

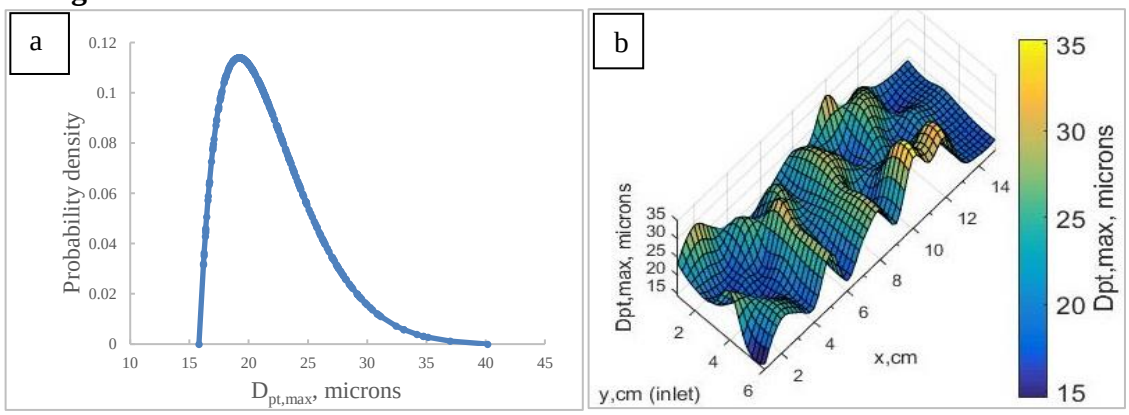

Figure 3-3—Maximum pore throat diameter ($D_{pt,max}$) distribution (a) Probability distribution function. (b) Three-dimensional map of maximum pore throat size in each gridblock.

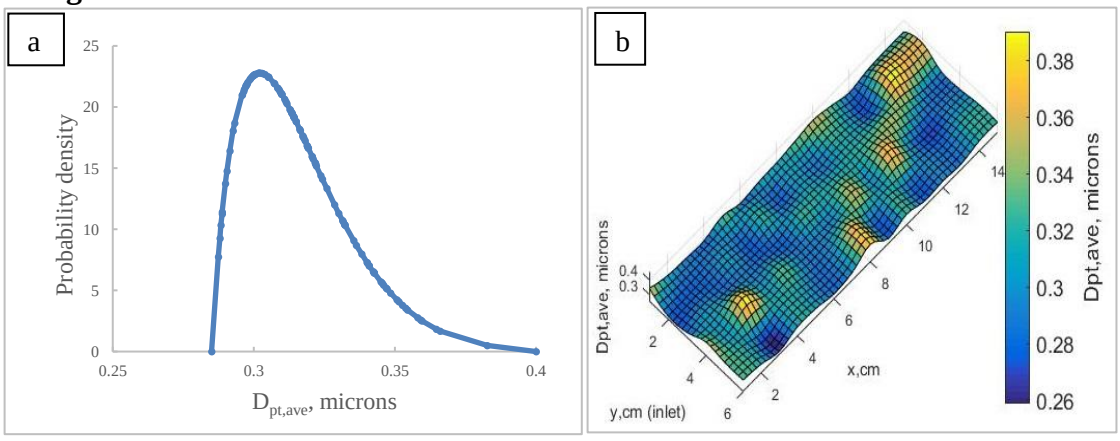

Figure 3-4—Average pore throat diameter (Dpt,ave) distribution (a) Probability distribution function. (b) Three-dimensional map of average pore throat size in each gridblock

Second, for the macroscopic scale, permeability distribution is generated as a function of the pore size distribution. The permeability is assumed to follow the same distribution as the average pore throat size. Assuming permeability will vary around the average permeability of the core measured from brine injection, the random permeability profile was generated. The standard deviation of the distribution was determined by the proper estimation of the range of distribution data points. For example, for average permeability of 10 md, the range of data points was estimated from 8 md to 18 md that matches the same shape of pore size distribution. Based on the average permeability and the range, the standard deviation is determined as 1.5. Fig. 3-5 shows the probability distribution function of permeability in the whole domain with the average permeability of the domain around 10 md. Fig. 3-6 shows the probability distribution function of permeability in one row in the domain of average permeability 9 md using a standard deviation of 1.5. Other rows are given different average permeability and the permeability is distributed around it using the same standard deviation.

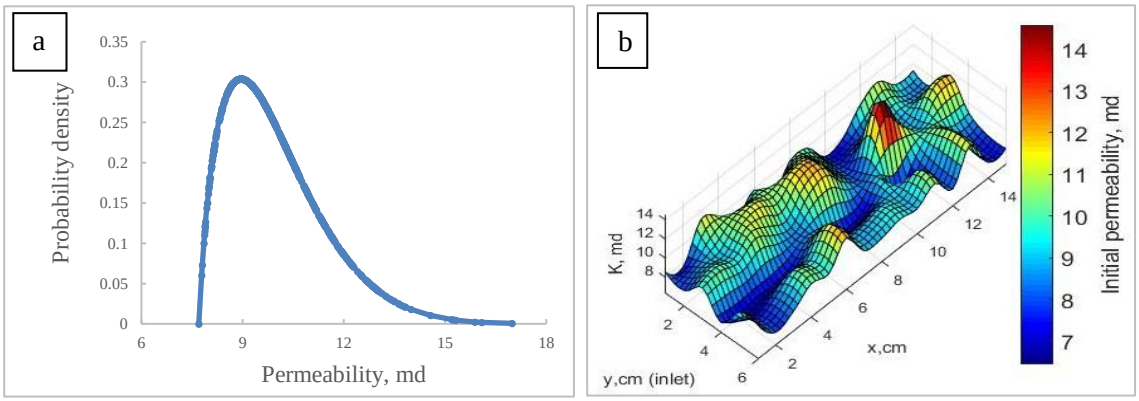

Figure 3-5—Distribution of initial permeability in the whole domain. (a) Probability distribution function (b) Three-dimensional map of permeability in each gridblock.

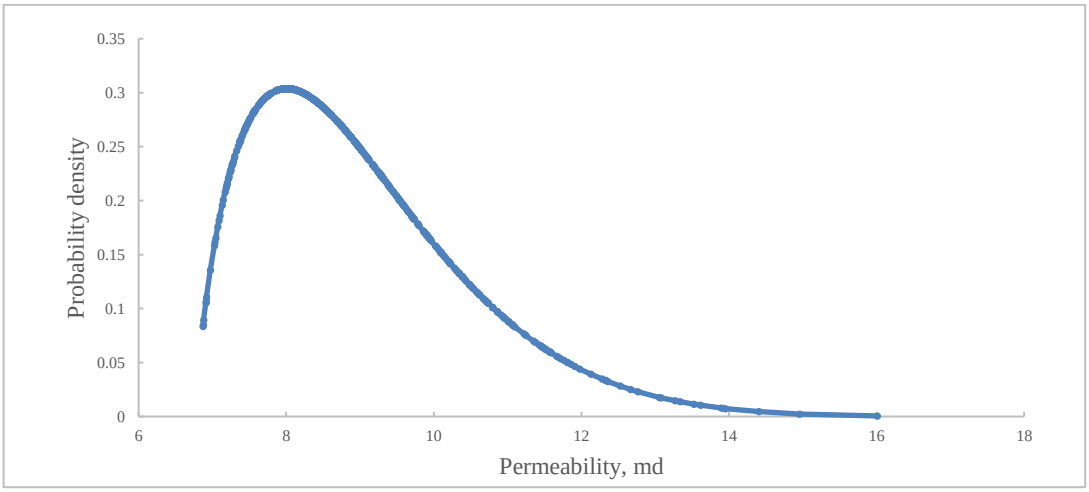

Figure 3-6—Probability distribution function of initial permeability in one row in the domain of average permeability 9 md.

Finally, to validate the geological model, a numerical tracer test is used to calculate the flowing fraction. In this case, the flowing fraction definition is how many pore volumes injected to produce 50% of the injected nonreactive tracer (Skauge et al. 2006). The flowing fraction for Indiana limestone is around 1 (Zakaria et al. 2015). The numerical model presented in section 4 is used to simulate the flow of non-reactive tracer. Fig. 3-7 shows that the computed flowing fraction for the geological model presented here is nearly equal to the flowing fraction calculated from the experimental test by Zakaria et al. (2015). This means that the geological model could effectively represent the actual rock since they have similar hydrodynamic properties.

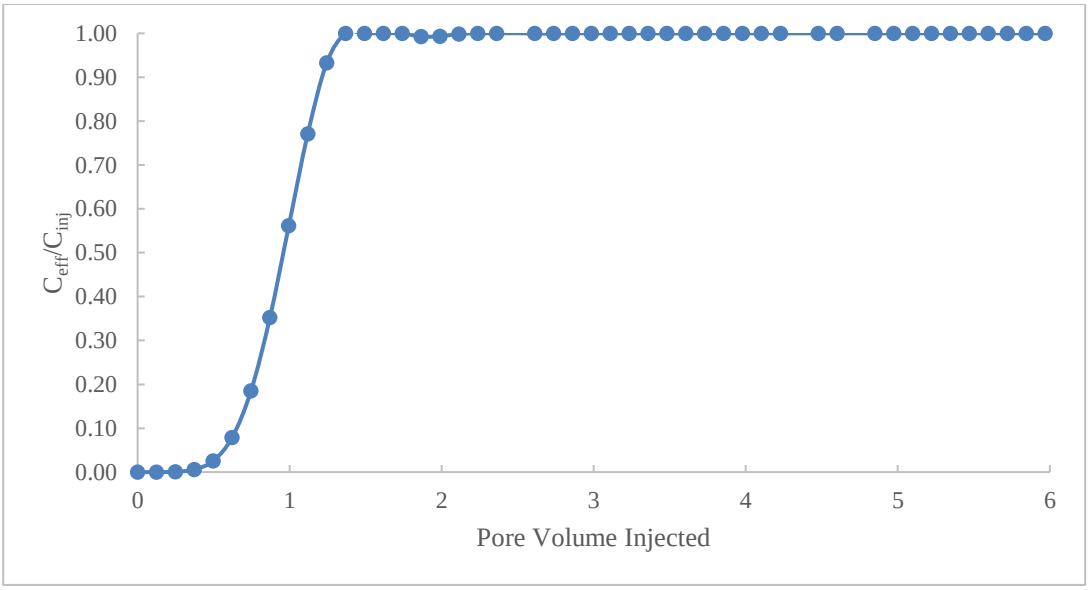

Figure 3-7—Dimensionless effluent concentration for numerical tracer test. The flowing fraction is ~1.

3.4. Numerical Model

The mathematical model presented in section 3.2 is solved using finite difference method on a two-dimensional domain using the geological model presented in section 3.3. Fig. 3-8 presented the two-dimensional computational domain and the applied boundary conditions. Alternating direction implicit method (ADI) is widely used for solving multidimensional reservoir flow problems (Aziz and Settari 1979). The alternating direction implicit method is a two-step numerical scheme. The first step is to discretize the derivatives in x-direction implicitly, while the derivatives in the y-direction are discretized explicitly. The system of equations renders a tridiagonal matrix that can be solved using Thomas algorithm to produce a provisional solution (Pletcher et al. 2012, Aziz and Settari 1979). In the second step, the derivatives in the y-direction are discretized implicitly, and the provisional solution is used for the derivatives in the x-direction. The resulting tridiagonal system is solved for the final solution at the given timestep.

Injection of nanoparticles into porous media that have different scales of heterogeneity imposes a direct interaction between the nanoparticle size and pore throats size distribution. As mentioned in section 3.2.3, the average particle size (~150 nm) can be reasonably used instead of the nanoparticles distribution. Different pore throat size and permeability values are imposed for each gridblock as explained in section 3. Pore size distribution changes with entrapment of nanoparticles in the porous media, however it's assumed that it maintains the same shape of the distribution curve. When deposition is the dominant damage mechanism and mono-particle and multi-particles plugging are negligible, Eqs. 15, 16 and 17 are solved simultaneously to compute the new minimum and maximum pore throat diameters, $D_{pt,min}$ and $D_{pt,max}$. However, if nanoparticle size is larger than the minimum pore throat diameter, the pores that are smaller than the nanoparticles will be plugged and the new minimum pore throat size ($D_{pt,min}$) is equal to the nanoparticle size. Increasing the nanoparticles concentration and/or velocity, increases the particle Reynolds number (Eq. 14). The critical pore throat size (Eq. 13) increases with increasing the particle Reynolds number. The critical pore throat size is the pore throat size required for multi-particles to form a plug at the entry of the pore throat. When the critical pore throat size is larger than the nanoparticle size, the critical pore throat size is used as the new minimum pore throat size ($D_{pt,min}$). As the maximum pore throat is much larger than nanoparticles size, the new maximum pore throat size ($D_{pt,max}$) is only updated as a function of deposition by integrating Eq. 15 and evaluating the right hand-side using Eq. 5.

The model involves transport and reaction in porous media. The interaction between nanoparticles and the porous system results in change in the pore structure such as pore

throat size distribution, permeability, and porosity. The solution algorithm can be summarized as the following:

1. Using Levenberg-Marquardt algorithm to fit the distribution function (Eqs. 8, 9, and 10) with the mercury injection data.
2. Initialize the pore throat size and permeability distribution as explained in section 3.
3. Solve the continuity equation (Eq. 1) for pressure
4. Use Darcy's law (Eq. 2) to calculate the velocity in each direction.
5. Solve the convection-diffusion equation (Eq. 3) to calculate the concentration distribution. In this step, the source term is evaluated explicitly from the previous timestep.
6. Then the source term can be calculated from Eqs. 5 and 6 using the velocity and concentration calculated from step 4 and 5, respectively. Then it is used in the next timestep for calculating the concentration in step 5.
7. Updating pore throat size distribution as explained earlier in this section, using Eqs. 13, 14,15,16, and 17.
8. Using Eqs. 11 and 12 to calculate the new flowing fraction (f)
9. Updating porosity using Eq. 18.
10. Updating permeability using Eq. 19.
11. Repeating step 2 through 10 for all the timesteps.

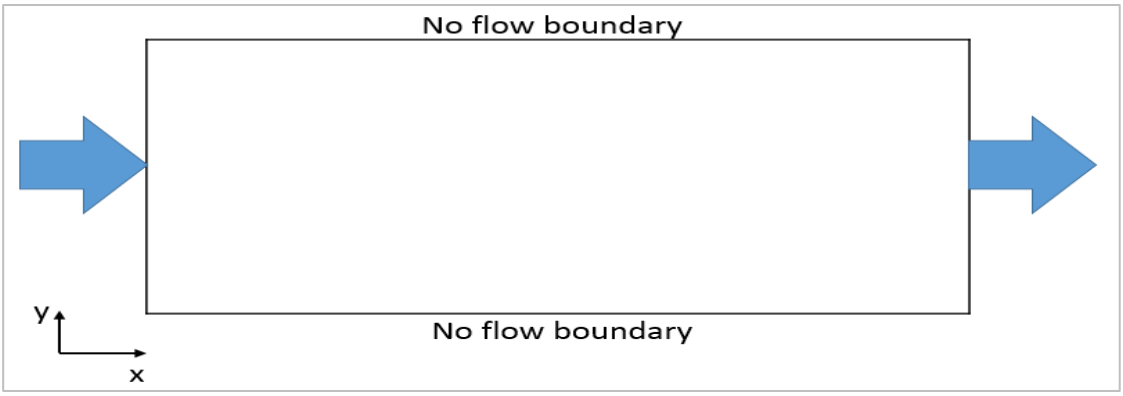

Figure 3-8—Numerical simulation domain representing a core plug of size (1.5x6"). Flow is coming from the left to the right with constant injection rate at the inlet and constant pressure at the outlet

3.5. Results and discussion

3.5.1. Model Validation

Herein, the numerical solution is validated using experimental data at different injection rates and concentrations of nanoparticles. Three coreflood data are used (Done by Sangho Bang at University of Oklahoma). The Coreflood experiments have been done using silica and alumina nanoparticles (~150 nm in diameter) injected into Indiana limestone core plugs at room temperature. The diameter and length of the cores are 3.81 cm and 15 cm, respectively. Permeability and porosity of the core plugs are around 10 md and 16%, respectively. The pore throat size distribution of the cores used in the experiments is presented in Fig. 3-1. Table 3-2 presents the values of the parameters used in the simulation that was matched with the experimental data. These values have been adopted by matching the simulation results with the Coreflood data. Sensitivity analysis was conducted to determine the significance of each parameter on the model results. Also a set of experimental results in the literature (Civan 2007) was used, to determine the trend of each parameter as a function of concentration, nanoparticle size, and injection rate.

Then the experimental data are matched with the model to determine the parameters within a specific range that were determined from the sensitivity analysis of the parameters. For other simulation conditions where we do not have experimental data, extrapolation/interpolation is performed to get the value of each parameter.

Fig. 3-9 presents the permeability reduction (k/k_0) with the pore volume of nanoparticles dispersion injected at high injection rate (3.5 cm^3/min) and low concentration (0.01 vol %) compared with the experimental data. Fig. 3-10 shows that considering the permeability distribution is effective to imitate the actual conditions of the porous media. This can be helpful in determining the pathways of the nanoparticles in the porous media and the interaction of the pore throat size distribution and the particles size. Also, it can be noticed that at higher injection rate, there is a fast exponential permeability reduction with pore volume injected. Increasing injection rate increases the particle Reynolds number. Hence, the critical pore throat size that promotes multi-particles plugging increases. This means that a higher fraction of the pore throats is prone to plugging with multiple nanoparticles that reach the pore throat simultaneously and jam together. Furthermore, the flowing fraction (Eq. 12) decreases rapidly. Eq. 19 shows that permeability decreases exponentially with flowing fraction reduction.

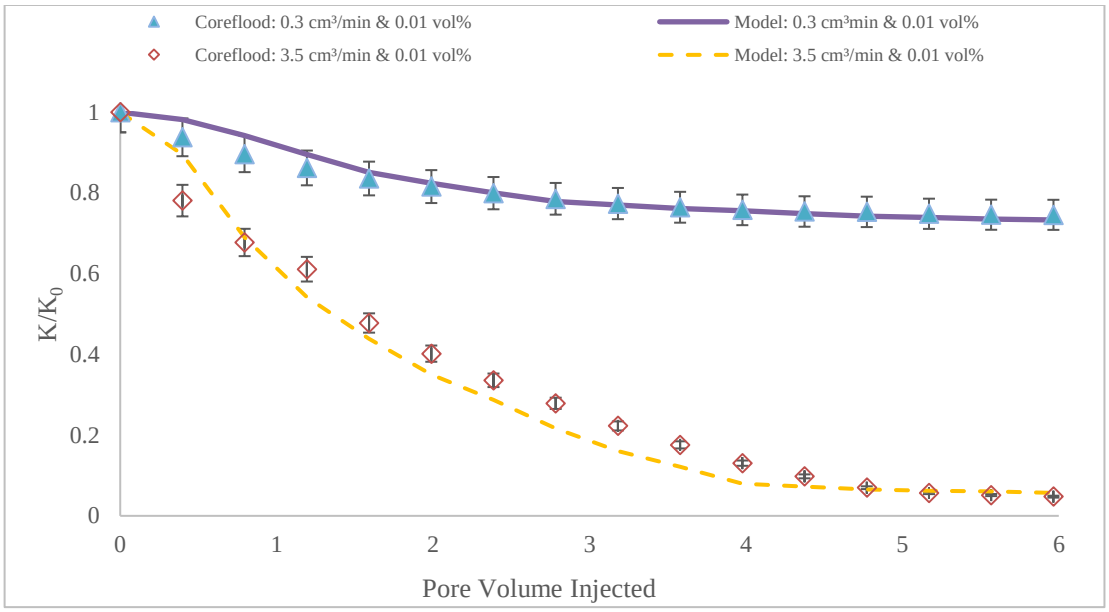

Figure 3-9—Permeability reduction with pore volume injected at 0.01 vol% concentration and different injection rates (0.3 and 3.5 cm3/min).

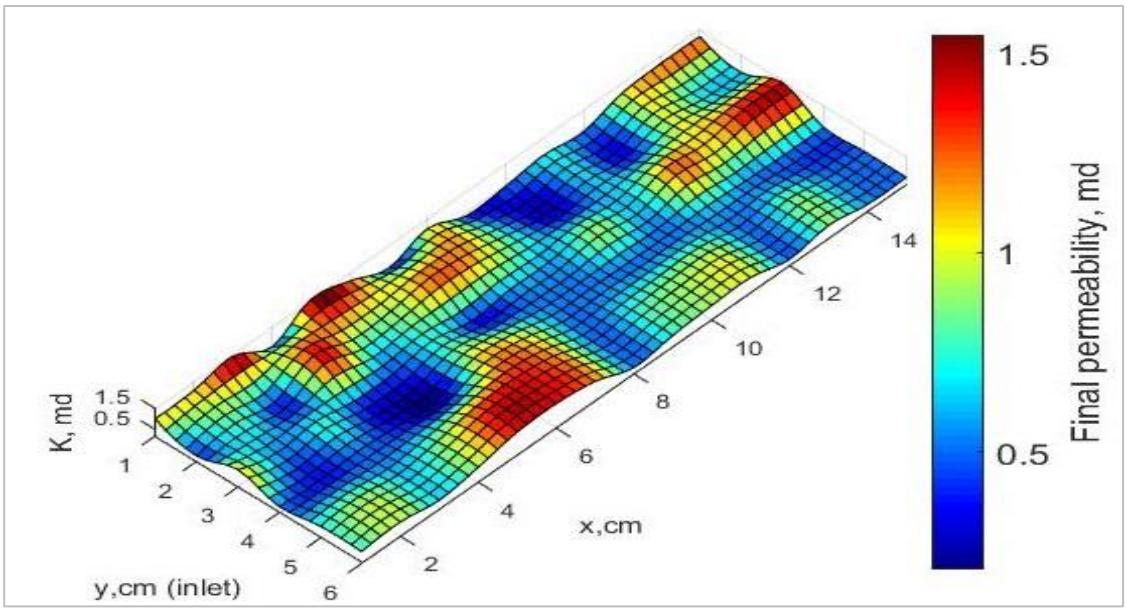

Figure 3-10— Three-dimensional map of permeability after injection of nanoparticles for 3.5 cm3/min and 0.01 vol%.

The model is also used at low injection rate (0.3 cm^3/min) and different concentrations of nanoparticles (0.01 and 0.5 vol %). The simulation results nearly match the experimental

data (Fig. 3-11). It can be seen that at low injection rate and low concentration of the nanoparticles, the permeability reduction is not significant. This means that the main damage mechanism at these conditions is the deposition of the nanoparticles on the pore surface. Also, mono-particle can play a major role since the average particle size is greater than the minimum pore throat size. The average pore throat diameter is around 340 nm (Fig. 3-1b) and the average particle size is 150 nm. This demonstrates that mono-particles plugging can occur for pore throats that are smaller than the average particle size. Hence, a considerable fraction of the pores can be plugged by the mono-particle mechanism. As the concentration of the nanoparticles increases, the degree of permeability reduction increases. Since the particle Reynolds number is directly proportional to the concentration of the nanoparticles (Eq. 14), at high concentration, the permeability decreases exponentially as compared with the previous case of high injection rate and low concentration. Multi-particles plugging conditions are promoted when a high concentration of nanoparticles reaches the pore throat entry at the same time. This could be the case when injection rate is high even if the concentration is very low. Since the water molecules are smaller than the nanoparticles size, the nanoparticles cannot accelerate as fast as the water molecules and lag behind at the entry of the pore throat (Skauge et al. 2010). Likely, higher injected concentration means that a large number of nanoparticles can reach the pore throat entry at the same time and jam together there. In order to assess the effect of each mechanism on the permeability reduction at different injection rates and nanoparticle concentrations, the contribution of each mechanism is presented in Table 3-3.

Table 3-2—Parameters used in 2D Nanofluid flow simulation. These values have been adopted from (Ju and Fan 2009). § These parameters have been calculated by matching the bimodal distribution function with the mercury injection data. ŧ These parameters have been matched by coreflood data.

Parameter	Symbol	Description	Value	Unit
Permeability reduction equation	$\alpha^{ŧ}$		2 to 7	–
	$n_1^{ŧ}$		1 to 3	–
	$n_2^{ŧ}$		3 to 5	–
Critical pore throat size calculation	$A^{ŧ}$		5	–
	$B^{ŧ}$		0.05	–
	$G^{ŧ}$		1 to 15	–
	D	Diffusion coefficient	0.0336	cm^2/min
	u_c^*	Critical velocity	0.0276	cm/min
C-D equation, for particle, retained in porous media	K_d^*	Constant of deposition rate	0.16	1/cm
	K_e^*	Constant of release rate	0.30	1/cm
	K_{pt}^*	Constant of plugging rate	0.0128	1/cm
Deposition equation	$\beta^{ŧ}$	Constant of change in pore throat size due to deposition and release	20	g/cm^3
Bimodal beta distribution function	$w^{§}$	Weight factor	0.45	–
	$a_1^{§}$	parameter	0.0015	–
	$m_1^{§}$	parameter	130	–
	$a_2^{§}$	parameter	0.01	–
	$m_2^{§}$	parameter	5	–

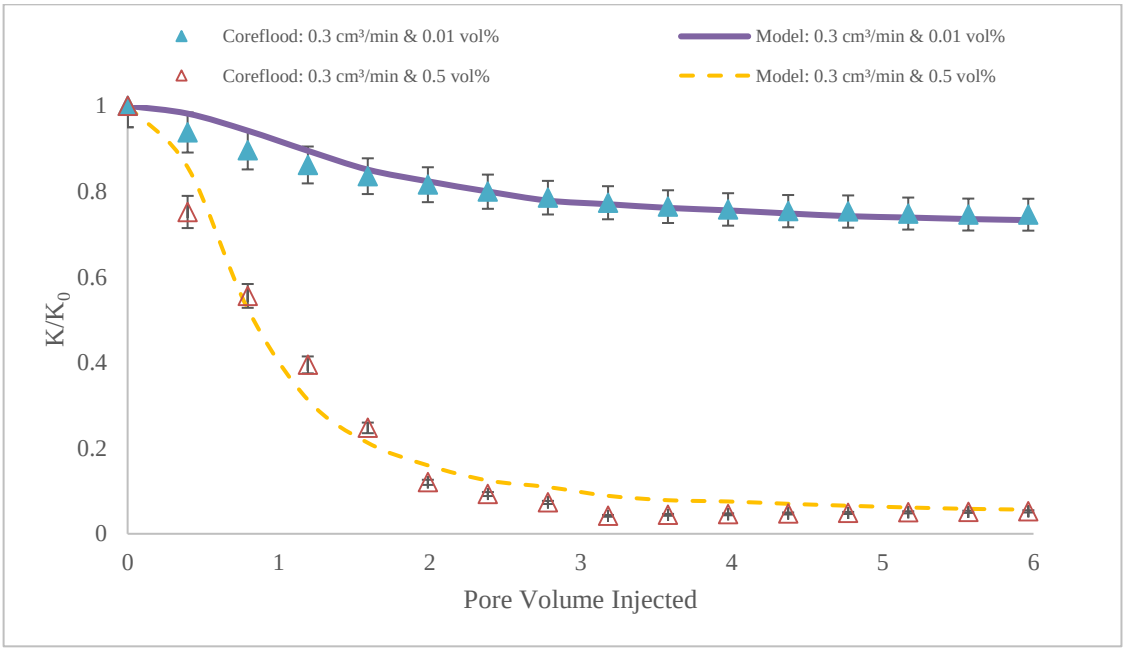

Figure 3-11— Permeability reduction with pore volume injected at low injection rate (0.3 cm3/min) and different concentrations (0.01 and 0.5 vol%).

Table 3-3—Contribution of each mechanism to permeability reduction

	Q_{inj}=0.3 cm^3/min C=0.01 vol%	Q_{inj}=3.5cm^3/min C=0.01 vol%	Q_{inj}=0.3 cm^3/min C=0.5 vol%
Final K/K_0	0.76	0.06	0.06
deposition	32.2%	0.2%	10.4%
Mono-particle	61.6%	26.1%	23.6%
Multi-Particle	6.2%	73.8%	66.0%

3.5.2. Sensitivity analysis

The model was matched with the coreflood data. The three formation damage mechanisms as explained earlier, are functions of the nanoparticles concentration, the injection rate, permeability and the interplay between particle size and the pore throat size. Surface deposition has a little effect on permeability reduction compared to mono-particle and multi-particle plugging. Surface deposition depends on the interplay between

the surface electric charges of the nanoparticles and the porous medium and the salinity of the environment. Also, the surface deposition increases proportionally with the volumetric flux of the nanoparticles (*uC*) as shown in Eq. 6. Meanwhile, increasing the volumetric flux raises the particle Reynolds number (Eq. 14). The critical pore throat size from Eq. 13 increases with increasing the particle Reynolds number. Consequently, multi-particles plugging increases with increasing the particle Reynolds number and the volumetric flux of the nanoparticles. Fig. 3-12 presents the average critical pore throat size for different injection rates and concentrations discussed in section 3.5.1. Increasing the concentration for 50 folds from 0.01 to 0.5 vol% is equivalent to increasing the injection rate for 12 folds from 0.3 cm^3/min to 3.5 cm^3/min.

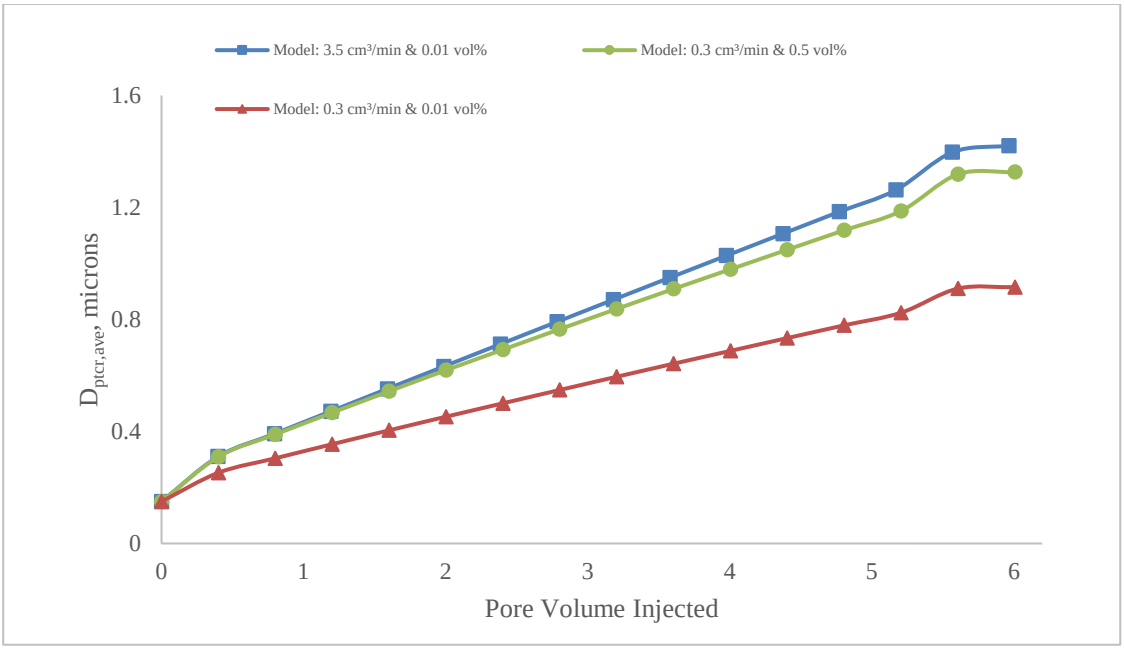

Figure 3-12—the average critical pore throat diameter for different injection rates (0.3 and 3.5 cm3/min) and different concentration (0.01 and 0.5 vol%).

3.5.2.1.injection rate

Several numerical simulations are prsented here to study the effect of injection rate on permeability reduction. A wide range of injection rates (0.3 to 3.5 cm^3/min) with a

constant concentration of nanoparticles (0.01 vol%) is simulated. Fig. 3-13a shows that with increasing the injection rate, the permeability reduction increases. The critical pore throat size increases with increasing the injection rate (Fig. 3-13b). Increasing the injection rate means that volumetric flux of nanoparticles that reaches the pore throat entry at a given moment increases and hence, the nanoparticles jam together to form a multi-particle plug. Here, we can conclude that the injection rate should be optimized to prevent the formation damage.

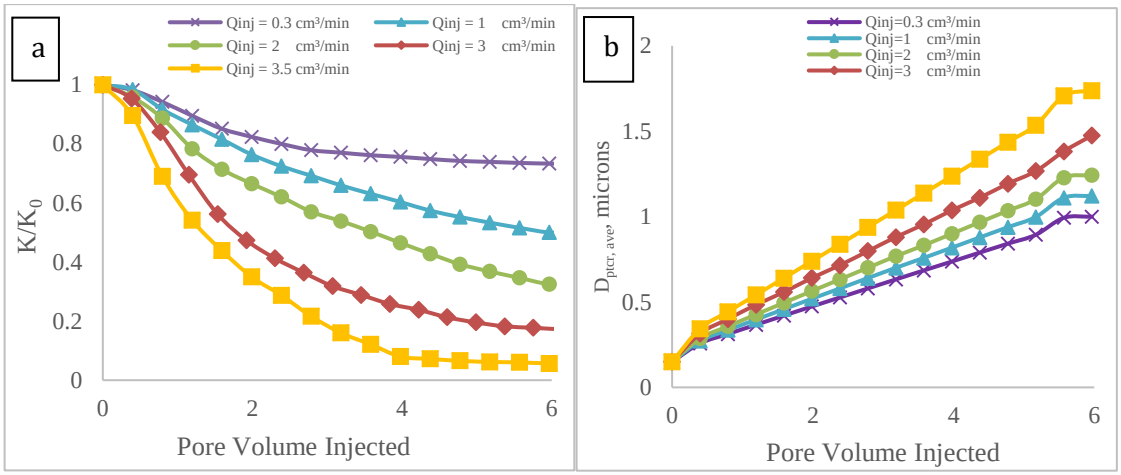

Figure 3-13—Permeability reduction (a) and average critical pore throat size (Dptcr, ave) (b) for a constant concentration of 0.01 vol % at different injection rates (0.3, 1, 2, 3, and 3.5 cm3/min).

3.5.2.2.Nanoparticles concentration

Similarly, the concentration of nanoparticles is another major parameter to be optimized for effective nanofluid treatment (Zhao et al. 2015, Hemmat Esfe et al. 2015). The volumetric flux can be also increased by increasing the concentration of nanoparticles. Numerical simulations for a wide range of nanoparticles concentrations (0.01 to 1 vol%) with a constant injection rate (0.3 cm^3/min) were conducted. Fig. 3-14a presents the permeability reduction at different concentrations of nanoparticles. Increasing the concentration of the nanoparticles causes more damage similar to increasing the injection

rate. Increasing the concentration of nanoparticles also causes the critical pore throat diameter to increase (Fig. 3-14b). However, the degree of permeability reduction with increasing the concentration is much higher than that with increasing the injection rate. Comparing Fig. 3-13a and Fig. 3-14a, we can see that for a three-fold increase in nanoparticles concentration (from 0.01 to 0.03 vol%), the degree of damage is much higher than that obtained by a three-fold increase in injection rate (from 0.3 to 1 cm^3/min). It can be concluded that increasing the concentration and/or injection rate cause severe permeability reduction. However, the concentration of nanoparticles has more severe impact on permeability reduction than the injection rate (Fig. 3-15).

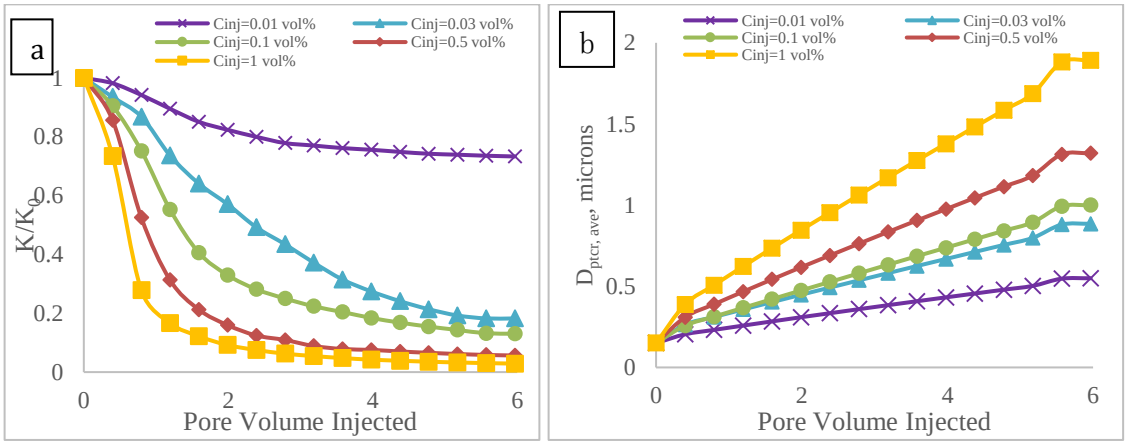

Figure 3-14—Permeability reduction (a) and average critical pore throat size ($D_{ptcr, ave}$) (b) for a constant injection rate of 0.3 cm^3/min at different concentrations of nanoparticles (0.01, 0.03, 0.1, 0.5, and 1 vol%).

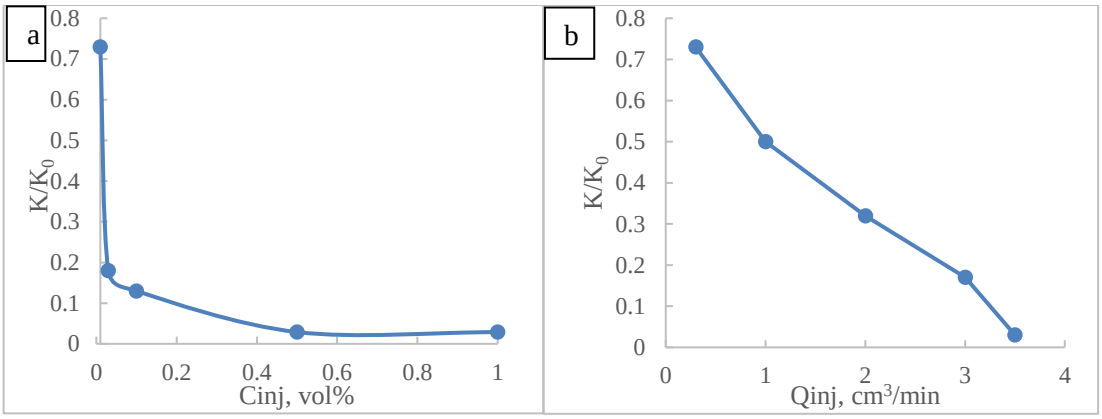

Figure 3-15— (a) effect of concentration with a constant injection rate of 0.3 cm^3/min and (b) injection rate with a constant concentration of 0.01 vol %, on permeability reduction after 6 pore volume injected.

3.5.2.3.Nanoparticle size

Nanoparticle size is also a major player that affects the functionality of nanoparticles in porous media (Ariana et al. 2015). Several numerical simulations are presented here to study the effect of nanoparticles size on the degree of permeability impairment at different injection rates and concentration of nanoparticles. Fig. 3-16a shows that at low injection rate (0.3 cm^3/min) and low concentration (0.01 vol%), permeability impairment is not severe as discussed earlier. However, with decreasing nanoparticles diameter the permeability impairment becomes negligible due to the reduction of critical pore throat diameter (Fig. 3-16b). Eqs. 13 and 14 demonstrate that the critical pore throat diameter directly depends on the nanoparticle diameter. Fig. 3-17a shows the similar behavior at high concentration (0.5 vol%) and low injection rate (0.3 cm^3/min). Fig. 3-17b shows that the critical pore throat diameter can be reduced significantly by reducing the nanoparticles diameter even if the concentration is high. Fig. 3-18a shows the effect of nanoparticles diameter at high injection rate (3.5 cm^3/min) and low concentration (0.01 vol%). As discussed earlier, the higher the injection rate, the more prone the nanoparticles

to be entrapped by multi-particles plugging mechanisms. However, Fig. 3-18b shows that the critical pore throat diameter could be decreased much further by reducing nanoparticle diameter. We can conclude that for injecting nanoparticles into petroleum reservoirs with negligible effect on permeability, the nanoparticles size should be as small as possible. However, the diameter of nanoparticles depends on the stability of nanoparticle dispersion at the reservoir conditions as discussed in section 3.1.

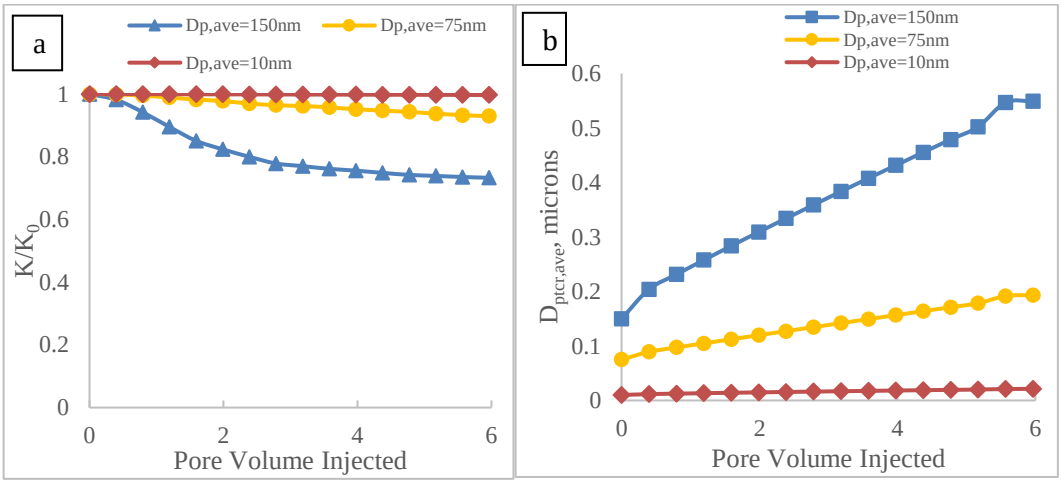

Figure 3-16—effect of nanoparticles size (10, 75, and 150 nm) with a constant concentration of 0.01 vol %, and injection rate of 0.3 cm3/min on permeability reduction after 6 pore volume injected.

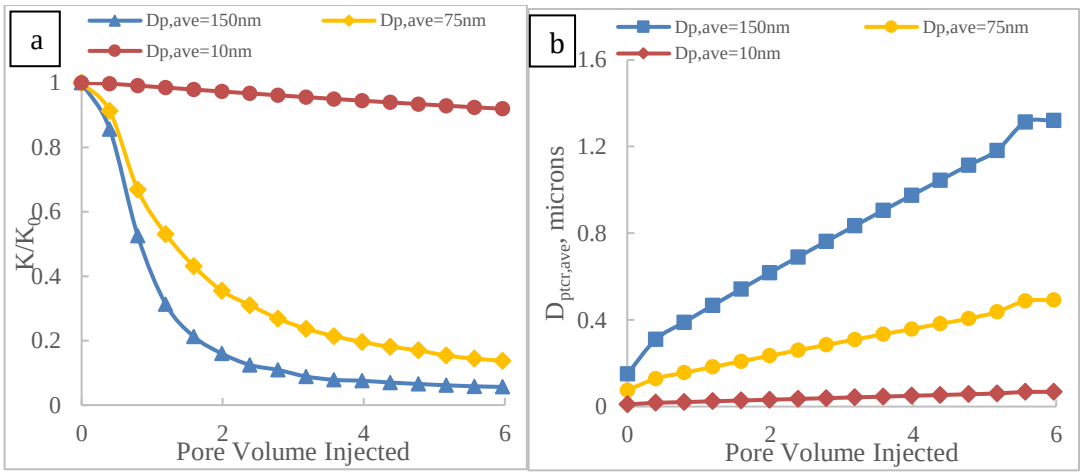

Figure 3-17—effect of nanoparticles size (10, 75, and 150 nm) with a constant concentration of 0.5 vol %, and injection rate of 0.3 cm3/min on permeability reduction after 6 pore volume injected.

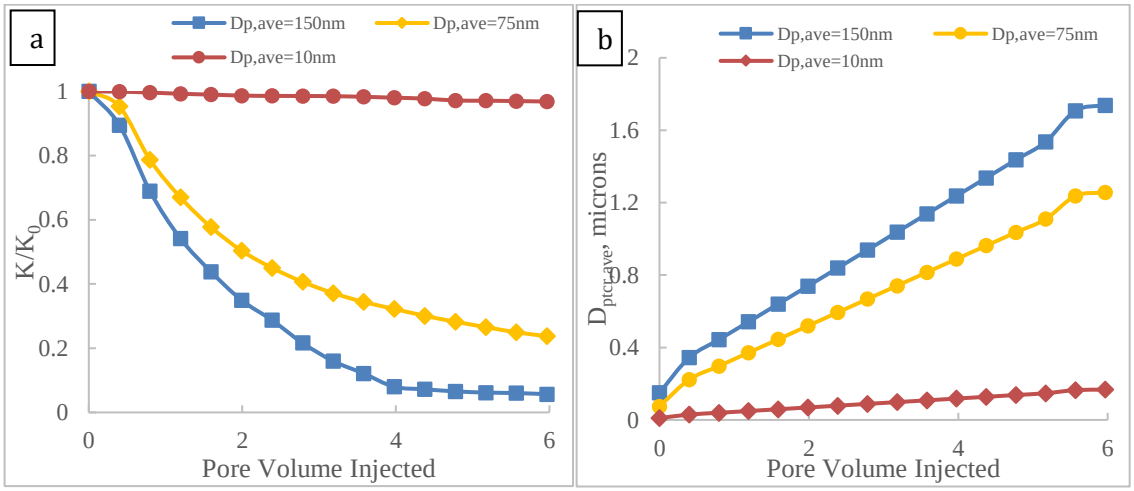

Figure 3-18—effect of nanoparticles size (10, 75, and 150 nm) with a constant concentration of 0.01 vol %, and injection rate of 3.5 cm3/min on permeability reduction after 6 pore volume injected.

3.5.2.4.Permeability

Finally, the effect of permeability on nanoparticles transport is studied here. Three different permeability are used here (10, 50, and 100 md). The permeability is assumed to be a function of pore throat size. The capillary pressure can be expressed using Laplace equation (Swanson 1981),

$$P_c = \frac{2\sigma\cos(\theta)}{r} \quad (20)$$

where r is pore throat radius. Swanson (1981) provided a correlation for permeability from capillary pressure:

$$K = a(\frac{S_b}{P_c})^c \quad (21)$$

Where S_b is mercury saturation, and c = 2 for carbonates and a is a constant. Therefore, combining Eqs. 20 and 21 indicates the dependence of permeability on the square of pore throat size. Table 3 shows the minimum, maximum and average pore throat sizes calculated for different permeability based on the mercury injection data for 10 md. These values have been used in the model to study the effect of permeability and pore throat size on the permeability reduction by nanoparticles. Fig. 3-19a shows that at higher injection rate (3.5 cm^3/min) and high concentration of nanoparticles (0.1 vol %), the permeability reduction is steep and close for the three-different permeability used. This could be explained as discussed earlier, that at high injection rate and concentration of nanoparticles, the multi-particle plugging mechanism is the major player and causes steep permeability reduction. When decreasing the concentration of nanoparticles to (0.01 vol %), and keep the same injection rate (3.5 cm^3/min), Fig. 3-19b shows that the higher the permeability the lower the permeability reduction. As discussed earlier in section 3.5.2.2 that the concentration has greater impact on permeability reduction than the injection rate (Fig. 3-15). Decreasing the concentration of nanoparticles decreases the effect of multi-particles damage mechanism. This is also promoted by increasing the pore throat diameter with increasing the permeability (Table 3-4).

Table 3-4—Pore throat diameter in microns used for various permeability cases.

K, md	Minimum Pore Throat Diameter, microns	Average Pore Throat Diameter, microns	Maximum Pore Throat Diameter, microns
10	0.01	0.316	40
50	0.022	0.75	90
100	0.033	1	130

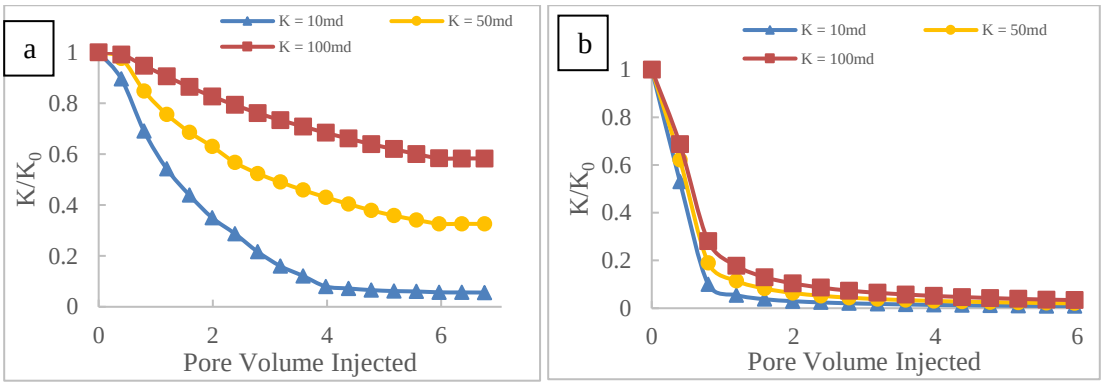

Figure 3-19—Permeability reduction with a constant injection rate of 3.5 cm^3/min for various permeability (10, 50, and 100 md) at low concentration of 0.01 vol% (a) and high concentration of 0.1 vol% (b).

3.5.3. Dimensional Analysis

This section presents the Dimensional analysis (Al-Ibadi et al. 2015, Al-Ibadi and Civan 2013, Churchill 1997) for the whole set of parameters that controls nanoparticles transport through porous media. Then, a correlation is fitted between the Damage Ratio $(DR) = (K_o - K)/K_o$ and the key Dimensionless numbers. Table 3-5 presents the main parameters that controls the degree of damage and the dimensionless groups that combine these parameters.

Then combining these dimensionless groups, we can get the main dimensionless numbers that control the damage.

$$\pi' = \frac{\pi_9}{\pi_8}\frac{1}{\pi_2} = \frac{u\,t}{\mathrm{D_{p,ave}}}\frac{\mathrm{D_{p,ave}^2}}{D\,t}\frac{1}{\phi} = \frac{u\,\mathrm{D_{p,ave}}}{D\,\phi} = Pe \tag{22}$$

$$\pi'' = \frac{\pi_7}{\pi_6}\frac{\pi_9}{\pi_2} = \frac{\rho D_{p,ave}^2}{\mu t}\frac{u\,t}{D_{p,ave}}\frac{C}{\phi} = \frac{\rho\,C\,u\,D_{p,ave}}{\mu\,\phi} = Re_p \tag{23}$$

$$\pi''' = \frac{\pi_9'}{\pi_2} = \frac{u\,t}{L\,\phi} = PVI \tag{24}$$

$$\pi'''' = \pi_3 = \frac{D_{pt,m}}{D_{p,ave}} = \varpi \tag{25}$$

Table 3-5—Dimensional analysis to determine the dimensionless groups controlling the damage ratio.

Parameters	Dimensions	Scaling variables	Dimensionless Groups	π
K	$\mathrm{L^2}$		$(K_o - K)/K_o$	π_1
ϕ	$\mathrm{L^3/L^3}$		ϕ	π_2
$\mathbf{D_{pt,ave}}$	L		$\mathrm{D_{pt,m}/D_{p,ave}}$	π_3
A	$\mathrm{L^2}$		$\mathrm{A/D_{p,ave}^2}$	π_4
L	L		$\mathrm{L/D_{p,ave}}$	π_5
μ	ML/T		$\mathrm{\mu t/\rho D_{p,ave}^2}$	π_6
ρ	$\mathrm{M/L^3}$	Scaling variable	—	—
$\mathbf{D_{p,ave}}$	L	Scaling variable	—	—
C	$\mathrm{L^3/L^3}$		C	π_7
D	$\mathrm{L^2/T}$		$\mathrm{D\,t/D_{p,ave}^2}$	π_8
u	L/T		$\mathrm{u\,t/D_{p,ave}}$	π_9
			$u\,t/L$	π_9'
t	T	Scaling variable	—	—

Fig. 3-20 shows the relationship between particle Reynolds number and the Damage ratio at different pore volume injected of nanofluid. It can be noticed that the Damage Ratio increases with particle Reynolds number. This indicates that to minimize the degree of damage, the particle Reynolds number can be minimized either by decreasing either the concentration or injection rate or both.

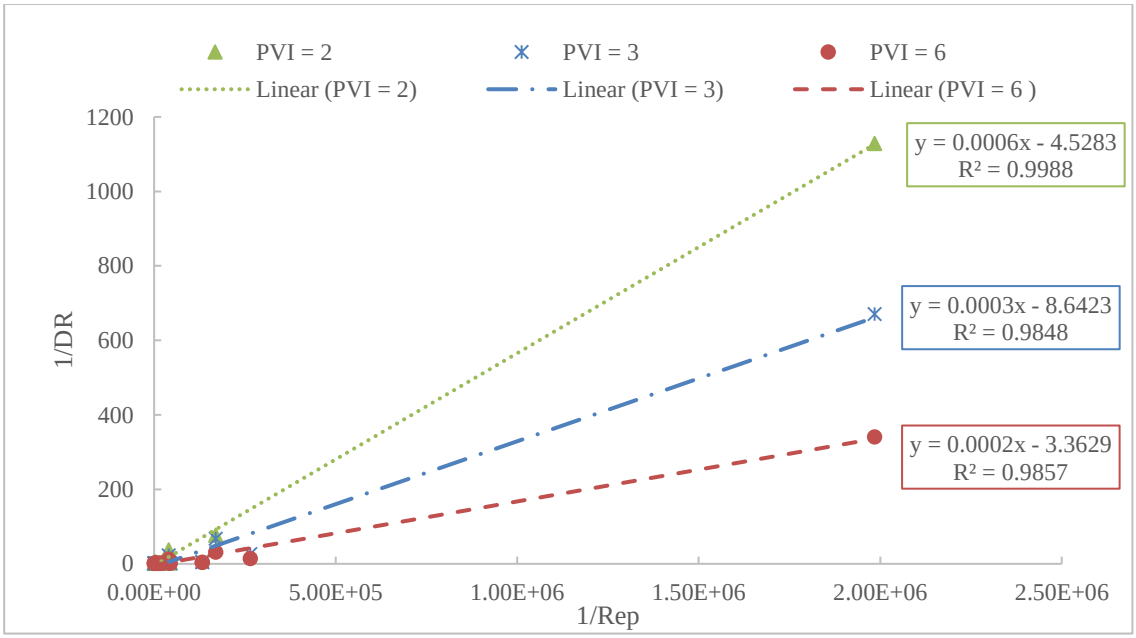

Figure 3-20—The relationship between Damage ratio and particle Reynolds number at different pore volume injected (PVI)

Buckingham $\boldsymbol{\pi}$ theorem (Churchill 1997) suggests that the damage ratio is a function of the combination of the main dimensionless numbers as the following.

$$DR = f(Pe, Re_p, \varpi, PVI) \tag{26}$$

$$DR = \xi \, Pe^{x_1} \, {Re_p}^{x_2} \, \varpi^{x_3} \, PVI^{x_4} \tag{27}$$

Where $x_1, x_2, x_3, and\ x_4$ are the exponents that could be matched with the experimental and numerical data presented in the previous sections. Then we can apply the logarithm to both sides of Eq. 27 to get the linear form of the equation.

$$DR = \log(\xi) + x_1 \log(Pe) + x_2 \log(Re_p) + x_3 \log(\varpi) + x_4 \log(PVI) \quad (28)$$

The exponents can be found using the experimental and simulated results presented in the previous sections.

$$DR = 56.5713\ Pe^{0.0267}\ {Re_p}^{0.493}\ \varpi^{0.9818}\ PVI^{0.781} \quad (29)$$

However, it can be seen that Pe does not have a significant effect on the correlation. Thereafter, we omitted the Pe, and used regression for the remaining dimensionless numbers.

$$DR = 64.219\ {Re_p}^{0.505}\ \varpi^{0.994}\ PVI^{0.783} \quad (30)$$

Fig. 3-21 presents the comparison between the Damage ratio of three numerical simulations that were presented in the previous section and the predicted Damage ratio from Eq. 30. Table 3-6 shows the values of Re_p, ϖ , and Pe for the presented data. The Dimensional analysis correlation shows quite match with the actual data.

Table 3-6— values of Re_p, ϖ , and Pe for the presented data in Fig. 3-21.

	Re_p	ϖ	Pe
DR_1	$2.519x10^{-5}$	0.4285	1.29
DR_2	$7.557x10^{-6}$	0.4285	0.386
DR_3	$3.778x10^{-6}$	0.2143	0.193

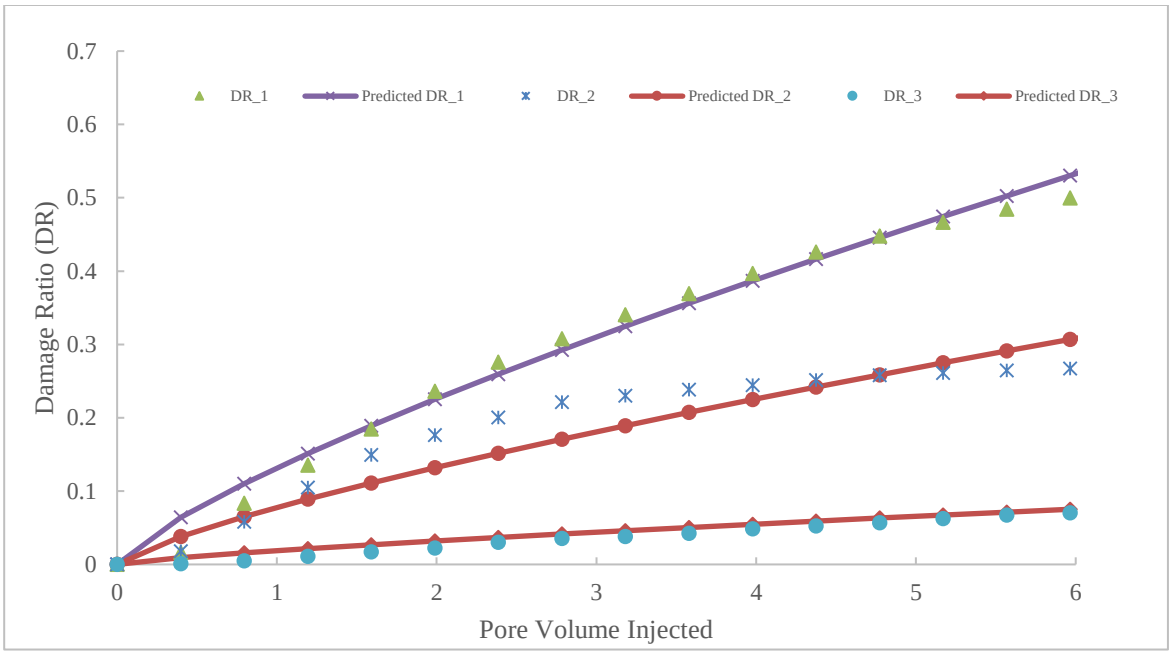

Figure 3-21—Comparison between the damage ratio (DR) from the numerical model and the Damage ratio predicted from the dimensional analysis correlation.

3.6. Conclusions

Nanotechnology has a broad application in oil and gas reservoirs. However, the interaction between nanoparticles and the porous media can cause formation damage. There are three mechanisms that can cause formation damage. The simulation tool presented here aids in the qualitative and quantitative understanding of the interaction between the nanoparticles and the porous media. The three damage mechanisms can contribute to the permeability reduction, but each one of them is dominant under certain conditions. Injection rate, nanoparticles concentration, nanoparticles size, and permeability are the critical parameters that control nanoparticles transport efficiency in porous media. Surface deposition causes a gradual permeability reduction. Mono-particle plugging is prompted due to poor stability of the suspension that causes the nanoparticles to aggregate and become much larger. Increasing the concentration of the nanoparticles,

makes the multi-particles damage mechanism to be dominant. Meanwhile, at the high injection rate and low concentration the permeability decreases exponentially because of higher particle Reynolds number. Therefore, the nanoparticles become more prone to jam at the pore throat entry. Meanwhile, reducing the nanoparticles size decreases the degree of formation damage significantly even if the injection rate and/or nanoparticles concentration are high.

The proposed model can be used for optimization of nanoparticles application in petroleum reservoirs. However, the optimization process depends on the intended applications to balance between the positive and negative effects of nanoparticles. For example, if the nanoparticles are used for wettability alteration to increase recovery of oil (Ju and Fan 2009), the increase of relative permeability should overweight the damage caused by nanoparticles entrapment. Hence, the critical parameters can be optimized to gain the maximum benefits of nanoparticles.

Acknowledgment

This work was supported by the Abu Dhabi National Oil Company (ADNOC) [grant number 880005]. The first author would like to thank Sangho Bang for sharing the experimental data used in this work, and Kang Kang for helping in the preparing this manuscript. The authors also would like to thank the anonymous reviewers for their thoughtful comments and review of this manuscript.

Nomenclatures

A, B, and G	constants for critical pore throat size relationship
a nd c	constants for permeability-capillary pressure relationship
C	concentration of the nanoparticles in the domain as a function of space and time, fraction
C_{inj}	injected concentration of the nanoparticles, fraction

C_{eff}	effluent concentration of the tracer, fraction
D	diffusion coefficient of nanoparticles in water, m^2/s
$D_{p.avg}$	average diameter of nanoparticles, m
D_{pt}	pore throat diameter, m
$D_{pt,cr}$	critical pore throat diameter, m
$D_{pt,min}$	minimum pore throat diameter, m
$D_{pt,max}$	maximum pore throat diameter, m
$D_{pt,m}$	mean pore throat diameter, m
DR	Damage ratio
f	flowing fraction
$F(D_{pt})$	bimodal probability distribution function
$F_1(D_{pt})$	fine portion of the bimodal probability distribution function
$F_2(D_{pt})$	coarse portion of the bimodal probability distribution function
k_d	deposition rate coefficient, m^{-1}
k_e	release rate coefficient, m^{-1}
k_{pt}	plugging rate coefficient, m^{-1}
K	instantaneous permeability, m^2
K_B	Boltzmann constant
K_0	initial permeability, m^2
$n_1 and\, n_2$	constant for permeability-porosity relationship
P_e	Peclet number
P_c	capillary pressure, Pa.s
Q_{inj}	injection rate of the fluid, m^3/s
r	pore throat radius, m
R	source/sink term for nanoparticles
S_b	mercury saturation injected into the core
T	Temperature, K
u	superficial velocity, m/s
u_c	critical superficial velocity, m/s
w	weight of the fine portion of the bimodal probability distribution function
∇p	pressure drop across the domain, Pa.s

Greek letters

ϕ	instanateous porosity
ϕ_o	initial porosity
μ	viscosity of the fluid
ε	volume fraction of nanoparticles retained per unit bulk volume
ε_d	volume fraction of nanoparticles retained due to deposition per unit bulk volume
ε_{pt}	volume fraction of nanoparticles retained due to plugging per unit bulk volume
$\dot{\varepsilon}_d$	rate of nanoparticle deposition per unit bulk volume
$\dot{\varepsilon}_e$	rate of nanoparticle release per unit bulk volume
τ	tortuosity of the porous medium
ρ_p	density of the nanoparticles, g/cm^3
α	constant for permeability-porosity relationship
β	constant for pore throat size and net rate of deposition.
θ	contact angle between fluid and rock

σ Interfacial tension between the wetting and non-wetting phases, N/m
ϖ Ratio of the average nanoparticle diameter to the mean pore throat diameter

Chapter 4 Modeling of Aggregation and Gelation of Nanoparticles Using Quadrature Method of Moments

Abstract

Applications of Nanotechnology are growing significantly in the petroleum industry such as oil recovery, and well stimulation. In aqueous media, silica nanoparticles aggregate if there is sufficient attractive energy between nanoparticles. Aggregate size distribution evolves as aggregation continues, and once it spans the space, it forms a gel. The objective of this study is to study the aggregation and gelation kinetics in the batch.

Population Balance equation (PBE) is used to model the kinetics of aggregation. Quadrature method of moments (QMOM) is used to convert the PBE with continuous distribution of nanoparticle size into a set of moment equations for efficient computation. The closure problem for moment transport equation is resolved using Gaussian Quadrature that requires estimation of roots orthogonal polynomials. Wheeler algorithm is then used for calculation of the coefficients of the recursive formula of the orthogonal polynomials.

This study shows that the PBE and the QMOM along with the effective medium theory can be used to model the aggregation and gelation of nanoparticles at different conditions of salinity and concentration. The modeled developed in this study is used to compare between the kinetics of aggregation and gelation of fumed silica and colloidal silica nanoparticles at the same conditions. The case studies presented show the unique behavior of fumed silica over colloidal silica nanoparticles for forming a gel network at significantly low concentration. This is basically due to the fractal structure of the fumed silica nanoparticles that has higher effective volume than the spherical particles of

colloidal silica of the same size. The model also shows that there is a critical concentration of salt and nanoparticles above which the viscosity increase and the gel network can be formed.

The model developed in this study can be coupled with a transport model to simulate nanoparticles transport aggregation and in situ gelation in porous media.

Keywords:

Fumed Silica Nanoparticles; colloidal silica nanoparticles; Population balance equation; Quadrature method of moments; Aggregation; Gelation

4.1. Introduction

Solid suspensions have a wide practical interest in many aspects of daily life such as foods, pharmaceuticals, household products, and the environment. Applications of solid suspensions in petroleum industry is quite important and widespread such as drilling fluids, enhanced oil recovery, water shutoff, etc (Liu et al. 1996, Huang et al. 2017, Metin et al. 2014, Jurinak and Summers 1991). Generally, there are two classes of silica nanoparticles; colloidal silica, and fumed silica nanoparticles (Iler 1979, Gun'ko et al. 2001). Colloidal silica nanoparticles are spherical particles formed by precipitation method. Fumed silica nanoparticles are composed of primary particles fused by pyrogenic process together to form hard aggregates of fractal structure. Fumed silica can display rheological properties similar to colloidal silica when scaled with the free volume in the suspension (Smith and Zukoski 2006). This means that fumed silica can give similar behavior with lower volume fraction in the suspension due to fractal structure that have lower packing factor compared to colloidal silica.

4.1.1. Principles of Aggregation

Aggregation of silica nanoparticles can be explained within the framework of DLVO (Elimelech et al. 2013, Russel et al. 1989). The most important forces that control the kinetics of aggregation and the properties of dispersion are dispersion and electrostatic forces. For silica dispersion in polar solvents, solvation forces due to the hydrogen bonding of the solvent to the surface silanol groups play a key role (Raghavan et al. 2000, Smith and Zukoski 2006). Theoretically, the kinetics of aggregation depends on the magnitude of energy barrier between nanoparticles. Nanoparticle that overcome the energy barrier will aggregate with another particle in the deep primary energy minimum. Smith and Zukoski (2006) studied the aggregation and gelation of fumed silica nanoparticles dispersed in ethanol. Ethanol is a very polar solvent due to the presence of hydroxyl group. They showed that at low concentration, gelation is arising from aggregation into a primary minimum due to hydrogen bonding and dispersion forces. The gelation is extremely slow due to an energetic barrier (~ 25kT) in the inter-particle potential associated with solvation forces. The solvation forces also contribute to the formation of a secondary minimum in the interparticle potential. The depth of this minimum (~ 3kT) is sufficient that, at a critical particle concentration, long-range diffusion is arrested due to the short-range attractions and the cooperative nature of particle interactions, as described by mode coupling theory.

Aggregation causes the particle size distribution (PSD) to change with time. Many evidences show that particle aggregates from natural waters and engineered systems have fractal structures. Lee et al. (2000) developed an innovative approach that models change

in PSD by incorporating recently proposed fractal mathematics and introduced a new conceptual framework called the coalesced fractal sphere (CFS) assumption. The rheological behavior of fumed silica suspensions depends on the structure of the aggregates formed in the suspension (Kawaguchi 2017). The mechanism of aggregation of fumed silica nanoparticles depends on the polarity of the solvent (Kawaguchi 2017, Kawaguchi et al. 1996a, Kawaguchi et al. 1996b). Primary hydrophilic fumed silica particles usually form chain-type aggregates of sub-micron size in air, with a density of ~3 surface silanol groups per nm^2, due to hydrogen bonding between the silanol groups on the particle surfaces. For fumed silica dispersed in nonpolar solvent, fumed silica nanoparticles attach through hydrogen bonding between the silanol groups on the surface of fumed silica nanoparticles. On the other hand, fumed silica nanoparticles dispersed in polar solvents like water that hydrogen bonding ability could retain a stable dispersion with limited or no aggregation due to preferential hydrogen bonding of surface silanol groups with the corresponding dispersing liquids (Kawaguchi et al. 1996b). Water for example, can form a structured layers of water molecules on the surface of fumed silica nanoparticles through hydrogen bonding. These structured layers of water molecules produce a steric repulsion between the fumed silica nanoparticles and prevent their aggregation.

Environmental conditions can promote silica inter-nanoparticle interaction to form larger fractal structures (Lee et al. 2000). There are many different parameters that control the aggregation and gelation of fumed silica nanoparticles in aqueous solvents such as concentration of nanoparticles, temperature, pH, and ionic strength (Amiri et al. 2011, 2009, Smith and Zukoski 2006, Russel et al. 1989). Aqueous suspensions of fumed silica

of concentration lower than a critical concentration are stable. However, above the critical particles concentration, aqueous suspensions of the fumed silica particles form gel-like structures, and the higher concentration the stronger the gel structure. This critical concentration marks the transition from Newtonian to shear thinning flow (Amiri et al. 2009).

Alternatively, salt can be added, which at high enough concentration, collapses the diffuse electrostatic double layer so that particles can approach closely enough to be drawn into near contact by van der Waals forces. The time required for particles to diffuse into their attractive minima scales to the exponential of height of energy barrier (Russel et al. 1989). Because of this exponential dependence, even small 100-nm-diameter particles in a low-viscosity solvent take months or even years to aggregate if the potential barrier is high. Aggregation could dramatically become faster at the electrolyte concentration at which the potential barrier is eliminated (critical coagulation concentration). Critical coagulation concentration (ccc) is the electrolyte concentration at which the transition from a slow to rapid aggregation regime occurs for a given suspension i.e. the electrostatic repulsion vanishes (Hiemenz 1986). Amiri et al. (2009) shows that in the absence of salt in dispersing water, fumed silica demonstrates negligible changes in viscosity at different pH of the solution. Increasing the salt concentration at any pH had increasing effect on viscosities of the fumed silica dispersions.

Oxides such as SiO_2, contain hydroxyl groups at their surfaces that can be hydrolyzed in aqueous media to form negative charges (Israelachvili 2011, Iler 1979, Adamson and

Gast 1967). Addition of an acid or base tends to neutralize these groups, and enhancing the interaction between particles.

$$\text{Acidic: } \mathrm{SiOH} + \mathrm{H_3O^+} \rightarrow \mathrm{SiOH_2^+} + \mathrm{H_2O} \quad \text{(a)}$$

$$\text{Basic: } \mathrm{SiOH} + \mathrm{OH^-} \rightarrow \mathrm{SiO^-} + \mathrm{H_2O} \quad \text{(b)}$$

Primary hydrophilic fumed silica particles usually form chain-type aggregates of sub-micron size in air, with a density of ~3 surface silanol groups per nm^2, due to hydrogen bonding between the silanol groups on the particle surfaces. Hydrophilic fumed silica powders are well dispersed at $\phi < 0.01$ in polar dispersing fluids or polar polymer melts, and their phase states change from sol to gel with increasing ϕ (Kawaguchi 2017). However, when fumed silica powders are dispersed in polar dispersing liquids, agglomerate formation is often suppressed, owing to preferential hydrogen bonding of surface silanol groups with the corresponding dispersing liquids. Below pH 2, the zeta potential of fumed silica is slightly positive and the values approach the isoelectric points, which are located in the range of pH 3–3.5. Amiri et al. (2009) found that at acidic pH of 2 and up to 4.5, increasing salt concentration did not change the viscosities effectively from that of water. This abnormal stability of fumed silica dispersion at acidic pH is related to the structural repulsion of the hydrated layers of water molecules (Yotsumoto and Yoon 1993). At acidic conditions, reaction (a) is dominant due to surplus of protons in the solution. This indicates higher ability of water to structure at the surface of fumed silica by hydrogen bonding with surface silanol groups. This structured layer of water molecules induces electrostatic repulsion that prevents bridging of nanoparticles. At basic pH, the zeta potentials of the suspensions in these ranges varied between 23-27 mV,

which is low enough to electrostatically stabilize the systems. However, Amiri et al. (2009) found that addition of salt to fumed silica dispersion at pH far enough from i.e.p produced stronger networks than that at i.e.p. Pronounced instability of fumed silica dispersion at basic pH is due dominance of reaction (b) that ion-exchange between the cations in the electrolyte and protons of the silanol groups that prevents water molecules binding to silica. Then coagulation occurs by the interaction of associated and disassociated silanol (SiO^{-} *and* SiOH).

It is assumed that there is a rather higher ability of water to form hydrated layer as discussed above for fumed silica (SiOH) surface compared to the colloidal silica (SiO_2). This is due to existence of OH bound to the silanol groups of fumed silicas. Such hydrated layer between the particles keeps particle surfaces apart from each other and prevents their bridging. On addition of electrolyte to the above system, the electrolyte cation ions can extract water from the silica surface and decrease the thickness of the hydration layer formed by water and reduce the extent of short-range repulsion. According to this hypothesis, the size of the cations and its affinity to the water are essentially important. van der Linden et al. (2015) shows that Hofmeister Series can explain the effect of different monovalent ions on the rheological properties of colloidal silica dispersions. Monovalent alkali ions are divided into two classes according to their ability to structure water molecules in their vicinity: smaller highly hydrated cations (known as structure maker); larger poorly hydrated cations (known as structure breaker). At basic pH (~9.8), less hydrated ions such as K^+ can adsorb easily on the silica surface to create bridging effect (Okazaki and Kawaguchi 2008).

The aggregation of nanoparticles is a function of the Brownian motion of the particle which increase significantly with increasing temperature. Amiri et al. (2011) shows that increasing the temperature increases the aggregation kinetics and reduced the gelation time. Also, the fractal dimension of the aggregates decreases with increasing the temperature. This means a more open gel network is formed at higher temperature. Once the aggregates form a network structure that spans the whole space to form infinite network, i.e. effective volume fraction of nanoparticles equals one, a pseudo-solid called gel is formed (Weston et al. 2014, Amiri et al. 2009, Smith and Zukoski 2006, Dickinson 2000, Family and Landau 2012, Almdal et al. 1993). This pseudo-solid gel exhibits a shear thinning behavior that applying stress could break the aggregates and destroying the structure (Raghavan and Khan 1995, Dolz et al. 2000). However, when the stress is ceased, the restoration of the network is instantaneous and the gel forms.

4.1.2. Models of Aggregation and Gelation

Inter–particle interactions can be described by the second order theoretical formulation proposed by Elimelech et al. (2013) based on Smoluchowski approach. Aggregation is the result of two events: the collision of particles, which is characterized by a collision frequency induced by hydrodynamics, and the attachment of particles which is represented by the collision efficiency because not all encountered collisions are necessarily successful. The efficiency is controlled by both the hydrodynamics and physiochemistry. In shear flow, larger aggregates can break down into smaller ones. There are different expressions for aggregation and breakage kernels in the literature. Population balance equation (PBE) that is the integral form of Smoluchowski equation

can efficiently model the aggregation and breakage of nanoparticles (Marchisio and Fox 2013, Ramkrishna 2000). PBE is essentially a transport equation that tracks number density of aggregates of certain size at any location and at any time in a system. There are different methods can be applied for solving PBE such as discretization methods (Raychoudhury et al. 2012, Chatterjee and Gupta 2009, Lee et al. 2000, Andrew et al. 1995), Lagrangian method (Taghavy et al. 2015), and quadrature method of moments (QMOM) (Vlieghe et al. 2016, Marchisio and Fox 2013, Yuan and Fox 2011, Su et al. 2008, Su et al. 2007).

Among all the available methods for solving PBE, the Quadrature Method of Moments (QMOM) is the most efficient one. QMOM transfers PBE into a set of moment equations. So that the lower-order moments of PSD are tracked with high accuracy with a low computational cost. QMOM was first proposed by McGraw (1997) for the description of aerosol dynamics by tracking the evolution of lower order moments of an unknown aerosol distribution. Moment methods are an important class of approximate models derived from kinetic equations, but require closure to truncate the moment set. In QMOM, closure is achieved by inverting a finite set of moments to reconstruct a point distribution from which all unclosed moments that can be related to the finite moment set. QMOM are widely used for modeling aggregation-breakage of particulate systems (Grosch et al. 2007, Marchisio et al. 2003b, Marchisio et al. 2003a, L. Marchisio et al. 2003). QMOM is also used for solving the kinetic equation arising in a wide variety of physical systems (Yuan and Fox 2011). Conventional QMOM usually fails when tracking more than four size classes, and thus, it is difficult to construct the PSD from the conventional QMOM. Also, numerical difficulties may arise in case of large variations of moments. Su et al.

(2007) and Su et al. (2008) employed adjustable factors assigned to different processes to track the moments of PSD with lower computational demands than that from the standard QMOM. This adjustable factor allows the moments of size distribution to be adjusted to improve the accuracy or reduce the computation time. QMOM with adjustable factor was used to model the evolution of floc size distribution (FSD) of kaolinite suspension and colloidal montmorillonite (Shen and Maa 2016, 2015).

This paper is divided into three main parts. In the first part, we provided an extensive literature review of the fundamentals of aggregations and gelation of nanoparticles. In the second part, a mechanistic model based on PBE and QMOM will be presented that can model the aggregation and gelation kinetics at different conditions. In the last part, some case studies of the kinetics of aggregation and gelation of fumed silica compared to colloidal silica will presented to show the capability of the mechanistic model presented in this paper. However, these case studies do not show all the capabilities of the model. Further discussion of the model will be presented in future papers.

4.2. Population Balance Model

Population balance equation (PBE) is a continuity statement that describes the evolution of a number density function (NDF) of particle volume dispersed in the system (Marchisio and Fox 2013). The particle size distribution (PSD) is a NDF representing the number concentration of particles with volumes between $v \; and \; v + dv$. PSD evolved with time due to particles aggregation. Under shear flow, large aggregate can break into smaller one that may aggregate with other particles again. The volume based PBE (Vlieghe et al. 2016) can be written as in Eqs. 1 through 5, where $n(v;t)$ is the NDF of

aggregates of volume v, $B_a(v;t)\ and\ D_a(v;t)$ are birth and death of aggregates of volume v due to aggregation, and $B_b(v;t)\ and\ D_b(v;t)$ are birth and death of aggregates of volume v due to breakage.

$$\frac{\partial(n(v;t))}{\partial t} = B_a(v;t) - D_a(v;t) + B_b(v;t) - D_b(v;t) \tag{1}$$

$$B_a(v;t) = \frac{1}{2}\int_0^v \alpha(v-u,u)\beta(v-u,u)n(v-u;t)n(u;t)du \tag{2}$$

$$D_a(v;t) = n(v;t)\int_0^\infty \alpha(v,u)\beta(v,u)n(u;t)du \tag{3}$$

$$B_b(v;t) = \int_v^\infty a(v,u)b(u)n(u;t)du \tag{4}$$

$$D_b(v;t) = b(v)n(v;t) \tag{5}$$

In these equation, $\beta(v,u)$ is the collision frequency of particles of volume $v\ and\ u$, $\alpha(v,u)$ is the collision efficiency of particles of volume $v\ and\ u$, $b(v)$ is the breakage kernel that represents the break frequency of aggregates of volume v, and $a(v,u)$ is the fragment distribution function that represent the number density function of aggregates of volume v produced by breakage of aggregates of volume u.

To involve the fractal dimension into the PBE, Vlieghe et al. (2016) proposed the following relationship between volume based NDF ($n(v;t)$) and length based NDF ($n(L;t)$).

$$n(v;t) = \frac{n(L;t)}{\Phi D_f L^{D_f-1}} \tag{6}$$

$$\Phi = \Phi_o {L_o}^{3-D_f} \tag{7}$$

$$\Phi_o = \frac{\pi}{6} \tag{8}$$

where D_f is the fractal dimension of the aggregates, L is the length of aggregates and L_o is the initial length of the particles assumed that the aggregates composed of identical particles.

Applying Eq. (6) into Eqs. (1)–(5), the length-based PBE can be derived as the following as a function of aggregate sizes ($L\ and\ \lambda$)

$$\frac{\partial(\boldsymbol{n}(\boldsymbol{L};\boldsymbol{t}))}{\partial \boldsymbol{t}} = \boldsymbol{B_a}(\boldsymbol{L};\boldsymbol{t}) - \boldsymbol{D_a}(\boldsymbol{L};\boldsymbol{t}) + \boldsymbol{B_b}(\boldsymbol{L};\boldsymbol{t}) - \boldsymbol{D_b}(\boldsymbol{L};\boldsymbol{t}) \tag{9}$$

$$\boldsymbol{B_a}(\boldsymbol{L};\boldsymbol{t}) = \frac{\boldsymbol{L}^{\boldsymbol{D_f}-\boldsymbol{1}}}{\boldsymbol{2}} \int_{\boldsymbol{0}}^{\boldsymbol{L}} \boldsymbol{\alpha}\left(\left(\boldsymbol{L}^{\boldsymbol{D_f}} - \boldsymbol{\lambda}^{\boldsymbol{D_f}}\right)^{\frac{\boldsymbol{1}}{\boldsymbol{D_f}}}, \boldsymbol{\lambda}\right).\boldsymbol{\beta}\left(\left(\boldsymbol{L}^{\boldsymbol{D_f}} - \boldsymbol{\lambda}^{\boldsymbol{D_f}}\right)^{\frac{\boldsymbol{1}}{\boldsymbol{D_f}}}, \boldsymbol{\lambda}\right).\boldsymbol{n}\left(\left(\boldsymbol{L}^{\boldsymbol{D_f}} - \boldsymbol{\lambda}^{\boldsymbol{D_f}}\right)^{\frac{\boldsymbol{1}}{\boldsymbol{D_f}}}; \boldsymbol{x}, \boldsymbol{t}\right).\boldsymbol{n}(\boldsymbol{\lambda};\boldsymbol{x},\boldsymbol{t}).\left(\left(\boldsymbol{L}^{\boldsymbol{D_f}} - \boldsymbol{\lambda}^{\boldsymbol{D_f}}\right)^{\frac{\boldsymbol{1}}{\boldsymbol{D_f}}-\boldsymbol{1}}\right)\boldsymbol{d\lambda} \tag{10}$$

$$\boldsymbol{D_a}(\boldsymbol{L};\boldsymbol{t}) = \boldsymbol{n}(\boldsymbol{L};\boldsymbol{t}) \int_{\boldsymbol{0}}^{\infty} \boldsymbol{\alpha}(\boldsymbol{L},\boldsymbol{\lambda})\boldsymbol{\beta}(\boldsymbol{L},\boldsymbol{\lambda})\boldsymbol{n}(\boldsymbol{\lambda};\boldsymbol{t})\boldsymbol{d\lambda} \tag{11}$$

$$\boldsymbol{B_b}(\boldsymbol{L};\boldsymbol{t}) = \int_{\boldsymbol{v}}^{\infty} \boldsymbol{a}(\boldsymbol{L},\boldsymbol{\lambda})\boldsymbol{b}(\boldsymbol{\lambda})\boldsymbol{n}(\boldsymbol{\lambda};\boldsymbol{t})\boldsymbol{d\lambda} \tag{12}$$

$$\boldsymbol{D_b}(\boldsymbol{L};\boldsymbol{t}) = \boldsymbol{b}(\boldsymbol{L})\boldsymbol{n}(\boldsymbol{L};\boldsymbol{t}) \tag{13}$$

$$\boldsymbol{\beta}(\boldsymbol{v},\boldsymbol{u}) = \frac{\boldsymbol{\beta}(\boldsymbol{L},\boldsymbol{\lambda})}{\boldsymbol{\Phi}\boldsymbol{D_f}\boldsymbol{L}^{\boldsymbol{D_f}-\boldsymbol{1}}} \tag{14}$$

4.3. Moment Transformation

Moment transform (McGraw 1997, McGraw and Saunders 1984, Hulburt and Katz 1964) can be applied to Eq. (9) using the following definition:

$$m_k = \int_0^\infty L^k n(L;t)dL \tag{15}$$

in which m_k is the kth order moment and the size class L varies from zero to infinity in the transformation. McGraw (1997) proposed applying Gaussian quadrature approximation to replace the integration terms by a set of weight and abscissas of the NDF.

$$m_k = \int_0^\infty L^k n(L;t)dL = \sum_{i=1}^{N_q} \omega_i L_i^k = \Omega \times (\Gamma^k)^T \left(k = 0,1,\dots,2N_q - 1\right) \tag{16}$$

$\Gamma = [L_1, L_2, .., L_{Nq}]$ is a vector with each component representing a node in the Gaussian quadrature approximation. $\Omega = [\omega_1, \omega_2, .., \omega_{Nq}]$ is also a vector in which each component is the weight (also the characteristic number density) corresponding to L_i. The superscript T stands for the transpose of a vector. N_q is the number of quadrature that represents the number of size classes of the aggregates.

Using this transformation, Eq. (16) can only allow to track three or four size classes that would be sufficient to track the lower order moments. To reasonably produce the PSD curve higher order moments are required. However, tracking higher order moments could produce ill-conditioned problem due to the higher difference between L_1 and L_{Nq} with larger k, i.e., $(L_1)^1 \ll (L_k)^k$(Gautschi 1968). This would produce unreliable results i.e.

negative weights and/or size that do not have physical meaning. To relax the severity of ill-condition by reducing the difference between $(L_1)^1 and (L_k)^k$, Su et al. (2007) added an adjustable factor, p in QMOM and re-defined the adjustable moments as

$$m_{k/p} = \int_0^\infty L^{k/p} n(L;t) dL = \sum_{i=1}^{N_q} \omega_i L_i^{k/p} = \Omega \times (\Gamma^{k/p})^T \left(k = 0,1,\dots,2N_q - 1\right) \tag{17}$$

In case of $p = 1$, this could be reduced back to the conventual QMOM as in Eq. (16). Applying the transformation in Eq. (17), the PBE in Eq. (9) is transformed into a set of moment equations ($k = 0,1,..,M$) that are a system of non-linear integro-differential equations (Eq. (18)). Applying the quadrature approach transform the integrals into simple summations (Eq. (19)).

$$\begin{aligned} \frac{\partial(m_{k/p})}{\partial t} = {} & \frac{1}{2}\int_0^\infty n(\lambda;t) \int_0^\infty \alpha(L,\lambda)\,.\,\beta(L,\lambda)\,(\,L^{D_f} + \lambda^{D_f})^{\frac{k/p}{D_f}}\,.\,n(L;t) dL d\lambda \\ & - \int_0^\infty L^{k/p} n(L;t) \int_0^\infty \alpha(L,\lambda)\,.\,\beta(L,\lambda) n(\lambda;t) d\lambda dL \\ & + \int_0^\infty L^{k/p} \int_0^\infty a(L,\lambda) b(\lambda) n(\lambda;t) d\lambda dL - \int_0^\infty L^{k/p} b(L) n(L;t) dL \end{aligned} \tag{18}$$

$$\begin{aligned} \frac{\partial(m_k)}{\partial t} = {} & \frac{1}{2}\sum_{i=1}^{N_q} \omega_i \sum_{j=1}^{N_q} \alpha(L_i,L_j)\beta(L_i,L_j)\omega_j \left(L_i{}^{D_f} + L_j{}^{D_f}\right)^{\frac{k}{pD_f}} \\ & - \sum_{i=1}^{N_q} \omega_i L_i^{k/p} \sum_{j=1}^{N_q} \alpha(L_i,L_j)\beta(L_i,L_j)\omega_j \\ & - \sum_{i=1}^{N_q} \bar{a}(L_i,L_j)^{k/p} b(L_i)\omega_i - \sum_{i=1}^{N_q} L_i^{k/p} b(L_i)\omega_i \end{aligned} \tag{19}$$

$$\bar{a}\left(L_i, L_j\right)^{(k/p)} = \int_0^{\infty} L^{k/p}\, a\left(L_i, L_j\right)\mathrm{dL} \tag{20}$$

Additionally, PSD can be estimated from moments is inverse problem. PSD, which is number density function can be estimated by using the following relationship (McGraw 1997):

$$n(L;t) \approx \sum_{i=1}^{N_q} \omega_i(t)\delta[L - L_i(t)] \tag{21}$$

where δ is the Dirac delta function which means at any time t, δ is zero except at $L = L_i(t)$.

4.4. Breakage and Aggregation Kernels

4.4.1. Collision frequency, β

Collision frequency represents the two number of collisions between two particles of given sizes L and λ. There are several expressions for collision frequency in the literature. Basically, collisions result from Brownian diffusion, differential sedimentation or shear flow. However, when particle size is submicron, Brownian diffusion is the dominant mechanism of collision (Elimelech et al. 2013, Thomas et al. 1999). With aggregation and increase of effective size of aggregates shear flow becomes more significant. For submicron particles, differential sedimentation can be neglected.

$$Perkinetic\text{:}\ \beta^{per}\left(L_i, L_j\right) = \frac{2}{3}\frac{k_B T}{\mu}\frac{(L_i + L_j)^2}{L_i L_j} \tag{22}$$

$$Orthokinetic:\ \beta^{orth}(L_i, L_j) = \frac{G}{6}(L_i + L_j)^3 \tag{23}$$

Where k_B is the Boltzmann constant, T is the temperature of the dispersion, μ is the viscosity of the dispersion, and G is the shear rate.

4.4.2. Collision efficiency, α

The effect of energy barrier on aggregation is to reduce the rate of aggregation due to electrostatic repulsion. Stability ratio (W), the reciprocal of the collision efficiency is simply the ratio of the aggregation rate in the absence of energy barrier to that with energy barrier (Elimelech et al. 2013). The stability ratio and collision efficiency can be calculated using the following:

$$W = 2\int_0^{\infty} \chi(\sigma) \frac{\exp\left(\frac{\phi_T}{k_B T}\right)}{(\sigma + 2)^2} d\sigma \tag{24}$$

$$\alpha(L_i, L_j) = 1/W$$

Where ϕ_T is the total electrostatic interaction between particles at separation distance h, and σ is a function of h and particle size.

$$\sigma = \frac{2h}{L_i + L_j} \tag{25}$$

$\chi(\sigma)$ is the hydrodynamic effect. As the particles approach close, it becomes increasingly difficult for liquid between them to be drained out the gap and this tends to slow the aggregation process.

$$\chi(\sigma) = \frac{6\sigma^2 + 13\sigma + 2}{6\sigma^2 + 4\sigma} \tag{26}$$

The total electrostatic interaction (ϕ_T) is the summation of electric double layer repulsion, van der Walls attraction, and in case of silica nanoparticles solvation force can be added

to accurately predict the interaction energy. Zeta potential is the main factor that controls the electrostatic interaction (Abdelfatah et al. 2017b).

$$\zeta = \begin{cases} s_1 \dfrac{0.85 k_B T}{f(\kappa a_p) e} (pH_{IEP} - pH)\left[1 + v_\zeta (T - T_0)\right] \\ \zeta_{cut-off} + \dfrac{s_2}{f(\kappa L_i)} \left(pH_{cut-off} - pH\right)\left[1 + v_\zeta (T - T_0)\right] \end{cases} \quad (27)$$

Ohshima (1994) presented a simple approximate expression for Henry's function which is applicable for any value of κL_i.

$$f(\kappa L_i) = 1 + \frac{1}{2\left[1 + \dfrac{2.5}{\kappa L_i (1 + exp^{-\kappa L_i})}\right]} \quad (28)$$

Van der Waals interactions (Berg 2010)

$$\phi_{vdw} = -\frac{A_H}{6}\left[\frac{2L_iL_j}{h^2 + 2L_ih} + \frac{2L_iL_j}{h^2 + 2L_ih + 2L_jh + 4L_iL_j} + \ln\left(\frac{h^2 + 2L_ih + 2L_jh}{h^2 + 2L_ih + 2L_jh + 4L_iL_j}\right)\right] \quad (29)$$

Where A_H is the Hamaker constant(Russel et al. 1989)

$$A_H = \frac{3}{4} k_B T \left(\frac{\varepsilon_p - \varepsilon_c}{\varepsilon_p + \varepsilon_c}\right)^2 + \frac{3 h_P v_e}{16\sqrt{2}} \frac{\left(n_p^2 - n_c^2\right)^2}{\left(n_p^2 + n_c^2\right)^{3/2}} \quad (30)$$

ε is the dielectric constant, n is the refractive index, the subscripts p *and* c correspond to the properties of the particle and continuous phase, respectively, h_P is the Planck constant, and v_e is the characteristic adsorption frequency. Electric double layer repulsion using linearized Poisson-Boltzmann equation(Hogg et al. 1966).

$$\boldsymbol{\phi_{EDL}} = \frac{\boldsymbol{\varepsilon_0 L_i L_j(\zeta_i{}^2 + \zeta_j{}^2)}}{\boldsymbol{4(L_i + L_j)}}\left[\frac{\boldsymbol{2\zeta_i\zeta_j}}{\boldsymbol{(\zeta_i{}^2 + \zeta_j{}^2)}}\ln\left(\frac{\boldsymbol{1 + exp(-\kappa h)}}{\boldsymbol{1 - exp(-\kappa h)}}\right) + \ln(\boldsymbol{1 - \exp(-2\kappa h)}\right] \quad (31)$$

Debye length

$$\boldsymbol{\kappa} = \left(\frac{\boldsymbol{e^2\sum_i z_i^2 c_{i0}}}{\boldsymbol{\varepsilon_c\varepsilon_0 k_B T}}\right)^{\boldsymbol{1/2}} \quad (32)$$

Where ε_0 is the vacuum permittivity, z is the valence number of the ion, e is the charge of an electron, $\zeta_i and\, \zeta_j$ are the zeta potentials of aggregates of size $L_i\, and\, L_j$, respectively. κ^{-1} is the Debye length, and c_{i0} is the bulk concentration of ion species i. Hydration repulsion originates from the overlap of structured layer of water molecules at the surfaces of hydrophilic nanoparticles (Pashley and Israelachvili 1984). Hydration force can be expressed by (P. Binks and O. Lumsdon 1999, Chapel 1994)

$$\boldsymbol{\phi_{HYD}} = \boldsymbol{\pi L_i N_A C_h c_{i0} \ell^2 \exp(-h\ell)} \quad (33)$$

Where C_h is hydration constant, ℓ is the decay length.

4.4.3. Breakup frequency

The breakup frequency including the fractal dimension can expressed by Eq. (34) (Vlieghe et al. 2016)

$$b(L_i) = cG^{5/2}(\frac{L_i}{L_0})^{3-2D_f/3} \quad (34)$$

Where G is the shear rate, *c* is a fitting parameter that depends on the strength of the aggregate.

4.4.4. Fragment distribution

Uniform fragmentation distribution is used in this work, meaning that all possibilities are equally probable (Vlieghe et al. 2016).

$$a(L_i, L_j) = \frac{2D_f {L_i}^{D_f-1}}{{L_j}^{D_f}}, \quad L_i < L_j \tag{35}$$

and the integrated adjustable daughter distribution function can be written as

$$\bar{a}(L_i, L_j)^{(k/p)} = {L_i}^{k/p} \frac{2D_f}{k/p + D_f}, \quad L_i < L_j \tag{36}$$

4.5. Viscosity model

Modified effective-medium theory (Lattuada et al. 2016, Takamura and Ven 2010) can be effectively used to model the viscosity evolution of aggregating dispersions and predicts the initiation of gelation.

$$\mu = \mu_0 \left[\frac{1 - \frac{\varphi}{\varphi_m}}{1 - \frac{(k_0 \varphi_m - 1)\varphi}{\varphi_m}} \right]^{\frac{-\varphi_m[\mu]}{2 - k_0 \varphi_m}} \tag{37}$$

Where φ is the particles/aggregates volume fraction and φ_m is the maximum packing factor. Intrinsic viscosity $[\mu] = 2.5$. For $D_f = 3$, $\varphi = k_V m_3$. Where k_V is the volumetric shape factor. Crowding factor $k_0 = \frac{2k_2}{[\mu]} - [\mu]$. k_0 is a function of shear rate (G), and the exact relationship between k_0 and G is a function of the surface properties of the colloidal particles and the electrolyte concertation. However, in this study k_2 is assumed between $5.2 - 6.2$ from low to high shear rate. Hence $k_0^0 = 3.05$ at low shear rate and $k_0^\infty = 1.7$

at high shear limit. The effect of shear rate can be calculated as the following: $k_0 = k_0^{\infty} + \frac{k_0^0 - k_0^{\infty}}{1+Pe^{0.35}}$. Where $Pe = \frac{3\pi\mu G R_{H,i} R_{H,j}(R_{H,i}+R_{H,j})}{2k_B T}$ and Hydrodynamic radius, $R_{H,i} = \frac{m_3}{m_2}$

4.6. Numerical Solution

The mathematical model presented in the previous sections is solved numerically to find the evolution of the moments and the viscosity as the following:

1. Knowing the volume fraction of the particles in the initial dispersion and assuming the initial particles has an average size of 150 nm, we can calculate the number of the particles and number density function at the initial conditions.
2. Using wheeler algorithm (Wheeler 1974), the weight and abscissas of the initial moments can be calculated. For more details about wheeler algorithm, readers are referred to Marchisio and Fox (2013)
3. Using the weight and abscissas of the initial moments, the initial source/sink term is then calculated.
4. Sweeping the time steps

4.1. Using initial source/sink term, the moments can be updated using backward Euler time discretization scheme.

4.2. Feeding the updated moments into wheeler algorithm, the updated weights and abscissae's can be calculated.

4.3. Using the updated the weights and abscissae's, the source/sink term for the next time step is calculated.

4.4. Using the updated moments, the new viscosity can be calculated.

5. Repeat step 4 and end the simulation when the total time of simulation is reached.

4.7. Results and Discussion

The mathematical model presented in this paper is used to study the aggregation and gelation of fumed silica nanoparticles compared to colloidal silica nanoparticles. Several hypothetical cases were run to compare the kinetics of aggregation of both silica nanoparticles at comparable conditions. Modified effective-medium theory is used for calculation of viscosity evolution with aggregation. Several experimental studies show that the maximum packing factor (φ_m) for fumed silica is ~0.20-0.3 while for colloidal silica it's ~ 0.7 (Smith and Zukoski 2004, Chen et al. 2005). For colloidal silica, the value of the maximum packing factor (φ_m) is close to the theoretical value of 0.74 for a close packed array of same size spheres. While for fumed silica, φ_m is much smaller due to the fractal structures that prevent tight packing of the primary particles. Two different regimes of aggregation are identified; diffusion limited aggregation (DLCA), and reaction limited aggregation (RLCA) (Sefcik et al. 2005). The network structure of DLCA is more open ($D_f = 1.8$) while that for RLCA is more close and compact ($D_f = 2.2$) (Russel et al. 1989). However, in this study, the fractal dimension is assumed to be 3. In this case, the conservation of mass per unit volume can be verified for $k = D_f = 3$. In this section, the simulation results for fumed silica and colloidal silica nanoparticles are presented at different electrolyte concentration represented by the collision efficiency as calculated from Eq. (24).

4.7.1. Fumed silica

Fumed silica is aggregates of spherical particles fused together on the flame (Smith and Zukoski 2004). In this study, it's assumed that the maximum packing factor (φ_m) for fumed silica is ~0.3 that is close to the value calculated from aggregation experiments of

fumed silica by Smith and Zukoski (2004). The effect of collision efficiency representing different salt concentration is presented in Fig. 4-1 for $D_f = 3$ and 1.25 vol% of fumed silica nanoparticles dispersion. With increasing the salt concentration (i.e. increasing collision efficiency), the gelation time (represented by sharp increase in viscosity) decreases significantly. At low collision efficiency, the gel cannot be formed. This can be explained that at low electrolyte concentration, the electrostatic repulsion between particles is significantly high (Abdelfatah et al. 2017a, Abdelfatah et al. 2017b). This high repulsion forces between particles can prevent the particles approaching each other and maintain the dispersion stability. Fig. 4-2 shows the evolution of aggregate size with time. The aggregate size reaches a stable plateau once gelation is triggered. According to Eq. (22), collision frequency depends on the aggregate size and viscosity. Once the effective volume fraction of aggregates reaches φ_m, the gel network spans the whole space and the viscosity increases sharply. Hence, the collision frequency will be reduced significantly and no further aggregation would occur. Fig. 4-2 also shows that at low collision efficiency, the aggregate size does not change indicating that the dispersion is highly stable against aggregation. Fig. 4-3 shows that volume fraction of the aggregates grows monotonically till it reaches the maximum packing factor beyond which there is no further aggregation and no further increase in volume of the aggregates. The increase of the volume with time is due to the fractal nature of the aggregates. However, the total mass of the aggregates is conserved. This can be checked that the moment at $k = D_f$ representing the total mass of the aggregates is constant.

Initial concentration of nanoparticles in the dispersion is one of the key factors that control aggregation and gelation. Smith and Zukoski (2006) shows that there is a critical

concentration of fumed silica nanoparticles below which the gel network cannot be formed. Herein, the study of aggregation and viscosity evolution with time is presented at different concentrations of fumed silica nanoparticles. Fig. 4-4 shows that at concentration as low as 0.5 vol% the gel cannot be formed. Also, Figs. 4-5 and 4-6 shows that there is a slight increase in the mean aggregate size and the volume fraction at low concentration, respectively. With increasing the concentration of nanoparticles, the gel network starts to form at 0.8 vol% of fumed silica nanoparticles. Above this critical concentration, the viscosity increases much further and the gelation decreases significantly with increasing the concentration of fumed silica (Fig. 4-4). However, Fig 4-5 shows that with increasing the concentration above the critical point, the aggregates size decreases significantly. This can be explained that at low concentration the aggregates size needs to grow greatly before it could form the gel network. While at high concentration, the particles are much closer together that larger number of moderate aggregate size can be formed initially before they can interconnect together to form the gel network. This explanation is supported by Fig. 4-6 which shows that high concentration of silica nanoparticles, the volume of aggregates reaches the maximum packing factor at significantly shorter time.

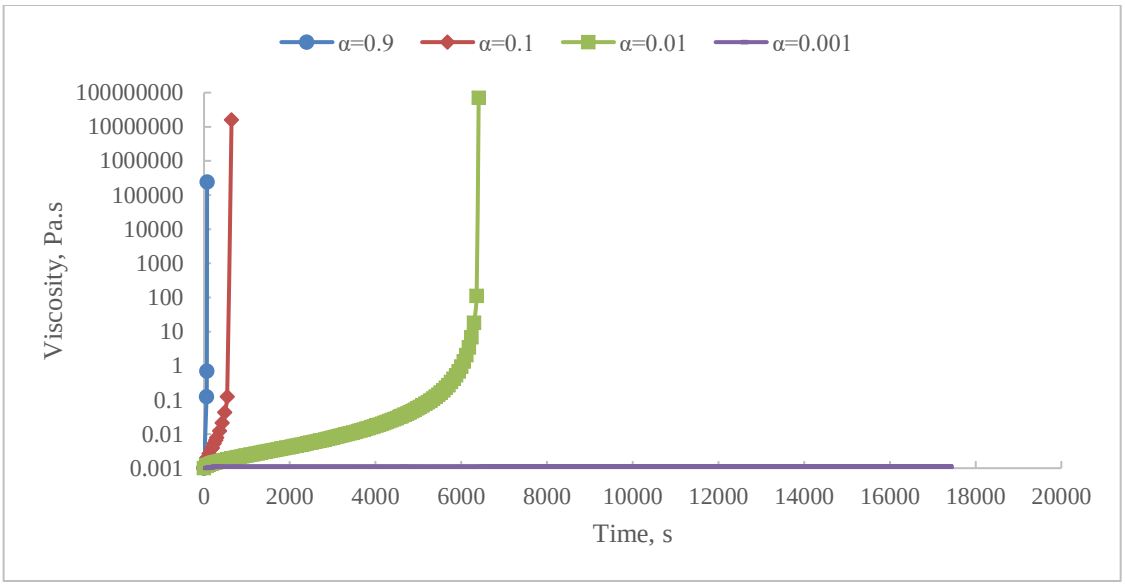

Figure 4-1—Viscosity evolution with time for fumed silica suspension with $D_f = 3$ at different collision efficiency

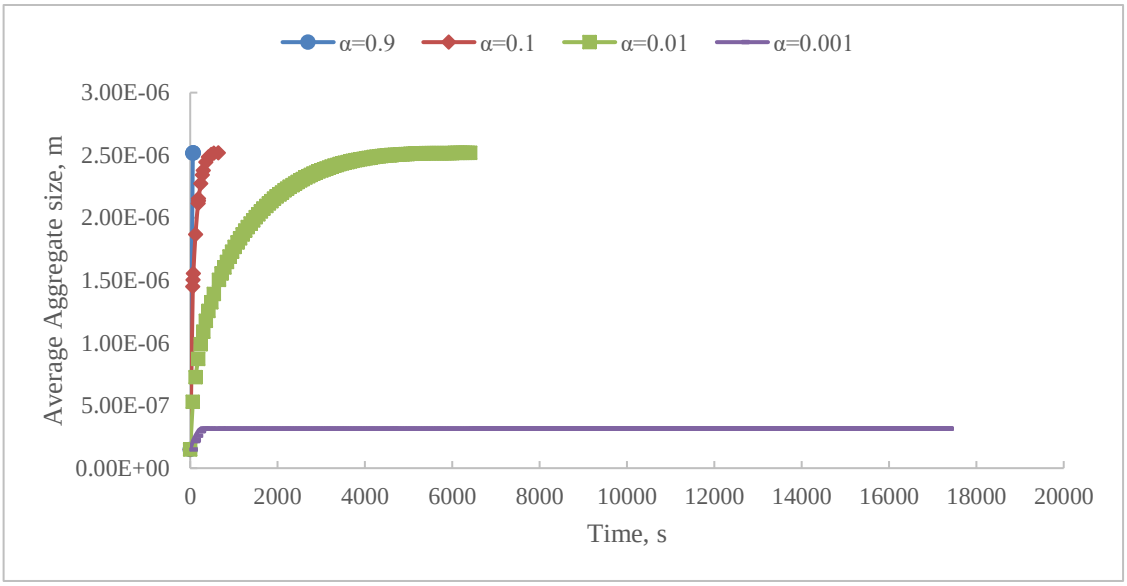

Figure 4-2—Aggregate size evolution with time for fumed silica suspension with $D_f = 3$ at different collision efficiency

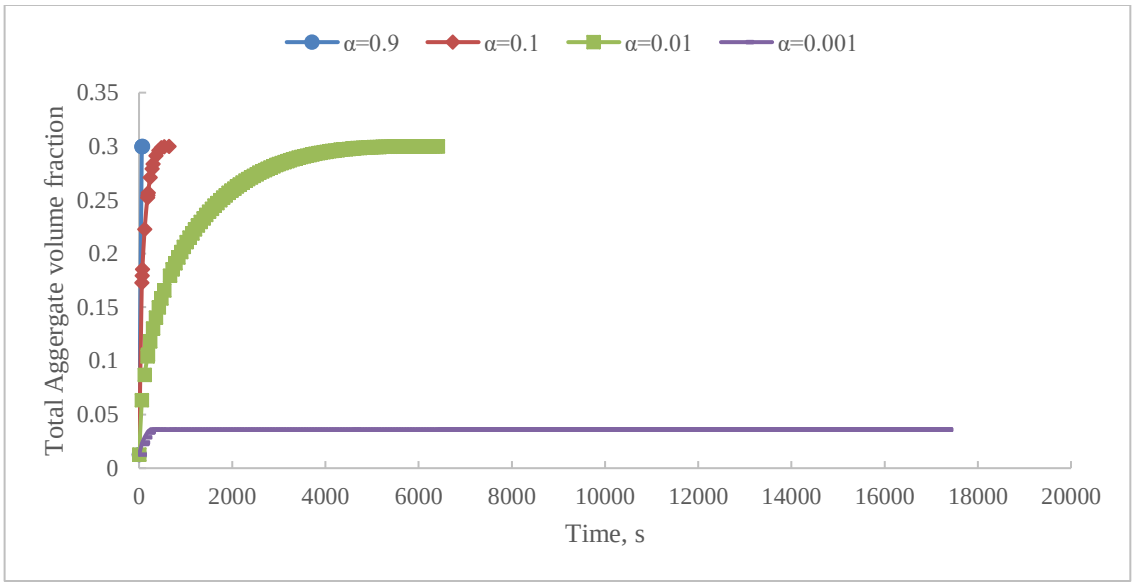

Figure 4-3—Aggregate volume fraction evolution with time for fumed silica suspension with $D_f = 3$ at different collision efficiency

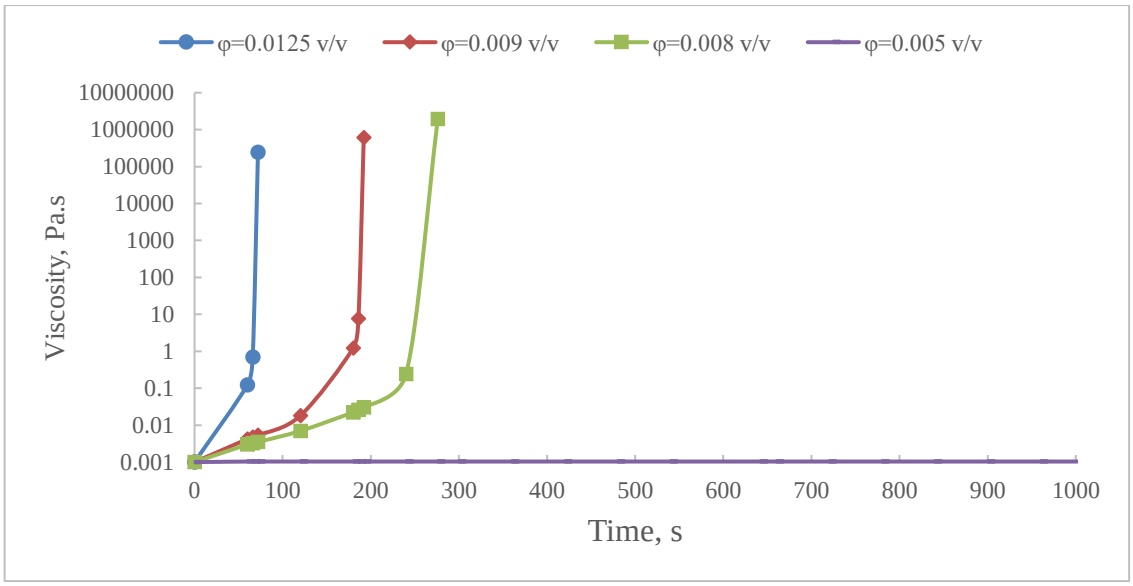

Figure 4-4—Viscosity evolution with time for fumed silica suspension with $D_f = 3$ at different initial concentration

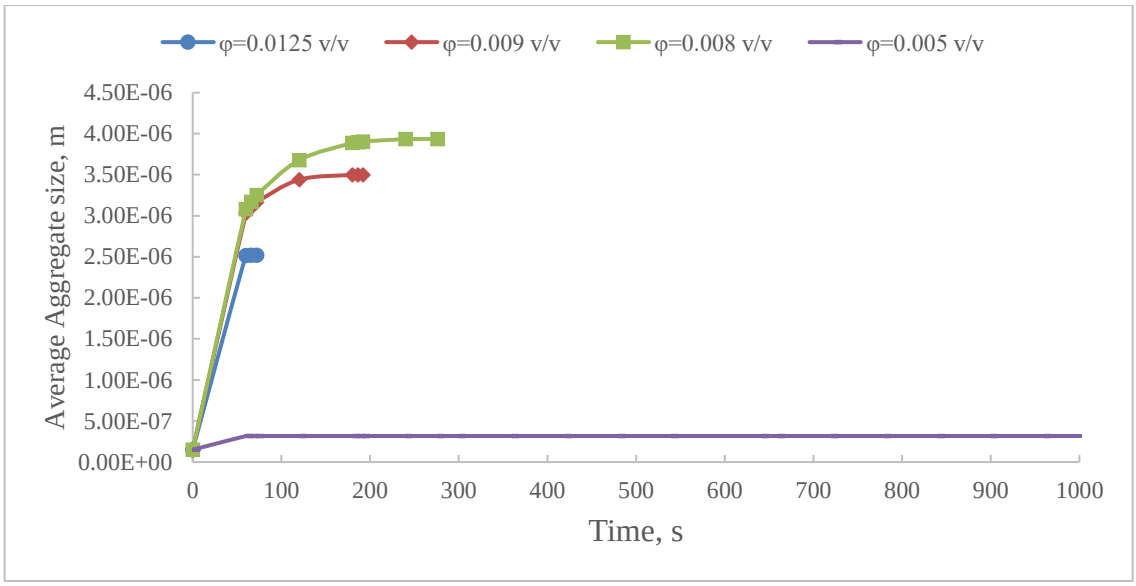

Figure 4-5—Aggregate size evolution with time for fumed silica suspension with $D_f = 3$ at different initial concentration

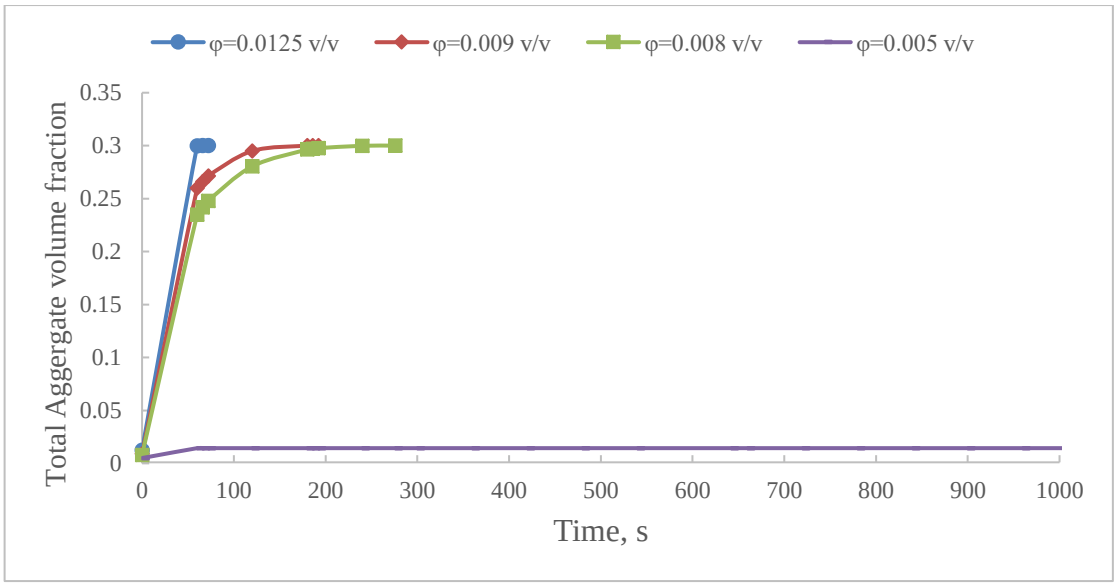

Figure 4-6—Aggregate volume fraction evolution with time for fumed silica suspension $D_f = 3$ at different initial concentration

4.7.2. Colloidal silica

Unlike fumed silica, colloidal silica is a single spherical particle (Chen et al. 2005). In this study, it's assumed that the maximum packing factor (φ_m) for colloidal silica is ~0.7. This value is close to the theoretically calculated value for packing of spheres ~ 0.74. Here, we modeled the aggregation and gelation of colloidal silica at similar conditions that presented in the previous section for fumed silica nanoparticles. The fractal dimension of the aggregates is also assumed to be constant and equal to 3. The effect of collision efficiency representing different salt concentration is presented in Fig. 4-7 for colloidal silica nanoparticles concentration of 1.25 vol%. With increasing the salt concentration (i.e. increasing collision efficiency), the viscosity of the dispersion increases significantly. Fig. 4-6 shows the evolution of aggregate size with time. At very low collision efficiency, the viscosity does have much increase beyond the initial viscosity of the stable dispersion. Comparing Fig. 4-7 to Fig. 4-1, colloidal silica does not form the gel network as in the case of fumed silica at 1.25 vol%. The aggregation and the crowing of the dispersion increases the viscosity slowly. However, this low concentration is not enough to form the gel network. Chen et al. (2005) shows that colloidal silica can form the gel network at concentration as high as 30 vol%. Fig. 4-8 shows that with increasing the collision frequency the aggregates size increases significantly. However, due to low concentration to form the gel network, the aggregate increases significantly as compared to the fumed silica nanoparticles in Fig. 4-2. The aggregate size plateau explains that there is not further aggregation due to large size of the aggregates and hence the lower the collision frequency. This is also affirmed by Fig. 4-9 that shows that the volume fraction of the aggregates no longer increases after a certain time.

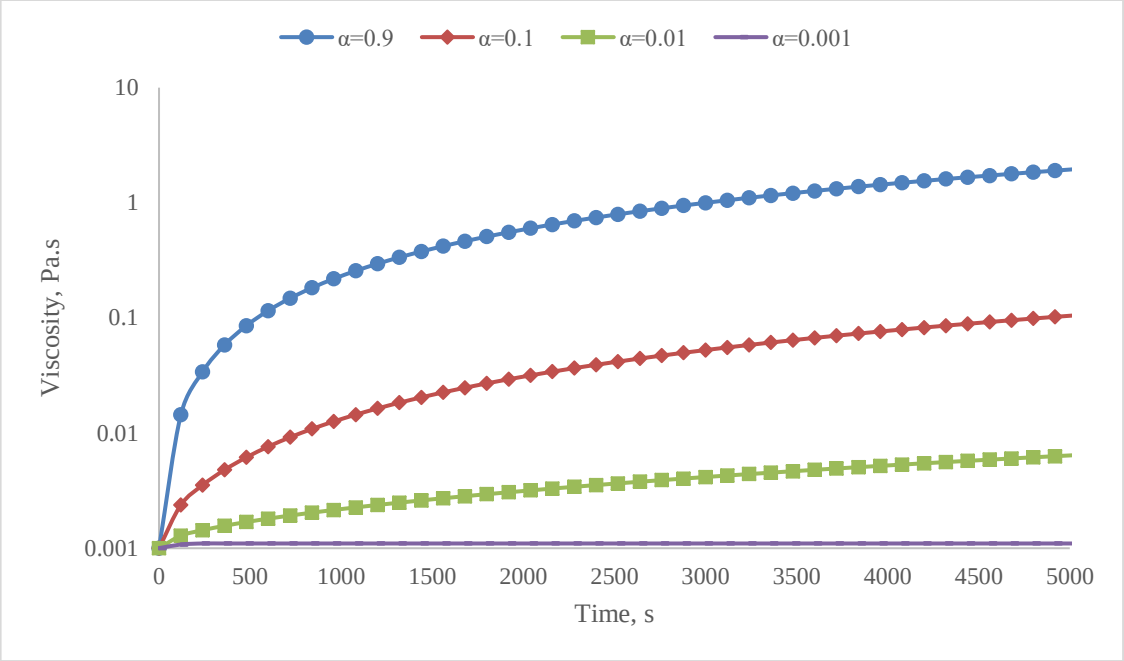

Figure 4-7—Viscosity evolution with time for colloidal silica suspension with $D_f = 3$ at different collision efficiency

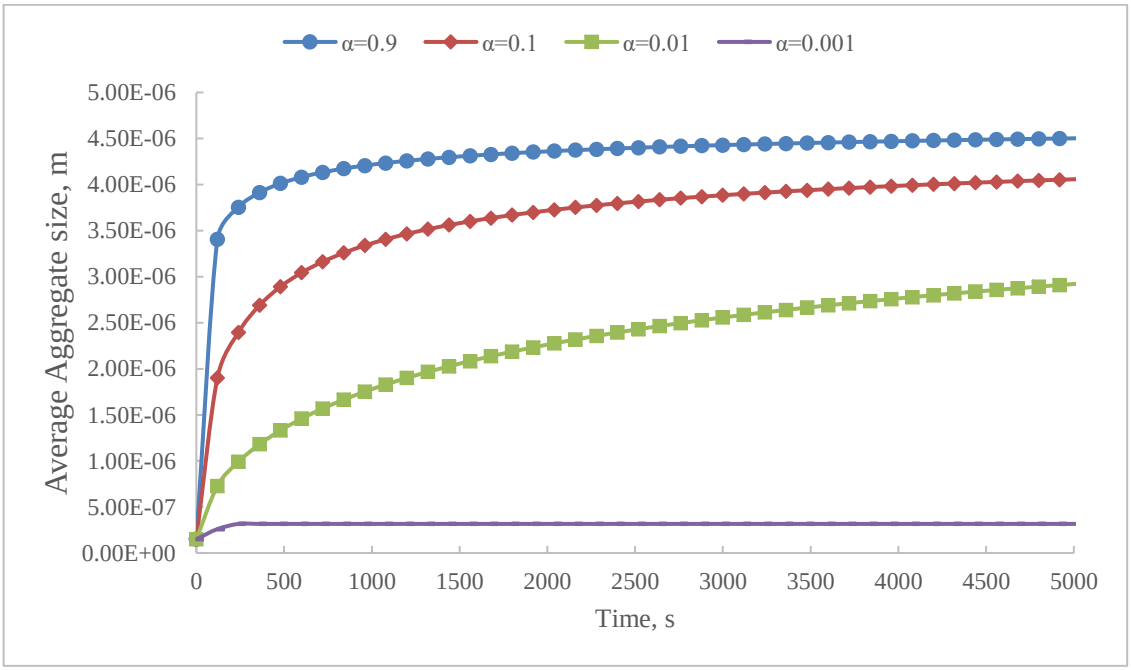

Figure 4-8—Aggregate size evolution with time for colloidal silica suspension with $D_f = 3$ at different collision efficiency

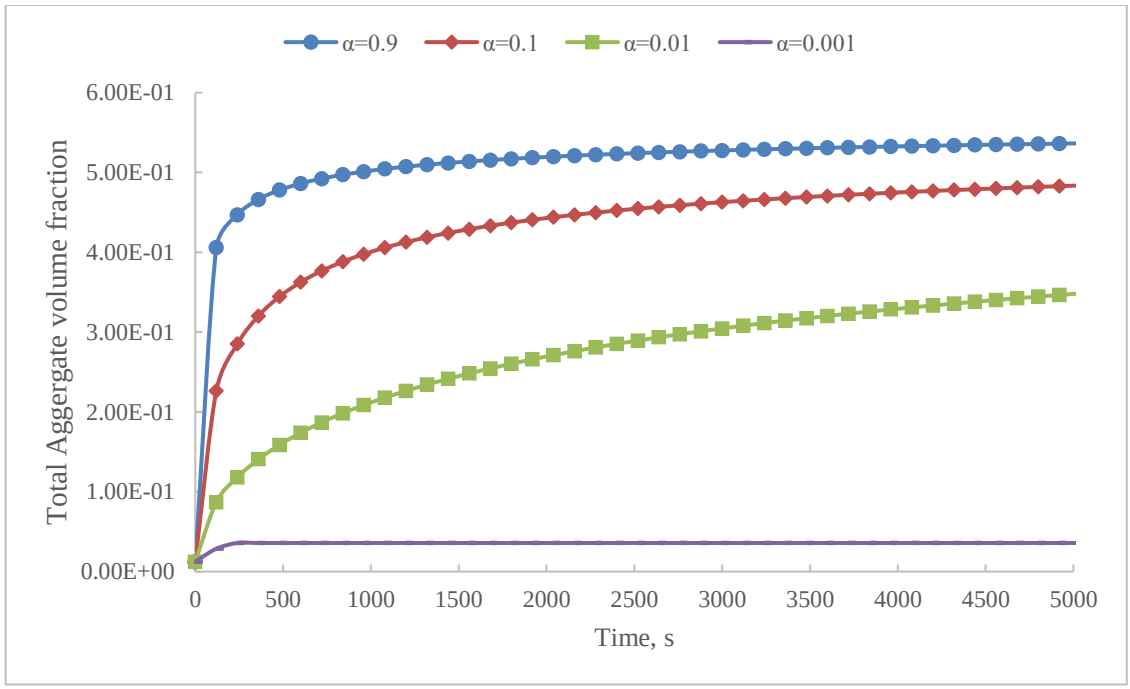

Figure 4-9—Aggregate volume fraction evolution with time for colloidal silica suspension with $D_f = 3$ at different collision efficiency

Herein, the effect of colloidal silica concentration is studied at two different collision efficiencies. At concentration of 5 vol%, the viscosity increases significantly compared to 1.25 vol%. However, 5 vol% is not enough to form the gel network as explained earlier. Fig. 4-10 shows that regardless of the collision efficiency, increases the viscosity few orders of magnitude. This is affirmed by Fig. 4-12 that shows that the volume fraction of the aggregates increases significantly with increasing the concentration of the nanoparticles. However, Fig. 4-11 shows that the aggregate size decreases significantly with increasing the concentration of nanoparticles. This is consistent with the results shown in Fig. 4-10 and Fig. 4-12.

With increasing the concentration, the number of initial particles is increases that form aggregates with the nearest particles or aggregates. Also as the viscosity increases significantly and the collision frequency decrease consequently. This means that we

would have larger number of aggregates with smaller size than in the case of low concentration.

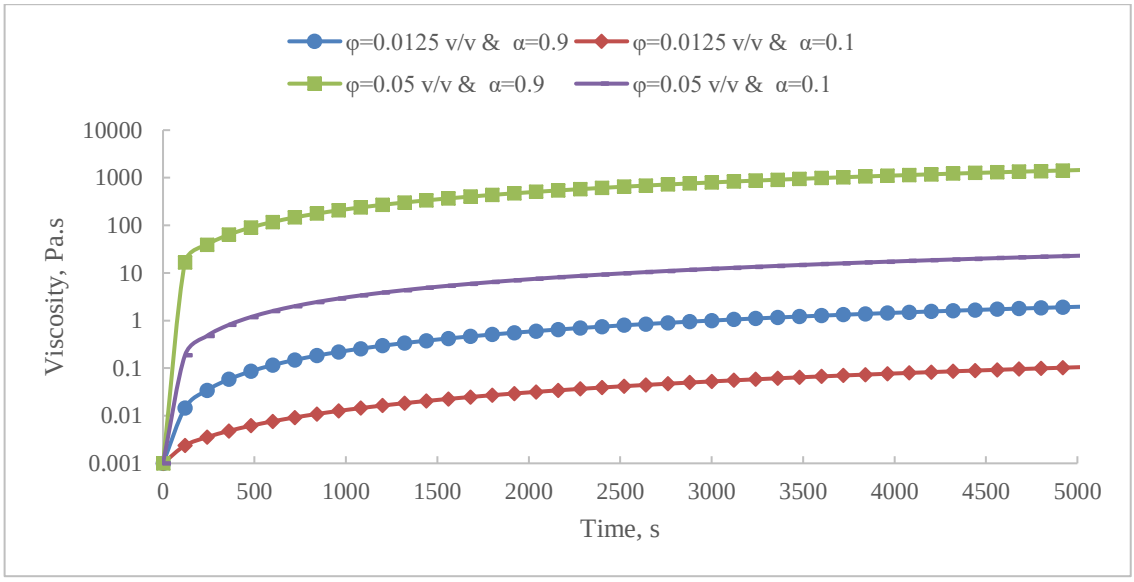

Figure 4-10—Viscosity evolution with time for colloidal silica suspension with $D_f = 3$ at different initial concentration

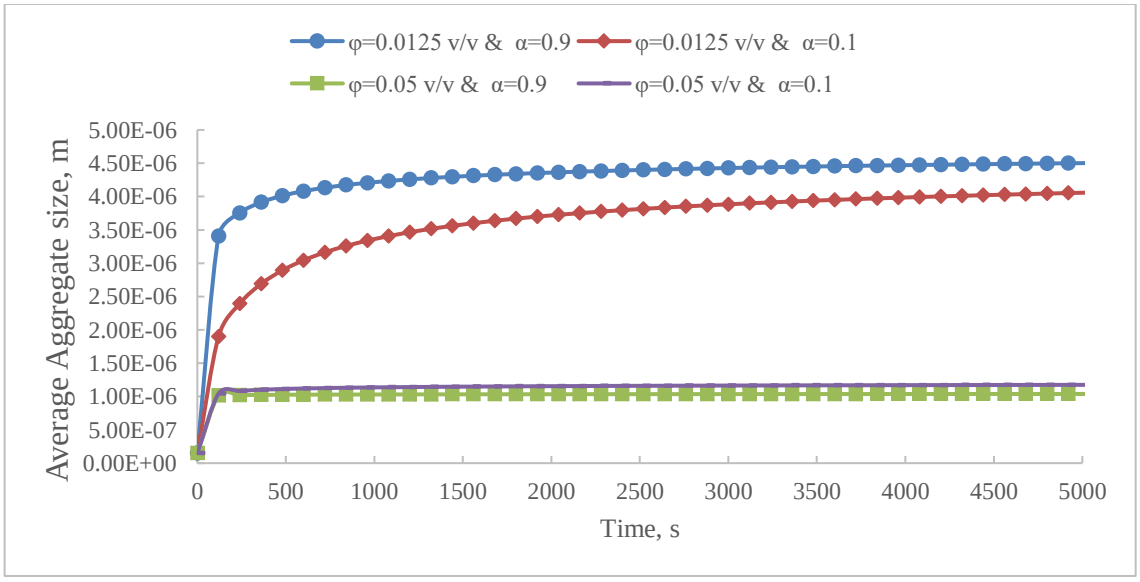

Figure 4-11—Aggregate size evolution with time for colloidal silica suspension with $D_f = 3$ at different initial concentration

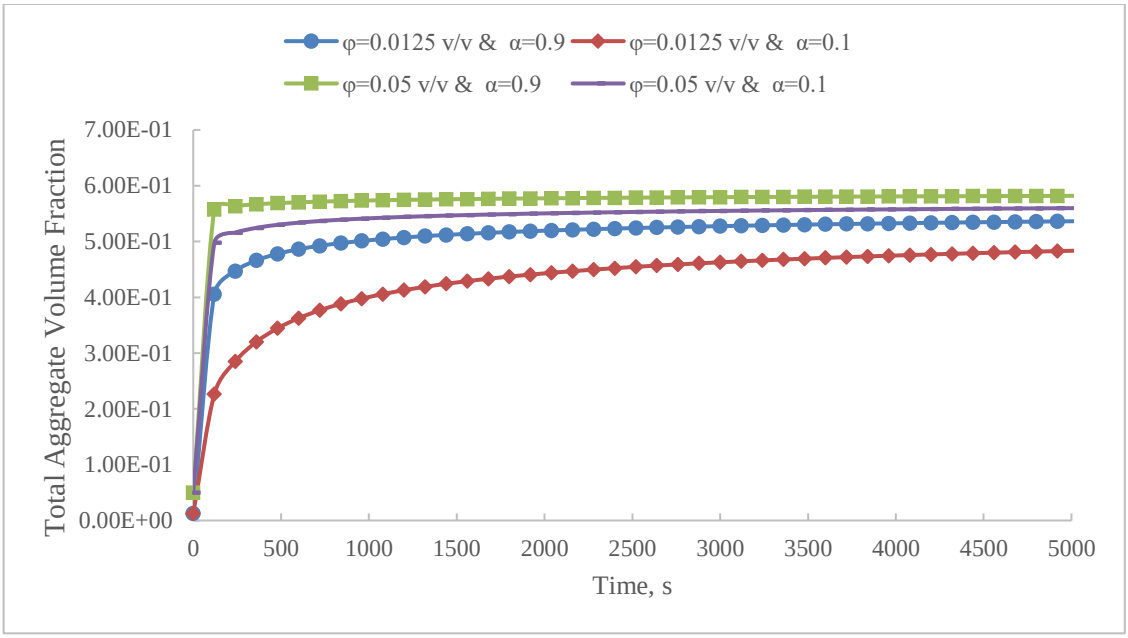

Figure 4-12—Aggregate volume fraction evolution with time for colloidal silica suspension with $D_f = 3$ at different initial concentration

4.8. Conclusion

This study shows that the population balance equation and the quadrature method of moments along with the effective medium theory can be used to model the aggregation and insitu at different conditions of salinity and concentration. The model developed in this study is used to compare between the kinetics of aggregation and gelation of fumed silica and colloidal silica nanoparticles at the same conditions. The case studies presented show that unique behavior of fumed silica over colloidal silica nanoparticles for forming a gel network a significantly low concentration. This is basically due to the fractal structure of the fumed silica nanoparticles that has higher effective volume than the spherical particles of colloidal silica of the same size. The model also shows that there is a critical concentration of salt and nanoparticles above which the viscosity increase and the gel network can be formed.

The model developed in this study can be coupled with a transport model to simulate nanoparticles transport aggregation and sin-situ gelation in porous media.

Acknowledgement

This work is supported by the Abu Dhabi National Oil Company (ADNOC) [grant number 880005].

Nomenclature

A_H	Hamaker constant
$a(L,\lambda)$	fragment distribution function for the diameter-based PBE
$a(v,u)$	fragment distribution function for the volume-based PBE
$b(L)$	diameter based breakage kernel
$b(u)$	volume-based breakage kernel
c	adjustable parameter in the breakage kernel model
$B_a(L;t)$	birth term due to aggregation in the diameter-based PBE
$B_b(L;t)$	birth term due to breakage in the diameter-based PBE
$B_a(v;t)$	birth term due to aggregation in the volume-based PBE
$B_a(v;t)$	birth term due to aggregation in the volume-based PBE
$D_a(L;t)$	death term due to aggregation in the diameter -based PBE
$D_b(L;t)$	death term due to breakage in the diameter -based PBE
$D_a(v;t)$	death term due to aggregation in the volume-based PBE
$D_b(v;t)$	death term due to breakage in the volume-based PBE
D_f	fractal dimension of the aggregates
e	Electronic charge

$f(\kappa \boldsymbol{L_i})$	Henry's function
G	Shear rate
k_B	Boltzmann constant
h	Separation distance between particles
L_i	nodes in the Gaussian quadrature approximation
L_0	Initial size of the nanoparticles
m_k	the kth order moment
N_q	number of quadrature that represent the number of size classes of the aggregates
$n(L;t)$	diameter-based number density function
$n(v;t)$	volume-based number density function
pH	pH of the solution
pH_{IEP}	isoelectric point of the nanoparticles
s_1, s_2	slopes for the zeta potential function of pH and temperature
T	temperature of the dispersion
T_0	initial temperature of the dispersion
W	stability ratio
$\alpha(L,\lambda)$	collision efficiency of particles of diameter $L\ and\ \lambda$
$\beta(L,\lambda)$	collision frequency of particles of diameter $L\ and\ \lambda$
ω_i	weight (also the characteristic number density) corresponding to L_i
$\chi(\sigma)$	hydrodynamic effect
ϕ_T	total electrostatic interaction between particles at separation distance h
ϕ_{vdw}	Van der Waals interactions

ϕ_{EDL}	Electric double layer repulsion
ϕ_{HYD}	Hydration force
σ	function of separation distance and particle size
ζ	zeta potential
κ	Debye length
z_i	valence number of the ion
v_ζ	Constant for temperature effect on zeta potential
ε_0	vacuum permittivity
ε_p	dielectric constant of the particles
ε_c	dielectric constant of the continuous phase
h_P	Planck constant
v_e	characteristic adsorption frequency
n_p	refractive index of the particles
n_c	refractive index of the continuous phase
c_{i0}	bulk concentration of ion species i
N_A	Avogadro number
C_h	hydration constant
ℓ	decay length of the hydration force
μ	viscosity of aggregating dispersions
μ_0	Initial viscosity of the continuous phase
$[\mu]$	intrinsic viscosity
φ	particles/aggregates volume fraction

φ_m	maximum packing fraction
k_0	Crowding factor
k_2	second virial coefficient
k_0^0	Crowding factor at low shear rate
k_0^∞	Crowding factor at high shear rate
Pe	Peclet number of the aggregates
$R_{H,i}$	Hydrodynamic radius of the aggregates

Chapter 5 Modeling Coupled Transport, Aggregation and In Situ Gelation of Nanoparticles in Porous Media

Abstract

Applications of Nanotechnology are growing significantly in the petroleum industry such as oil recovery, and well stimulation. In aqueous media, fumed silica nanoparticles aggregate if there is sufficient attractive energy between nanoparticles. Aggregate size distribution evolves as aggregation continues, and once it spans the space, it forms a gel. The objective of this study is to study evolution of nanoparticle size distribution during transport in porous media, including the aggregation, deposition, straining and initiation of gelation.

Population Balance equation (PBE) was used to model the growth of aggregates and the interaction between aggregates and porous media. Quadrature method of moments (QMOM) was used to convert the PBE with continuous distribution of nanoparticle size into moment transport equations for efficient computation. The closure problem for moment transport equation was resolved using Gaussian Quadrature that requires estimation of roots orthogonal polynomials. Wheeler algorithm was used for calculation of the coefficients of the recursive formula of the orthogonal polynomials. Finite volume method was used for discretization of mass transport equations, continuity equation and Darcy law.

Changes in nanoparticle size and shape due to inter–particle interactions (i.e., aggregation) can significantly affect particle mobility and retention in porous media. To date, however, few modeling studies have considered the coupling of transport and particle aggregation processes. Model sensitivity analysis explained the influence of

particle concentration, and interstitial velocity gradient on particle–particle, and, consequently, particle–collector interactions. Model simulations demonstrate that, when environmental conditions can promote inter–particle interactions, neglecting aggregation effects can lead to over-estimation of nanoparticle mobility. Results also suggest that the extent to which higher order inter–particle collisions influence aggregation kinetics will increase with the volume fraction of primary particles. The model shows that when nanoparticles dispersions are injected into free media like large pores or fractures that the effect of filtration is negligible, the gelation can be achieved but after longer time compared to the batch experiments. However, when including the effect of filtration, the viscosity of the does not increase due to exclusion of larger aggregates once they are formed. This prevents the growth of the gel network.

The model developed in this work accurately captures aggregation and initiation of gelation of silica in porous media. This work demonstrates the potential importance of time-dependent aggregation processes on nanoparticle mobility and provides a numerical model capable of capturing/describing these interactions in water-saturated porous media. This modeling study attempts to answer the critical questions pertaining the coupling of aggregation and in situ gelation on the nanoparticles transport in porous media.

Keywords:

Fumed Silica Nanoparticles; Population balance equation; Quadrature method of moments; In Situ Gelation; Aggregation; Deposition, Straining; Porous Media

5.1.Introduction

Nanotechnology recently gained a wide interest for different applications in oil and gas industry especially for upstream technologies such as hydraulic fracturing, drilling fluids, fines migration, and enhanced oil recovery (Fakoya and Shah 2017, Abdelfatah et al. 2014). There are two main classes of silica nanoparticles that are widely used in dispersions; fumed silica and colloidal silica nanoparticles (Gun'ko et al. 2001, Iler 1979). Transport of silica Nanoparticles in porous media can encounter several mechanisms of interactions either inter-nanoparticle or nanoparticles-porous medium interactions. In our previous papers, we discussed the different mechanisms of nanoparticles-porous medium interactions (Abdelfatah et al. 2017c, Abdelfatah et al. 2017d, Abdelfatah et al. 2017b). Assuming inter-nanoparticle interaction is negligible, there are basically three mechanisms of interaction between nanoparticles and porous media; surface deposition, single particle plugging, multi-particle plugging. The intense of these mechanisms depends on injection rate, nanoparticle concentration, size of nanoparticles and pore throat size.

Aggregation of fumed silica nanoparticles can be explained within the framework of DLVO (Elimelech et al. 2013, Russel et al. 1989). The most important forces that control the kinetics of aggregation and the properties of dispersion are dispersion and electrostatic forces. for Fumed silica dispersion in polar solvents solvation forces due to the hydrogen bonding of the solvent to the surface silanol groups can play a major role (Smith and Zukoski 2006, Raghavan et al. 2000). Theoretically, the kinetics of aggregation depends on the magnitude of energy barrier between nanoparticles. Nanoparticles that overcome the energy barrier will aggregate with another particle in

deep primary energy minimum. Smith and Zukoski (2006) studied the aggregation and gelation of fumed silica nanoparticles dispersed in ethanol. Ethanol is a very polar solvent due to the presence of hydroxyl group. They showed that at low concentration, gelation is arising from aggregation into a primary minimum due to hydrogen bonding and dispersion forces. The gelation is extremely slow due to an energetic barrier ($\sim$ 25kT) in the interparticle potential associated with solvation forces. The solvation forces also contribute to the formation of a secondary minimum in the interparticle potential. The depth of this minimum ($\sim$ 3kT) is sufficient that, at a critical particle concentration, long-range diffusion is arrested due to the short-range attractions and the cooperative nature of particle interactions, as described by mode coupling theory.

In the previous paper, the aggregation and gelation of fumed silica nanoparticles in batch experiments was discussed. Quadrature method of moments was used to solve the population balance equation for the evolution of particles size distribution due to aggregation. The model successfully can trigger the initiation of gelation and the viscosity increase of the dispersion. Particle aggregation has a significant effect on nanoparticle transport in porous media (Kim et al. 2015). The objective of this paper is to couple the QMOM model developed in the previous paper with a fluid flow model to simulate coupled nanoparticles transport, aggregation, and in situ gelation in porous media.

5.2.Mathematical Model

5.2.1. Continuity and Momentum Equation

Pressure gradient in the computational domain is governed by the continuity equation for linear flow under conditions of variable porosity

$$\frac{\partial \phi}{\partial t} + \nabla . U = 0 \tag{1}$$

Once the gelation state is triggered the fluid will be non-Newtonian and shear-thinning. Modified Darcy law would be use with an apparent viscosity.

$$U = -\frac{k}{\mu}\nabla P \tag{2}$$

$$\frac{\partial \phi}{\partial t} - \nabla.\left(\frac{k}{\mu}\nabla P\right) = 0 \tag{3}$$

Where ϕ is the porosity of the porous medium, μ is the apparent viscosity of the dispersion, and ∇P is the pressure gradient, and U is the Darcy velocity.

5.2.2. Salt Transport Equations

In this model, the salt is assumed to work as a catalyst and does not get involved in any reaction. Hence, the convection-dispersion equation is used to model the salt distribution in the computational domain.

$$\frac{\partial \phi C_{salt}}{\partial t} + \nabla.UC_{salt} - \nabla.(\phi D^*_{salt}\nabla C_{salt}) = 0 \tag{4}$$

Where C_{salt} is the concentration of the salt, and D^*_{salt} is the dispersion coefficient of the salt.

5.2.3. Nanoparticles Transport Equations

5.2.3.1. Population Balance Equation

Population balance equation (PBE) is a continuity statement that describes the evolution of a number density function (NDF) of particle volume dispersed in the system (Marchisio and Fox 2013). The particle size distribution (PSD) is a NDF representing the number concentration of particles with volumes between $v\ and\ v + dv$. PSD evolved with time due to particles aggregation. Under shear flow, large aggregate can break into smaller one that may aggregate with other particles again. The volume based PBE

(Vlieghe et al. 2016) can be written as in Eqs. (5)–(11), where $n(v;x,t)$ is the NDF of aggregates of volume v, $B_a(v;x,t)\ and\ D_a(v;x,t)$ are birth and death of aggregates of volume v due to aggregation, $B_b(v;x,t)\ and\ D_b(v;x,t)$ are birth and death of aggregates of volume v due to breakage, $D_d(v;x,t)$ is the death of aggregates of volume v due to deposition on the rock surface, and $D_s(v;x,t)$ is the death of aggregates of volume v due to straining at small pore throats.

$$\frac{\partial\left(\phi.n(v;x,t)\right)}{\partial t}+\nabla.\left(U.n(v;x,t)\right)-\nabla.\left(\phi D_{agg}^{*}\nabla.\left(n(v;x,t)\right)\right) \tag{5}$$
$$=\phi[B_a(v;x,t)-D_a(v;x,t)+B_b(v;x,t)-D_b(v;x,t)$$
$$-D_d(v;x,t)-D_s(v;x,t)]$$

$$B_a(v;x,t)=\frac{1}{2}\int_0^v \alpha(v-u,u)\beta(v-u,u)n(v-u;x,t)n(u;x,t)du \tag{6}$$

$$D_a(v;x,t)=n(v;x,t)\int_0^\infty \alpha(v,u)\beta(v,u)n(u;x,t)du \tag{7}$$

$$B_b(v;t)=\int_v^\infty a(v,u)b(u)n(u;t)du \tag{8}$$

$$D_b(v;t)=b(v)n(v;t) \tag{9}$$

$$D_d(v;x,t)=\int_0^\infty k_d(v)n(v;x,t)dv \tag{10}$$

$$D_s(v;x,t)=\int_0^\infty k_s(v)n(v;x,t)dv \tag{11}$$

In these equation $\beta(v,u)$ is the collision frequency of particles of volume $v\ and\ u$, $\alpha(v,u)$ is the collision efficiency of particles of volume $v\ and\ u$, $b(v)$ is the breakage

kernel that represents the break frequency of aggregates of volume v, $a(v,u)$ is the fragment distribution function that represent the number density function of aggregates of volume v produced by breakage of aggregates of volume u, $k_d(v)$ is the deposition kernel of aggregates of volume v, and $k_s(v)$ is the straining kernel of aggregates of volume v. D_{agg}^{*} is the dispersion coefficient of the aggregates.

To involve the fractal dimension into the PBE, Vlieghe et al. (2016) proposed the following relationship between volume based NDF ($n(v;t)$) and length based NDF ($n(L;t)$).

$$\frac{v}{v_o} = \left(\frac{L}{L_o}\right)^{D_f} \tag{12}$$

$$n(v;x,t) = \frac{n(L;x,t)}{\Phi D_f L^{D_f-1}} \tag{13}$$

$$\Phi = \Phi_o {L_o}^{3-D_f} \tag{14}$$

$$\Phi_o = \frac{\pi}{6} \tag{15}$$

where D_f is the fractal dimension of the aggregates, L is the length of aggregates and L_o is the initial length of the particles assumed that the aggregates composed of identical particles.

Applying Eq. (13) into Eqs. (5)–(11), the diameter-based PBE can be derived as the following as a function of aggregate sizes ($L\ and\ \lambda$)

$$\frac{\partial(\phi.n(L;x,t))}{\partial t} + \nabla.\left(U.n(L;x,t)\right) - \nabla.\left(\phi D_{agg}^{*}\nabla.\left(n(L;x,t)\right)\right) \tag{16}$$

$$= \phi[B_a(L;x,t) - D_a(L;x,t) + B_b(L;x,t) - D_b(L;x,t)$$

$$- D_d(L;x,t) - D_s(L;x,t)]$$

$$B_a(L;x,t) = \frac{L^{D_f-1}}{2}\int_0^L \alpha\left(\left(L^{D_f} - \lambda^{D_f}\right)^{\frac{1}{D_f}},\lambda\right).\beta\left(\left(L^{D_f} - \lambda^{D_f}\right)^{\frac{1}{D_f}},\lambda\right).n\left(\left(L^{D_f}\right.\right. \tag{17}$$

$$\left.\left. - \lambda^{D_f}\right)^{\frac{1}{D_f}};x,t\right).n(\lambda;x,t).\left(\left(L^{D_f} - \lambda^{D_f}\right)^{\frac{1}{D_f}-1}\right)d\lambda$$

$$D_a(L;x,t) = n(L;x,t)\int_0^\infty \alpha(L,\lambda)\beta(L,\lambda)n(\lambda;x,t)d\lambda \tag{18}$$

$$B_b(L;t) = \int_\lambda^\infty a(L,\lambda)b(\lambda)n(\lambda;t)d\lambda \tag{19}$$

$$D_b(L;t) = b(L)n(L;t) \tag{20}$$

$$\beta(v,u) = \frac{\beta(L,\lambda)}{\Phi D_f L^{D_f-1}} \tag{21}$$

$$D_d(L;x,t) = k_d(L)n(L;x,t) \tag{22}$$

$$D_s(L;x,t) = k_s(L)n(L;x,t) \tag{23}$$

5.2.3.2. Moment Transformation

Moment transform (McGraw 1997, McGraw and Saunders 1984, Hulburt and Katz 1964) can be applied to Eq. (9) using the following definition:

$$m_k = \int_0^\infty L^k n(L;t)dL \tag{24}$$

in which m_k is the kth order moment and the size class L varies from zero to infinity in the transformation. McGraw (1997) proposed applying Gaussian quadrature approximation to replace the integration terms by a set of weight and abscissas of the NDF.

$$m_k = \int_0^\infty L^k n(L;t)dL = \sum_{i=1}^{N_q} \omega_i L_i^k = \Omega \times (\Gamma^k)^T \left(k = 0,1,\dots,2N_q - 1\right) \tag{25}$$

$\Gamma = [L_1, L_2, .., L_{Nq}]$ is a vector with each component representing a node in the Gaussian quadrature approximation. $\Omega = [\omega_1, \omega_2, .., \omega_{Nq}]$ is also a vector in which each component is the weight (also the characteristic number density) corresponding to L_i. The superscript T stands for the transpose of a vector. N_q is the number of quadrature that represents the number of size classes of the aggregates.

Using this transformation, Eq. (25) can only allow to track three or four size classes that would be sufficient to track the lower order moments. To reasonably produce the PSD curve higher order moments are required. However, tracking higher order moments could produce ill-conditioned problem due to the higher difference between L_1 and L_{Nq} with larger k, i.e., $(L_1)^1 \ll (L_k)^k$(Gautschi 1968). This would produce unreliable results i.e. negative weights and/or size that do not have physical meaning. To relax the severity of ill-condition by reducing the difference between $(L_1)^1 and (L_k)^k$, Su et al. (2007) added an adjustable factor, p, in QMOM and re-defined the adjustable moments as

$$m_{k/p} = \int_0^\infty L^{k/p} n(L;t)dL = \sum_{i=1}^{N_q} \omega_i L_i^{k/p} = \Omega \times (\Gamma^{k/p})^T \left(k = 0,1,\dots,2N_q - 1\right) \tag{26}$$

In case of $p = 1$, this could be reduced back to the conventual QMOM. Applying the transformation in Eq. (26), the PBE in Eq. (16) is transformed into a set of moment equations ($k = 0,1,..,M$) that are a system of non-linear integro-differential equations (Eq. (27)). Applying the quadrature approach transform the integrals into simple summations (Eq. (28)).

$$\frac{\partial(\phi m_{k/p})}{\partial t} + \nabla.\left(U.m_{k/p}\right) - \nabla.\left(\phi D_{agg}^{*} \nabla.m_{k/p}\right) \tag{27}$$

$$= \phi\left[\frac{1}{2}\int_0^\infty n(\lambda;t)\int_0^\infty \alpha(L,\lambda).\beta(L,\lambda)\left(L^{D_f}\right.\right.$$

$$\left.+\lambda^{D_f}\right)^{\frac{\frac{k}{p}}{D_f}}.n(L;t)dLd\lambda$$

$$-\int_0^\infty L^{\frac{k}{p}} n(L;t)\int_0^\infty \alpha(L,\lambda).\beta(L,\lambda)n(\lambda;t)d\lambda dL$$

$$+\int_0^\infty L^{\frac{k}{p}}\int_0^\infty a(L,\lambda)b(\lambda)n(\lambda;t)d\lambda dL - \int_0^\infty L^{\frac{k}{p}} b(L)n(L;t)dL$$

$$\left.-\int_0^\infty L^{k/p}\, k_d(L).n(L;t)\mathrm{dL} - \int_0^\infty L^{k/p}\, k_s(L).n(L;t)\mathrm{dL}\right]$$

$$\frac{\partial(\phi m_{k/p})}{\partial t} + \nabla.\left(U.m_{k/p}\right) - \nabla.\left(\phi D_{agg}^{*}\nabla.m_{k/p}\right) \tag{28}$$

$$= \phi\left[\frac{1}{2}\sum_{i=1}^{N_q}\omega_i\sum_{j=1}^{N_q}\alpha\left(L_i,L_j\right)\beta\left(L_i,L_j\right)\omega_j\left({L_i}^{D_f}+{L_j}^{D_f}\right)^{\frac{k}{pD_f}}\right.$$

$$-\sum_{i=1}^{N_q}\omega_i L_i^{k/p}\sum_{j=1}^{N_q}\alpha\left(L_i,L_j\right)\beta\left(L_i,L_j\right)\omega_j$$

$$-\sum_{i=1}^{N_q}\bar{a}\left(L_i,L_j\right)^{\frac{k}{p}}b(L_i)\omega_i-\sum_{i=1}^{N_q}L_i^{k/p}b(L_i)\omega_i$$

$$\left.-\sum_{i=1}^{N_q}L^{k/p}k_d(L_i)\omega_i-\sum_{i=1}^{N_q}L^{k/p}k_s(L_i)\omega_i\right]$$

$$\bar{a}\left(L_i,L_j\right)^{(k/p)} = \int_0^{\infty} L^{k/p}\,a\left(L_i,L_j\right)\mathrm{dL} \tag{29}$$

Additionally, PSD can be estimated from moments is inverse problem. PSD, which is number density function can be estimated by using the following relationship (McGraw 1997):

$$n(L;t) \approx \sum_{i=1}^{N_q}\omega_i(t)\delta[L-L_i(t)] \tag{30}$$

where δ is the Dirac delta function which means at any time t, δ is zero except at $L = L_i(t)$.

5.2.3.3. PBE Kernels

Collision frequency:

Collision frequency represents the two number of collisions between two particles of given sizes L and λ. There are several expressions for collision frequency in the literature. Basically, collisions result from Brownian diffusion, differential sedimentation or shear flow. However, when particle size is submicron Brownian diffusion is the dominant mechanism of collision (Elimelech et al. 2013, Thomas et al. 1999). With aggregation and increase of effective size of aggregates shear flow becomes more significant. For submicron particles, differential sedimentation can be neglected.

$$Perkinetic: \beta_{agg}(L_i, L_j) = \frac{2}{3}\frac{k_B T}{\mu}\frac{(L_i + L_j)^2}{L_i L_j} \tag{31}$$

$$Orthokinetic: \beta_{agg}(L_i, L_j) = \frac{G}{6}(L_i + L_j)^3 \tag{32}$$

Collision efficiency:

The effect of energy barrier on perikinetic aggregation is to reduce the rate of aggregation due to electrostatic repulsion. Stability ratio (W), the reciprocal of the collision efficiency is simply the ratio of the aggregation rate in the absence of energy barrier to that with energy barrier. The stability ratio and collision efficiency can be calculated using the following

$$W = 2\int_0^\infty \chi(\theta)\frac{\exp\left(\frac{\phi_T}{k_B T}\right)}{(\zeta + 2)^2}d\theta \tag{33}$$

$$\alpha_{agg}(L_i, L_j) = 1/W \tag{34}$$

Where ϕ_T is the total electrostatic interaction between particles at separation distance h, and θ is a function of h and particle size.

$$\theta = \frac{2h}{L_i + L_j} \tag{35}$$

$\chi(\theta)$ is the hydrodynamic effect. As the particles approach close, it becomes increasingly difficult for liquid between them to drain out the gap and this tends to slow the aggregation process.

$$\chi(\theta) = \frac{6\theta^2 + 13\theta + 2}{6\sigma^2 + 4\theta} \tag{36}$$

When two particles encounter each other, hydrodynamic interactions induce trajectory modifications. However, the hydrodynamic interaction depends on the aggregates structure (porosity) and sizes. Selomulya et al. (2003) proposed a collision efficiency model that accounts for aggregates structure (porosity) and the sizes.

$$\alpha_{agg}(L_i, L_j) = \alpha_{max}.\frac{\exp\left(-x\left(1 - \frac{n_i}{n_j}\right)^2\right)}{(n_i.n_j)^y} \tag{37}$$

$$n_i = \left(\frac{\min(L, \lambda)}{L_0}\right)^{D_f};\ n_j = \left(\frac{\max(L, \lambda)}{L_0}\right)^{D_f}$$

Where $\alpha_{max} = 1/W$ from Eq. 33 and 34.

The total electrostatic interaction (ϕ_T) is the summation of electric double layer repulsion, van der Walls attraction, and in case of silica nanoparticles solvation force can be added to accurately predict the interaction energy. Zeta potential is the main factor that controls the electrostatic interaction (Abdelfatah et al. 2017b).

$$\zeta = \begin{cases} m_1 \dfrac{0.85 k_B T}{f(\kappa a_p) e} (pH_{IEP} - pH)\left[1 + v_\zeta (T - T_0)\right] \\ \zeta_{cut-off} + \dfrac{m_2}{f(\kappa a_p)} \left(pH_{cut-off} - pH\right)\left[1 + v_\zeta (T - T_0)\right] \end{cases} \quad (38)$$

Ohshima (1994) presented a simple approximate expression for Henry's function which is applicable for any value of κa_p.

$$f(\kappa L_i) = 1 + \frac{1}{2[1 + \frac{2.5}{\kappa L_i (1 + e^{-\kappa L_i})}]} \quad (39)$$

Van der Waals interactions (Berg 2010)

$$\Phi_{vdw} = -\frac{A_H}{6}\left[\frac{2L_iL_j}{h^2 + 2L_ih} + \frac{2L_iL_j}{h^2 + 2L_ih + 2L_jh + 4L_iL_j} + \ln\left(\frac{h^2 + 2L_ih + 2L_jh}{h^2 + 2L_ih + 2L_jh + 4L_iL_j}\right)\right] \quad (40)$$

Where A_H is the Hamaker constant(Russel et al. 1989)

$$A_H = \frac{3}{4} k_B T \left(\frac{\varepsilon_p - \varepsilon_c}{\varepsilon_p + \varepsilon_c}\right)^2 + \frac{3 h_P v_e}{16\sqrt{2}} \frac{\left(n_p^2 - n_c^2\right)^2}{\left(n_p^2 + n_c^2\right)^{3/2}} \quad (41)$$

k_B is the Boltzmann constant, T is the temperature, ε is the dielectric constant, n is the refractive index, the subscripts $p\ and\ c$ correspond to the properties of the particle and continuous phase, respectively, h_P is the Planck constant, and v_e is the characteristic adsorption frequency. Electric double layer repulsion using linearized Poisson-Boltzmann equation(Hogg et al. 1966).

(42)

$$\Phi_{EDL} = \frac{\varepsilon_0 L_i L_j (\zeta_i{}^2 + \zeta_j{}^2)}{4(L_i + L_j)} \left[\frac{2\zeta_i \zeta_j}{(\zeta_i{}^2 + \zeta_j{}^2)} \ln\left(\frac{1 + exp(-\kappa h)}{1 - exp(-\kappa h)}\right) + \ln(1 - \exp(-2\kappa h)\right]$$

Debye length

$$\kappa = \left(\frac{e^2 \sum_i z_i^2 c_{i0}}{\varepsilon_c \varepsilon_0 k_B T} \right)^{1/2} \tag{43}$$

Where ε_0 is the vacuum permittivity, z is the valence number of the ion, e is the charge of an electron, $\zeta_i and\, \zeta_j$ are the zeta potentials of aggregates of size $L_i\, and\, L_j$, respectively. κ^{-1} is the Debye length, and c_{i0} is the bulk concentration of ion species i.

Hydration repulsion originates from the overlap of structured layer of water molecules at the surfaces of hydrophilic nanoparticles (Pashley and Israelachvili 1984). Hydration force can be expressed by (P. Binks and O. Lumsdon 1999, Chapel 1994)

$$\Phi_{HYD} = \pi L_i N_A C_h c_{i0} \ell^2 \exp(-h\ell) \tag{44}$$

Where C_h is hydration constant, ℓ is the decay length.

Breakup frequency:

The breakup frequency including the fractal dimension can expressed by Eq. 41 (Vlieghe et al. 2016)

$$b(L_i) = cG^{5/2} \left(\frac{L_i}{L_0}\right)^{3-2D_f/3} \tag{45}$$

Where G is the shear rate, *c* is a fitting parameter.

Fragment distribution:

Uniform fragmentation distribution is used in this work, meaning that all possibilities are equally probable (Vlieghe et al. 2016).

$$a(L_i, L_j) = \frac{2D_f {L_i}^{D_f-1}}{{L_j}^{D_f}}, \quad L_i < L_j \tag{46}$$

and the integrated adjustable daughter distribution function can be written as

$$\bar{a}(L_i, L_j)^{(k/p)} = {L_i}^{k/p} \frac{2D_f}{k/p + D_f}, \quad L_i < L_j \tag{47}$$

Deposition and Straining Frequencies:

However, the pore size distribution can be used to model the interaction between particles aggregate and porous media, this would be highly computation demanded (Abdelfatah et al. 2017d, Abdelfatah et al. 2017c). In this paper, two pore model developed by Todd (1990) is adopted to divide the pores into two categories; straining bores and deposition pores.

$$k_d(L_i) = \alpha_d(L_i)\beta_d(L_i)U \tag{48}$$

$$k_s(L_i) = \alpha_s(L_i)\beta_s(L_i)U \tag{49}$$

$$\sigma(L; x, t) = \sigma_d(L; x, t) + \sigma_s(L; x, t) \tag{50}$$

$$\frac{\partial \sigma_d}{\partial t} = D_d(L; x, t) \tag{51}$$

$$\frac{\partial \sigma_s}{\partial t} = D_s(L; x, t) \tag{52}$$

Deposition frequency using sphere-in-cell model

$$\beta_d(L_i) = \beta_d^{diff}(L_i) + \beta_d^{intr}(L_i) \tag{53}$$

$$\beta_d^{diff}(L_i) = 4.04 \left[\frac{2(1-q^5)}{\varpi}\right]^{1/3} {N_{Pe}}^{-2/3} \tag{54}$$

$$\beta_d^{intr}(L_i) = 1.5q^2 \left[\frac{2(1-q^5)}{\varpi}\right] {N_r}^2 \tag{55}$$

Geometry parameters (56)

$$q = (1 - \phi)^{1/3} \tag{57}$$

$$\varpi = 2 - 3q + 3q^5 - 2q^6 \tag{58}$$

$$N_r = \frac{L_i}{d_g} \tag{59}$$

$$N_{Pe} = \frac{12\pi\mu L_i d_g \mathrm{u}}{k_B T} \tag{60}$$

Deposition and Straining Efficiency:

$$\alpha_d = \alpha_{d,0}\left(1 - \frac{\sigma_d}{\sigma_{d,max}}\right) \tag{61}$$

$\alpha_{d,0}$ can be calculated from XDLVO and surface roughness of the rock grain surface (Abdelfatah et al. 2017b) or used as an adjusted parameter. For straining, it's assumed that strainable aggregates are larger than the straining pores. Hence, for any large pore venturing into a small pore throat, the particle aggregates travel no farther than a single pore length. So, the frequency and efficiency of straining are one. This leads to the straining rate; $\Gamma_s = 1/\ell_{p,s}$.

5.2.4. Porosity Evolution

Porosity changes due to the combination effect of dissolution deposition, and straining of nanoparticles/aggregates. The change of permeability and pore size as a function of porosity can be calculated using modified Carmen-Kozeny relationship proposed by Civan (2007)

$$\frac{\partial \phi}{\partial t} = \left(\frac{\partial \phi}{\partial t}\right)_d + \left(\frac{\partial \phi}{\partial t}\right)_s \tag{62}$$

$$\left(\frac{\partial \phi}{\partial t}\right)_d = -\phi \frac{\partial \sigma_d}{\partial t} \tag{63}$$

$$\left(\frac{\partial \phi}{\partial t}\right)_s = -\phi \frac{\partial \sigma_s}{\partial t} \tag{64}$$

$$\frac{k}{k_o} = \left(\frac{\phi}{\phi_o}\right)^{\gamma} \left(\frac{\phi(1-\phi_o)}{\phi_o(1-\phi)}\right)^{2\beta} \tag{65}$$

$$\frac{r_p}{r_o} = \sqrt{\frac{\phi_o k}{\phi\, k_o}} \tag{66}$$

$$\frac{D^*}{D_m} = \alpha_{os} + \lambda_L \frac{2|U| r_p}{\phi D_m} \tag{67}$$

Where, $\left(\frac{\partial \phi}{\partial t}\right)_d$ is the change of porosity dues to deposition, $\left(\frac{\partial \phi}{\partial t}\right)_s$ is the change of porosity due to straining, σ_d is the volume of aggregates deposited per unit bulk volume, σ_s the volume of aggregates strained per unit bulk volume, ϕ and ϕ_o are the instantaneous and initial porosities, respectively, k and k_o are the instantaneous and initial permeabilities, respectively, r_p and r_o are the instantaneous and initial pore radius, D^* is the dispersion coefficient, D_m is the molecular diffusion coefficient, α_{os} is a dispersion constant depends on the pore structure, λ_L is the dispersivity of the porous medium, and γ and β are two constants control the relationship between porosity and permeability.

5.2.4. Viscosity model

Modified effective-medium theory (Takamura and Ven 2010, Lattuada et al. 2016) can be effectively used to model the viscosity evolution of aggregating dispersions and predicts the initiation of gelation.

$$\mu = \mu_0 \left[\frac{1 - \frac{\varphi}{\varphi_m}}{1 - \frac{(C_0 \varphi_m - 1)\varphi}{\varphi_m}} \right]^{\frac{-\varphi_m[\mu]}{2 - C_0 \varphi_m}} \quad (68)$$

Where φ is the particles/aggregates volume fraction and φ_m is the maximum packing fraction. Intrinsic viscosity $[\mu] = 2.5$. For $D_f = 3$, $\varphi = k_V m_3$. Where k_V is the volumetric shape factor. Crowding factor $C_0 = \frac{2C_2}{[\mu]} - [\mu]$. C_0 is a function of shear rate (G), and the exact relationship between C_0 and G is a function of the surface properties of the colloidal particles and the electrolyte concertation. However, in this study C_2 is between $5.2 - 6.2$ from low to high shear rate. Hence $C_0^0 = 3.05$ at low shear rate and $C_0^\infty = 1.7$ at high shear limit. The effect of shear rate can be calculated as the following: $C_0 = C_0^\infty + \frac{C_0^0 - C_0^\infty}{1 + Pe^{0.35}}$. Where $Pe = \frac{3\pi\mu G R_{H,i} R_{H,j} (R_{H,i} + R_{H,j})}{2k_B T}$ and Hydrodynamic radius: $R_{H,i} = \frac{m_3}{m_2}$. Shear rate in porous medium can be calculated using the following equaton (Cannella et al. 1988):

$$G = SF \frac{4|\mathrm{U}|}{\sqrt{8K\phi}} \quad (69)$$

Where shear factor (SF) $SF = \left[\frac{3n+1}{4n}\right]^{\frac{n}{n+1}} \sim 0.8$ and n is the power law exponent.

5.3.Numerical Implementation

The mathematical model presented in section 5.2 is solved using finite volume method on a one-dimensional domain (Versteeg and Malalasekera 2007). Staggered grid method is used to avoid any oscillations in the solution by solving for velocity (Eq. 2) on the cell faces, and pressure (Eq. 3) on the cell center. Advection-dispersion equations (Eqs. 4) is solved for salt distribution within the computation domain. Upwind scheme is used to

discretize the advection term and second orders scheme for the dispersion term. For moment transport equation (Eq. 28), operator splitting is used to solve the transport in one step and the right-hand side representing the source/sink term in a second step. For salt the transport equation, implicit scheme is used. However, using implicit scheme for the moment transport equation produces unrealizable moments (Marchisio and Fox 2013). Hence, explicit scheme with operator splitting is used for solving the moment transport equation.

The major point in solving Multiphysics phenomena is how the different physics are coupled together and the efficiency of the feedback between them (Zhang and Cen 2015). Sequential non-iterative algorithm (SNIA) is used in this study, to couple the Multiphysics and ensure efficient feedback between them. The steps followed in solving the model are as the following:

1. Start the model by reading the initial conditions and the input data.
2. Pressure in calculated by solving Eq. 3 at the center of the gridblocks.
3. Velocity is the calculated at the faces of the gridblocks using Eq. 2.
4. Salt concentration is calculated from Eq. 4.
5. Nanoparticles transport and aggregation is modeled by solving Eq. 28 as the following:

5.1. Knowing the volume fraction of the particles in the injected dispersion and assuming the initial particles has an average size of 150 nm, we can calculate the number of the particles and number density function at the initial conditions. Then use this as a boundary condition for moment transport equation (Eq. 28).

5.2. Transport moments using convection-dispersion terms in Eq. 28.

5.3. Using wheeler algorithm (Wheeler 1974), the weight and abscissas of the transported moments can be calculated at each node in the domain. For more details about wheeler algorithm, readers are referred to Marchisio and Fox (2013).

5.4. Using the weight and abscissas of the initial moments, the source/sink term in Eq. 25 is then calculated at each node in the domain.

5.5. Using source/sink term, the moments can be updated using backward Euler time discretization scheme.

6. Using Eq. 61-66, the new porosity, permeability, and pore size can be updated.
7. Using the updated moments, the new viscosity can be calculated using Eq. 68.
8. Then go to the next time step and repeat the steps 2-7.
9. End the calculation when the total time of simulation is reached.

5.4. Results and Discussion

The mathematical model presented in this paper is used to study the aggregation and gelation of fumed silica nanoparticles during injection into porous media. Several hypothetical cases were run to compare the kinetics of aggregation of fumed silica nanoparticles in porous media with and without including the effect of filtration. Modified effective-medium theory is used for calculation of viscosity evolution with aggregation. Several experimental studies in the literature show that the maximum packing factor (φ_m) for fumed silica is ~0.20-0.3 (Smith and Zukoski 2004, Chen et al. 2005). For fumed silica, the φ_m is very small due to the fractal structures that prevent tight packing of the primary particles. Two different regimes of aggregation are identified; diffusion limited aggregation (DLCA), and reaction limited aggregation (RLCA) (Sefcik et al. 2005). The network structure of DLCA is more open ($D_f = 1.8$) while that for RLCA is more close

and compact ($D_f = 2.2$) (Russel et al. 1989). However, in this study, it's assumed that the fractal dimension $D_f = 3$. The conservation of mass per unit volume can be verified for $k = D_f = 3$ (Vlieghe et al. 2016). In this section, the simulation results for fumed silica and colloidal silica nanoparticles are presented at high electrolyte concentration that the collision efficiency as calculated from Eq. (31) is ~1. The parameters used for the model are as presented in table 5-1.

The model developed in this study can be used for various applications of nanoparticles including aggregation and in situ gelation in porous media and fractures. In previous work, we have validated the model developed for nanoparticles transport in porous media including deposition and straining processes. However, there is no available data in the literature about coupled nanoparticles transport, aggregation, and in situ gelation in porous media. Hence, there is no available experiments data that can be used to for validation of the novel approach presented in this work for coupled nanoparticles transport, aggregation, and in situ gelation in porous media. Therefore, in this section a sensitivity analysis will be presented for few controlling parameters to show the capabilities of the developed model.

Table 5-1—Parameters used for the simulation

Parameter	Value	Unit
k	2	md
ϕ	0.2	-
Core size	3.81x3.81x 10.2	cm
α_{os}	0.005	m
λ_L	0.001	m

μ_0	0.001	Pa.s
D_f	3	-
N_q	3	-
p	1	-
L_o	150	nm
α_{agg}	1	-
c	$2x10^{-10}$	-
α_d	0.5	-
α_s	1	-
β_s	0.1	-

In our previous work, we showed that nanoparticles concentrations and injection rates are parameters that control nanoparticle's transport and filtration in porous media of a given porosity and permeability (Abdelfatah et al. 2017a, Abdelfatah et al. 2017b, Abdelfatah et al. 2017d, Abdelfatah et al. 2017c). For aggregation and gelation in the previous chapter, we also showed that nanoparticles concentration is a key factor that controls the gelation time. Hence, in this section, a sensitivity analysis for injection rate and nanoparticles concentration will presented.

5.4.1. Aggregation and Gelation with no Filtration

First, we studied the effect of injection rate and nanoparticles concentration on aggregation and moment transport in porous media neglecting the effect of filtration on aggregation kinetics. This would be like the case of aggregation and in situ gelation in free media like fractures or injection downhole the wellbore. In this study, we used the

three different concentrations (0.5, 0.8, and 1.25 vol%) used in the previous chapter to show the effect of moment transport and accumulation in porous media on the kinetics of aggregation. Two different injection rates are used; 0.6 and 1.2 ml/min.

Fig. 5-1 shows the viscosity contours at different times and locations along the computational domain for injection rate of 0.6 ml/min and injected concentration of 0.5 vol%. Comparing Fig. 5-1 to Fig. 4-4, we can see that in the batch there in no increase in the viscosity of fumed silica dispersion of 0.5 vol% at aggregation efficiency of 1. However, Fig. 5-1 shows that the gelation initiation can be triggered after ~5 pore volume of injection (PVI). This is clearly due to the accumulation of nanoparticles and aggregates with injection. That the effective volume fraction of the aggregates increases with injection time and hence the viscosity increases. Fig. 5-2 shows the mean aggregates size in porous media is growing with time at different locations in the computation domain unlike the case in the batch (Fig. 4-5). Fig. 5-3 shows the aggregate volume fraction contours. It shows that aggregate volume fraction starts to increase till it reach the maximum packing factor where gelation initiates. Fig. 5-4 shows that increasing the injection rate to 1.2 ml/min for the same nanoparticles concentration of 0.5 vol%, enhances the aggregation kinetics as orthokinetic aggregation increases with increasing the shear rate. The aggregate size is higher for high injection rate (Fig. 5-5) compared to low injection rate (Fig. 5-2) due to enahced aggregation by shear. Fig. 5-6 is comparable to Fig 5-3. However, the maximum packing factor for high injection rate is reached at lower PVI compared to low injection rates.

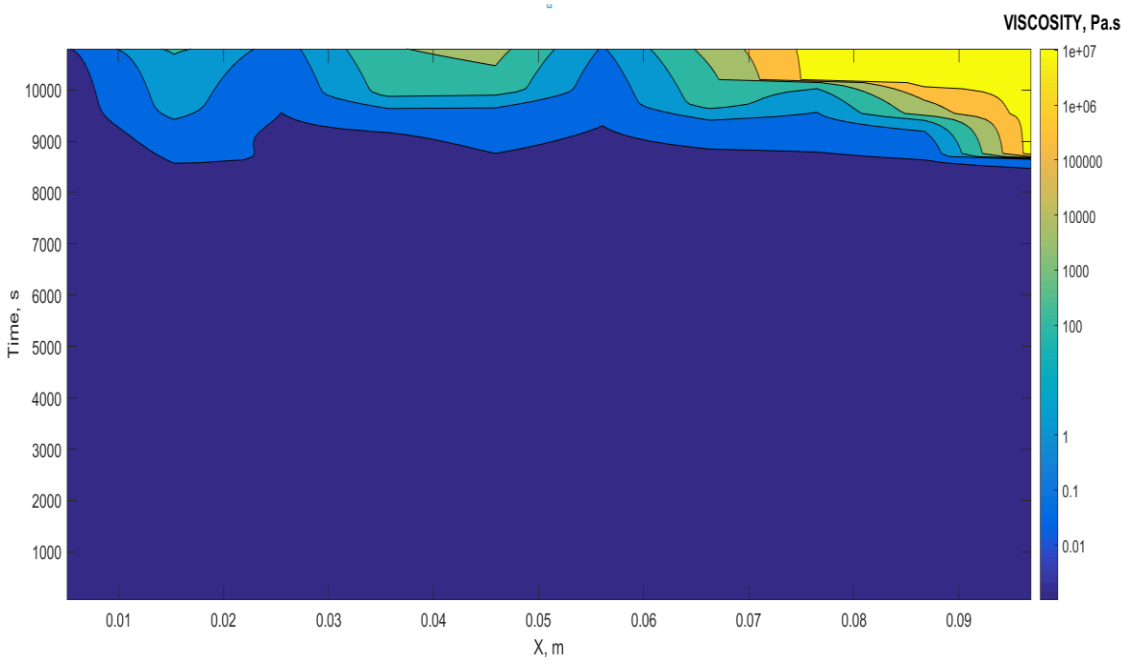

Figure 5-1—Viscosity contours for Injection rate =0.6 ml/min and Injected concentration = 0.5 vol%

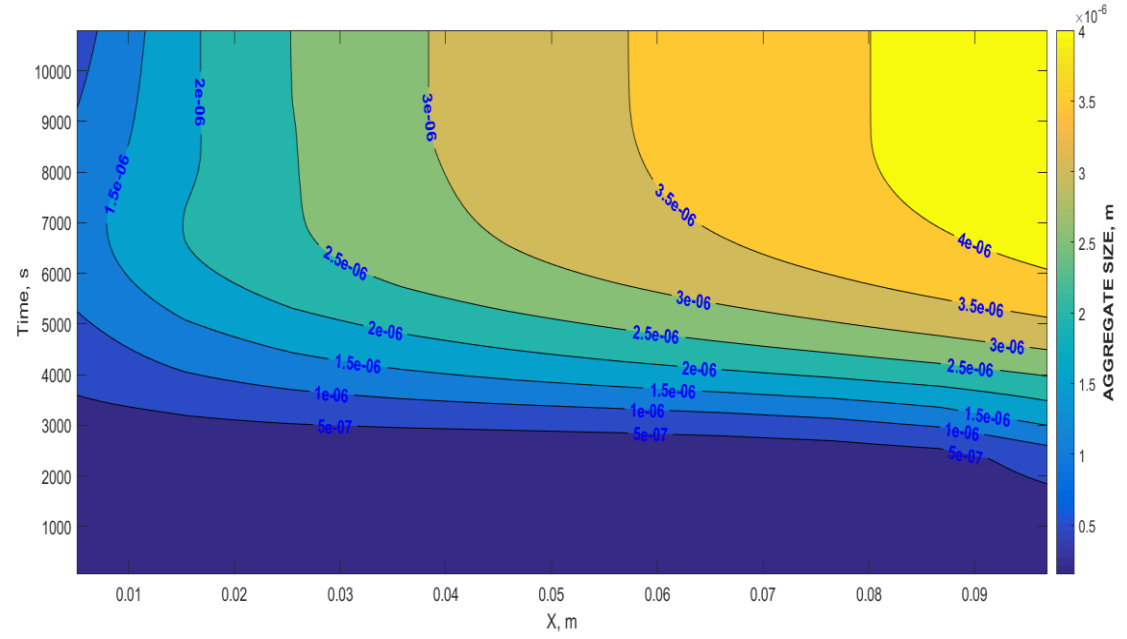

Figure 5-2—Aggregate size contours for Injection rate =0.6 ml/min and Injected concentration = 0.5 vol%.

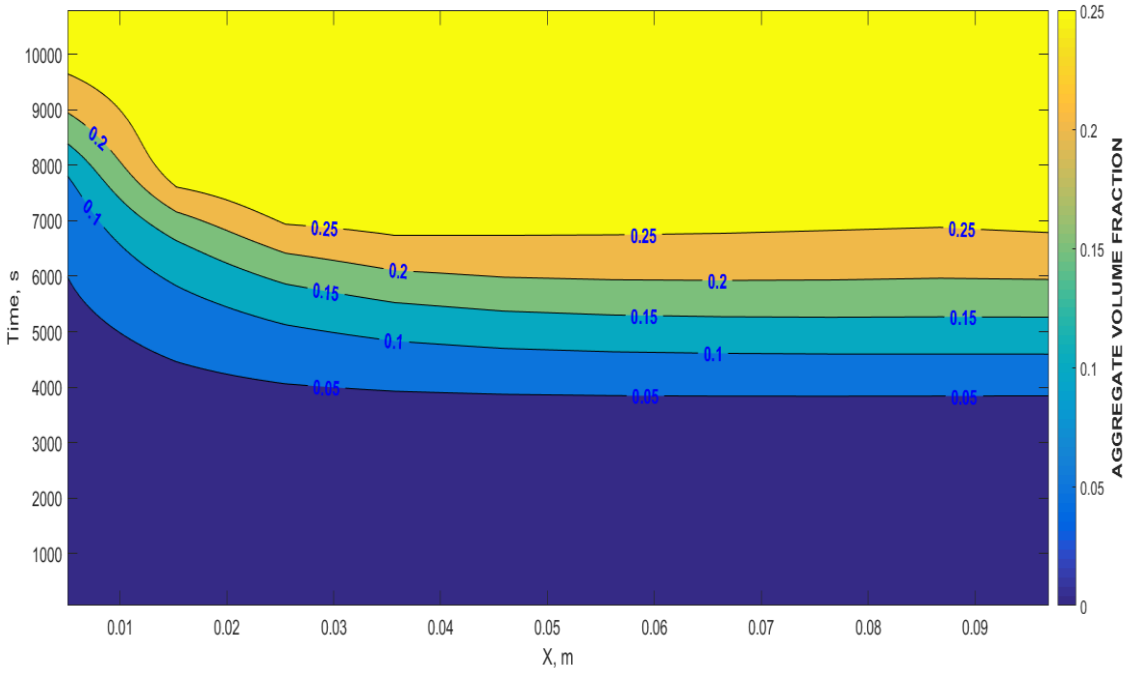

Figure 5-3— Aggregates volume fraction contours for Injection rate =0.6 ml/min and Injected concentration = 0.5 vol%.

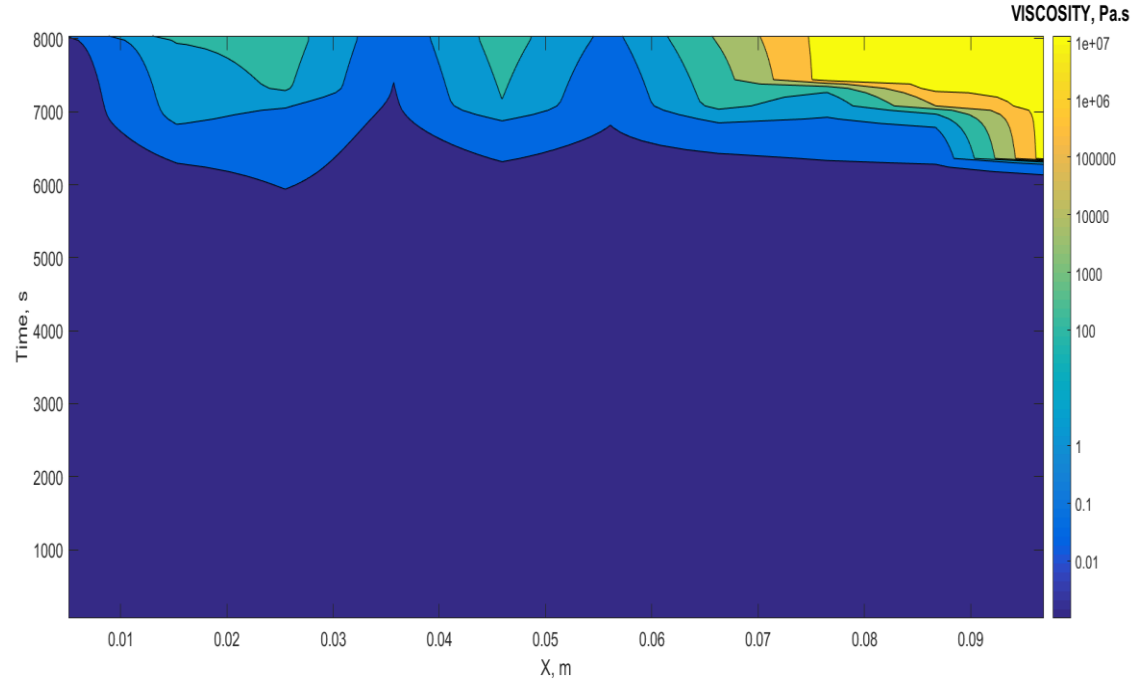

Figure 5-4—Viscosity contours for Injection rate =1.2 ml/min and Injected concentration = 0.5 vol%.

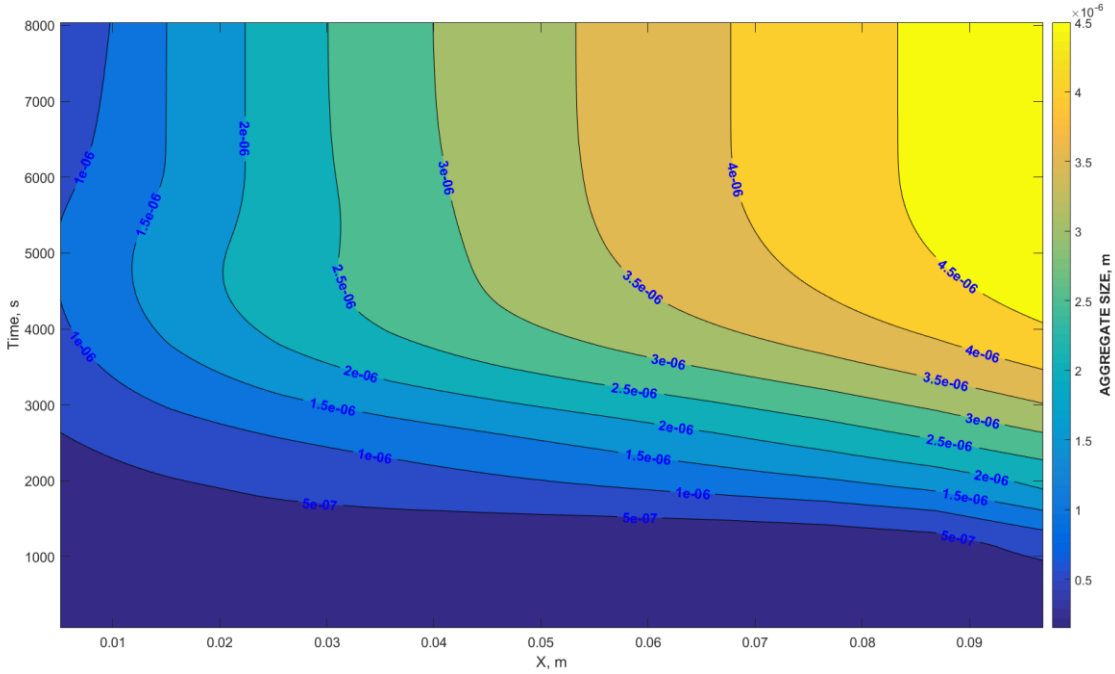

Figure 5-5—Aggregate size contours for Injection rate =1.2 ml/min and Injected concentration = 0.5 vol%.

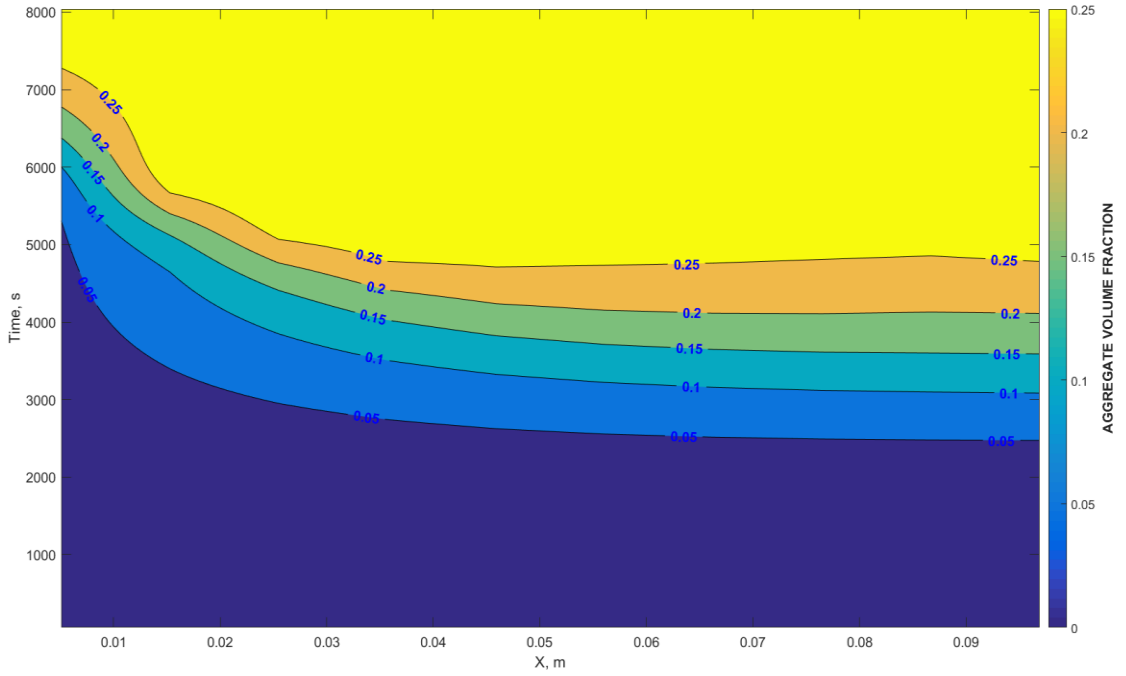

Figure 5-6— Aggregates volume fraction contours for Injection rate =1.2 ml/min and Injected concentration = 0.5 vol%.

Increasing the concentration of injected nanoparticles to 0.8 vol% and keeping all other parameters the same, Fig. 5-7 shows that the high viscosity front is formed earlier than the previous case for 0.5 vol% of nanoparticles. This is consisted with the results presented in the previous chapter (Fig. 4-4) that increasing the concentration would enhance the aggregation and gelation kinetics. However, Fig. 4-4 that shows sharp increase in viscosity after ~ 300 seconds. While Fig 5-7 shows that gelation initiates after ~4 PVI. This is expected because of the effect of moment transport in porous media that would need higher time for the effective volume of aggregates to grow by accumulation at certain node in the computational domain. Comparing Fig. 4-5 and Fig. 5-8, supports this analysis. Fig. 4-5 shows that the aggregates size increases very fast. While Fig. 5-8 shows that aggregates size reaches similar values of Fig. 4-5 after long time of injection and nearly at the exit of the computation domain. Fig. 5-9 shows the aggregate volume fraction contours. Fig. 5-10 shows that increasing the injection rate to 1.2 ml/min for the same nanoparticles concentration of 0.8 vol%, enhances the aggregation kinetics as orthokinetic aggregation increases with increasing the shear rate. This is clear that the aggregate size is much higher for high injection rate (Fig. 5-11) compared to low injection rate (Fig. 5-8). Fig. 5-12 shows the aggregate volume fraction contours.

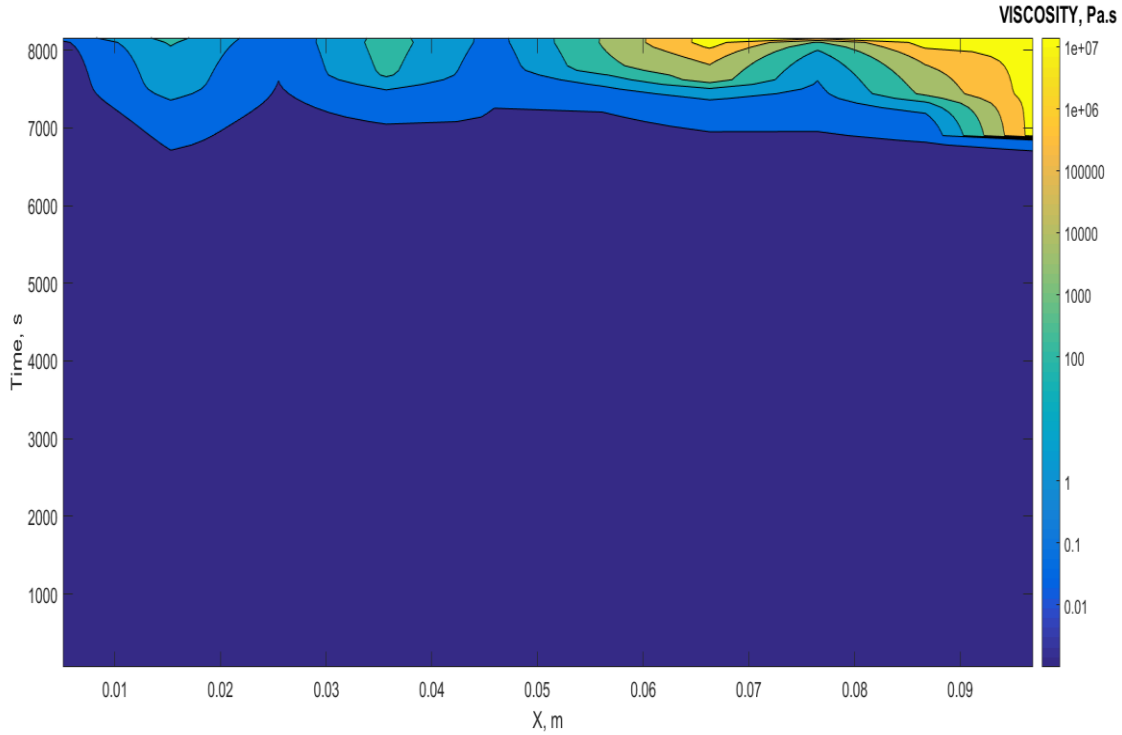

Figure 5-7—Viscosity contours for Injection rate =0.6 ml/min and Injected concentration = 0.8 vol%.

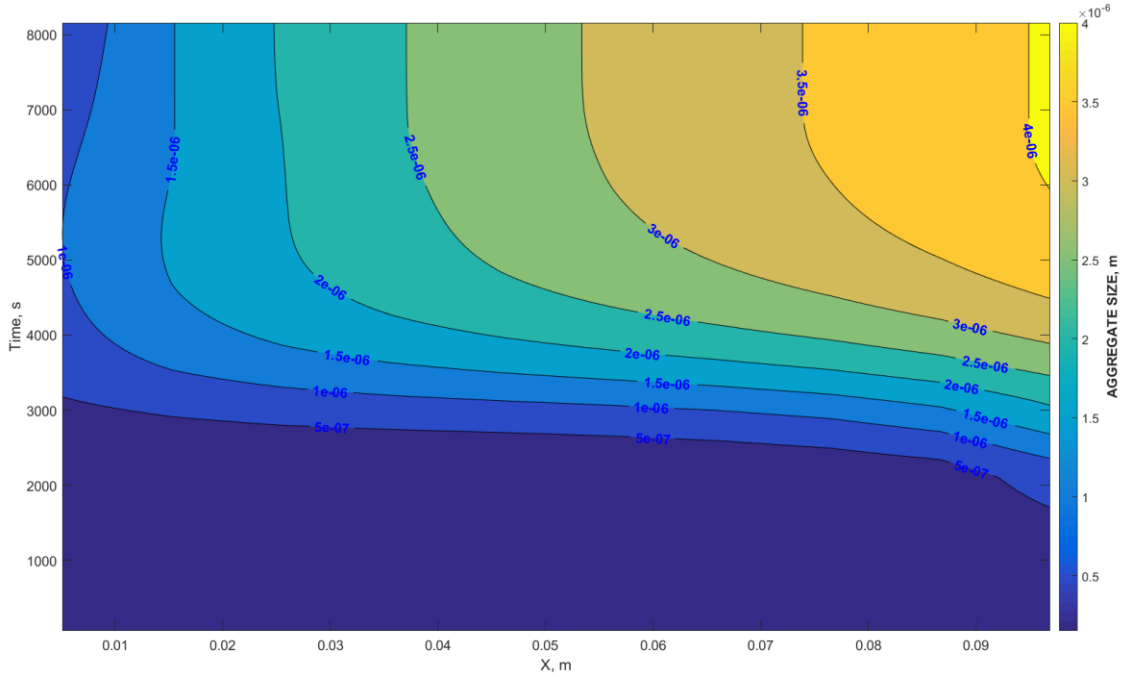

Figure 5-8—Aggregate size contours for Injection rate =0.6 ml/min and Injected concentration = 0.8 vol%.

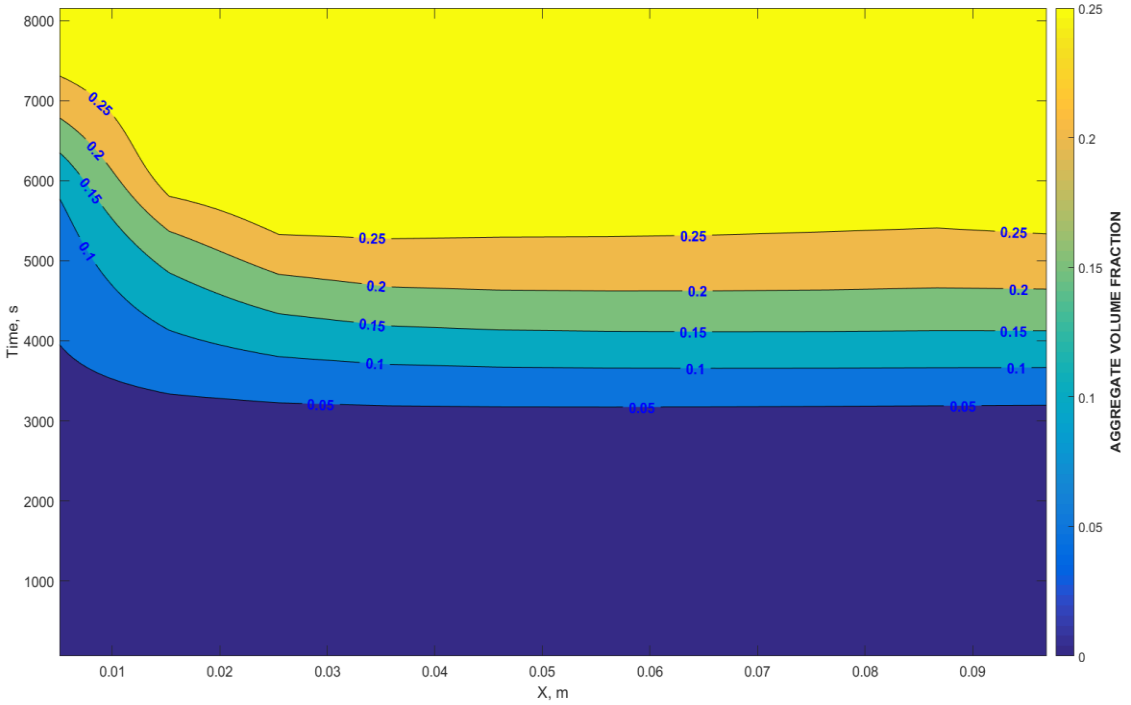

Figure 5-9—Aggregates volume fraction contours for Injection rate =0.6 ml/min and Injected concentration = 0.8 vol%.

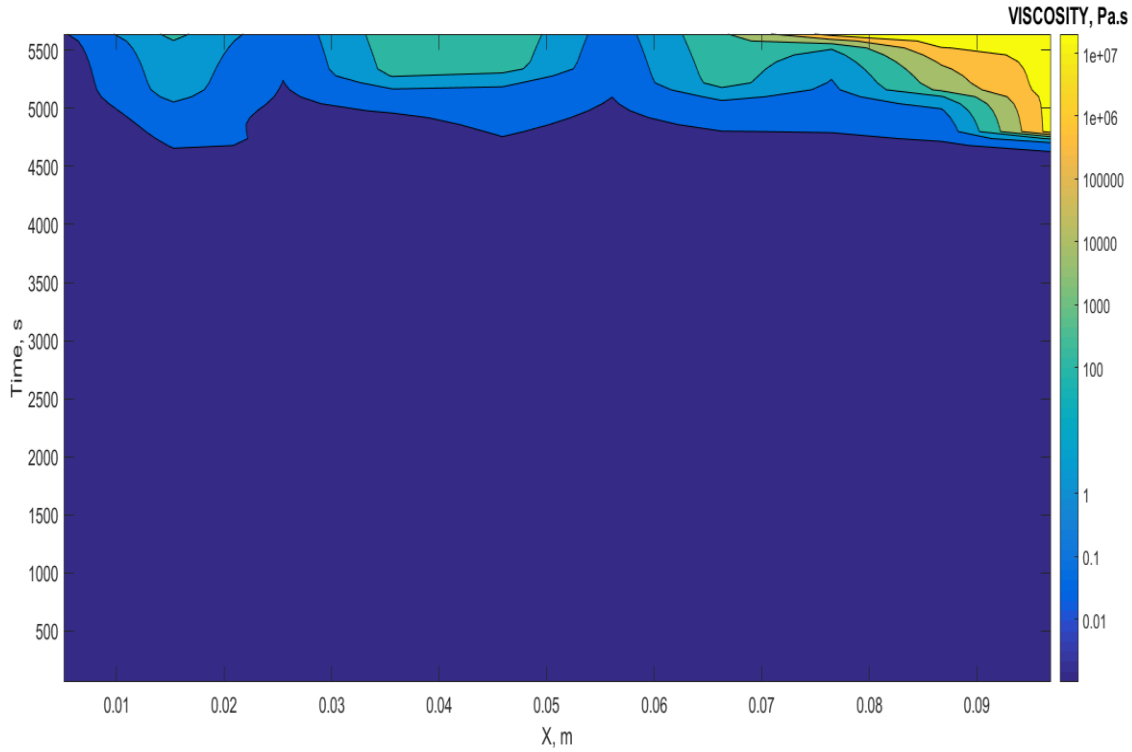

Figure 5-10—Viscosity contours for Injection rate =1.2 ml/min and Injected concentration = 0.8 vol%.

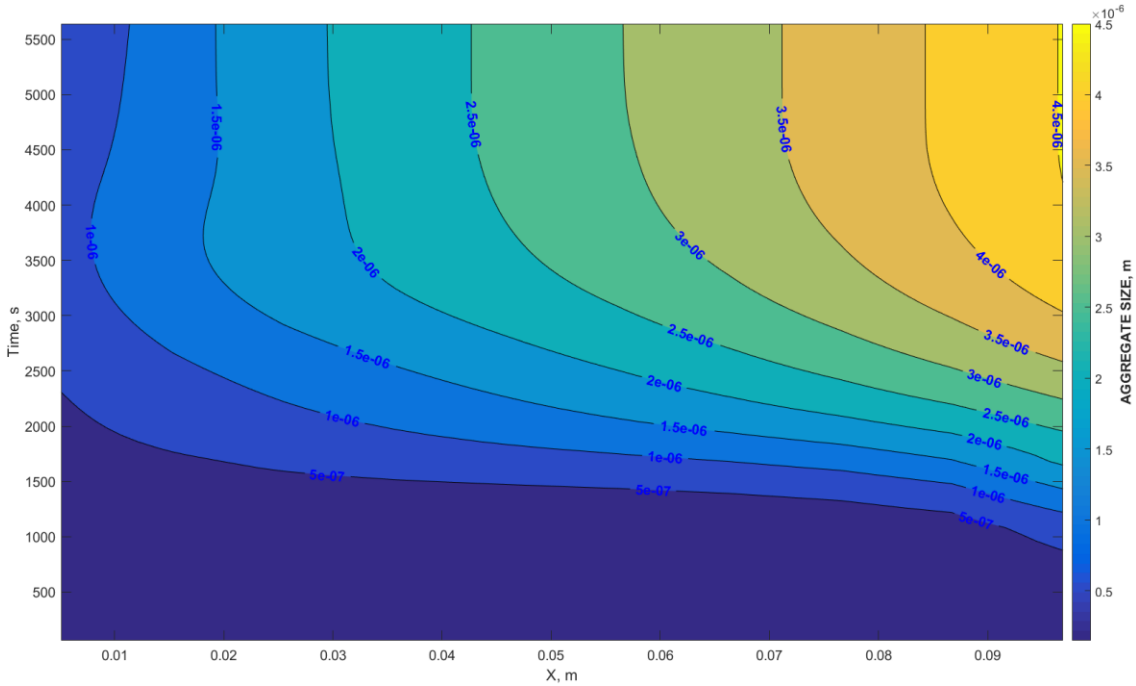

Figure 5-11—Aggregate size contours for Injection rate =1.2 ml/min and Injected concentration = 0.8 vol%.

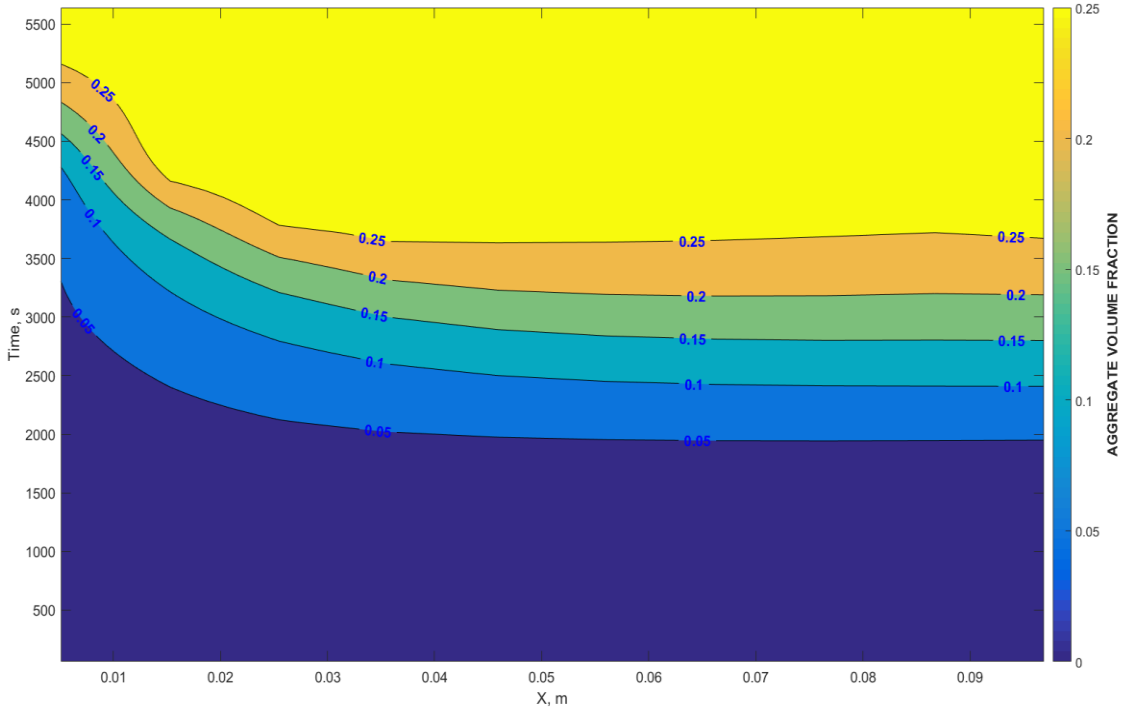

Figure 5-12—Aggregate volume fraction contours for Injection rate =1.2 ml/min and Injected concentration = 0.8 vol%.

Fig. 5-13 shows that increasing the concentration of injected nanoparticles to 1.25 vol% decreases the time required for building up the high viscosity front. However, it's still much higher than this predicted in the batch (Fig. 4-4). This affirms that the effect of moment transport is reducing the aggregation and gelation kinetics even for concentration as high as 1.25 vol%. Fig. 5-14 also shows that the aggregation and breakage is enhanced because of the shear in the porous media compared to batch (Fig. 4-5). Fig. 5-15 shows the aggregate volume fraction contours. Fig. 5-16 shows that increasing the injection rate to 1.2 ml/min for the same nanoparticles concentration of 1.25 vol%, enhances the aggregation kinetics as orthokinetic aggregation increases with increasing the shear rate. This is clear that the aggregate size is much higher for high injection rate (Fig. 5-17)

compared to low injection rate (Fig. 5-14). Fig. 5-18 shows the aggregate volume fraction contours.

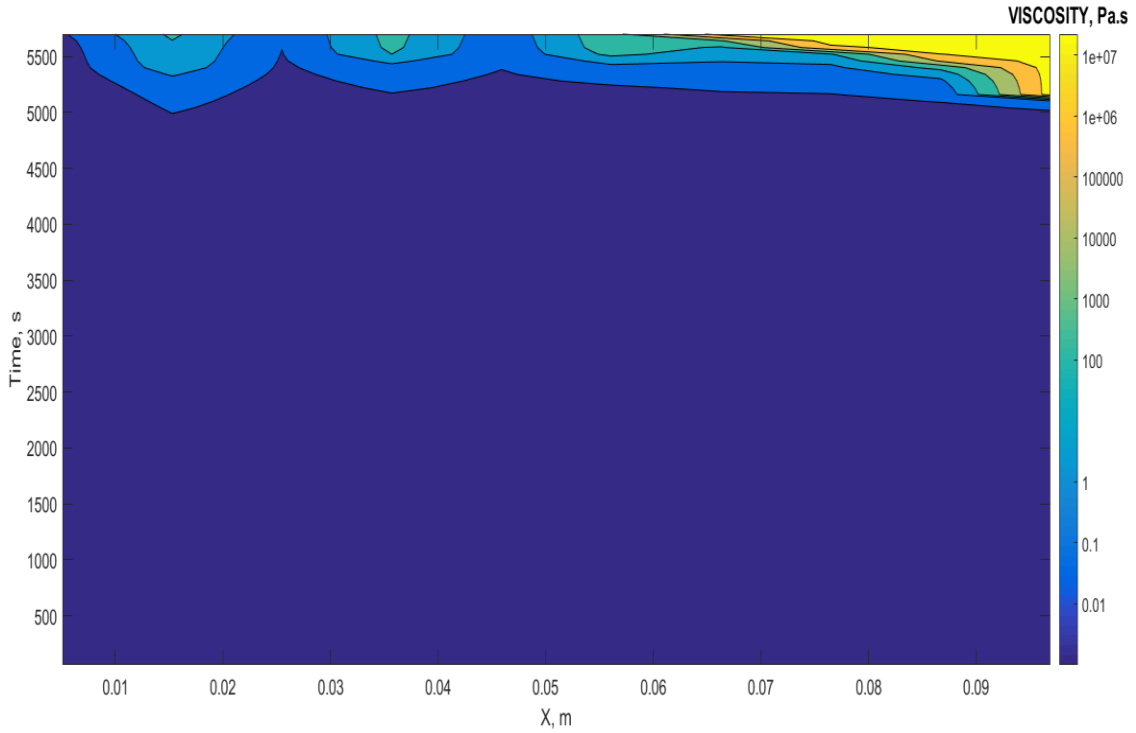

Figure 5-13—Viscosity contours for Injection rate =0.6 ml/min and Injected concentration = 1.25 vol%.

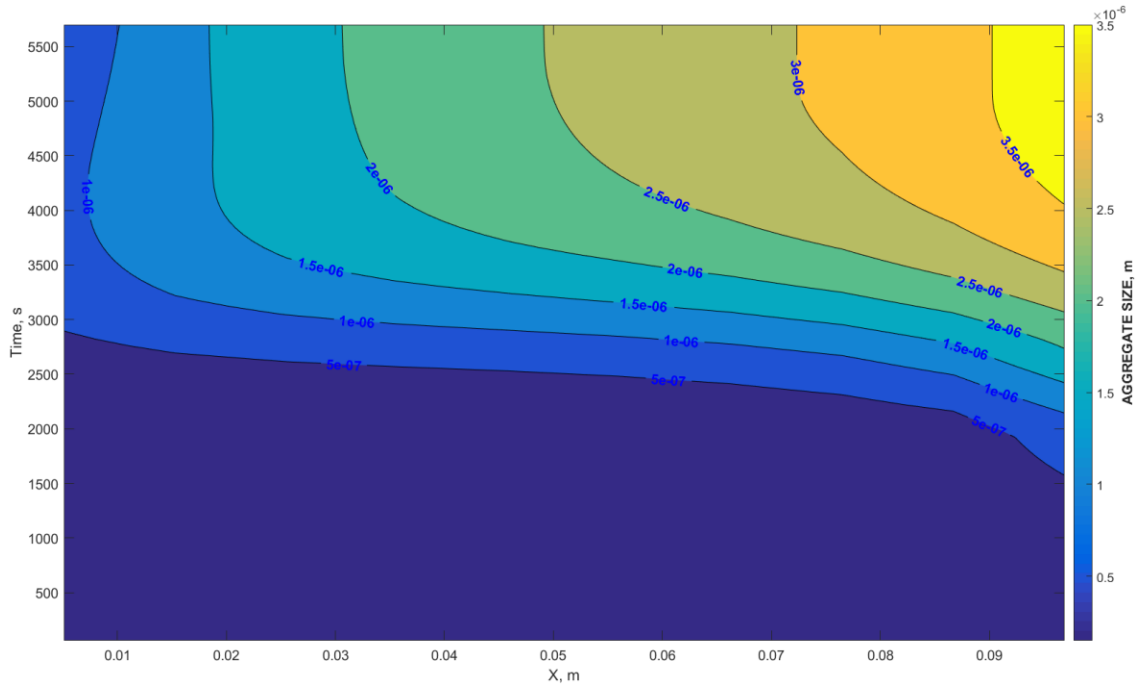

Figure 5-14—Aggregate size contours for Injection rate =0.6 ml/min and Injected concentration = 1.25 vol%.

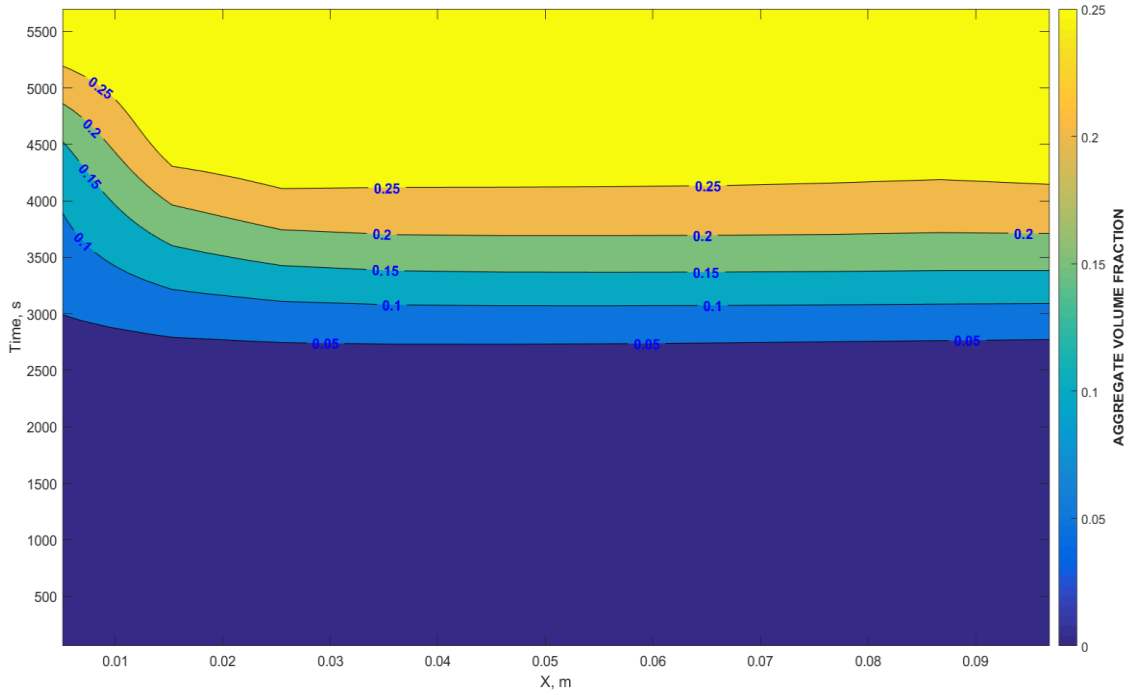

Figure 5-15—Aggregate volume fraction contours for Injection rate =0.6 ml/min and Injected concentration = 1.25 vol%.

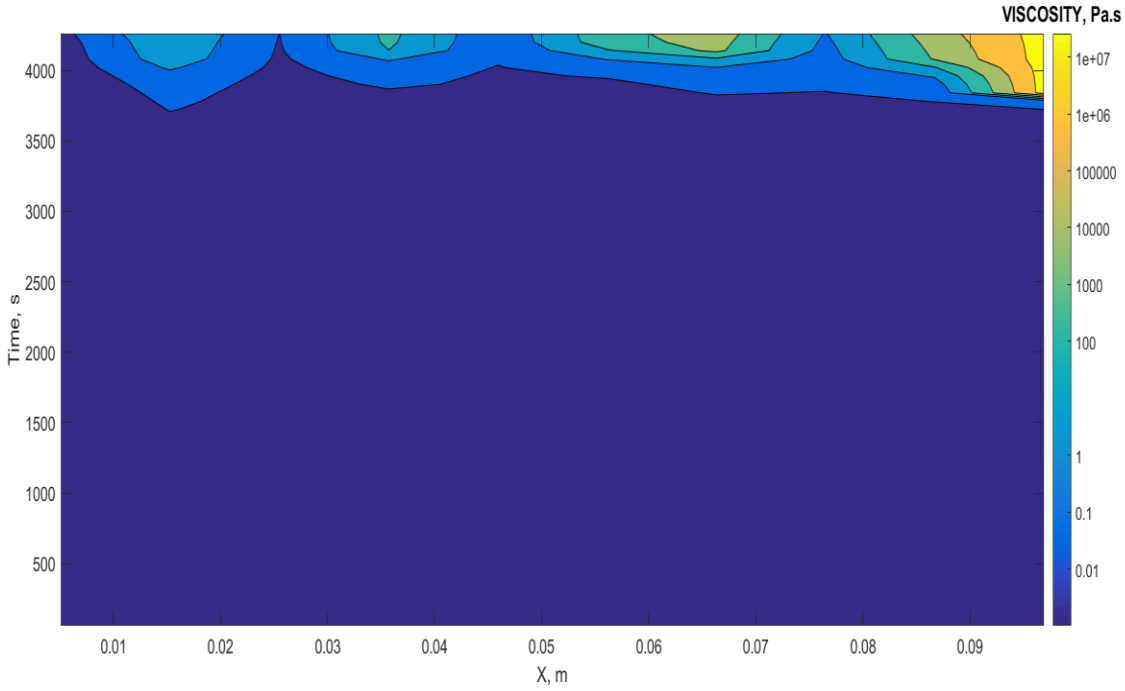

Figure 5-16—Viscosity contours for Injection rate =1.2 ml/min and Injected concentration = 1.25 vol%.

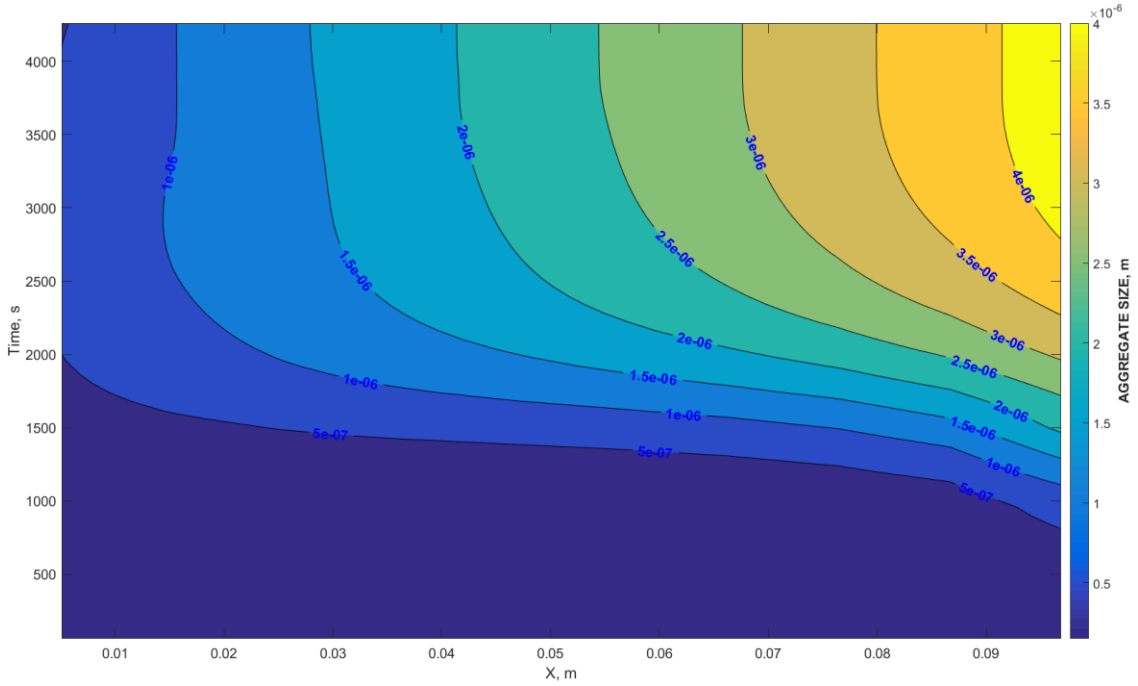

Figure 5-17—Aggregate size contours for Injection rate =1.2 ml/min and Injected concentration = 1.25 vol%.

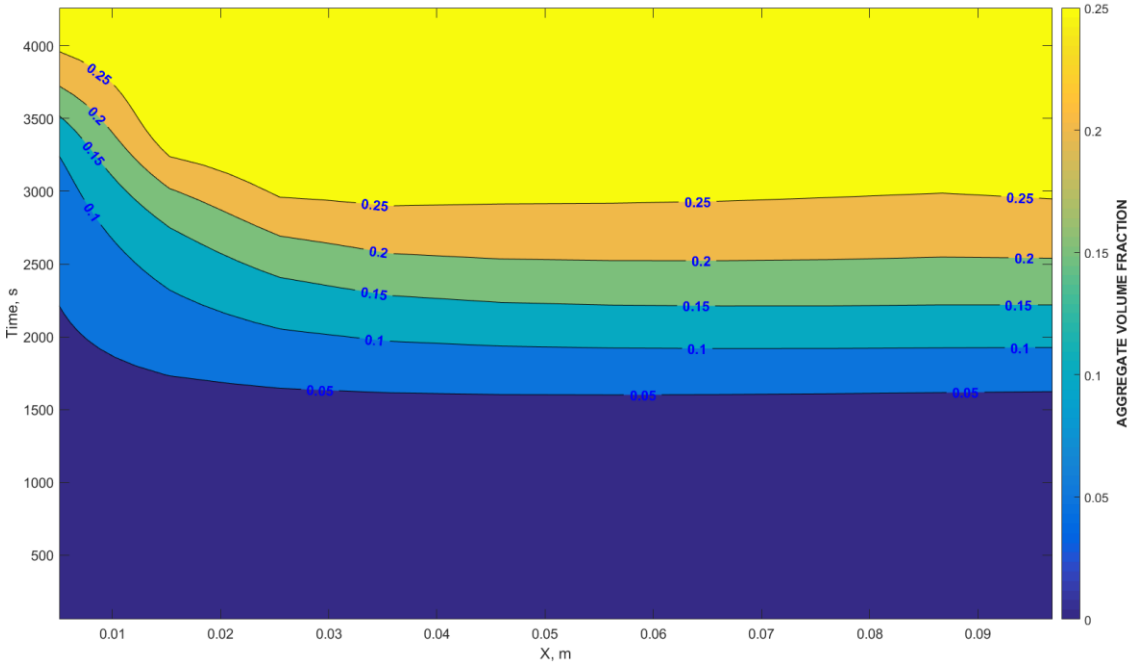

Figure 5-18—Aggregate volume fraction contours for Injection rate =1.2 ml/min and Injected concentration = 1.25 vol%.

5.4.2. Aggregation and Gelation with Filtration

The aggregation kinetics were studied ignoring the effect of filtration basically by deposition and straining of nanoparticles/aggregates in the porous media. Herein, the effect of filtration is included to the cases studied in the previous section.

It's clear that the filtration by deposition and straining excludes the large aggregates immediately. This is clearly indicated in Fig. 5-19 that there is no significant increase in viscosity when filtration is included. Fig. 5-20 also shows the aggregates size does not increase much further beyond the initial particle size. As presented in our previous work (Abdelfatah et al. 2017d), the increase in concentration and/or injection rate make the filtration more severe. Fig. 5-21 through 5-24, clearly shows that increasing the concentration of nanoparticles would not even help to enhance the aggregation kinetics due to dominant effect of filtration in this case.

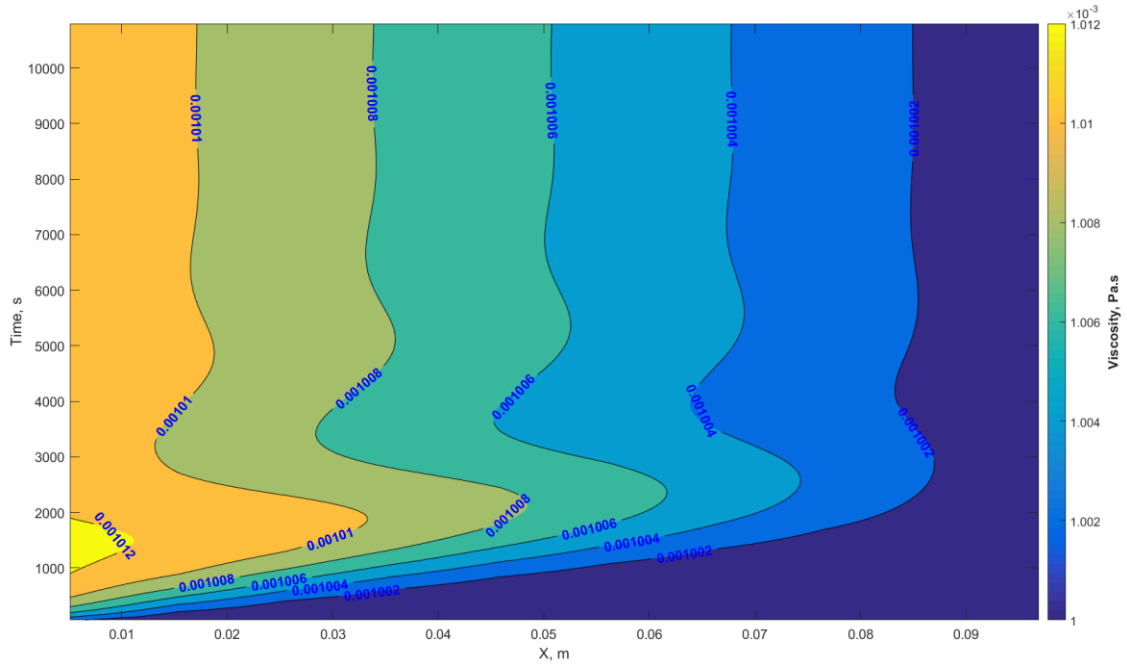

Figure 5-19—Viscosity contours for Injection rate =0.6 ml/min and Injected concentration = 0.5 vol% including filtration effect.

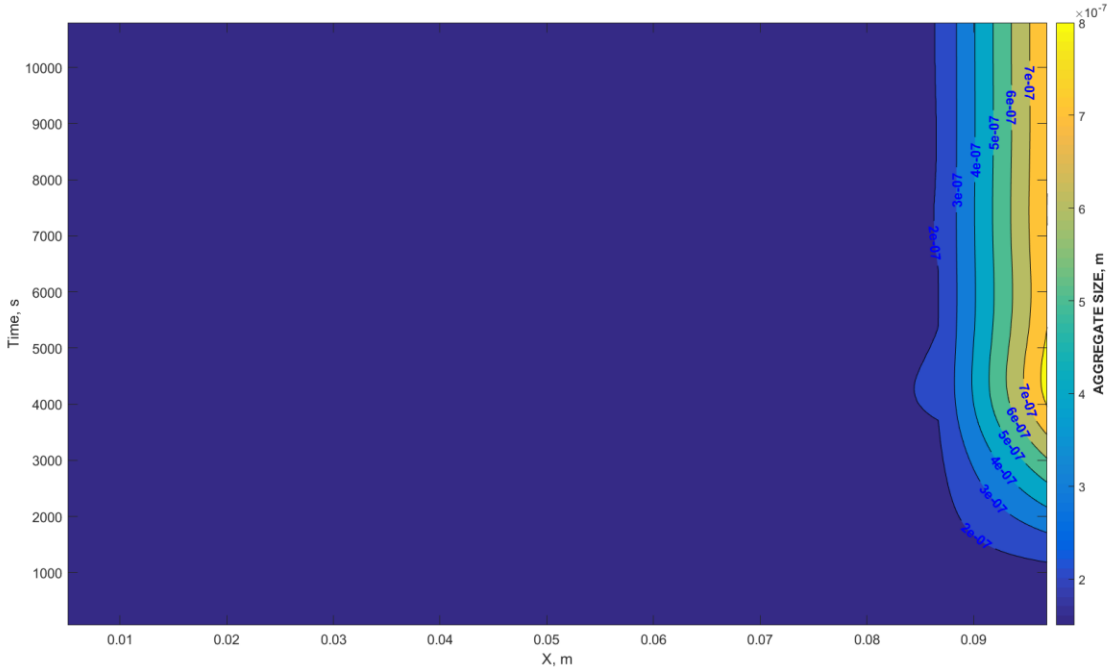

Figure 5-20—Aggregate size contours for Injection rate =0.6 ml/min and Injected concentration = 0.5 vol% including filtration effect.

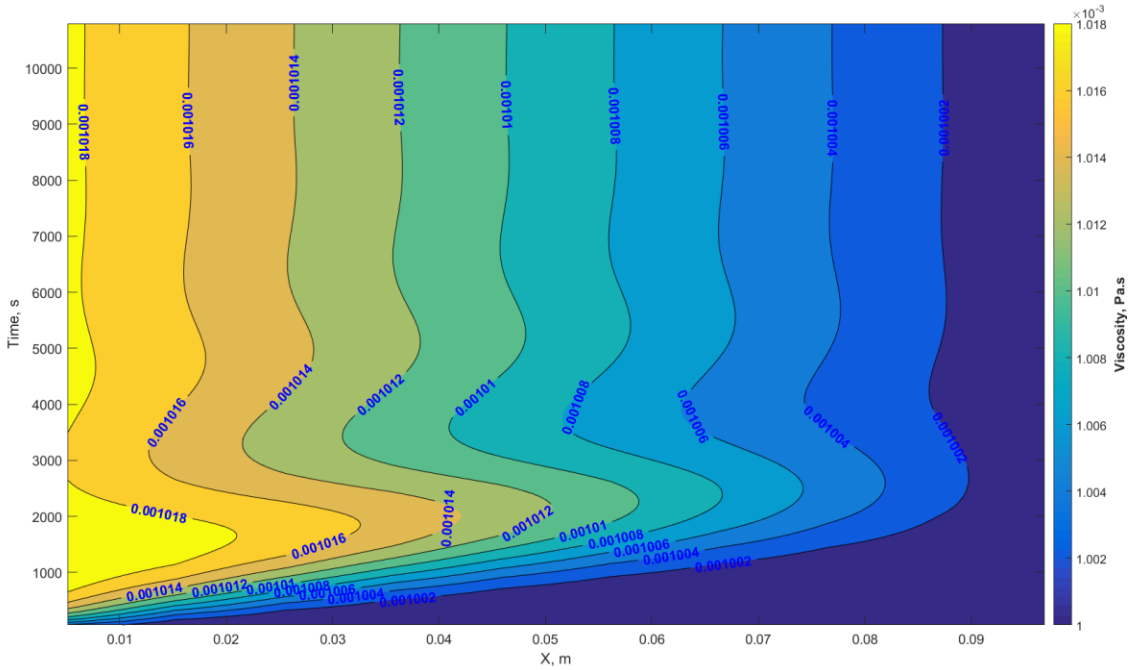

Figure 5-21—Viscosity contours for Injection rate =0.6 ml/min and Injected concentration = 0.8 vol% including filtration effect.

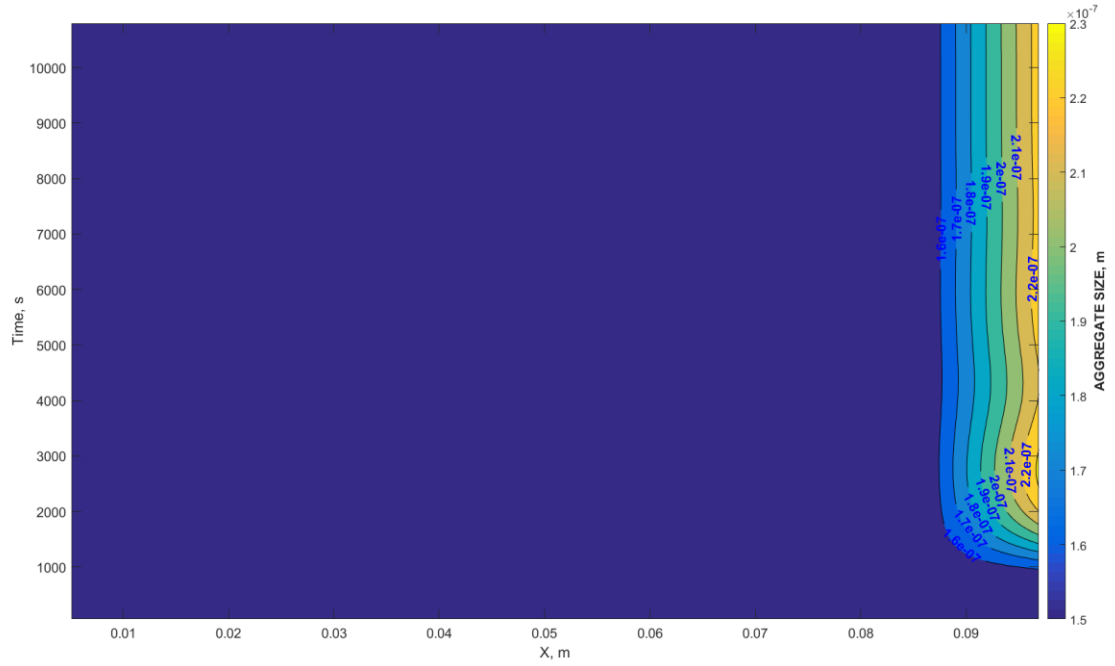

Figure 5-22—Aggregate size contours for Injection rate =0.6 ml/min and Injected concentration = 0.8 vol% including filtration effect.

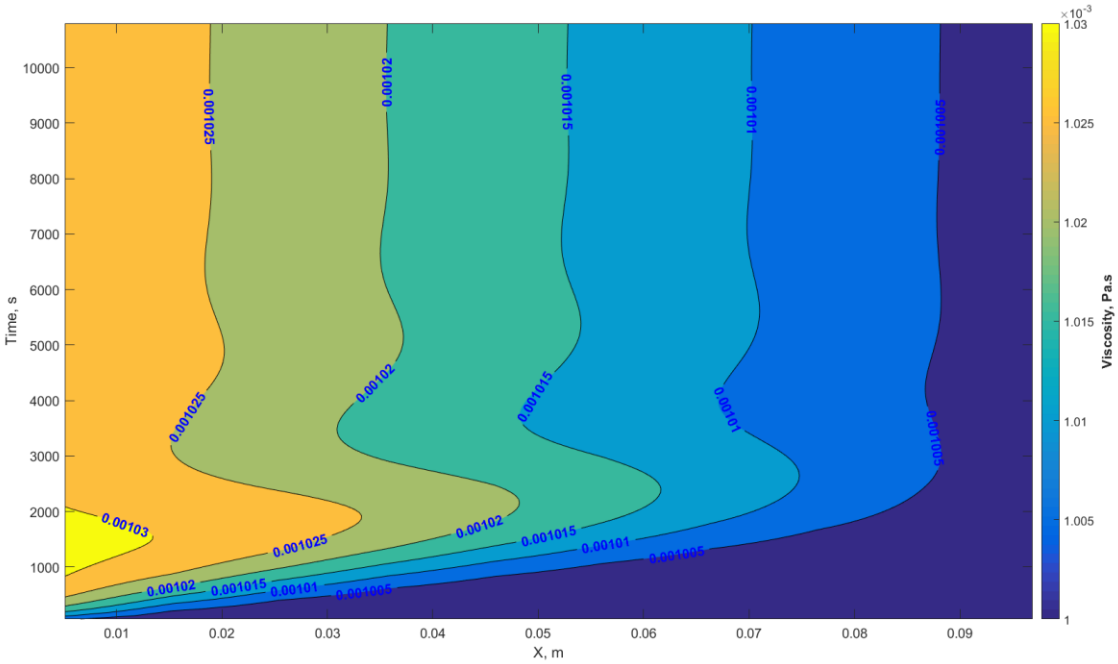

Figure 5-23—Viscosity contours for Injection rate =0.6 ml/min and Injected concentration = 1.25 vol% including filtration effect.

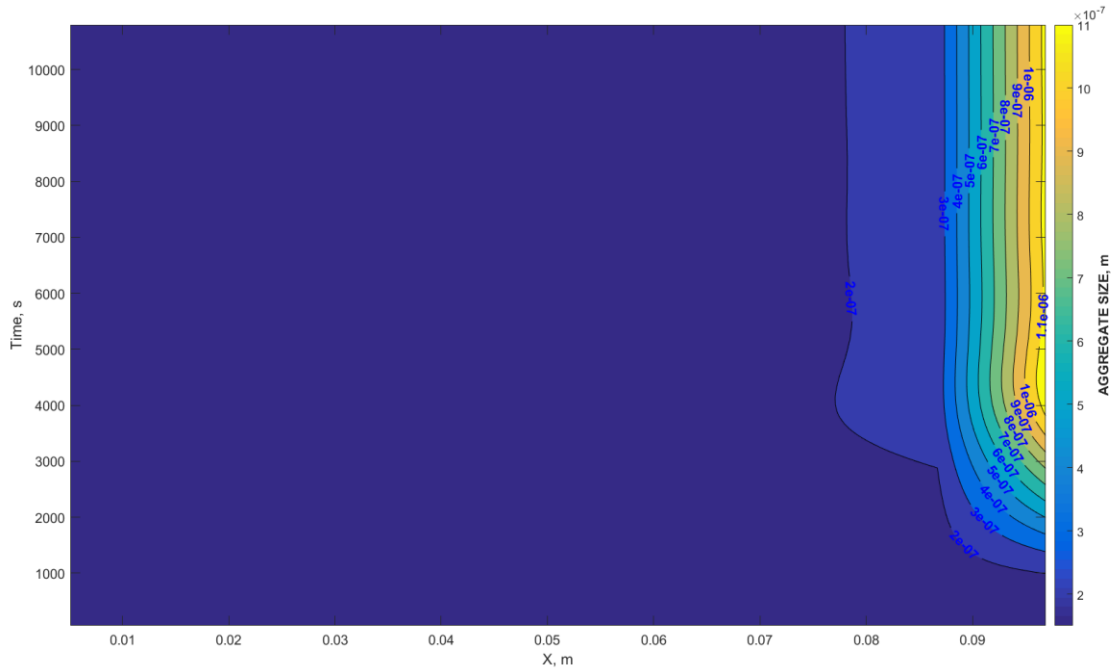

Figure 5-24—Aggregate size contours for Injection rate = 0.6 ml/min and Injected concentration = 1.25 vol% including filtration effect.

5.5. Conclusion

The model developed in this study can simulate coupled transport, aggregation, and in-situ gelation of nanoparticles in porous media. The cases presented in the previous section shows the capability of the model. The model shows that when nanoparticles dispersions are injected into free media like large pores or fractures that the effect of filtration is negligible, the gelation can be achieved but after longer time compared to the batch experiments. Increasing the concentration and/or injection rate decreases the gelation time significanetly. However, when including the effect of filtration, the viscosity of the does not increase due to exclusion of larger aggregates once they are formed. This prevents the growth of the gel network.

The model can also be coupled with acidizing model to simulate acidizing and acid diversion in carbonate reservoirs with nanoparticles-based in-situ gelled acid. This be addressed in future work. Also, the model can be coupled discrete fracture network (DFN) to simulate water shutoff and conformance control with fumed silica gel.

Acknowledgement

This work is supported by the Abu Dhabi National Oil Company (ADNOC) [grant number 880005].

Nomenclature

A_H	Hamaker constant
$a(L,\lambda)$	fragment distribution function for the diameter-based PBE
$a(v,u)$	fragment distribution function for the volume-based PBE
$b(L)$	diameter based breakage kernel
$b(u)$	volume-based breakage kernel
c	adjustable parameter in the breakage kernel model
$B_a(L;t)$	birth term due to aggregation in the diameter-based PBE
$B_b(L;t)$	birth term due to breakage in the diameter-based PBE
$B_a(v;t)$	birth term due to aggregation in the volume-based PBE
$B_a(v;t)$	birth term due to aggregation in the volume-based PBE
C_{salt}	Concentration of the salt per unit pore volume
$D_a(L;t)$	death term due to aggregation in the diameter -based PBE
$D_b(L;t)$	death term due to breakage in the diameter -based PBE
$D_a(v;t)$	death term due to aggregation in the volume-based PBE

$D_b(v;t)$	death term due to breakage in the volume-based PBE
D_f	fractal dimension of the aggregates
D^*_{salt}	dispersion coefficient of the salt
D^*_{agg}	dispersion coefficient of the aggregates
D_m	Molecular diffusion of the species
e	Electronic charge
$f(\kappa \boldsymbol{L_i})$	Henry's function
G	Shear rate
k	permeability of the porous medium
k_B	Boltzmann constant
$k_d(L)$	deposition kernel of aggregates of volume L
$k_s(L)$	straining kernel of aggregates of volume L
$k_d(v)$	deposition kernel of aggregates of volume v
$k_s(v)$	straining kernel of aggregates of volume v
h	Separation distance between particles
L_i	nodes in the Gaussian quadrature approximation
L_0	Initial size of the nanoparticles
m_k	the kth order moment
N_q	number of quadrature that represent the number of size classes of the aggregates
$n(L;t)$	diameter-based number density function
$n(v;t)$	volume-based number density function

pH	pH of the solution
pH_{IEP}	isoelectric point of the nanoparticles
s_1, s_2	slopes for the zeta potential function of pH and temperature
T	temperature of the dispersion
T_0	initial temperature of the dispersion
U	Darcy's velcoity
W	stability ratio
$\alpha_{agg}(L, \lambda)$	collision efficiency of particles of diameter L and λ
$\beta_{agg}(L, \lambda)$	collision frequency of particles of diameter L and λ
$\alpha_d(L_i)$	collision efficiency of particles of diameter L with the rock surface
$\beta_d(L_i)$	collision frequency of particles of diameter L with the rock surface
$\alpha_s(L_i)$	collision efficiency of particles of diameter L with the pore throats
$\beta_s(L_i)$	collision frequency of particles of diameter L with the pore throats
ω_i	weight (also the characteristic number density) corresponding to L_i
$\chi(\sigma)$	hydrodynamic effect
Φ_T	total electrostatic interaction between particles at separation distance h
Φ_{vdw}	Van der Waals interactions
Φ_{EDL}	Electric double layer repulsion
Φ_{HYD}	Hydration force
θ	function of separation distance and particle size
ζ	zeta potential
κ	Debye length

z_i	valence number of the ion
v_ζ	Constant for temperature effect on zeta potential
ε_0	vacuum permittivity
ε_p	dielectric constant of the particles
ε_c	dielectric constant of the continuous phase
h_P	Planck constant
v_e	characteristic adsorption frequency
n_p	refractive index of the particles
n_c	refractive index of the continuous phase
c_{i0}	bulk concentration of ion species i
N_A	Avogadro number
C_h	hydration constant
ℓ	decay length of the hydration force
μ	viscosity of aggregating dispersions
μ_0	Initial viscosity of the continuous phase
$[\mu]$	intrinsic viscosity
ϕ	Instantaneous porosity of the porous medium
ϕ_o	Initial porosity of the porous medium
φ	particles/aggregates volume fraction
φ_m	maximum packing fraction
C_0	crowding factor
C_2	second virial coefficient

C_0^0	crowding factor at low shear rate
C_0^∞	crowding factor at high shear rate
Pe	Peclet number of the aggregates
$R_{H,i}$	hydrodynamic radius of the aggregates
γ, β	coefficients for modified Kozeny-Carmen equation
r_p	Instantaneous pore radius
r_o	Initial pore radius
σ	Total retained volume of nanoparticles aggregates per unit pore volume
σ_d	Deposited volume of nanoparticles aggregates per unit pore volume
σ_s	Strained volume of nanoparticles aggregates per unit pore volume

Chapter 6 Conclusions and Recommendations

6.1. Summary and Conclusions

This chapter summarizes the conclusion and remarks of the previous chapters in this dissertation. Overall, this work focuses on nanoparticles transport in porous media, including inter-nanoparticle and nanoparticle-porous media interactions.

In Chapter 2, mechanistic model based on Extended DLVO theory was developed to study the rate of deposition and release of nanoparticles in porous media at different temperature, ionic strength, and pH. Empirical equation has been derived to calculate zeta potential at different temperature, ionic strength, and pH. The interaction energy can be with/without energy barrier between the nanoparticles and the pore surface. The rate of deposition and release of nanoparticles in each case has been derived. Numerical model has been used to compare the theoretically calculated rates with several experimental data. Increasing the temperature decreases the energy barrier height and increases the rate of deposition. With increasing the ionic strength, the thickness of the electrostatic double layer decreases and hence the rate of deposition increases. The effect of pH on the rate of deposition depends on the location of environment pH with respect to the isoelectric point of the nanoparticles and rock. For the extreme values of pH, energy barrier exists and rate of deposition is low. However, when the pH of the solution is between the isoelectric points of the nanoparticles and rock, the energy barrier decreases and the rate of deposition increases. The rate of deposition is time dependent as it decreases with increasing the covered rock surface. The effect of surface roughness has been included in the model using the effective height and density of the surface roughness distribution. Finally, these theoretically calculated rate values are used in a numerical model of the

advection-dispersion equation with source/sink term. Several experimental results have been perfectly matched that validate the theoretical calculations of the rate of deposition. The new mechanistic model for nanoparticles can be used to determine the fate of nanoparticles in porous media under different conditions of temperature, ionic strength, concentration, and pH. This model can help to understand the nanoparticles transport in porous media and effectively design nanoparticles fluid for injection into oil and gas reservoirs.

In Chapter 3, a numerical model that accurately describes different damage mechanisms associated with nanoparticles transport in porous media. This model is essential for forecasting and optimization of nanoparticles transport in porous media. In this paper, we have developed a mathematical model that combines Darcy and convection-diffusion equation to describe fluid flow, nanoparticles transport, and interaction in porous media. Pore throat size distribution is used to characterize the heterogeneity. Permeability field is generated as a function of the pore throat size distribution. Pore throat size and permeability distributions are dynamic functions of the nanoparticles deposition and plugging. The mathematical model is solved on a two-dimensional domain using alternating direction implicit scheme. The model is validated with experimental data to obtain the model parameters. Sensitivity analysis is presented using the proposed numerical model. The model shows that each of the three damage mechanisms could be dominant at specific conditions. Dimensional analysis is then used to derive a correlation that relates the degree of damage to main dimensionless numbers that control the efficiency of nanoparticle transport. The preliminary numerical results demonstrate that

nanoparticle size, concentration, injection rate and permeability are the dominant factors that control the degree of formation damage.

In Chapter 4, Population Balance equation (PBE) was used to model the kinetics of aggregation. Quadrature method of moments (QMOM) was used to convert the PBE with continuous distribution of nanoparticle size into moment transport equations for efficient computation. This study shows that the population balance equation and the quadrature method of moments along with the effective medium theory can be used to model the aggregation and insitu at different conditions of salinity and concentration. The modeled developed in this study is used to compare between the kinetics of aggregation and gelation of fumed silica and colloidal silica nanoparticles at the same conditions. The case studies presented show that unique behavior of fumed silica over colloidal silica nanoparticles for forming a gel network a significantly low concentration. This is basically due to the fractal structure of the fumed silica nanoparticles that has higher effective volume than the spherical particles of colloidal silica of the same size. The model also shows that there is a critical concentration of salt and nanoparticles above which the viscosity increase and the gel network can be formed. The model developed in this study can be coupled with a transport model to simulate nanoparticles transport aggregation and sin-situ gelation in porous media.

In Chapter 5, model is developed to simulate coupled transport, aggregation, and in situ gelation of nanoparticles in porous media. The model coupled fluid transport model with population balance equation solved with the Quadrature method of moments. Several cases were presented that shows the capability of the model. The model shows that when nanoparticles dispersions are injected into free media like large pores or fractures that the

effect of filtration is negligible, the gelation can be achieved but after longer time compared to the batch experiments. However, when including the effect of filtration, the viscosity of the does not increase due to exclusion of larger aggregates once they are formed. This prevents the growth of the gel network. The model can also be coupled with acidizing model to simulate acidizing and acid diversion in carbonate reservoirs with nanoparticles-based in-situ gelled acid. This be addressed in future work. Also, the model can be coupled discrete fracture network (DFN) to simulate water shutoff and conformance control with fumed silica gel.

6.2. Recommendations and Future Plan

This dissertation provided a framework for modeling nanoparticles transport in porous media including different interaction mechanisms. The applications of silica gel in water shutoff and conformance control have not been explored yet using the model framework developed in this dissertation. Here I list some recommendations future plan that needs to be further studied:

1. Experimental study will be conducted using micromodels and microscopy images to validate the model by matching the simulation moments with experimental moments derived from image analysis of the dispersion at different time step.
2. Expand the model to 2D and 3D to simulate actual reservoirs conditions coupled with geostatistical model for porosity and permeability distributions.
3. Couple the model with matrix acidizing model, to simulate matrix acidizing and acid diversion with nanoparticles-based in situ gelled acids.

4. Couple the model with discrete fracture network, to simulate water shutoff and conformance control in fractured reservoirs nanoparticles-based in situ gelled solutions.

References

1. Abdelfatah, Elsayed, Kang Kang, Maysam Pournik, B. Shiau, J. Harwell, M. R. Haroun, M. M. Rahman. 2017a. Study of Nanoparticle Adsorption and Release in Porous Media Based on the DLVO Theory. Presented at the SPE Latin America and Caribbean Petroleum Engineering Conference, Buenos Aires, Argentina, 18-19 May, https://doi.org/10.2118/185484-MS.

2. Abdelfatah, Elsayed, Kang Kang, Maysam Pournik, Bor Jier Ben Shiau, Jeffrey Harwell. 2017b. Study of Nanoparticle Retention in Porous Media: A Perfect Sink Model. Presented at the EAGE 19th European Symposium on Improved Oil Recovery, At Stavanger, Norway., http://dx.doi.org/10.3997/2214-4609.201700233

3. Abdelfatah, Elsayed, Hamid Khattab, Mohamed Soliman. 2014. Improving Heavy Oil Recovery by Nanofluid Injection: The factors Affecting and Mathematical Modelling. Journal of Petroleum and Mining Engineering 17: 88-89. Retrieved from http://www.researchgate.net/publication/292970343.

4. Abdelfatah, Elsayed, Maysam Pournik, Bor Jier Ben Shiau, Jeffery Harwell. 2017c. Mathematical Modeling and Simulation of Formation Damage Associated with Nanoparticles Transport in Porous Media. Presented at the SPE Latin America and Caribbean Mature Fields Symposium, Salvador, Bahia, Brazil, 15-16 March, https://doi.org/10.2118/184894-MS.

5. Abdelfatah, Elsayed, Maysam Pournik, Bor Jier Ben Shiau, Jeffrey Harwell. 2017d. Mathematical modeling and simulation of nanoparticles transport in heterogeneous porous media. Journal of Natural Gas Science and Engineering 40: 1-16. http://dx.doi.org/10.1016/j.jngse.2017.01.028.

6. Adamczyk, Zbigniew, Paweł Weroński. 1999. Application of the DLVO theory for particle deposition problems. Advances in Colloid and Interface Science 83 (1–3): 137-226. http://dx.doi.org/10.1016/S0001-8686(99)00009-3.

7. Adamson, Arthur W, Alice Petry Gast. 1967. Physical chemistry of surfaces.

8. Al-Ibadi, Adnan, Faruk Civan. 2013. Evaluation of Near-Wellbore Formation Treatment by Gel Particles Using Dimensional Analysis. Presented at the SPE Production and Operations Symposium, Oklahoma City, Oklahoma, USA, 23-26 March, 10.2118/164507-MS.

9. Al-Ibadi, Adnan, Faruk Civan, Larry Eoff. 2015. Experimental Investigation and Correlation of Particle-Gel Systems for Near-Wellbore Water Shutoff Treatments. Presented at the SPE Production and Operations Symposium, Oklahoma City, Oklahoma, USA, 1-5 March, http://dx.doi.org/10.2118/173627-MS.

10. Alaskar, Mohammed N., Morgan F. Ames, Steve T. Connor, Chong Liu, Yi Cui, Kewen Li, Roland N. Horne. 2012. Nanoparticle and Microparticle Flow in Porous and Fractured Media--An Experimental Study. SPE Journal 17 (04). 10.2118/146752-PA.

11. Almdal, K., J. Dyre, S. Hvidt, O. Kramer. 1993. Towards a phenomenological definition of the term 'gel'. Polymer Gels and Networks 1 (1): 5-17. http://dx.doi.org/10.1016/0966-7822(93)90020-I.

12. Alshakhs, Mohammed J., Anthony R. Kovscek. 2015. An Experimental Study of the Impact of Injection Water Composition on Oil Recovery from Carbonate Rocks. Presented at the SPE Annual Technical Conference and Exhibition, Houston, Texas, USA, 28-30 September, 10.2118/175147-MS.

13. Amankonah, J. Ofori, P. Somasundaran. 1985. Effects of dissolved mineral species on the electrokinetic behavior of calcite and apatite. Colloids and Surfaces 15: 335-353. http://dx.doi.org/10.1016/0166-6622(85)80082-2.

14. Amiri, Asal, Gisle Øye, Johan Sjöblom. 2009. Influence of pH, high salinity and particle concentration on stability and rheological properties of aqueous suspensions of fumed silica. Colloids and Surfaces A: Physicochemical and Engineering Aspects 349 (1–3): 43-54. http://doi.org/10.1016/j.colsurfa.2009.07.050.

15. Amiri, Asal, Gisle Øye, Johan Sjöblom. 2011. Temperature and pressure effects on stability and gelation properties of silica suspensions. Colloids and Surfaces A: Physicochemical and Engineering Aspects 378 (1–3): 14-21. http://doi.org/10.1016/j.colsurfa.2011.01.048.

16. Andrew, N. Ernest, S. Bonner James, L. Autenrieth Robin. 1995. Determination of Particle Collision Efficiencies for Flocculent Transport Models. Journal of Environmental Engineering 121 (4): 320-329. 10.1061/(ASCE)0733-9372(1995)121:4(320).

17. Antonio Alves Júnior, J. , J. Baptista Baldo. 2014. The Behavior of Zeta Potential of Silica Suspensions. New Journal of Glass and Ceramics 4: 29-37.

18. Ariana, M. A., B. Vaferi, G. Karimi. 2015. Prediction of thermal conductivity of alumina water-based nanofluids by artificial neural networks. Powder Technology 278: 1-10. http://dx.doi.org/10.1016/j.powtec.2015.03.005.

19. Aziz, Khalid, Antonin Settari. 1979. Petroleum reservoir simulation, Chapman & Hall (Reprint).

20. Berg, John C. 2010. An introduction to interfaces & colloids: the bridge to nanoscience, World Scientific (Reprint).

21. Bhattacharjee, Subir, Chun-Han Ko, Menachem Elimelech. 1998. DLVO interaction between rough surfaces. Langmuir 14 (12): 3365-3375. http://dx.doi.org/10.1021/la971360b.

22. Binks, Bernard P., Wenhui Liu, Jhonny A. Rodrigues. 2008. Novel Stabilization of Emulsions via the Heteroaggregation of Nanoparticles. Langmuir 24 (9): 4443-4446. 10.1021/la800084d.

23. Bird, R Byron, Warren E Stewart, Edwin N Lightfoot. 2007. Transport phenomena, revised, New York: John Wiley & Sons, Inc (Reprint).

24. Bos, Rolf, Henny C. van der Mei, Henk J. Busscher. 1999. Physico-chemistry of initial microbial adhesive interactions – its mechanisms and methods for study. FEMS Microbiology Reviews 23 (2): 179-230. 10.1111/j.1574-6976.1999.tb00396.x.

25. Bousse, Luc, J. D. Meindl. 1987. Surface Potential-pH Characteristics in the Theory of the Oxide-Electrolyte Interface. In Geochemical Processes at Mineral Surfaces, Chap. 5, 79-98. ACS Symposium Series, American Chemical Society.

26. Bousse, Luc, Nico F. de Rooij, P. Bergveld. 1983. The influence of counter-ion adsorption on the ?0/pH characteristics of insulator surfaces. Surface Science 135 (1-3): 479-496. 10.1016/0039-6028(83)90237-6.

27. Brant, Jonathan, Hélène Lecoanet, Matt Hotze, Mark Wiesner. 2005. Comparison of Electrokinetic Properties of Colloidal Fullerenes (n-C60) Formed Using Two Procedures. Environmental Science & Technology 39 (17): 6343-6351. 10.1021/es050090d.

28. Burdick, G.M., N.S. Berman, S.P. Beaudoin. 2001. Describing Hydrodynamic Particle Removal from Surfaces Using the Particle Reynolds Number. Journal of Nanoparticle Research 3 (5): 453-465. 10.1023/a:1012593318108.

29. Caldelas, F.M. . 2010. Experimental Parameter Analysis of Nanoparticle Retention in Porous Media. Master, University of Texas at Austin, Austin, Texas.

30. Caldelas, Federico Manuel, Michael Murphy, Chun Huh, Steven Lawrence Bryant. 2011. Factors Governing Distance of Nanoparticle Propagation in Porous Media. Presented at the SPE Production and Operations Symposium, Oklahoma City, 27-29 March, 10.2118/142305-MS.

31. Cannella, W. J., C. Huh, R. S. Seright. 1988. Prediction of Xanthan Rheology in Porous Media. Presented at the SPE Annual Technical Conference and Exhibition, Houston, Texas, 2-5 October, https://doi.org/10.2118/18089-MS.

32. Chang, Frank, Faruk Civan. 1991. Modeling of Formation Damage Due to Physical and Chemical Interactions Between Fluids and Reservoir Rocks.

Presented at the SPE Annual Technical Conference and Exhibition, Dallas, Texas, 6-9 October, 10.2118/22856-MS.

33. Chapel, J. P. 1994. Electrolyte Species Dependent Hydration Forces between Silica Surfaces. Langmuir 10 (11): 4237-4243. 10.1021/la00023a053.

34. Chatterjee, Jaideep, Santosh Kumar Gupta. 2009. An Agglomeration-Based Model for Colloid Filtration. Environmental Science & Technology 43 (10): 3694-3699. 10.1021/es8029973.

35. Chen, Changlong, Mohannad J. Kadhum, Marissa C. Mercado, Benjamin Shiau, Jeffrey H. Harwell. 2016. Surfactant-Only Stabilized Dispersions of Multiwalled Carbon Nanotubes in High-Electrolyte-Concentration Brines. Energy & Fuels 30 (11): 8952-8961. https://doi.org/10.1021/acs.energyfuels.6b01389.

36. Chen, Shukun, Gisle Øye, Johan Sjöblom. 2005. Rheological Properties of Aqueous Silica Particle Suspensions. Journal of Dispersion Science and Technology 26 (4): 495-501. http://dx.doi.org/10.1081/DIS-200054608.

37. Churaev, NV, BV Derjaguin. 1985. Inclusion of structural forces in the theory of stability of colloids and films. Journal of colloid and interface science 103 (2): 542-553. http://dx.doi.org/10.1016/0021-9797(85)90129-8.

38. Churchill, Stuart W. 1997. A New Approach To Teaching Dimensional Analysis. Chemical Engineering Education (CEE) 31 (3): 158-65.

39. Civan, Faruk. 2007. Reservoir Formation Damage - Fundamentals, Modeling, Assessment, and Mitigation, second edition. Burlington, Vermont, Gulf Professional Publishing (Reprint).

40. Civan, Faruk, Vinh Nguyen. 2005. Modeling Particle Migration and Deposition in Porous Media by Parallel Pathways with Exchange. In Handbook of Porous Media, Second Edition, 457-484. CRC Press.

41. Derjaguin, B., L. Landau. 1993. Theory of the stability of strongly charged lyophobic sols and of the adhesion of strongly charged particles in solutions of electrolytes. Progress in Surface Science 43 (1): 30-59. http://dx.doi.org/10.1016/0079-6816(93)90013-L.

42. Dickinson, Eric. 2000. Structure and Rheology of Simulated Gels Formed from Aggregated Colloidal Particles. Journal of Colloid and Interface Science 225 (1): 2-15. http://dx.doi.org/10.1006/jcis.1999.6662.

43. Ding, Wuquan, Xinmin Liu, Li Song, Qiang Li, Qihong Zhu, Hualing Zhu, Feinan Hu, Yaxue Luo, Longhui Zhu, Hang Li. 2014. An approach to estimate the position of the shear plane for colloidal particles in an electrophoresis experiment. Surface Science 632: 50-59. http://dx.doi.org/10.1016/j.susc.2014.08.024.

44. Dolz, M., F. González, J. Delegido, M. J. Hernández, J. Pellicer. 2000. A time-dependent expression for thixotropic areas. Application to Aerosil 200 hydrogels. Journal of Pharmaceutical Sciences 89 (6): 790-797. 10.1002/(SICI)1520-6017(200006)89:6<790::AID-JPS11>3.0.CO;2-2.

45. Elimelech, M., J. Gregory, X. Jia, R. A. Williams. 1995. Chapter 3 - Surface interaction potentials. In Particle Deposition & Aggregation, 33-67. Woburn, Butterworth-Heinemann.

46. Elimelech, Menachem, John Gregory, Xiadong Jia. 2013. Particle deposition and aggregation: measurement, modelling and simulation, Butterworth-Heinemann (Reprint).

47. Elimelech, Menachem, Charles R O'Melia. 1990. Kinetics of deposition of colloidal particles in porous media. Environmental science & technology 24 (10): 1528-1536. http://dx.doi.org/10.1021/es00080a012.

48. Ersoy, Bahri. 2005. Effect of pH and polymer charge density on settling rate and turbidity of natural stone suspensions. International Journal of Mineral Processing 75 (3–4): 207-216. http://dx.doi.org/10.1016/j.minpro.2004.08.011.

49. Esfandyari Bayat, Ali, Radzuan Junin, Shahaboddin Shamshirband, Wen Tong Chong. 2015. Transport and retention of engineered Al2O3, TiO2, and SiO2 nanoparticles through various sedimentary rocks. Scientific Reports 5 (14264). 10.1038/srep14264.

50. Evonik. 2016. Basic characteristics of AEROSIL® fumed silica (Reprint).

51. Fakoya, M. F., S. N. Shah. 2014. Enhancement of Filtration Properties in Surfactant-Based and Polymeric Fluids by Nanoparticles. Presented at the SPE Eastern Regional Meeting 21-23 October, 10.2118/171029-MS.

52. Fakoya, M. F., S. N. Shah. 2016. Relative Viscosity of Hydraulic Fracturing Fluids Containing Nanoparticles. Presented at the SPE Western Regional Meeting, Anchorage, Alaska, USA, 23-26 May, 10.2118/180458-MS.

53. Fakoya, Muili Feyisitan, Subhash Nandlal Shah. 2017. Emergence of nanotechnology in the oil and gas industry: Emphasis on the application of silica nanoparticles. Petroleum. http://doi.org/10.1016/j.petlm.2017.03.001.

54. Family, Fereydoon, David P Landau. 2012. Kinetics of aggregation and gelation, Elsevier (Reprint).

55. Fisher, Matthew L., Miroslav Colic, Masa P. Rao, Fred F. Lange. 2001. Effect of Silica Nanoparticle Size on the Stability of Alumina/Silica Suspensions. Journal of the American Ceramic Society 84 (4): 713-718. 10.1111/j.1151-2916.2001.tb00731.x.

56. Fletcher, Alistair, John Davis. 2010. How EOR Can be Transformed by Nanotechnology. Presented at the SPE Improved Oil Recovery Symposium, Tulsa, Oklahoma, USA, 24-28 April 2010, 2010/1/1/, 10.2118/129531-MS.

57. Gautschi, Walter. 1968. Construction of Gauss-Christoffel quadrature formulas. Mathematics of Computation 22 (102): 251-270. https://doi.org/10.1090/S0025-5718-1968-0228171-0

58. Ghadimi, A., R. Saidur, H. S. C. Metselaar. 2011. A review of nanofluid stability properties and characterization in stationary conditions. International Journal of Heat and Mass Transfer 54 (17–18): 4051-4068. http://dx.doi.org/10.1016/j.ijheatmasstransfer.2011.04.014.

59. Ghanaei, Ehsan, Mohammad Reza Rahimpour. 2010. Evaluation of orthogonal collocation and orthogonal collocation on finite element method using genetic algorithm in the pressure profile prediction in petroleum reservoirs. Journal of Petroleum Science and Engineering 74 (1–2): 41-50. http://dx.doi.org/10.1016/j.petrol.2010.08.005.

60. Ghosh, Pallab. 2009. Colloid and interface science. In, Chap. 5. PHI Learning Pvt. Ltd.

61. Greff, John, Tayfun Babadagli. 2011. Catalytic Effects of Nano-Size Metal Ions in Breaking Asphaltene Molecules during Thermal Recovery of Heavy-Oil. Presented at the SPE Annual Technical Conference and Exhibition Denver, Colorado, , 30 October-2-November, 10.2118/146604-MS.

62. Gregory, John. 1981. Approximate expressions for retarded van der waals interaction. Journal of Colloid and Interface Science 83 (1): 138-145. http://dx.doi.org/10.1016/0021-9797(81)90018-7.

63. Gringarten, Alain C., Henry J. Ramey, Jr. 1973. The Use of Source and Green's Functions in Solving Unsteady-Flow Problems in Reservoirs. SPE Journal. 10.2118/3818-PA.

64. Grosch, R., H. Briesen, W. Marquardt, M. Wulkow. 2007. Generalization and numerical investigation of QMOM. AIChE Journal 53 (1): 207-227. 10.1002/aic.11041.

65. Gruesbeck, C., R. E. Collins. 1982. Entrainment and Deposition of Fine Particles in Porous Media. Society of Petroleum Engineers Journal 22 (06). 10.2118/8430-PA.

66. Gun'ko, V. M., V. I. Zarko, R. Leboda, E. Chibowski. 2001. Aqueous suspension of fumed oxides: particle size distribution and zeta potential. Advances in Colloid and Interface Science 91 (1): 1-112. http://doi.org/10.1016/S0001-8686(99)00026-3.

67. Hemmat Esfe, Mohammad, Seyfolah Saedodin, Nima Sina, Masoud Afrand, Sara Rostami. 2015. Designing an artificial neural network to predict thermal conductivity and dynamic viscosity of ferromagnetic nanofluid. International Communications in Heat and Mass Transfer 68: 50-57. http://dx.doi.org/10.1016/j.icheatmasstransfer.2015.06.013.

68. Hendraningrat, Luky, Li Shidong, Ole Torsaeter. 2012. A Glass Micromodel Experimental Study of Hydrophilic Nanoparticles Retention for EOR Project. Presented at the SPE Russian Oil and Gas Exploration and Production Technical Conference and Exhibition, Moscow, Russia, 16-18 October, 10.2118/159161-MS.

69. Hendraningrat, Luky, O. Torsæter. 2014. Understanding Fluid-Fluid and Fluid-Rock Interactions in the Presence of Hydrophilic Nanoparticles at Various Conditions. Presented at the SPE Asia pacific oil & gas conference and Exhbition, Adelaide, Australia, 14-16 October, 10.2118/171407-MS.

70. Herzig, J. P., D. M. Leclerc, P. Le Goff. 1970. Flow of Suspensions through Porous Media—Application to Deep Filtration. Industrial & Engineering Chemistry 62 (5): 8-35. 10.1021/ie50725a003.

71. Hiemenz, Paul C. 1986. Principles of colloid and surface chemistry, Vol. 188, M. Dekker New York (Reprint).

72. Hoek, Eric , Subir MV Bhattacharjee, Menachem Elimelech. 2003. Effect of membrane surface roughness on colloid-membrane DLVO interactions. Langmuir 19 (11): 4836-4847. http://dx.doi.org/0.1021/la027083c.

73. Hoek, Eric MV, Gaurav K Agarwal. 2006. Extended DLVO interactions between spherical particles and rough surfaces. Journal of Colloid and Interface science 298 (1): 50-58. http://dx.doi.org/10.1016/j.jcis.2005.12.031.

74. Hogg, R., T. W. Healy, D. W. Fuerstenau. 1966. Mutual coagulation of colloidal dispersions. Transactions of the Faraday Society 62 (0): 1638-1651. 10.1039/TF9666201638.

75. Huang, Jin, Ayman Al-Mohsin, Mohammed Bataweel, Prasad Karadkar, Wengang Li, Abrar Shaikh. 2017. Systematic Approach to Develop a Colloidal Silica Based Gel System for Water Shut-Off. Presented at the 2017/3/6/, 10.2118/183942-MS.

76. Huang, Tianping, James B. Crews, John Robert Willingham. 2008. Using Nanoparticle Technology to Control Fine Migration. Presented at the SPE annual technical conference and exhibition, Denver, Colorado, 12-14 June, 10.2118/115384-MS.

77. Hubbe, Martin A. 1984. Theory of detachment of colloidal particles from flat surfaces exposed to flow. Colloids and Surfaces 12: 151-178. http://dx.doi.org/10.1016/0166-6622(84)80096-7.

78. Hulburt, H. M., S. Katz. 1964. Some problems in particle technology. Chemical Engineering Science 19 (8): 555-574. http://dx.doi.org/10.1016/0009-2509(64)85047-8.

79. Hyne, T.B. 1986. Aquathermolysis a synopsis of work on the chemical reaction between water (steam) and heavy oil sands during simulated steam stimulation (Reprint).

80. Iler, Ralph Kingsley. 1979. The chemistry of silica : solubility, polymerization, colloid and surface properties, and biochemistry, New York : Wiley (Reprint).

81. Israelachvili, Jacob N. 2011. Intermolecular and Surface Forces In Intermolecular and Surface Forces (Third Edition). Boston, Academic Press.

82. Johnson, Philip R., Menachem Elimelech. 1995. Dynamics of Colloid Deposition in Porous Media: Blocking Based on Random Sequential Adsorption. Langmuir 11 (3): 801-812. 10.1021/la00003a023.

83. Ju, Binshan, Tailiang Fan. 2009. Experimental study and mathematical model of nanoparticle transport in porous media. Powder Technology 192 (2): 195-202. http://dx.doi.org/10.1016/j.powtec.2008.12.017.

84. Jurinak, J. J., L. E. Summers. 1991. Oilfield Applications of Colloidal Silica Gel. 10.2118/18505-PA.

85. Kadhum, Mohannad J., Daniel P. Swatske, Changlong Chen, Daniel E. Resasco, Jeffrey H. Harwell, Ben Shiau. 2015. Propagation of Carbon Nanotube Hybrids through Porous Media for Advancing Oilfield Technology. Presented at the SPE International Symposium on Oilfield Chemistry, The Woodlands, Texas, USA, 13-15 April, https://doi.org/10.2118/173781-MS.

86. Kaszuba, Michael, Jason Corbett, Fraser Mcneil Watson, Andrew Jones. 2010. High-concentration zeta potential measurements using light-scattering techniques. Philosophical transactions. Series A, Mathematical, physical, and engineering sciences 368 (1927): 4439-4451. 10.1098/rsta.2010.0175.

87. Kawaguchi, Masami. 2017. Dispersion stabilities and rheological properties of fumed silica suspensions. Journal of Dispersion Science and Technology 38 (5): 642-660. 10.1080/01932691.2016.1185952.

88. Kawaguchi, Masami, Atsushi Mizutani, Yushu Matsushita, Tadaya Kato. 1996a. Molecular Weight Dependence of Structures and Rheological Properties for Fumed Silica Suspensions in Polystyrene Solutions. Langmuir 12 (26): 6179-6183. http:dx.doi.org/10.1021/la9508396.

89. Kawaguchi, Masami, Takashi Yamamoto, Tadaya Kato. 1996b. Rheological Studies of Hydrophilic and Hydrophobic Silica Suspensions in the Presence of Adsorbed Poly(N-isopropylacrylamide). Langmuir 12 (26): 6184-6187. http:dx.doi.org/10.1021/la960147x.

90. Khadivi, Kourosh, Mohammad Soltanieh. 2014. Numerical solution of the nonlinear diffusivity equation in heterogeneous reservoirs with wellbore phase redistribution. Journal of Petroleum Science and Engineering 114: 82-90. http://dx.doi.org/10.1016/j.petrol.2014.01.004.

91. Kim, Ijung, Amir Taghavy, David DiCarlo, Chun Huh. 2015. Aggregation of silica nanoparticles and its impact on particle mobility under high-salinity conditions. Journal of Petroleum Science and Engineering 133: 376-383. https://doi.org/10.1016/j.petrol.2015.06.019.

92. Kim, Jin-Keun, Desmond F. Lawler. 2005. Characteristics of Zeta Potential Distribution in Silica Particles. Bulletin of the Korean Chemical Society 26 (7): 1083-1089. 10.5012/bkcs.2005.26.7.1083.

93. L. Marchisio, Daniele, R. Dennis Vigil, Rodney O. Fox. 2003. Implementation of the quadrature method of moments in CFD codes for aggregation–breakage problems. Chemical Engineering Science 58 (15): 3337-3351. http://doi.org/10.1016/S0009-2509(03)00211-2.

94. Lattuada, Marco, Alessio Zaccone, Hua Wu, Massimo Morbidelli. 2016. Population-balance description of shear-induced clustering, gelation and suspension viscosity in sheared DLVO colloids. Soft Matter 12 (24): 5313-5324. 10.1039/C6SM01097K.

95. Lee, Du Gon, James S. Bonner, Laurie S. Garton, Andrew N. S. Ernest, Robin L. Autenrieth. 2000. Modeling coagulation kinetics incorporating fractal theories: a fractal rectilinear approach. Water Research 34 (7): 1987-2000. http://doi.org/10.1016/S0043-1354(99)00354-1.

96. Lieu, Kim Phuong. 2014. Sediment diagenesis and characteristics of grains and pore geometry in sandstone reservoir rocks from a well of the North German Basin, Ludwig Maximilian University of Munich.

97. Liu, D. . 1994. Chemical Aspects of Particle Deposition Dynamics in Porous Media. . Ph.D. , University of California, Los Angeles, California.

98. Liu, S, JH Masliyah, LL Schramm. 1996. Suspensions: fundamentals and applications in the petroleum industry. Advances in Chemistry (American Chemical Society, Washington, DC, 1996) 251.

99. Mahmoud, Omar, Hisham A. Nasr-El-Din, Zisis Vryzas, Vassilios C. Kelessidis. 2016. Nanoparticle-Based Drilling Fluids for Minimizing Formation Damage in HP/HT Applications. Presented at the SPE International Conference and

Exhibition on Formation Damage Control, Lafayette, Louisiana, USA, 24-26 February 10.2118/178949-MS.

100. Mandal, Ajay, Achinta Bera, Keka Ojha, Tarkeshwar Kumar. 2012. Characterization of Surfactant Stabilized Nanoemulsion and Its Use in Enhanced Oil Recovery. Presented at the SPE international oilfield nanotechnology conference, Noordwijk, The Netherlands, 12-14 June, 10.2118/155406-MS.

101. Mandel, K., Stra, T. Granath, S. Dembski, G. Sextl. 2015. Surfactant free superparamagnetic iron oxide nanoparticles for stable ferrofluids in physiological solutions. Chemical Communications 51 (14): 2863-2866. 10.1039/C4CC09277E.

102. Marchisio, Daniele L, Rodney O Fox. 2013. Computational models for polydisperse particulate and multiphase systems, Cambridge University Press (Reprint).

103. Marchisio, Daniele L., Jesse T. Pikturna, Rodney O. Fox, R. Dennis Vigil, Antonello A. Barresi. 2003a. Quadrature method of moments for population-balance equations. AIChE Journal 49 (5): 1266-1276. 10.1002/aic.690490517.

104. Marchisio, Daniele L., R. Dennis Vigil, Rodney O. Fox. 2003b. Quadrature method of moments for aggregation–breakage processes. Journal of Colloid and Interface Science 258 (2): 322-334. http://doi.org/10.1016/S0021-9797(02)00054-1.

105. McElfresh, Paul M, David Lee Holcomb, Daniel Ector. 2012a. Application of Nanofluid Technology to Improve Recovery in Oil and Gas Wells. Presented at the SPE international oilfield nanotechnology conference, Noordwijk, The Netherlands, 12-14 June, 10.2118/154827-MS.

106. McElfresh, Paul M, Marodi Wood, Daniel Ector. 2012b. Stabilizing Nano Particle Dispersions in High Salinity, High Temperature Downhole Environments. Presented at the SPE international oilfiled nanotechnology conference Noordwijk, The Netherlands, 12-14 June 2012, 10.2118/154758-MS.

107. McGraw, Robert. 1997. Description of Aerosol Dynamics by the Quadrature Method of Moments. Aerosol Science and Technology 27 (2): 255-265. 10.1080/02786829708965471.

108. McGraw, Robert, James H. Saunders. 1984. A Condensation Feedback Mechanism for Oscillatory Nucleation and Growth. Aerosol Science and Technology 3 (4): 367-380. 10.1080/02786828408959025.

109. Mehana, Mohamed, Mohamed Al Salman, Mashhad Fahes. 2017. The Impact of Salinity on Water Dynamics, Hydrocarbon Recovery and Formation Softening in Shale: Experimental Study. Presented at the SPE Kingdom of Saudi Arabia

Annual Technical Symposium and Exhibition, Dammam, Saudi Arabia, 24-27 April, https://doi.org/10.2118/188131-MS.

110. Metin, Cigdem O., Kelli M. Rankin, Quoc P. Nguyen. 2014. Phase behavior and rheological characterization of silica nanoparticle gel. Applied Nanoscience 4 (1): 93-101. 10.1007/s13204-012-0168-7.

111. Moré, Jorge J. 1978. The Levenberg-Marquardt algorithm: implementation and theory. In Numerical analysis, 105-116. Springer.

112. O'Neill, M. E. 1968. A sphere in contact with a plane wall in a slow linear shear flow. Chemical Engineering Science 23 (11): 1293-1298. http://dx.doi.org/10.1016/0009-2509(68)89039-6.

113. Ogolo, N. A., O. A. Olafuyi, M. O. Onyekonwu. Enhanced Oil Recovery Using Nanoparticles. Al-Khobar, Saudi Arabia SPE: Society of Petroleum Engineers.

114. Ohen, Henry Abuya. 1989. Modelling and simulation of the effects of clay swelling and fines migration on formation damage. PhD, Oklahoma Univ., Norman, OK (USA).

115. Ohshima, Hiroyuki. 1994. A Simple Expression for Henry's Function for the Retardation Effect in Electrophoresis of Spherical Colloidal Particles. Journal of Colloid and Interface Science 168 (1): 269-271. http://dx.doi.org/10.1006/jcis.1994.1419.

116. Okazaki, Ken, Masami Kawaguchi. 2008. Influence of Monovalent Electrolytes on Rheological Properties of Gelled Colloidal Silica Suspensions. Journal of Dispersion Science and Technology 29 (1): 77-82. 10.1080/01932690701688425.

117. Oldham, Keith B. 2008. A Gouy–Chapman–Stern model of the double layer at a (metal)/(ionic liquid) interface. Journal of Electroanalytical Chemistry 613 (2): 131-138. http://dx.doi.org/10.1016/j.jelechem.2007.10.017.

118. Omosebi, Omotayo, Himanshu Maheshwari, Ramadan Ahmed, Subhash Shah, Samuel Osisanya. 2017. Experimental study of the effects of CO2 concentration and pressure at elevated temperature on the mechanical integrity of oil and gas well cement. Journal of Natural Gas Science and Engineering 44: 299-313. https://doi.org/10.1016/j.jngse.2017.04.009.

119. P. Binks, B., S. O. Lumsdon. 1999. Stability of oil-in-water emulsions stabilised by silica particles. Physical Chemistry Chemical Physics 1 (12): 3007-3016. 10.1039/A902209K.

120. Pashley, R. M. 1982. Hydration forces between mica surfaces in electrolyte solutions. Advances in Colloid and Interface Science 16 (1): 57-62. http://dx.doi.org/10.1016/0001-8686(82)85006-9.

121. Pashley, Richard M, Jacob N Israelachvili. 1984. Molecular layering of water in thin films between mica surfaces and its relation to hydration forces. Journal of colloid and interface science 101 (2): 511-523. http://dx.doi.org/10.1016/0021-9797(84)90063-8.

122. Pearson, Karl. 1895. Contributions to the Mathematical Theory of Evolution. II. Skew Variation in Homogeneous Material. Philosophical Transactions of the Royal Society of London. (A.) 186: 343-414. 10.1098/rsta.1895.0010.

123. Pfeiffer, Christian, Christoph Rehbock, Dominik Hühn, Carolina Carrillo-Carrion, Dorleta Jimenez de Aberasturi, Vivian Merk, Stephan Barcikowski, Wolfgang J. Parak. 2014. Interaction of colloidal nanoparticles with their local environment: the (ionic) nanoenvironment around nanoparticles is different from bulk and determines the physico-chemical properties of the nanoparticles. Journal of The Royal Society Interface 11 (96). 10.1098/rsif.2013.0931.

124. Pham, Ngoc H., Jeffrey H. Harwell, Daniel E. Resasco, Dimitrios V. Papavassiliou, Changlong Chen, Benjamin Shiau. 2016. Transport and deposition kinetics of polymer-coated multiwalled carbon nanotubes in packed beds. AIChE Journal 62 (10): 3774-3783. https://doi.org/10.1002/aic.15273.

125. Pletcher, Richard H, John C Tannehill, Dale Anderson. 2012. Computational fluid mechanics and heat transfer, CRC Press (Reprint).

126. Popplewell, LM, OH Campanella, M Peleg. 1989. Simulation of bimodal size distributions in aggregation and disintegration processes. Chemical engineering progress 85 (8): 56-62.

127. Raghavan, Srinivasa R., Saad A. Khan. 1995. Shear-induced microstructural changes in flocculated suspensions of fumed silica. Journal of Rheology 39 (6): 1311-1325. 10.1122/1.550638.

128. Raghavan, Srinivasa R., H. J. Walls, Saad A. Khan. 2000. Rheology of Silica Dispersions in Organic Liquids: New Evidence for Solvation Forces Dictated by Hydrogen Bonding. Langmuir 16 (21): 7920-7930. 10.1021/la991548q.

129. Rahman, Tanzina, Harry Millwater, Heather J. Shipley. 2014. Modeling and sensitivity analysis on the transport of aluminum oxide nanoparticles in saturated sand: Effects of ionic strength, flow rate, and nanoparticle concentration. Science of The Total Environment 499: 402-412. http://dx.doi.org/10.1016/j.scitotenv.2014.08.073.

130. Ramkrishna, Doraiswami. 2000. Population balances: Theory and applications to particulate systems in engineering, Academic press (Reprint).

131. Raychoudhury, Trishikhi, Nathalie Tufenkji, Subhasis Ghoshal. 2012. Aggregation and deposition kinetics of carboxymethyl cellulose-modified zero-

valent iron nanoparticles in porous media. Water Research 46 (6): 1735-1744. http://doi.org/10.1016/j.watres.2011.12.045.

132. Revil, A., H. Schwaeger, L. M. Cathles, P. D. Manhardt. 1999. Streaming potential in porous media: 2. Theory and application to geothermal systems. Journal of Geophysical Research: Solid Earth 104 (B9): 20033-20048. 10.1029/1999JB900090.

133. Reyes Bahena, J. L., A. Robledo Cabrera, A. López Valdivieso, R. Herrera Urbina. 2002. Fluoride adsorption onto α-Al2O3 and its effect on the zeta potential at the alumina–aqueous electrolyte interface. Separation Science and Technology 37 (8): 1973-1987. 10.1081/SS-120003055.

134. Ruckenstein, Eli, Dennis C. Prieve. 1976. Adsorption and desorption of particles and their chromatographic separation. AIChE Journal 22 (2): 276-283. http://dx.doi.org/10.1002/aic.690220209.

135. Russel, William Bailey, Dudley Albert Saville, William Raymond Schowalter. 1989. Colloidal dispersions, Cambridge university press (Reprint).

136. Ryan, Joseph N., Menachem Elimelech. 1996. Colloid mobilization and transport in groundwater. Colloids and Surfaces A: Physicochemical and Engineering Aspects 107: 1-56. http://dx.doi.org/10.1016/0927-7757(95)03384-X.

137. Ryan, Joseph N., Philip M. Gschwend. 1994. Effects of Ionic Strength and Flow Rate on Colloid Release: Relating Kinetics to Intersurface Potential Energy. Journal of Colloid and Interface Science 164 (1): 21-34. http://dx.doi.org/10.1006/jcis.1994.1139.

138. Sefcik, J., R. Grass, P. Sandkühler, M. Morbidelli. 2005. Kinetics of Aggregation and Gelation in Colloidal Dispersions. Chemical Engineering Research and Design 83 (7): 926-932. http://dx.doi.org/10.1205/cherd.05027.

139. Shellenberger, Karl, Bruce E Logan. 2002. Effect of molecular scale roughness of glass beads on colloidal and bacterial deposition. Environmental science & technology 36 (2): 184-189. http://dx.doi.org/10.1021/es015515k.

140. Shen, Xiaoteng, Jerome P. Y. Maa. 2015. Modeling floc size distribution of suspended cohesive sediments using quadrature method of moments. Marine Geology 359: 106-119. http://doi.org/10.1016/j.margeo.2014.11.014.

141. Shen, Xiaoteng, Jerome P. Y. Maa. 2016. Numerical simulations of particle size distributions: Comparison with analytical solutions and kaolinite flocculation experiments. Marine Geology 379: 84-99. http://doi.org/10.1016/j.margeo.2016.05.014.

142. Shokrlu, Yousef Hamedi, Tayfun Babadagli. 2010. Effects of Nano-Sized Metals on Viscosity Reduction of Heavy Oil/Bitumen During Thermal Applications.

Presented at the Canadian unconventional resources and international petroleum conference, Calgary, Alberta, Canada, 19-21 October, 2010/1/1/, 10.2118/137540-MS.

143. Shokrlu, Yousef Hamedi, Tayfun Babadagli. 2011. Transportation and Interaction of Nano and Micro Size Metal Particles Injected to Improve Thermal Recovery of Heavy-Oil. Presented at the SPE Annual Technical Conference and Exhibition Denver, Colorado, 30 October-2 November, 10.2118/146661-MS.

144. Skauge, Arne, S Pourmohammadi, B Vik, Kristine Spildo. Dispersion measurements used in special core analysis of carbonates. Trondheim, Norway, Sept. 12 − 16.

145. Skauge, Tormod, Kristine Spildo, Arne Skauge. 2010. Nano-sized Particles For EOR. Presented at the SPE Improved Oil Recovery Symposium, Tulsa, Oklahoma, USA, 24-28 April, 10.2118/129933-MS.

146. Smith, W. E., C. F. Zukoski. 2004. Flow properties of hard structured particle suspensions. Journal of Rheology 48 (6): 1375-1388. http://dx.doi.org/10.1122/1.1807846.

147. Smith, William E., Charles F. Zukoski. 2006. Aggregation and gelation kinetics of fumed silica–ethanol suspensions. Journal of Colloid and Interface Science 304 (2): 359-369. http://doi.org/10.1016/j.jcis.2006.09.016.

148. Spielman, Lloyd A., S. K. Friedlander. 1974. Role of the electrical double layer in particle deposition by convective diffusion. Journal of Colloid and Interface Science 46 (1): 22-31. http://dx.doi.org/10.1016/0021-9797(74)90021-6.

149. Su, Junwei, Zhaolin Gu, Yun Li, Shiyu Feng, X. Yun Xu. 2008. An adaptive direct quadrature method of moment for population balance equations. AIChE Journal 54 (11): 2872-2887. 10.1002/aic.11599.

150. Su, Junwei, Zhaolin Gu, Yun Li, Shiyu Feng, X. Yun Xu. 2007. Solution of population balance equation using quadrature method of moments with an adjustable factor. Chemical Engineering Science 62 (21): 5897-5911. http://doi.org/10.1016/j.ces.2007.06.016.

151. Swanson, B. F. 1981. A Simple Correlation Between Permeabilities and Mercury Capillary Pressures. Journal of Petroleum Technology. 10.2118/8234-PA.

152. Taghavy, Amir, Kurt D. Pennell, Linda M. Abriola. 2015. Modeling coupled nanoparticle aggregation and transport in porous media: A Lagrangian approach. Journal of Contaminant Hydrology 172: 48-60. https://doi.org/10.1016/j.jconhyd.2014.10.012.

153. Takamura, Koichi, Theo G. M. van de Ven. 2010. Comparisons of modified effective medium theory with experimental data on shear thinning of concentrated

latex dispersions. Journal of Rheology 54 (1): 1-26. http://dx.doi.org/10.1122/1.3263700.

154. Thomas, D. N., S. J. Judd, N. Fawcett. 1999. Flocculation modelling: a review. Water Research 33 (7): 1579-1592. https://doi.org/10.1016/S0043-1354(98)00392-3.

155. Thongmoon, M., R. McKibbin. 2006. A comparison of some numerical methods for the advection-diffusion equation- See more at: . Research Letters in the Information and Mathematical Sciences 10: 49-62.

156. Todd, B. J. . 1990. Numerical modeling of in situ gelation in porous media.

157. Trefalt, Gregor, Sven Holger Behrens, Michal Borkovec. 2016. Charge Regulation in the Electrical Double Layer: Ion Adsorption and Surface Interactions. Langmuir 32 (2): 380-400. 10.1021/acs.langmuir.5b03611.

158. Vaferi, B., V. Salimi, D. Dehghan Baniani, A. Jahanmiri, S. Khedri. 2012. Prediction of transient pressure response in the petroleum reservoirs using orthogonal collocation. Journal of Petroleum Science and Engineering 98–99: 156-163. http://dx.doi.org/10.1016/j.petrol.2012.04.023.

159. Vaferi, Behzad, Reza Eslamloueyan. 2015. Simulation of dynamic pressure response of finite gas reservoirs experiencing time varying flux in the external boundary. Journal of Natural Gas Science and Engineering 26: 240-252. http://dx.doi.org/10.1016/j.jngse.2015.06.026.

160. van den Vlekkert, Hans, Luc Bousse, Nico de Rooij. 1988. The temperature dependence of the surface potential at the Al2O3/electrolyte interface. Journal of Colloid and Interface Science 122 (2): 336-345. http://dx.doi.org/10.1016/0021-9797(88)90369-4.

161. van der Linden, Marte, Breanndán O. Conchúir, Elisabetta Spigone, Arun Niranjan, Alessio Zaccone, Pietro Cicuta. 2015. Microscopic Origin of the Hofmeister Effect in Gelation Kinetics of Colloidal Silica. The Journal of Physical Chemistry Letters 6 (15): 2881-2887. http:dx.doi.org/10.1021/acs.jpclett.5b01300.

162. Versteeg, Henk Kaarle, Weeratunge Malalasekera. 2007. An introduction to computational fluid dynamics: the finite volume method, Pearson Education (Reprint).

163. Verwey, E. J. W. , J. Th. G. Overbeek. 1948. Theory of the stability of lyophobic colloids. Amsterdam, Elsevier Publishing Co. (Reprint).

164. Visser, J. 1995. PARTICLE ADHESION AND REMOVAL: A REVIEW. Particulate Science and Technology 13 (3-4): 169-196. 10.1080/02726359508906677.

165. Vlieghe, Mélody, Carole Coufort-Saudejaud, Alain Liné, Christine Frances. 2016. QMOM-based population balance model involving a fractal dimension for the flocculation of latex particles. Chemical Engineering Science 155: 65-82. https://doi.org/10.1016/j.ces.2016.07.044.

166. Wang, Chao, Aparna Devi Bobba, Ramesh Attinti, Chongyang Shen, Volha Lazouskaya, Lian-Ping Wang, Yan Jin. 2012. Retention and Transport of Silica Nanoparticles in Saturated Porous Media: Effect of Concentration and Particle Size. Environmental Science & Technology 46 (13): 7151-7158. 10.1021/es300314n.

167. Weston, J. S., D. Venkataramani, C. P. Aichele, B. P. Grady, J. Harwell, D. Resasco. 2014. Pseudosolid, Shear-Thinning Gel Formation in Binary Dispersions of Metal Oxide Nanoparticles at Low Volume Fractions. Langmuir 30 (49): 14982-14990. http:dx.doi.org/10.1021/la503442a.

168. Wheeler, John C. 1974. Modified moments and Gaussian quadratures. 287-296. 10.1216/RMJ-1974-4-2-287.

169. Yao, Kuan-Mu, Mohammad T. Habibian, Charles R. O'Melia. 1971. Water and waste water filtration. Concepts and applications. Environmental Science & Technology 5 (11): 1105-1112. 10.1021/es60058a005.

170. Yotsumoto, Hiroki, Roe-Hoan Yoon. 1993. Application of Extended DLVO Theory. Journal of Colloid and Interface Science 157 (2): 434-441. http://dx.doi.org/10.1006/jcis.1993.1206.

171. Yu, Jianjia, Cheng An, Di Mo, Ning Liu, Robert L. Lee. 2012. Study of Adsorption and Transportation Behavior of Nanoparticles in Three Different Porous Media. Presented at the SPE Improved Oil Recovery Symposium, Tulsa, Oklahoma, USA, 14-18 April, 10.2118/153337-MS.

172. Yuan, C., R. O. Fox. 2011. Conditional quadrature method of moments for kinetic equations. Journal of Computational Physics 230 (22): 8216-8246. http://doi.org/10.1016/j.jcp.2011.07.020.

173. Zakaria, A. S., H. A. Nasr-El-Din, M. Ziauddin. 2015. Flow of Emulsified Acid in Carbonate Rocks. Industrial & Engineering Chemistry Research 54 (16): 4190-4202. 10.1021/ie504167y.

174. Zhang, Qun, Song Cen. 2015. Multiphysics Modeling: Numerical Methods and Engineering Applications: Tsinghua University Press Computational Mechanics Series, Elsevier (Reprint).

175. Zhang, T. . 2012. Modeling of Nanoparticle Transport in Porous Media. Ph.D., University of Texas at Austin, Austin, Texas.

176. Zhang, Tiantian, Drew Davidson, Steven Lawrence Bryant, Chun Huh. 2010. Nanoparticle-Stabilized Emulsions for Applications in Enhanced Oil Recovery. Presented at the SPE Improved Oil Recovery Symposium, Tulsa, Oklahoma, USA, 24-28 April 2010, 10.2118/129885-MS.

177. Zhao, Ningbo, Xueyou Wen, Jialong Yang, Shuying Li, Zhitao Wang. 2015. Modeling and prediction of viscosity of water-based nanofluids by radial basis function neural networks. Powder Technology 281: 173-183. http://dx.doi.org/10.1016/j.powtec.2015.04.058.

178. Ziauddin, Murtaza E., Emmanuel Bize. 2007. The Effect of Pore Scale Heterogeneities on Carbonate Stimulation Treatments. Presented at the SPE Middle East Oil and Gas Show and Conference, Manama, Bahrain, 11-14 March, 10.2118/104627-MS.